

DTIC FILE COPY

2

AD-A218 330

# BOEING

PROCESSING, FABRICATION, CHARACTERIZATION  
AND DEVICE DEMONSTRATION OF HIGH  
TEMPERATURE SUPERCONDUCTING CERAMICS

F49620-88-C-0143

Air Force Annual Technical Report

1 October, 1988 - 30 November, 1989

DTIC  
SELECTE  
FEB 23 1990  
S W D

Approved for public release;  
distribution unlimited.

AIR FORCE OFFICE OF SCIENTIFIC RESEARCH (AFSC)  
POINT OF TRANSMISSION TO DTIC  
This document report is approved and is  
approved for public release (AR 190-12).  
Distribution is unlimited.  
MATTHEW J. KERPER  
Chief, Technical Information Division

## DISTRIBUTION STATEMENT A

Approved for public release;  
Distribution Unlimited

90 02 23 030

Approved for public release;

2

The views and conclusions contained in this document are those of the authors and should not be interpreted as necessarily representing the official policies or endorsements, either expressed or implied, of the Defense Advanced Research Projects Agency or the U.S. Government

**PROCESSING, FABRICATION, CHARACTERIZATION  
AND DEVICE DEMONSTRATION OF HIGH  
TEMPERATURE SUPERCONDUCTING CERAMICS**

F49620-88-C-0143

Air Force Annual Technical Report

1 October, 1988 - 30 November, 1989

Submitted by:

**BOEING AEROSPACE AND ELECTRONICS**

Sponsored by:

Defence Advanced Research Projects Agency  
DARPA Order No. 6499

Monitored by:

AFOSR Under Contract No. F49620-88-C-0143

PM: Dr. Thomas S. Luhman  
(206) 234-2683

PI's: Dr. Thomas S. Luhman  
(206) 234-2683

Dr. Ilhan Aksay  
(206) 543-2625

DTIC  
ELECTE  
FEB 23 1990  
D

**DISTRIBUTION STATEMENT A**  
Approved for public release  
Distribution unlimited

# REPORT DOCUMENTATION PAGE

Form Approved  
OMB No. 0704-0188

Public reporting burden for this collection of information is estimated to average 1 hour per response, including the time for reviewing instructions, searching existing data sources, gathering and maintaining the data needed, and completing and reviewing the collection of information. Send comments regarding this burden estimate or any other aspect of this collection of information, including suggestions for reducing this burden, to Washington Headquarters Services, Directorate for Information Operations and Reports, 1215 Jefferson Davis Highway, Suite 1204, Arlington, VA 22202-4302, and to the Office of Management and Budget, Paperwork Reduction Project (0704-0188), Washington, DC 20503.

1. AGENCY USE ONLY (Leave blank)		2. REPORT DATE January 1990	3. REPORT TYPE AND DATES COVERED Final Report 9-30-88 to 9-29-89	
4. TITLE AND SUBTITLE Processing, Fabrication, Characterization, and Device Demonstration of High Temperature-Superconducting Ceramics			5. FUNDING NUMBERS 62310E 6499/01	
6. AUTHOR(S) Thomas Luhman				
7. PERFORMING ORGANIZATION NAME(S) AND ADDRESS(ES) Boeing Aerospace Co. Seattle, WA 98124 <b>AFOSR-TR-</b>			8. PERFORMING ORGANIZATION REPORT NUMBER <b>90-0236</b>	
9. SPONSORING/MONITORING AGENCY NAME(S) AND ADDRESS(ES) AFOSR/NC Building 410 Bolling AFB, DC 20332-6448			10. SPONSORING/MONITORING AGENCY REPORT NUMBER F49620-88-C-0143	
11. SUPPLEMENTARY NOTES				
12a. DISTRIBUTION/AVAILABILITY STATEMENT Approved for public release; Distribution is unlimited			12b. DISTRIBUTION CODE	
13. ABSTRACT (Maximum 200 words) See Atch.				
14. SUBJECT TERMS			15. NUMBER OF PAGES 180	
			16. PRICE CODE	
17. SECURITY CLASSIFICATION OF REPORT UNCLASSIFIED	18. SECURITY CLASSIFICATION OF THIS PAGE UNCLASSIFIED	19. SECURITY CLASSIFICATION OF ABSTRACT UNCLASSIFIED	20. LIMITATION OF ABSTRACT UL	

R

13. Success with organometallics, citrates, and sintered powder compacts has resulted in two approaches for further development of strain tolerant conductors. They are, thin fibers and tapes, and bulk monoliths.

A thorough understanding of the phase relationships in high temperature superconductors, including those phase relationships exhibited by the oxygen sublattice has been developed. This has allowed approaches for addressing the weak-link problem. Processes are being developed to reduce the grain size of fibers, tapes and monoliths. This approach offers the potential to deliver strong, fine-grained material and, with the correct alteration of grain boundaries, the elimination of poor electrical conduction across the weak=links. Other facets of this approach include attempts to texture the fine grains, produce adequate porosity to ensure good oxygenation, and the possible incorporation of silver for matrix strengthening. Work was pursued for producing candidate material for devices based on controlling high temperature peritectic reactions, for example seeding of fibers and tapes with  $Y_2O_3$ .

15

## TABLE OF CONTENTS

<b>PROGRAM SUMMARY</b>	5
<b>PROGRAM OBJECTIVES</b>	5
<b>PROGRAM STATUS (MILESTONE SCHEDULES)</b>	5
<b>SUMMARY OF PROGRAM TASK SELECTIONS FOR SECOND YEAR</b>	8
<b>SPECIFIC TECHNICAL ACCOMPLISHMENTS IN FOURTH QUARTER</b>	8
<b>ACCOMPLISHMENTS - (i) TECHNICAL PROBLEM</b>	13
<b>(A) CHEMISTRY AND PROCESSING</b>	15
Fibers	15
Powders	15
Tapes	16
Films	16
<b>(B) CHARACTERIZATION--MICROSTRUCTURE AND         SUPERCONDUCTING PROPERTIES</b>	17
<b>(C) MODELING</b>	18
<b>(D) DEVICE REQUIREMENTS AND FABRICATION APPROACHES</b>	19
<b>ACCOMPLISHMENTS - (ii) GENERAL METHODOLOGY</b>	20
<b>(A) CHEMISTRY AND PROCESSING</b>	21
Chemical Synthesis	21
Powders	21
Tapes	22
Fiber Spinning and Processing	23
Sputter Deposition of Superconducting Thin Films	23
Laser Ablation of Superconducting Thin Films	24
Barrier Films	24
<b>(B) CHARACTERIZATION--MICROSTRUCTURE AND         SUPERCONDUCTING PROPERTIES</b>	25

(C)	MODELING	25
(D)	DEVICE REQUIREMENTS AND FABRICATION APPROACHES	26
ACCOMPLISHMENTS - (iii) TECHNICAL RESULTS		28
(A)	CHEMISTRY AND PROCESSING	29
	General Synthesis	29
	Powders	29
	Tapes	41
	Fibers	44
	Thin Films by Reactive Sputtering Using A Single, Multicomponent, Spherical Target	50
	Thin Films by Laser Ablation	55
	Thick Films by Plasma Spraying	57
(B)	CHARACTERIZATION--MICROSTRUCTURE AND SUPERCONDUCTING PROPERTIES	58
	<u>MICROSTRUCTURE</u>	58
	Firing In Air	58
	Formation of Tetragonal 123 in Helium	61
	Reversibility of High Temperature Phases	61
	Formation of Orthorhombic 123	64
	Tape Texture	66
	Heat Treatment Effects On Grain Size	66
	<u>SUPERCONDUCTING PROPERTIES</u>	71
(C)	MODELING	79
	Phase Diagrams	79
	XAFS Modeling	79
	La <sub>2</sub> CuO <sub>4</sub>	79
	Superconducting Properties	81
(D)	DEVICE REQUIREMENTS AND FABRICATION APPROACHES	86

Superconducting Rivet Gun	86
Electromagnetic Window	98
Q Measurements on ICI's Superconducting Coil	99
<b>GOALS FOR THE NEXT REPORTING PERIOD</b>	105
<b>PROBLEM AREAS</b>	105
<b>CORRECTIVE ACTION</b>	105
<b>FOURTH QUARTER PUBLICATIONS</b>	105
<b>RECENT PRESENTATIONS</b>	106
<b>FOURTH QUARTER PATENT DISCLOSURES</b>	106
<b>ATTACHMENTS: FOURTH QUARTER WORK BEING PREPARED FOR PUBLICATION</b>	

"Effects of Silver on Microstructural and Superconducting Properties of  $\text{YBa}_2\text{Cu}_3\text{O}_{7-x}$ ", Michael Strasik, Thomas Luhman, Kay Youngdahl, and James Pillers.

"Effects of Metal Doping on the Shape of AC Susceptibility Curves of  $\text{YBa}_2\text{Cu}_3\text{O}_{7-x}$ ", Thomas Luhman, Mike Strasik and Kay Youngdahl.

"Effects of Metal Doping on the Superconducting Properties of  $\text{YBa}_2\text{Cu}_3\text{O}_{7-x}$ ", Thomas Luhman, Mike Strasik, and Kay Youngdahl.

"Summary of Lattice Parameter Variation Analysis in  $\text{YBa}_2\text{Cu}_3\text{O}_{7-x}$  by a Novel Technique", Brad Thiel.



Accession For	
NTIS CRA&I	<input checked="" type="checkbox"/>
DTIC TAB	<input type="checkbox"/>
Unannounced	<input type="checkbox"/>
Justification	
By	
Date	
DTIC	
A-1	

# AIR FORCE FINAL TECHNICAL REPORT

## PROGRAM SUMMARY

BOEING-UN. of WASHINGTON-WSU-BATTELLE

*Col + 1/2 hr by B*  
*thru*  
**PROGRAM OBJECTIVES** The goal of ~~our~~ program is to develop material processes for new high temperature superconducting ceramics and to demonstrate these processes in a high current device. We believe that if these new materials are to be useful for high current applications (where magnetic fields are necessarily present) two major problems must be solved:

o reliable, cost-effective processes must be developed to produce mechanically stable, strain-tolerant, superconducting fibers, tapes, or monoliths, and;

o significantly larger critical current densities must be achieved in applied magnetic fields, e.g., probably  $10^5$  amp/cm<sup>2</sup> at 1 tesla and 77K is required as a minimum for most applications.

*Keywords: Current density (AC)*

**PROGRAM STATUS** Information regarding program status in relation to originally scheduled milestones is presented in the accompanying Program Master Schedule.

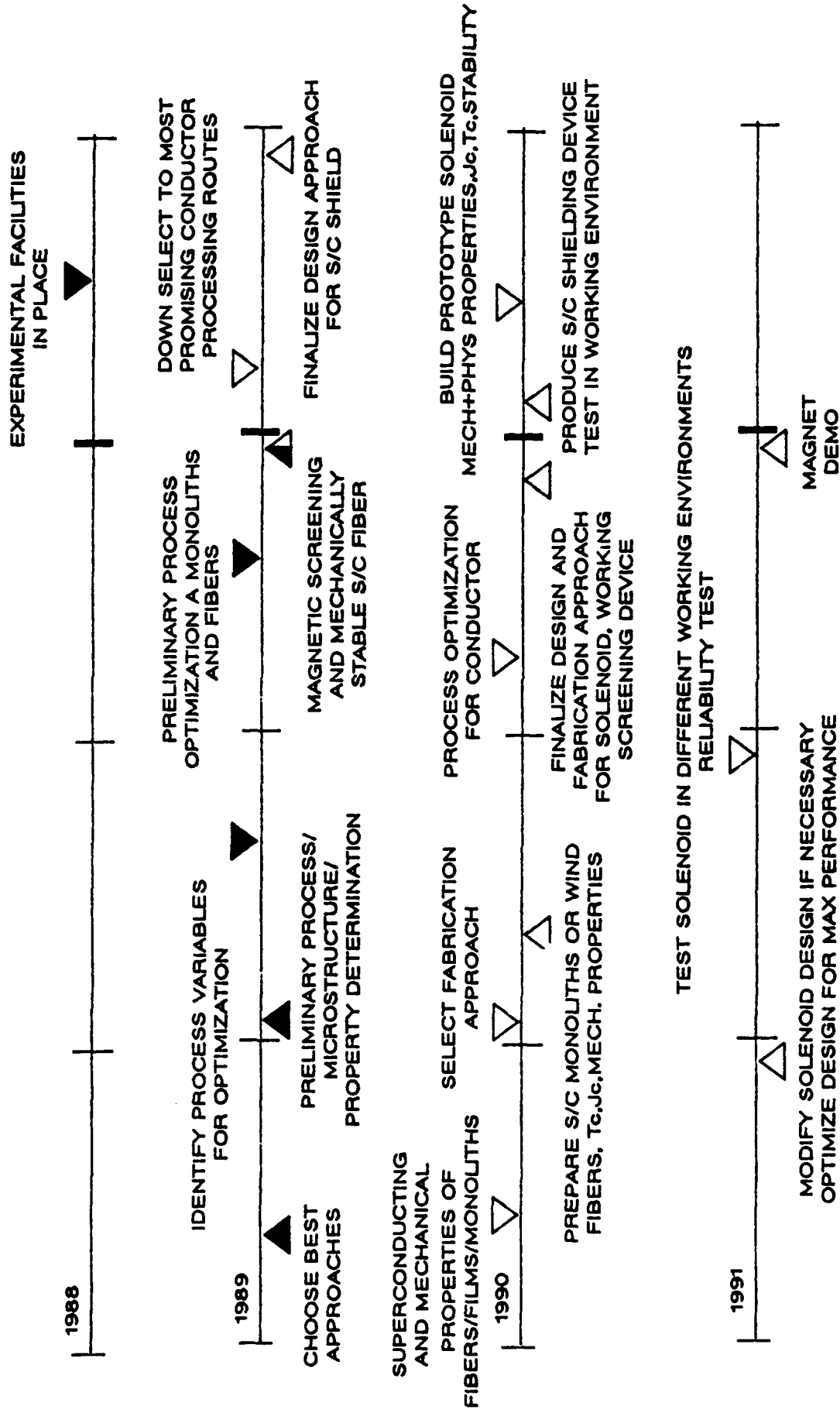
Our work in this first year was directed toward very specific objectives. Each of these objectives represent milestones for the development of high current devices in the third year of a three year program. For reference, we have included in the present status report a copy of the overall three year program milestone schedule. We have successfully accomplished each of the planned first year objectives. These objectives are presented in the accompanying Program Master Schedule.

The objectives were strongly influenced by our early perception of the need to understand the fundamental relationships between processes, microstructure, and superconducting properties. They are related to work in the following tasks: a) construction of experimental facilities, b) selection of approaches for producing strain tolerant conductors, c) selection of approaches for elimination of weak-links, and d) assessment of the potential for electromagnetic screening devices.





# 3 YEAR PROGRAM MAJOR MILESTONE SCHEDULE



**SUMMARY OF PROGRAM TASK SELECTIONS FOR THE SECOND YEAR** We now have a complete facility for the characterization of superconducting properties, including a.c. susceptibility, resistivity, and current density as a function of temperature and magnetic field. We are finishing the construction of an electromagnetic copper coil to enhance the ease of routine  $J_c$  measurements in a magnetic field. In addition, we have constructed an experimental facility for the determination of electromagnetic screening characteristics of superconductors.

Success with organometallics, citrates, and sintered powder compacts has enabled us to select two approaches for further development of strain tolerant conductors in the second year. They are, thin fibers and tapes, and bulk monoliths.

We now have a thorough understanding of the phase relationships in high temperature superconductors, including those phase relationships exhibited by the oxygen sublattice. This knowledge has allowed us to select two approaches for addressing the weak-link problem. First we will continue to develop processes to reduce the grain size of fibers, tapes and monoliths. We believe this approach offers the potential to deliver strong, fine-grained material and, with the correct alteration of grain boundaries, the elimination of poor electrical conduction across the weak-links. Other facets of this approach include attempts to texture the fine grains, produce adequate porosity to ensure good oxygenation, and the possible incorporation of silver for matrix strengthening. Secondly, we will continue to pursue work on producing candidate material for devices based on controlling high temperature peritectic reactions, for example seeding of fibers and tapes with  $Y_2O_3$ .

Finally, we have shown the near-term potential of thin films to meet Boeing program requirements for improved electromagnetic screening. Our experimental work has lead to the selection of laser ablation and sintered powder films as processes which show high potential for early program implementation. These processes were, therefore, selected for further testing and process optimization in the second year's effort. In addition, our analyses revealed the potential for bulk flux-trapped magnets to be operated in a superconducting rivet gun. This system remains the most likely first use for our monolithic material.

**SPECIFIC TECHNICAL ACCOMPLISHMENTS IN THE FOURTH QUARTER** Research efforts in the fourth quarter focused on the following areas: (A) processing of ceramics; (B) characterization, microstructure, and superconducting properties; (C) modeling; and (D) device requirements/fabrication approaches.

## (A) PROCESSING OF CERAMICS

In the processing area we concentrated on four superconductor forms: fibers, powders, tapes, and films.

**Fibers** -- Studies continued on the nature of citrate sol-gel evolution of the tetragonal phase from precursor mixtures, in particular the low temperature development of a tetragonal phase which could be converted into the superconducting orthorhombic phase without high temperature heat treatment and the accompanying grain growth from liquid phase sintering. Changes in the structure of the 123 phase as function of temperature and gas environment were identified by DXRD. In air, a low temperature tetragonal (LTT) phase is always formed initially at about 750C followed by the formation of the well-split high temperature tetragonal (HTT) phase at about 875C. The LTT phase cannot be directly converted to the superconducting, orthorhombic phase. In an oxygen-deficient environment, the HTT phase can be formed directly starting at about 625C. In order for the orthorhombic phase to be formed, it is necessary to heat samples to higher temperatures (750C) and hold there for a sufficient length of time.

We also determined: 1) the HTT phase is not stable in an oxygen-deficient environment at temperatures above 700C, 2) the drying process for the citrate sol-gel precursor influences the rate and extent of the decomposition of the HTT phase in an oxygen-deficient environment, and 3) the similarities and differences between our freeze-dried precursors and those from SRI Intn'l.

A series of low temperature pyrolysis experiments in air and oxygen were initiated to improve cross-linking in the evolving precursors. These experiments are designed to prevent the formation of elemental oxides and promote direct formation of the ternary 123 compound.

**Powders** -- In this area we continued our efforts to optimize powder sintering behavior for grain size and  $J_c$  control. The influence of  $\text{CO}_2$  was studied. Removal of  $\text{CO}_2$  during heat treatment of co-precipitated powder promoted the low temperature decomposition of  $\text{BaCO}_3$  and associated liquid phase sintering allowed formation of tetragonal 123 at 700C.

We found that very small additions of Ag (1 at. %) catalyze the decomposition of  $\text{BaCO}_3$  which promotes the direct formation of the tetragonal phase without the intermediate formation of  $\text{BaCuO}_2$ . This eliminated much of the eutectic melting associated with  $\text{BaCuO}_2 + \text{CuO}$ , and produced fine grained high  $T_c$  material even at a heat treatment temperature of 970C. The material was friable in nature with a low  $J_c$  ( $< 50 \text{ A/cm}^2$ ). Subsequent thermal cycling to 1010C for short times improved the connectivity between grains and  $J_c$  increased by an order of magnitude without significant grain growth. This produced a porous sample which was strong and easily

oxygenated at 450C.

**Tapes** -- Nitrate (123)/silver nitrate precursor solutions were prepared containing 2.5, 12.5, 25, and 50 wt. % Ag. The solutions were spray-dried for thick-film tapes. Heat treatments were performed at 915C for 1hr., well below the melting temperature of Ag. The 2.5 and 12.5 % materials exhibited microstructures similar to unalloyed samples with occasional large (20 micron) sized grains. Higher Ag contents eliminated these excessively large grains. The addition of Ag was also seen to catalyze formation of the tetragonal phase at lower temperatures in these materials.

**Films** -- Epitaxial, superconducting YBaCuO thin films were grown in-situ on (100)-SrTiO<sub>3</sub> by excimer laser ablation from a multicomponent target. This quarter the films were grown in a new deposition chamber, which allows precise control of important parameters including substrate temperature, oxygen partial pressure, target rotation, and laser energy density. By growing the films in-situ, the maximum substrate temperature was 700°C, compared to more than 900°C needed for films deposited at room temperature, thus minimizing substrate-film reactions.

Films grown by laser ablation showed an onset of superconductivity at 91K and zero resistance at 86.5K. Transport critical current densities in zero field were  $1.9 \times 10^6$ ,  $6.7 \times 10^4$ , and  $1.9 \times 10^4$  amps/cm<sup>2</sup> at 20, 60, and 77K, respectively, using a  $5 \times 10^{-9}$  ohm-cm resistivity criterion.

The substrate, (100)-SrTiO<sub>3</sub>, in the present work, was heated to 700°C during deposition. Following growth of an epitaxial thin film, which ranged from 0.1-0.4 microns in thickness, the laser was turned off and the oxygen pressure was increased to 1 atm. The substrate temperature was then decreased to 450°C for several hours to convert the film to the orthorhombic structure. XRD analysis showed the films to be highly oriented, with the c-axis perpendicular to the substrate. The degree of alignment of the films with respect to the a- and b-axes has not yet been determined.

While much progress has been made during the past quarter in growing high quality superconducting thin films, further optimization of processing conditions is needed to reach the target critical current densities of greater than  $10^5$  A/cm<sup>2</sup> at 77K in fields of 1 tesla. The rate of deposition is likely to be a critical parameter; if the deposition is too fast, the films are misaligned with regard to the a- and b-axes and thus limited in their current-carrying capacity. Contact resistivities must be improved. While mechanically pressed indium dots have been used extensively in the past, our present direction is to deposit silver contacts by sputtering/evaporation, followed by annealing in oxygen. To minimize joule heating of the films during critical current density determinations, contact resistances of

approximately 1 micro-ohm or less are desired.

#### **(B) CHARACTERIZATION -- MICROSTRUCTURE AND SUPERCONDUCTING PROPERTIES**

**Microstructure** -- A study of alloy additions to the 123 structure across the first row of the periodic chart (electron to atom ratios,  $e/a$ ) revealed systematic variations in  $T_c$ , a.c. susceptibility, and transport critical current densities. The approach used alloy additions rather than substitutions in an attempt to place these dopants at the grain boundaries. Substitutions create an enhanced solubility for the new solute element thus enabling the solute to enter the lattice. Additions maintain the point stoichiometry of the 123 compound which favors placement of the solute addition outside of the lattice, at the grain boundaries. The systematic nature of the property changes appears to be related to effects on the nature and extent of liquid phases during heat treatment. Grain sizes and twinning structure varies with  $e/a$  ratios. This investigation is now expanding to development of optimized heat treatments for improved  $J_c$  performance in magnetic fields.

A TEM investigation emphasized further development of correlations between nano-scale structural variations and a.c. susceptibility measurements. Traces of reciprocal lattice vectors were used to deconvolute the twin-split spots and give the  $(\Delta a)/a$  distribution. Most grains appear to have one major  $(\Delta a)/a$ , varying amounts of tetragonal phase, and some lesser amounts of secondary  $(\Delta a)/a$ . These distributions are empirically reflected in the onset of the a.c. susceptibility measurement of  $T_c$ .

**Superconducting Properties** -- We have developed a method for electrical contacts which provide a contact resistivity of  $10^{-7} \text{ ohm-cm}^2$ . This process utilizes metallic silver foils and is compatible with heat treatment procedures. As inferred above we routinely make  $J_c$  measurements on all of our samples. We have shown that these measurements are influenced by poorly made contacts,  $>10^{-4} \text{ ohm-cm}^2$ , when the sample currents exceed about 3 amps. Using the new contact method we have produced melt textured material according to the method employed by the University of Houston. These samples were selected to contain some grain boundaries. Current densities were  $440 \text{ amp/cm}^2$  in a self field of 21 gauss. Clearly higher  $J_c$  values in melt textured samples are simply obtained on selected single crystal samples.

#### **(C) MODELING**

Electrical contacts to the superconductor were modeled in terms of the stress imposed by differences in expansion coefficients of the

superconductor and contact material. The significance of sample porosity and contact thickness was confirmed by experimentally measuring the contact resistance and observing the thicknesses associated with contact separation from the sample.

A program was written to calculate the surface energies of various basal plane orientations. Variations in energy were predicted as a function of ordering in the oxygen sublattice.

#### **(D) DEVICE REQUIREMENTS/FABRICATION APPROACHES**

Among the potential devices we are exploring for application of superconductors is an electromagnetic rivet gun. In it, capacitors are replaced by magnetic energy stored in a flux-trapping magnet. Electrical and physical property requirement calculations and preliminary designs were updated based on the critical current performance now obtainable in bulk materials. Studies show that higher critical current densities are still required before the 123 compounds can be efficiently utilized. Several patent disclosures were submitted pertaining to the design, configuration, and operation of the gun.

Calculations were also performed on the concept of an electromagnetic window using superconducting coatings. These calculations were directed to a problem recently identified on a Boeing product. Results of these calculations suggest the possibility of a near-term use of thin film coatings to solve and meet the program requirement. Experimentation is now underway to determine the frequency specific response of such coating. The near-term status of this application is related to fact that the superconductor does not have to be formed directly on the window material but may be fabricated first and then simply incorporated into the device.

ACCOMPLISHMENTS - (i) TECHNICAL PROBLEM



## ACCOMPLISHMENTS - (i) TECHNICAL PROBLEM

Each major section of this report is organized in a similar manner. For more details on fibers, powders, monoliths, and films please refer to the appropriate subsections on Chemistry, Microstructure, Device Requirements etc.

The objective of our program is to develop material processes for the new high temperature superconducting ceramics and to demonstrate these processes in a high current device. We believe if these new materials are to be useful for such high current applications (where magnetic fields are necessarily present) two major problems must be solved:

- \* Reliable, cost effective, processes must be developed to produce mechanically stable, strain tolerant, superconducting fibers, tapes, films, or monoliths, and;

- \* Significantly larger critical current densities must be achieved in applied magnetic fields, e.g., probably  $10^5$  A/cm<sup>2</sup> at 1 Tesla and 77K is required as a minimum for most applications.

Our research program is designed to identify and solve problems related to the:

- \* synthesis and processing of superconducting oxide powders, monoliths, films, tapes and fibers;

- \* role of microstructure on flux pinning (lattice strain, twins, grain boundaries, chemical inhomogeneity, dislocations, and point defects);

- \* development of protocols for the characterization of physical and superconducting properties of the intermediate and final materials involved in processing;

- \* development of mathematical models that describe the physical and superconducting behavior of the materials being processed; and,

- \* design, building and testing of a prototype aerospace devices.

These focus areas are designated as (A) "Chemistry and Processing", (B) "Characterization", (C) "Modeling", and (D) "Device Requirements/Fabrication Approaches".

After nine months of work on the DARPA/AFOSR contract we have had many accomplishments and thus far met all of our milestones. We

expect the remainder of this year's effort to be as successful. The following table presents a short synopsis of our views on future material development issues; required now if the goal of producing high current devices is to be reached.

#### (A) CHEMISTRY AND PROCESSING

In the processing area, we concentrated on four superconductor forms; fibers, powders, tapes, and films.

##### Fibers

Fibers of  $\text{YBa}_2\text{Cu}_3\text{O}_{7-x}$  were prepared by a novel hydrogel-based spinning fluid. A process was developed to produce continuous precursor fibers with diameters as fine as 12 microns. Conversion to the orthorhombic phase was confirmed by XRD. The mechanical strength appears to be limited by micro-porosity which is not eliminated during heat treatment.

Work on Ag-doped  $\text{YBa}_2\text{Cu}_3\text{O}_{7-x}$  fibers explored high heat treatment temperatures where it was found that silver lowered the melting temperature of the sol produced fibers. The lower melting temperatures resulted in a "localized" melt-textured effect for large silver concentrations (exceeding 10% in  $\text{YBa}_2\text{Cu}_3\text{O}_{7-x}\text{Ag}_y$ ). Critical current density measurements are planned for each of the above fibers.

##### Powders

Silver doping of freeze-dried powders has led to increases in the critical current density. Sintered compacts of silver alloyed  $\text{YBa}_2\text{Cu}_3\text{O}_{7-x}\text{Ag}_y$  showed evidence of "localized" melt-texturing. Our highest  $J_c$  to date is a 10% Ag addition to the 123 composition. The material was prepared by our freeze-drying technique and exhibited  $J_c(H_{\text{applied}}=0)=4.2 \times 10^4$  amp/cm<sup>2</sup>. This compares, for example, with a value of  $0.9 \times 10^4$  amp/cm<sup>2</sup> for the ICI material (our measurement). These numbers are based on an electrical resistivity criterion of  $5 \times 10^{-9}$  ohm cm and the data has been corrected for self field effects on Josephson Junctions at the grain boundary (see Modeling under Technical results).

We examined the effects of calcination conditions, including calcination temperature, soaking time and atmosphere on the thermal conversion of precursor powder to orthorhombic 123 powder. The precursor powder, provided by the Seattle Superconductor Company, was a mixture of  $\text{Y}_2\text{O}_3$ ,  $\text{BaCO}_3$  and  $\text{CuO}$ , carbonate, and copper (II) oxide. The superconducting properties of the calcined product, as measured by flux exclusion techniques, were very sensitive to the calcination conditions.

Finally, we have developed a method for making coil shapes. The approach uses freeze-dried powders sintered together with a YBCO sol-gel. Property characterization is just underway.

### Tapes

A new route was developed for the fabrication of tapes using fine precursor powders. Conversion to the 123 Orthorhombic phase was accomplished in the tape form. This minimized the grain growth problems encountered when we started with 123 powders.

Orientation effects in tape-cast  $\text{YBa}_2\text{Cu}_3\text{O}_{7-x}$  were studied by means of XRD texture analysis and TEM diffraction. We observed evidence of preferred grain growth and orientation of the [001] planes. We have also identified a possible trend linking the statistical distribution of  $\Delta a/a$  values measured across a grain with transition temperature widths. The distributions also seem to be reflected in changes to the onset superconducting temperature.

### Films

Thin films have provided the highest critical current densities obtained for HTSC materials to date. The presence of localized strains and impurities acting as pinning centers are among several possible explanations why thin films have outperformed bulk single crystals. An understanding of processes controlling critical current densities in thin films would be beneficial to efforts aimed at improving critical properties of bulk materials.

We have chosen two primary methods to prepare thin films: reactive sputtering, using a single, multicomponent target of spherical geometry, and laser ablation. In addition, plasma spraying processes have been developed to prepare thick superconducting films, utilized to make spherical sputtering targets. Any thin film preparation technique, if those films are to be useful in a high current device, must be able to produce a smooth surface texture with the appropriate composition, correct crystal phase, and with the optimum oxygen stoichiometry. Critical properties of the thin films are a high  $T_c$ , small transition width, and high  $J_c$  ( $>10^5 \text{ A/cm}^2$  in a field of 1 Tesla). Laser ablation technology has been pursued elsewhere with some success; spherical target sputtering using a single, water-cooled, multicomponent target is unique to this program.

Plasma-sprayed films of  $\text{YBaCuO}$  on  $\text{MgO}$  and stabilized zirconia have been prepared that exhibited zero resistivity by 85.5K. Onset temperatures ranged from 88-92K for these films having thicknesses ranging from 10-100 microns. Present results are a significant improvement over those obtained earlier, where transition widths typically of 15K were observed. Because relatively large areas can be readily coated using plasma spraying, these methods may be very useful in preparing coatings for electromagnetic shielding

applications.

Improvements in the critical properties of YBaCuO thin films produced by reactive sputtering (using a multicomponent spherical target geometry) have been made. We showed that the multicomponent, spherical target geometry eliminated angular dependencies in the deposition stoichiometry that have been observed for planar targets. Onset temperatures in the range 85-92K have been typically observed, with transition widths of approximately 15K. Some of the broadening in the resistive transition has been attributed to low levels of iron contamination in the target material.

Critical currents rose to more than 300 A/cm<sup>2</sup>, as determined by dc-transport using a 1 microvolt criterion, for Ag-doped cermets deposited by plasma spraying.

Thin YBaCuO films prepared by laser ablation using a neodymium YAG laser at 532 nm have yielded onset temperatures of 89-93K. Although resistivities fell by three or more orders of magnitude by 77K, a low resistance tail persisted to the limit of the cryostat at 55K. These results were similar to those obtained using reactive sputtering.

Electrical contacts to YBaCuO thin films with resistances less than 10<sup>-6</sup>-10<sup>-7</sup> ohm-cm<sup>2</sup> are being made routinely. Silver contacts are deposited onto the films by evaporation to a thickness of 3000 Å followed by mechanical contact with indium wire; annealing following silver contact application has given the lowest resistances thus far.

#### (B) CHARACTERIZATION-- MICROSTRUCTURE AND SUPERCONDUCTING PROPERTIES

**Microstructure** -- We studied DXRD reaction sequencing experiments on three citrate gels (123, Ag-doped 123, and 248) in an oxygen-free environment. Two observations were made: (1) the tetragonal 123 phase begins to form at much lower temperatures, about 600°C, and (2) the HTT phase tends to decompose in an oxygen-free environment at temperatures greater than 700°C. It was not possible to form fully developed orthorhombic 123 when the HTT phase was immediately cooled in air from temperatures between 700-800°C. However we have been able to form orthorhombic 123 (with a diffuse T<sub>c</sub> of 93 K) when the samples are switched from helium to air at 700°C and then raised to 800°C in air and held for 15 hours. Because the HTT decomposition can be reversed in an oxygen environment (above 625°C), we believe this success is due to the almost complete reversibility of the decomposition by virtue of its hold in air at 800°C for 15 hours. Experimentation is continuing to determine the optimum time-temperature-oxygen pressure necessary to

prevent (or minimize) the decomposition so that phase pure orthorhombic 123 can be formed without exceeding a maximum temperature of 800°C.

Preliminary TEM studies on a  $\text{YBa}_2\text{Cu}_3\text{O}_{7-x}\text{Ag}_{0.1}$  sample heat treated at 930°C revealed that the silver addition was located primarily within an amorphous 123 phase located in the intergrain regions. Some evidence exists in the  $T_c$  measurements that the distribution of silver is a function of the heat treatment environment.

Finally, we have conducted several studies correlating grain size with various heat treatment conditions.

**Superconducting Properties** -- We developed a theoretical interpretation of our a.c. susceptibility measurement of the superconducting transition temperature. We showed that the ac susceptibility measurement is capable of discriminating between inter- and intragrain contributions to ac loss properties. This analysis of superconducting property behavior near the onset of the transition will greatly enhance our understanding of important microstructure/process/property relations in YBCO materials. Publication is planned in the Fall MRS meeting.

Using the above interpretation of the ac susceptibility we began an investigation of Ag and Pt doping. Measurements are currently being correlated with  $J_c$  data.

### (C) Modeling

Modeling focused on: (1) use of statistical mechanics of equilibrium and irreversible phenomena to develop mathematical models of microscopic properties, (2) use of mathematical modeling studies of XAFS to develop a detailed picture of the atomic structure and electronic behavior, and (3) calculation of the transport critical current density for bulk sintered monolithic samples of  $\text{YBa}_2\text{Cu}_3\text{O}_{7-x}$  in magnetic fields, and in particular, the self-field induced by the measurement itself.

We modified our computer program so that it is possible to make calculations in the low temperature region without any numerical underflow. Also developed were a set of codes for x-ray absorption fine structure simulations. Simulations using these programs suggest: (1) differences in electronic charge between the Cu-O bonds in 123 and those in  $\text{La}_2\text{CuO}_4$  and, (2) significant structural disorder in the oxygen positions.

The field dependence was assumed to be controlled by intra- and intergranular Josephson junctions. The results of these calculations show that (a) the grain boundaries are limiting the performance of transport critical current densities and, (b) the

intragrain  $J_c$ 's, i.e., the critical current densities of the grains themselves, are as high as those reported for single crystals, typically about  $10^4$  amp/cm<sup>2</sup> at zero fields. This work helps us focus our microstructural and alloying activities toward eliminating the weak-link problem.

#### (D) DEVICE REQUIREMENTS AND FABRICATION APPROACHES

Among the potential devices we have been exploring for application of superconductors is an electromagnetic rivet gun. In it, capacitors are replaced by magnetic energy stored in a flux-trapping magnet. Electrical and physical property requirements were calculated and preliminary designs were obtained. Our studies show that higher critical current densities are required before the 123 compounds can be efficiently utilized. Several patent disclosures are being prepared pertaining to the design, configuration, and operation of the gun.

Calculations were also performed on the concept of an electromagnetic window using superconducting coatings. Results of these calculations suggest the coating thicknesses required is about 1-2 microns. Measurements of the dielectric properties of films prepared by chemical solution techniques and plasma spraying are planned. An experimental apparatus for measuring permeability and reflectivity was modified for operation at liquid nitrogen temperatures.

A superconducting coil was obtained from ICI and its Q value was determined as a function of frequency, from 6-23 MHz. This material showed clear signs of being limited by weak-links. Measurements are continuing to higher frequencies. An interpretation was made of the sample's  $J_c$  in terms of microstructure.

ACCOMPLISHMENTS - (ii) METHODOLOGY

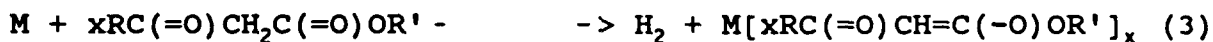
## ACCOMPLISHMENTS - (ii) METHODOLOGY

### (A) CHEMISTRY AND PROCESSING

#### Chemical Synthesis

An array of experimental methods are being employed to prepare thin films, coatings, monoliths and fibers. Among the approaches in this task is an examination of the utility of "molecular processing" or materials chemistry for the preparation of thin films and fibers. Our methodology has centered on the use of tractable organometallic polymer preceramics to first form precursor fibers which can then be pyrolytically transformed into superconducting ceramic fibers.

The general processing scheme involves the synthesis of metal carboxylates and beta-ketoesters under dry-box conditions (exclusion of moisture and air). The synthetic routes examined so far are those shown in the following reactions:



The end components of these reactions are then dissolved as mixtures of appropriate stoichiometry, typically in tetrahydrofuran solutions. The solutions are carefully filtered and solvent is removed to adjust the rheology such that the mixture can be extruded as fibers.

An alternative approach examined to produce spinnable superconductor precursor involves the citric acid/ethylene glycol sol-gel system. The process begins with a liquid mix procedure that uses a polymeric blend of yttrium, barium, and copper acetates. These acetates are dissolved individually in a mixture of ethylene glycol and citric acid. The mixture is then heated to promote polymerization and cross-linking of resulting metal citrates. The resulting glassy mixture is then calcined to remove the organics and produce polymerized hydroxides. Sintering the dried hydroxides produces the desired superconducting oxides.

#### Powders

Many of the practical applications of 123 superconducting materials will rely on the ability to sinter powders to fully dense, strong ceramic monoliths. One methodology we are concentrating on is the cryogenic processing of precursor solutions. We have examined freeze-drying of precursor solutions since this approach offers excellent mixing and does not require any external agents. Freeze-



drying consists of mixing solutions, freezing a solution in liquid nitrogen, sublimation of solution, and calcination. The resulting material is very homogeneous, pure, and of uniform morphology.

Required dense monoliths can be produced by sintering a 123 powder compact or by reaction sintering a 123 powder precursor compact. In the first approach, the only requirement is an ultrafine 123 powder, whereas the second approach requires a chemically homogeneous ultrafine precursor powder which will process into the target 123 ceramic at reduced temperatures--thus enabling smaller grain sizes and fewer defects.

In either case, it is necessary to generate a well-mixed chemically, homogeneous precursor powder. The methodology for preparing such powder begins with the preparation of homogeneous solutions containing the correct stoichiometries of the desired chemical species. For the solution to solid conversion, various techniques may be employed, such as co-precipitation, spray drying/spray pyrolysis, freeze-drying, or sol-gel methods. A certain degree of inhomogeneity is inevitably introduced during processing. This inhomogeneity is proportional to the reaction bath/solution drop size. Our methodology is guided by the requirement to produce a precursor powder with fine scale inhomogeneities so that it converts to a superconducting phase at low temperatures; the reaction vesicle/solution drop size must be minimized. In order to satisfy this condition, we are using microemulsion and freeze-drying techniques. In the microemulsion technique, the typical size of a reaction vesicle is 500-1000Å. Thus, even if chemical inhomogeneities are introduced during the solution to solid conversion, the scale will be smaller than the size of the micelle as will the size of the resulting superconductor powder. In freeze-drying, mixing is achieved on a molecular scale.

#### Tapes

Our initial approach to fabricating tapes is to disperse 123 powders in a suitable binder vehicle and then cast the slurry on a mylar film using the doctor-blade process. The unsintered tape is flexible and can be cut into a variety of shapes prior to sintering. We are currently exploring the effects of heating schedules and atmospheres on the mechanical and superconducting properties of the tapes.

Very little data is available on either the tape casting process or the electrical/mechanical properties of 123 superconducting tapes. One recent critical current density measurement on a 123 tape indicated a zero-field critical current of 25-35 A/cm<sup>2</sup>. With regard to the mechanical properties, recent reports indicate that the compressive fracture strengths in bulk sintered samples of 123 range from 180 to 280 Mpa. The indentation strength data on bulk samples are on the order of 50 Mpa. We believe that there is

significant room for improvement in both the electrical and mechanical properties of properly processed 123 materials.

#### Fiber Spinning and Processing

To develop a detailed process for the spinning, curing and pyrolysis of precursors and precursor fibers it was necessary to construct a continuous fiber fabrication apparatus. (See the First Quarterly Technical Report for a schematic of the apparatus). It consists of a piston-cylinder arrangement wherein gas pressure applied behind the piston causes the polymer/solvent mixture ahead of the piston to extrude through a small die of 70 or 150 microns in diameter. As the fiber is extruded, the solvent can be removed either by evaporation, flash evaporation or solvent exchange. The resulting fiber is then wound around a take-up spool, which can be used to "draw" (ie. lengthen under tension) the fiber. The spooled fiber(s) can be removed from the spool for subsequent conversion to ceramic.

The bulk of the literature on superconducting materials deals with thin films and powders. Far less has been reported concerning the fabrication of superconducting ceramic fibers or wires. The literature that is available on the fabrication of fibers or wires describes several general fabrication methods. One such method involves "canning" wherein a metal (gold or silver) tube is filled with superconducting powder and drawn, by standard die processing to form "composite wires" approximately 1000 microns in diameter. These "wires" exhibit low critical current densities ( $J_c = 50 \text{ A/cm}^2$  at 0 T fields) and are susceptible to core/metal sheath reaction. An alternate approach, wherein a suspension of 123 powder in a solution containing an organic polymer (polyvinylalcohol), to enhance the viscosity, is extruded and pyrolyzed. The highest  $J_c$  (at 77K and 0 T) was  $680 \text{ A/cm}^2$  with a maximum fiber strength of  $\approx 25 \text{ MPa}$ . The sol-gel route and the organometallic precursor route have also been investigated by a few researchers including members of this consortium.

We also have a commercial fiber extruder/spinner in which we have successfully extruded fiber precursors down to 10 microns in diameter.

#### Sputter Deposition of Superconducting Thin Films

We are utilizing the PNL-designed spherical-geometry sputtering system to prepare thin superconducting 123 films [15,16]. The target, source of the sputtered material, is a 5 cm diameter, water-cooled Cu sphere coated with a 0.5-1.0 mm thick plasma-sprayed 123 layer. A single, multicomponent target is used rather than multiple, single component targets. A xenon plasma is produced in the annulus between the target and a hemispherical cap. When the target is biased negatively,  $\text{Xe}^+$  ions attracted from the plasma bombard and sputter atoms from the target surface.

Single multicomponent targets rather than multiple single component targets are used to reduce the operational complexity of the system. Spherical geometry rather than the more common planar geometry is used to overcome problems associated with sputtering multicomponent materials such as  $\text{YBa}_2\text{Cu}_3\text{O}_x$ .

Due to symmetry considerations, the spherical target causes the different angular distributions to be averaged out. Therefore, films with the same composition as the target are produced over the entire top hemisphere. This condition is true only if the plasma density is uniform over the entire hemisphere, which has been verified using Langmuir probe measurements and metal targets. The spherical geometry also averages out effects of  $\text{O}^+$  ions that are emitted from the target surface and which bombard and resputter the deposited film.

Another unique benefit of our design is that it overcomes some problems inherent with use of bulk  $\text{YBa}_2\text{Cu}_3\text{O}_x$  targets. First, plasma sprayed coatings can be easily applied to complex shapes, allowing simple fabrication of spherical and other nonplanar targets. Second, because of the relatively low thermal conductivity of the  $\text{YBa}_2\text{Cu}_3\text{O}_x$  compound, target surface heating occurs in bulk targets. This enhances oxygen ion emission from the target as well as bulk diffusion in the target. Efficient cooling of the thin plasma-sprayed ceramic layer helps to minimize these effects, allowing higher power densities and thus greater deposition rates.

#### Laser Ablation of Superconducting Thin Films

The second harmonic from a neodymium YAG laser at 532 nm is used to ablate bulk  $\text{YBa}_2\text{Cu}_3\text{O}_x$  targets approximately  $1 \text{ cm}^2$  in area. The repetition rate is 10 Hz and energy deposition is 260 mJ/pulse for a spot focused to approximately 50 microns. Substrates were positioned approximately 4 cm from the target. Following deposition, the films were heat treated to 850°C, followed by cooling to and maintaining at 540°C for 1 hour in flowing oxygen.

#### Barrier Films

Zirconia and yttria-stabilized zirconia thin films are prepared by the amino acid-metal nitrate method. An aqueous solution of 0.1 molar zirconium nitrate and 0.3 molar glycine is prepared, which is used to spin coat sapphire and quartz substrates. Spinning rates ranged from 1000-3000 rpm. Multiple coats were applied at room temperature, with the substrates fired to 700°C between successive layers. After typically five layers were applied, the substrate is heated to 900°C for approximately 15 minutes in air. Microstructures were examined in cross-section by TEM; crystal habit is determined using laser Raman spectroscopy.

## **(B) CHARACTERIZATION-- MICROSTRUCTURE AND SUPERCONDUCTING PROPERTIES**

**Microstructure--**The basic microstructural characterization techniques used in the evaluation of microstructures are transmission electron microscopy (TEM), scanning transmission electron microscopy (STEM), x-ray absorption fine structure (XAFS), X-ray diffraction (XRD), dynamic X-ray diffraction (DXRD), and electron energy loss spectroscopy (EELS). Experiments were performed using all modes of analysis including: imaging, diffraction and spectroscopy at resolution levels from 2.0 to 1000Å.

Thin foils for TEM studies are prepared by hand on dry lapping disks to avoid contamination and reduce mechanically induced defects. It is now well established that ion milling introduces defects into the microstructure. Extreme precaution is taken both during the ion milling and during the TEM studies to reduce or eliminate damage to the samples. 40-50 microns thick disks were ion milled in a cold stage (liquid-N<sub>2</sub> temperatures) with a dual ion miller (GATAN 600) at an angle of 20-25 degrees with a specimen current of 0.4 A using 6kV in an argon gas. Samples were kept in a desiccator for storage.

TEM observations are performed in a double tilt (145°,130°) cold stage (liquid N<sub>2</sub>) holder which kept the specimen temperature at 120 K. A Philips 430 T TEM/STEM, which is fitted with a twin objective lens and a LaB<sub>6</sub> filament as the electron source, is used at emission voltages between 200-300 kV. The diffraction experiments were repeated three times over the span of 20 days by leaving the sample in the microscope column (10<sup>-7</sup> torr) to check the reproducibility of the diffraction results. It was determined that there is no detectable damage to the structure during this period.

**uperconducting Properties--**The characterization techniques used for determining superconducting properties include: a.c. susceptibility and resistivity measurements of the superconducting transition; magnetization, as a function of magnetic field (to 6T) and temperature (to 1.5K); and critical current density, as a function of magnetic field (to 6T) and temperature (to 1.5K).

## **(C) MODELING**

The phase diagram of the 123 basal plane is being studied using the Cluster Variation Method (CVM). This method is hierarchical in the sense that it contains a series of results obtained by different basic clusters going from crude to more refined ones.

Generally, the larger the cluster, the better are the results. Our computer program has been modified to make calculations in the low temperature region possible without numerical underflow. By increasing the accuracy of the calculation, we could also refine the phase diagram. The energy parameters used are  $e = 0.09$  eV,  $V_a = -0.2$  eV and  $V_b = 0.05$  eV.

Professor Y. Yacoby of the Racah Institute of Physics, Hebrew University of Jerusalem, Israel, designed a set of fitting programs including multiple scattering. These techniques were employed in developing our new modeling programs.

Professor Yacoby's concept is as follows: Use an ideal structure instead of the real structure to reduce the number of independent scattering paths and reduce the theoretical calculation time (normally three weeks). Calculate the XAFS for this ideal structure and for derivatives resulting from small distance or angular distortions. From this information, one then calculates all the sets of paths corresponding to the real distorted structure, using the distortion as parameters to fit the data. Yacoby's original program was for only one center atom. For the 123 compound, he modified the program to handle up to five different atoms. The executable fitting programs uses 200 KB of RAM and the running time is 3 hours per fitting.

The model potential used was a muffin-tin, atomic potential renormalized at the Wigner-Seitz radius ( $r_s$ ). Different values for the Wigner-Seitz radii were used, finding the best agreement with experiment for values obtained from band structure calculations.

We also model microstructural features in terms of their effects on superconducting properties.

Modeling of grain boundaries as a random array of Josephson Junctions has allowed us to interpret our critical current density measurements in terms of self-field effects. Modeling of ac susceptibility in terms of inter- and intragrain properties has provided valuable guidance in process development activities.

#### (D) DEVICE REQUIREMENTS AND FABRICATION APPROACHES

Among the approaches being considered for device demonstration is the fabrication of a permanent trapped flux magnet from powders sintered into a monolithic cylindrical shape.

There are several advantages to permanent magnets made from bulk sintered powdered rather than solenoidal wound from conductors. Many of these advantages accrue from avoidance of fabrication problems associated with the brittle nature of the Perovskite compounds. The permanent magnet approach alleviates many of the

difficulties associated with fabricating brittle materials into wire, cable or tape and also avoids the need for making current contacts between normal conductors and superconductors.

The idea for using bulk permanent magnets, as contrasted with solenoidal wound magnets, was first proposed by Onnes in 1914. It was demonstrated by Laquer with bulk  $\text{Nb}_3\text{Sn}$  and shown by Dahlgren for tape wound  $\text{Nb}_3\text{Sn}$  solenoids to be capable of producing highly uniform magnetic fields.

The advantages of storing magnetic fields in permanent cylindrical tubes are significant. For example, fields can be reproduced many times from a pattern magnet and used in place of the magnet. Thus only one expensive pattern magnet is required. The stored fields are expected to be extremely stable for  $\text{YBa}_2\text{Cu}_3\text{O}_{7-x}$  and thus should be valuable for many electric applications such as motors, generators, and switches.

ACCOMPLISHMENTS - (iii) TECHNICAL RESULTS

## ACCOMPLISHMENTS - (iii) TECHNICAL RESULTS

### (A) CHEMISTRY AND PROCESSING

#### **General Synthesis**

Synthesis of very pure starting materials in the last quarter has permitted us to begin pyrolysis studies directed towards establishing the chemistry and kinetics of curing of the 123 carboxylate precursors. We have begun to collect TGA data for a large number of Y, Ba, and Cu(I) and Cu(II) carboxylate precursors. Data is shown for  $Y(O_2CCHMe_2)_2$  in air and oxygen in Figure 1. In  $O_2$  we observed actual combustion of the ligand beginning at  $250^\circ C$ . Figure 2, the thermogram for decomposition of  $Cu(O_2CCHMe_2)_2$ , indicates a weight loss consistent with initial decomposition to Cu metal followed by oxidation to  $CuO$ . We are presently analyzing the data for phase stability information.

Results obtained from studies on the 123 carboxylate system containing various amounts of a Ag carboxylate were discouraging. Silver carboxylates in general tended to exhibit poor solubility in THF, our solvent of choice for the carboxylate 123 precursor system. The fluorinated silver carboxylates exhibit much better solubility; however, XRD studies on the powders prepared from precursor mixtures containing 1%, 10% and 20% added silver consistently showed the formation of  $BaF_2$  (Figures 3-5 respectively). The conclusion is that fluoride containing carboxylates cannot be used for any type of precursor.

Initial results on the bismuth 2223 precursor system are more encouraging. The XRD spectrum of the powder produced on pyrolysis of the precursor to  $860^\circ C$  is shown in Figure 6. We currently do not have a literature standard for the 2223 phase for comparison. Tests for the Meissner effect using the powder produced via this technique were negative.

The SEM of a fully pyrolyzed fiber of the 2223 precursor is shown in Figure 7. The formation of crystallites is a positive development for these systems. However, adjustments in the pyrolysis protocols need to be made to increase the density and enhance the mechanical strength of these fibers.

#### **Powders**

Figures 8-11 show the effects of calcination conditions on the superconducting properties of 123 powders prepared by Seattle Superconducting Ceramics (SSC). When the powder was calcined in air, the transition signal became stronger, i.e., a greater magnetic susceptibility. With higher temperatures and longer soaking times the susceptibility increased, Figures 8 and 9.



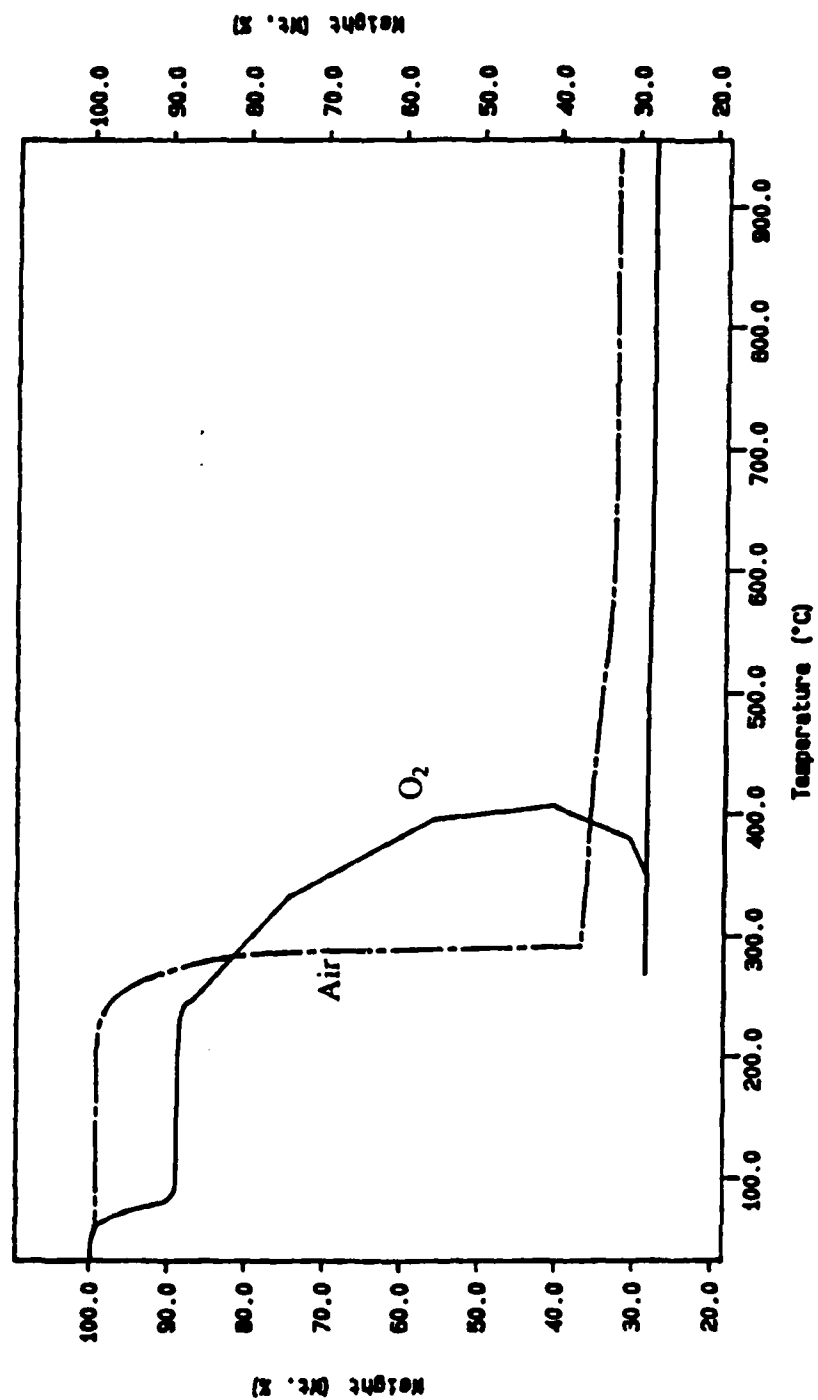


Figure 1. TGA of Y Isobutyrate showing burning in O<sub>2</sub>

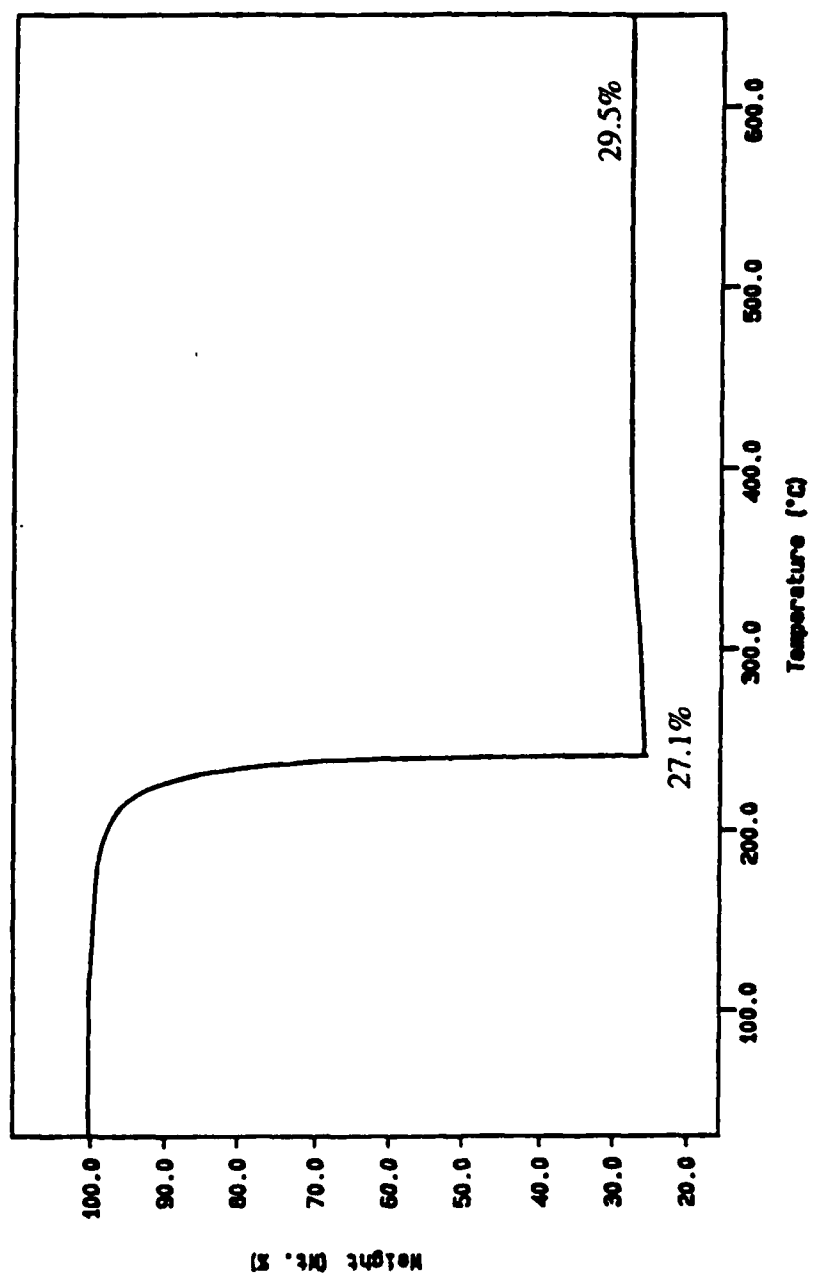


Figure 2. TGA of Cu Isobutyrate in Air

Sample: 123 + 1%AG TO 925 File: 1AGDK.3M

6-MAR-83 11:44

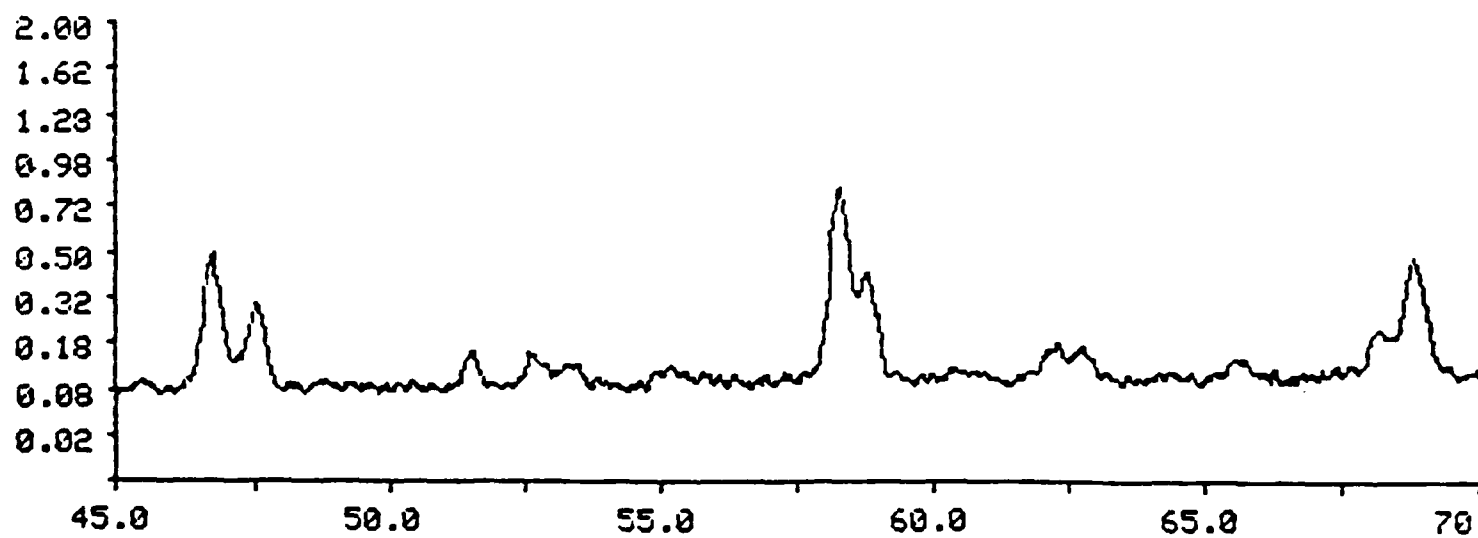
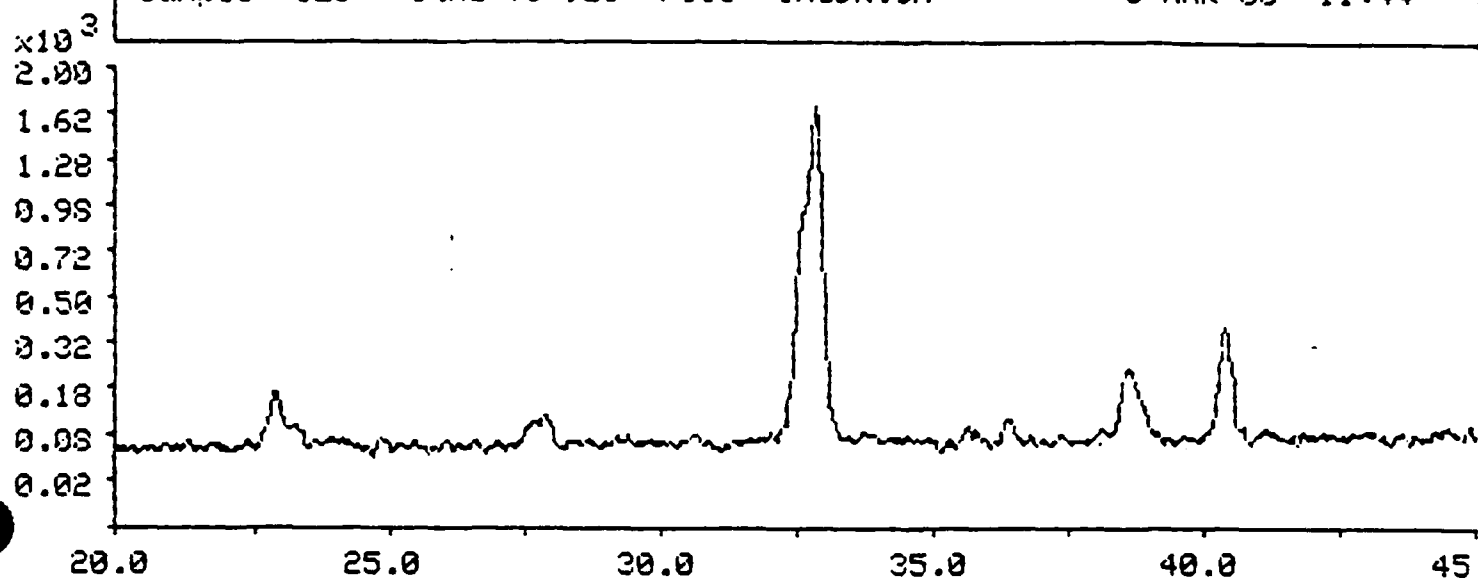


Figure 3

I 971k

Sample: 123 + 10% Ag TD 925 File: 10AGDK.3M

6-MAR-93 11:42

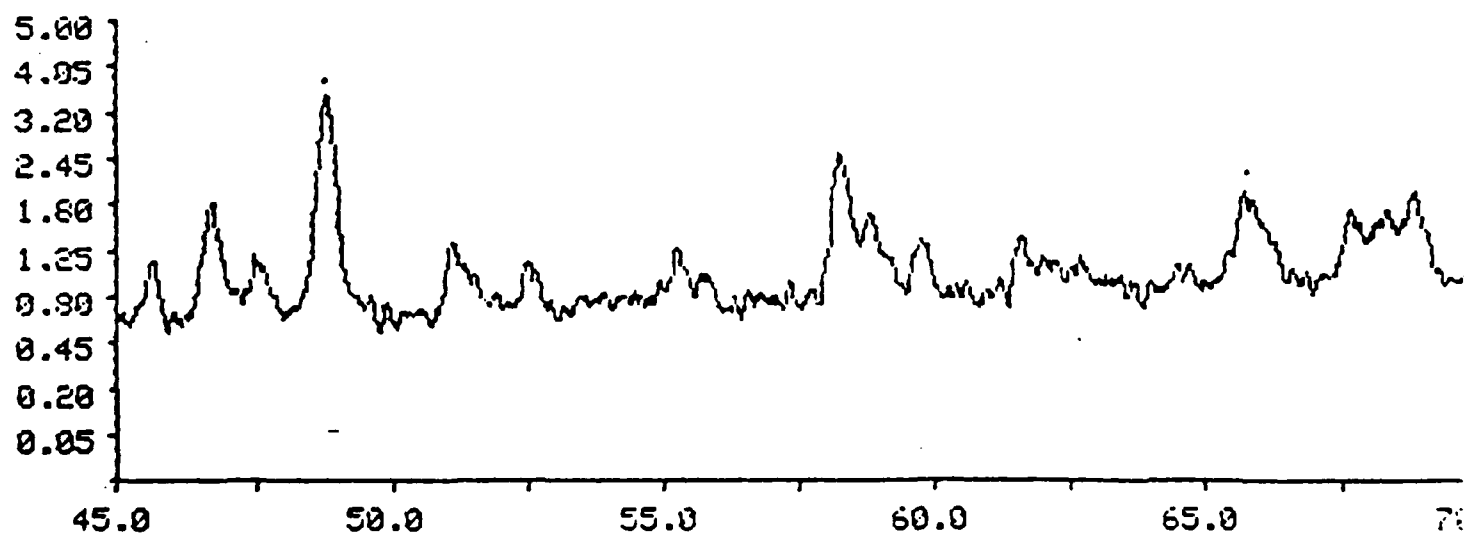
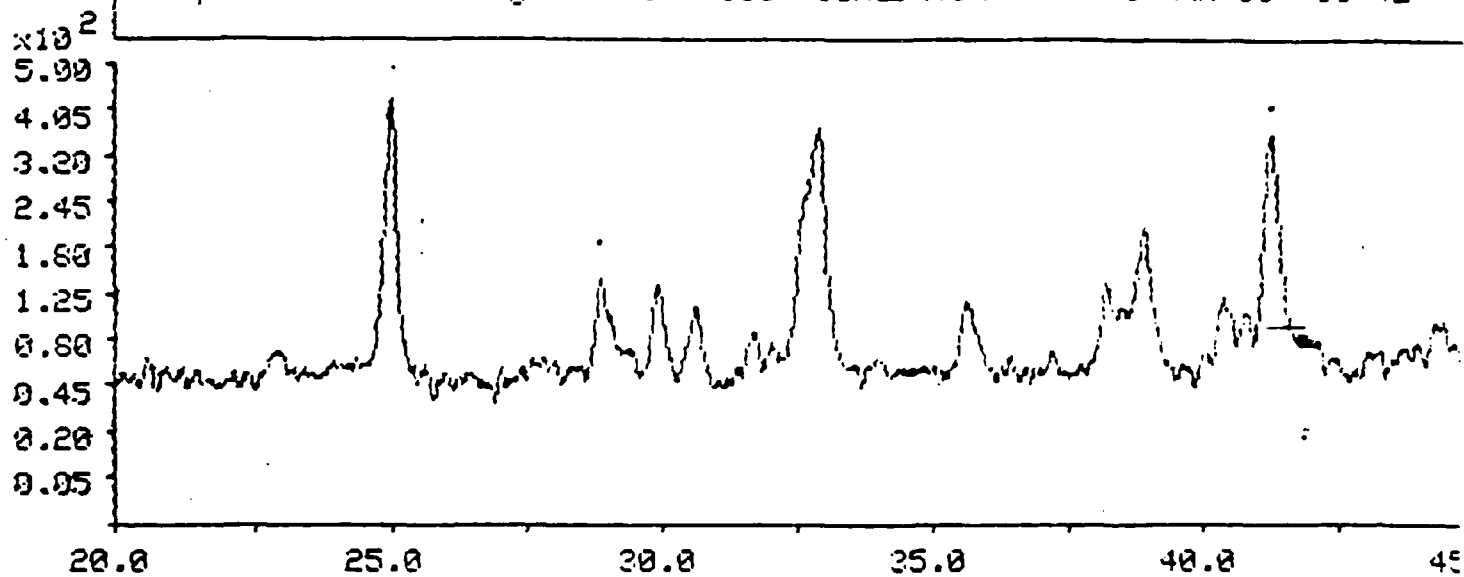


Figure 4

I97DK

Sample: 123 + 23% Ag 70 325 File: 23400K.SM

6-MAR-93 11:33

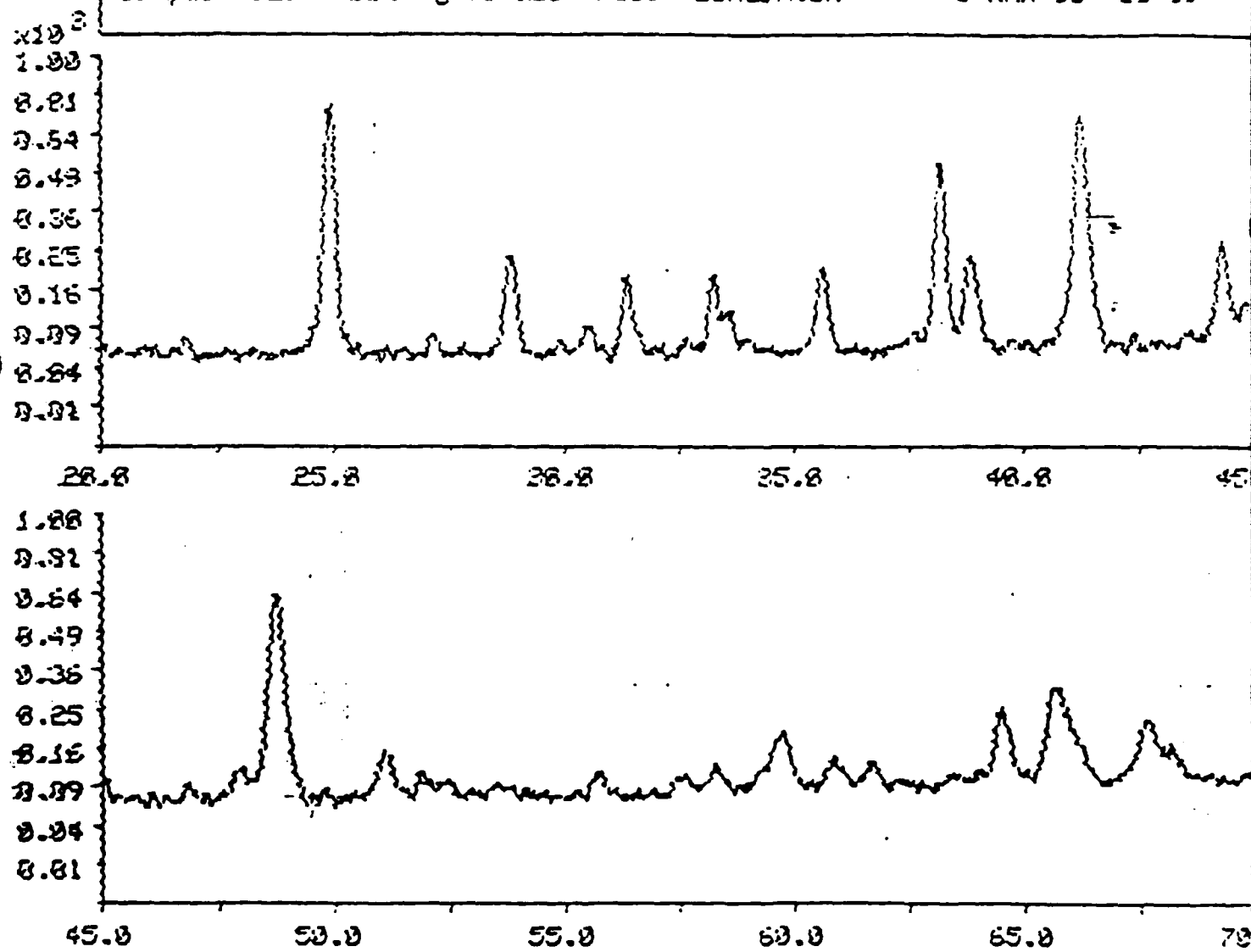


Figure 5

I93DK

Sample: 012223 File: 22202.0M

4-FEB-88 16:49

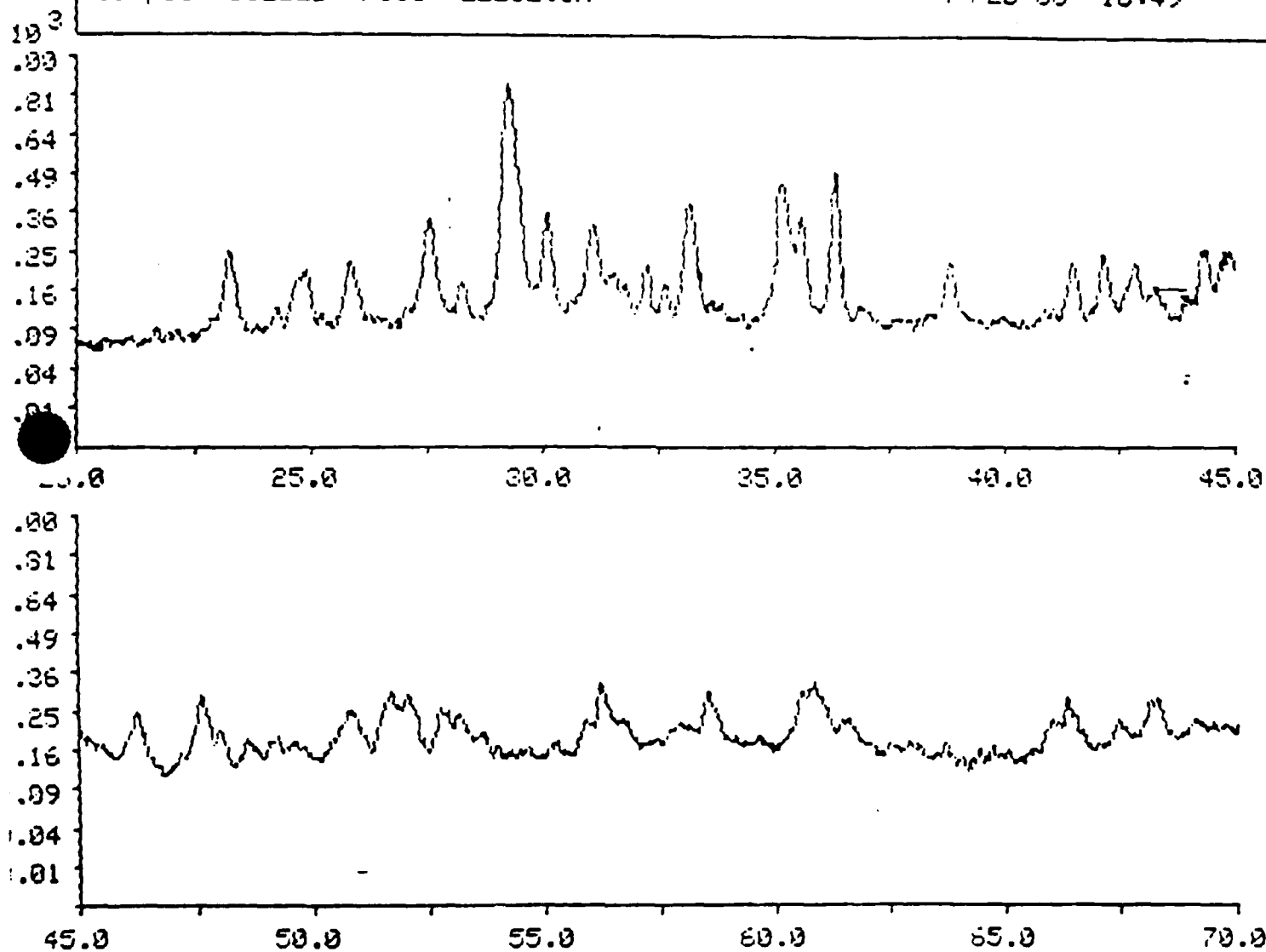
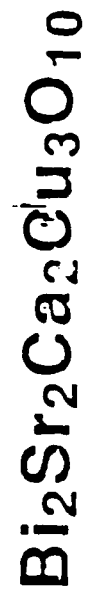


Figure 6

## SEM'S of Superconductor Fibers



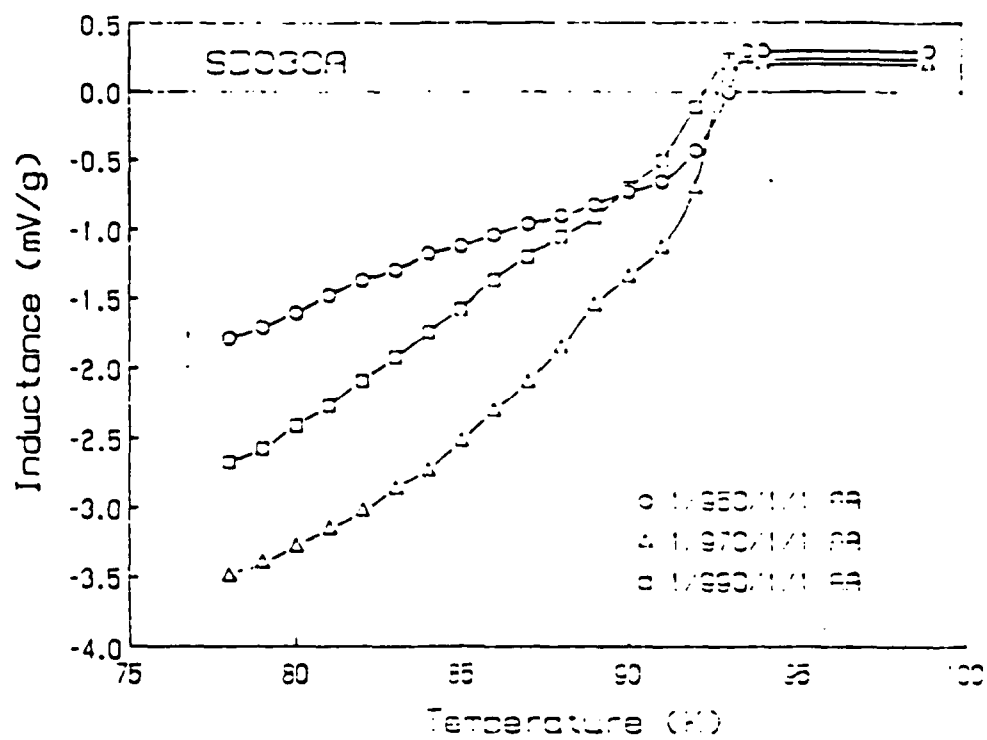


Figure 8



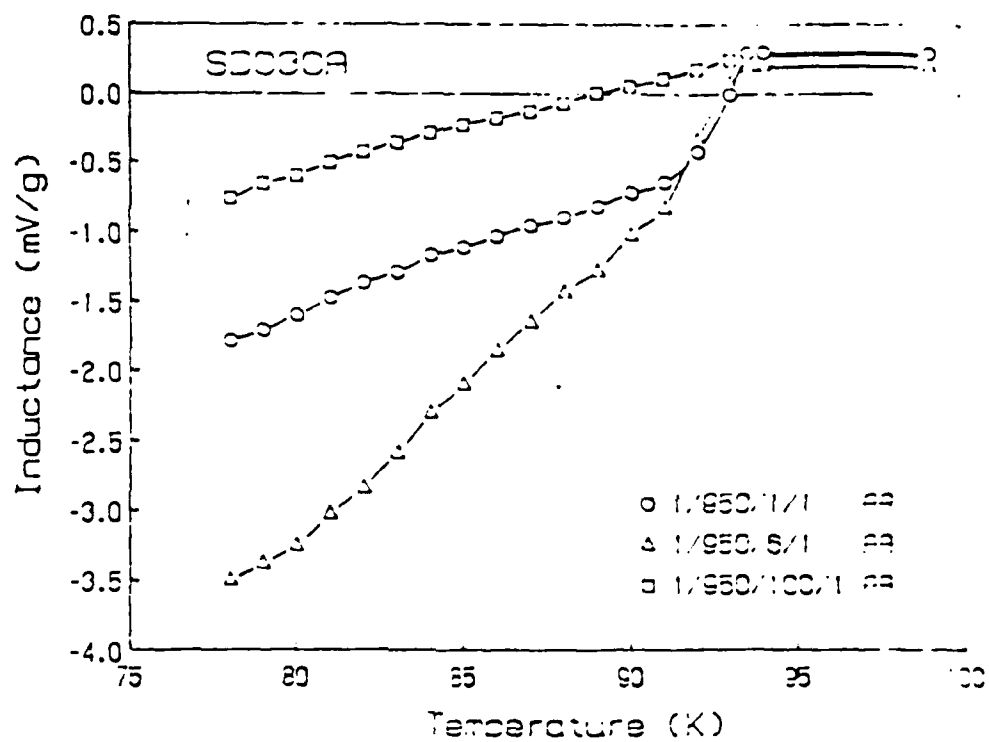


Figure 9

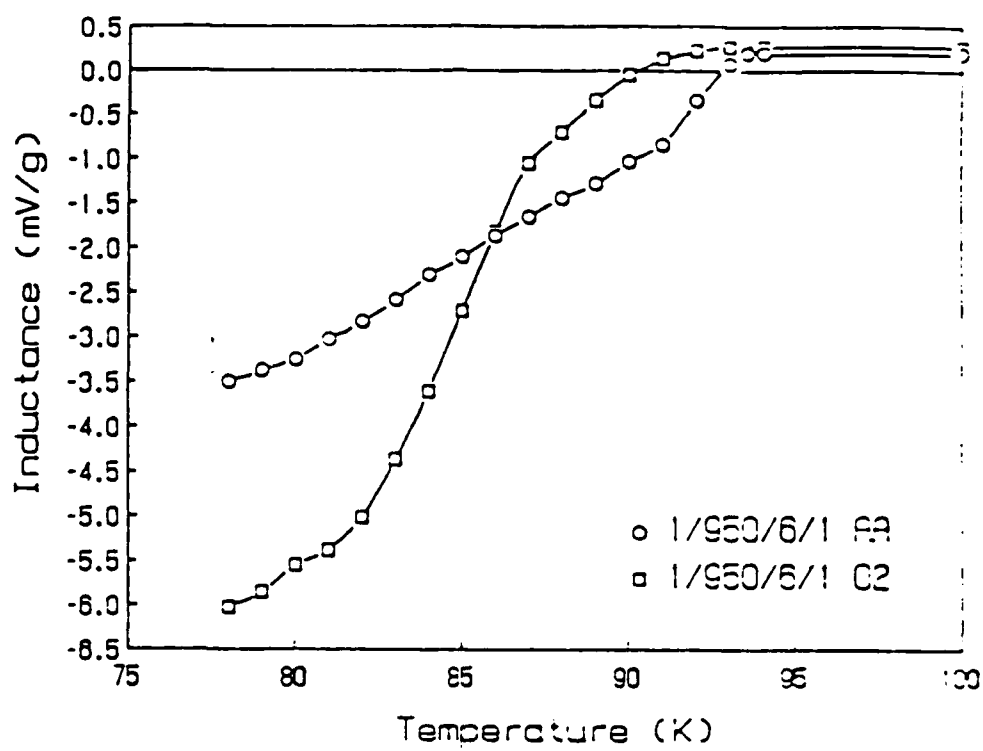


Figure 10

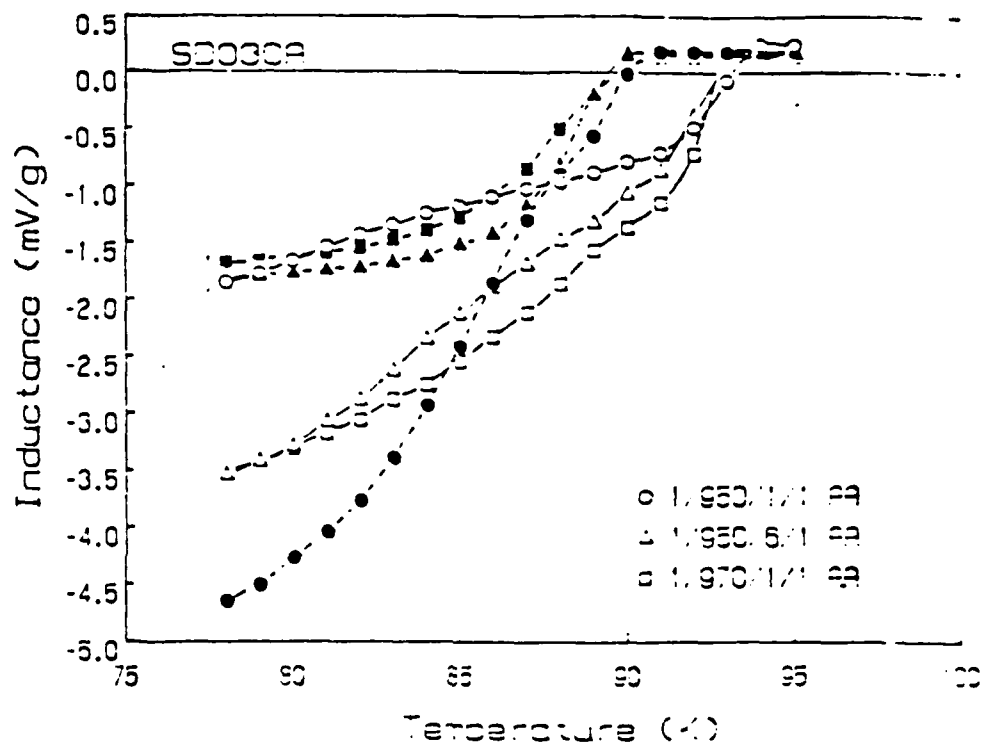


Figure 11

However, the superconducting onset temperature remained constant at approximately 93K, regardless of calcination temperature and soaking time.

The flux exclusion behavior of powder calcined at 950°C for 6h in flowing oxygen shows larger susceptibility changes and a sharper  $T_c$ , **Figure 10**. The change in onset temperature, by 4K, was greater in samples which were subjected to low temperature oxygen annealing (450°C for 24 h) after high temperature calcination, **Figures 11**.

### Tapes

SSC powder precursor (see section on powder processing) used in our studies on tape fabrication was typically calcined at 950C for 6 h in air. To break up the agglomerated particles, the powder was milled and subsequently classified to obtain particles with less than a 2 micron size.

Tape preparation with powder precursor begins with the suspension of 30 vol% precursor powder in a solvent composed of methylethylketone and ethanol. The particles are dispersed by the addition of an appropriate amount of Menhaden fish oil determined from sedimentation studies. Flexibility and strength of the unfired tape was enhanced by the addition of polyvinyl butyral resin to suspension. The resulting stable suspension was cast onto a mylar film using a doctor blade.

The use of precursor powder is a new approach to tape fabrication. It offers two advantages in that it simplifies the number of steps required to prepare the tape and, it employs fine precursor powders, thereby reducing the potential for contamination.

The organic binder vehicle is then burned off the cast tapes by heating slowly (12 h) to 500C. The sintering of the tapes is carried out over the temperature range 800-950C in air. The microstructure of the sintered tapes was examined by SEM.

Microstructure of tape sintered at 800C for 1 h, **Figure 12**, shows no evidence of densification. At 900C and 1 h, we observe grain sizes of 2-3 microns with incomplete densification and pores of 1 micron diameter at the grain boundaries. The tapes become fully dense after soaking at 900C for 12 h. Full densification could also be obtained by increasing the temperature to 930C for 1 h, **Figure 13**. Further increases in temperature lead to an increase in grain size. Grains as large as 60-70 microns are seen in



Figure 12

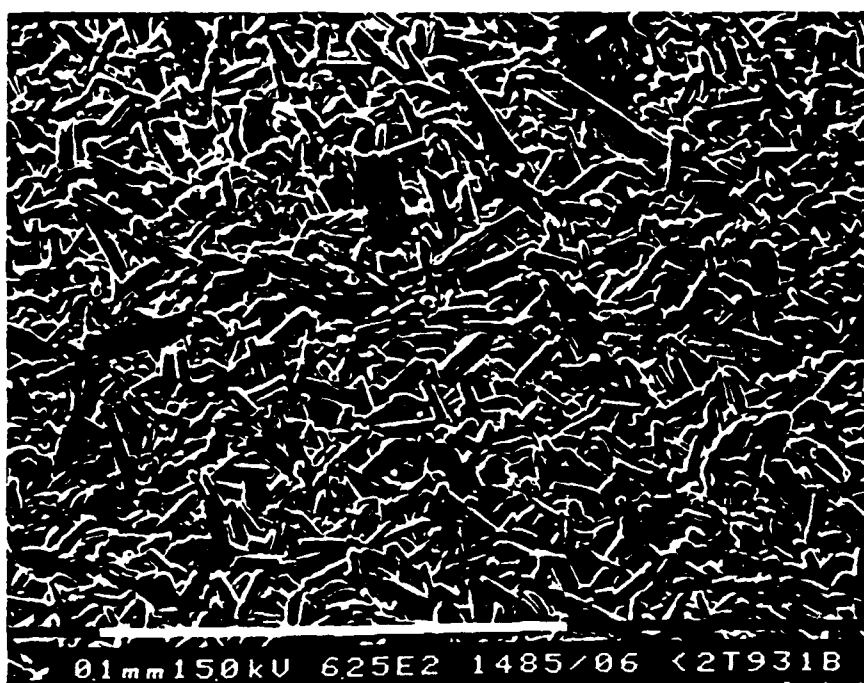


Figure 13

**Figure 12** where the tape was sintered at 950C for 1 h.

One possible explanation for this change in rate of densification and grain growth at temperatures above 900C is the presence of a liquid phase. Formation of the liquid phase at temperatures around 900C has been attributed to the eutectic melting of a barium cuprate phase.<sup>1</sup> To verify this point a differential thermal analysis run was performed on the starting powder. The results show an endothermic peak around 920C which is in agreement with the previous study.

### **Fibers**

Two precursor fluids have been identified for use in superconductor fiber preparation: (i) metal carboxylate solutions and (ii) hydrogel-based mixtures. Work this reporting period focused on the latter.

Two methods of fiber spinning were investigated, "dry-spinning" and "wet-spinning", **Figures 14 and 15**. By dry-spinning we have produced dense dried, **Figure 16A**, and heat-treated, **Figure 16B**, fibers.

The rate of solvent evaporation from the fiber prior to collection on the take-up spool was not sufficient to prevent the fiber from deforming from its cylindrical shape to a flattened (ribbon-like) shape as it is taken up on the spool. Fibers as those shown in **Figures 16A and 16B**, were possible only when the drying time was tightly controlled.

In the wet-spinning process the fibers readily solidify before reaching the take-up spool, thus flattening is eliminated, and continuous, long lengths of green fibers can be produced. Micro-pores form in the wet-spun fibers. **Figure 17** shows the type of micro-porosity that results.

X-ray diffraction showed evidence for complete conversion to the 123 phase. It appears the final microstructure depends principally on the microstructure of the dried precursor fibers.

Electromagnetic property measurements were limited to a single a-c susceptibility measurement, because of the mechanical instability of the final ceramic fibers. **Figure 18**, shows a  $T_c$  onset of 91-92K.

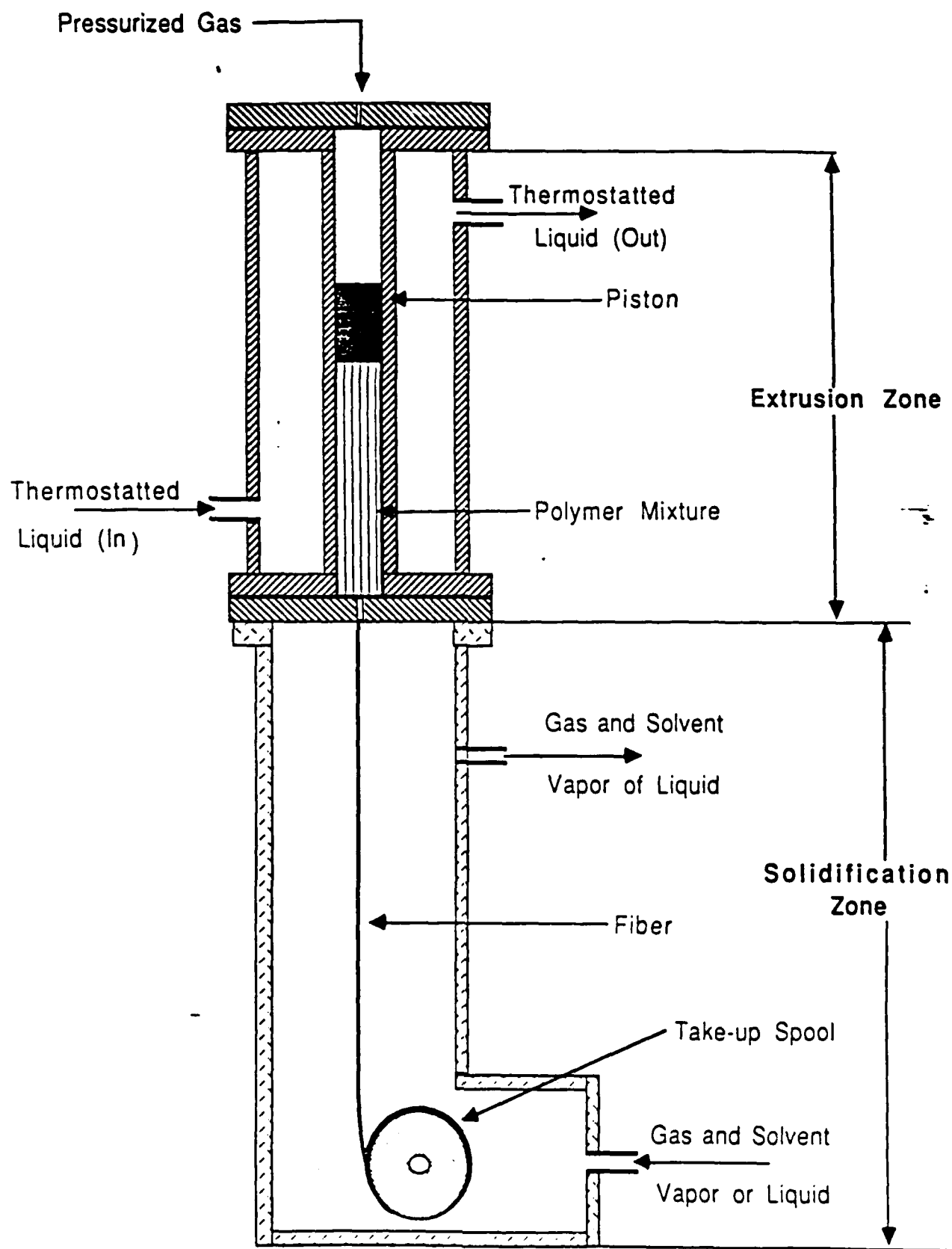


Figure 14



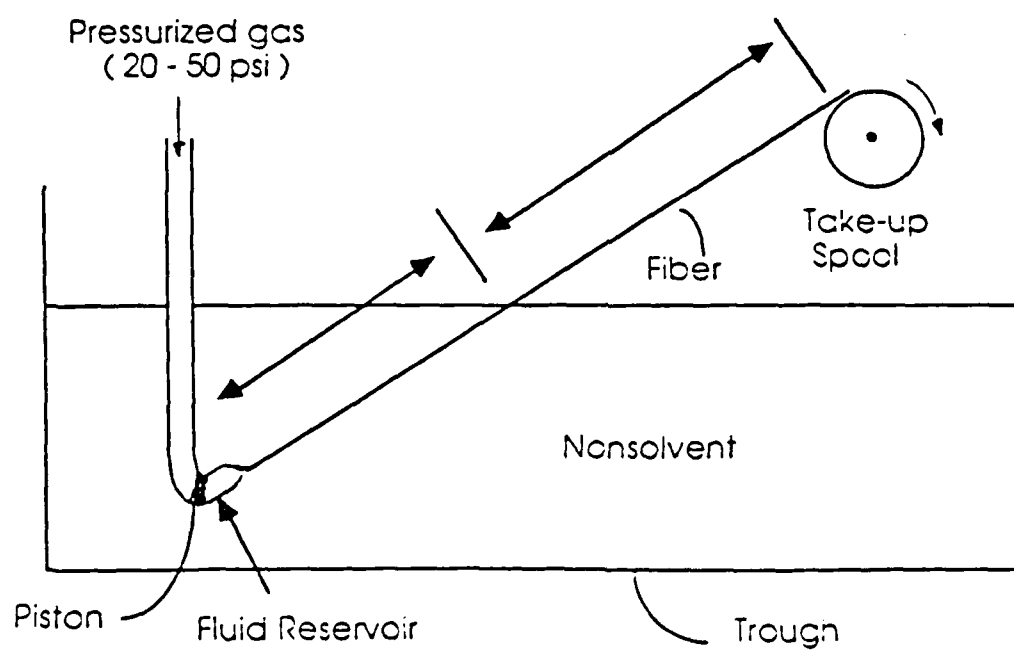


Figure 15

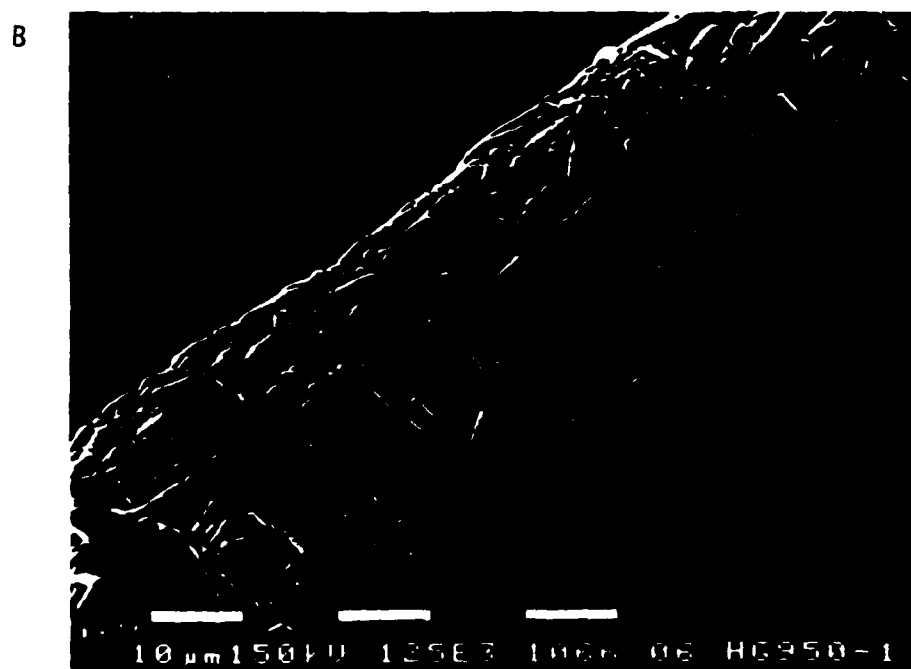
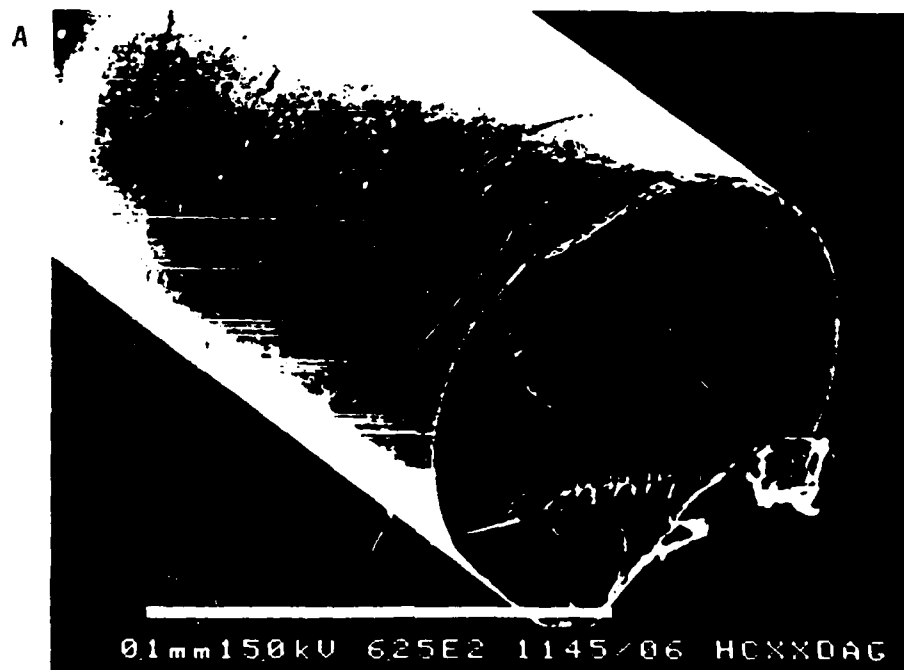


Figure 16



Figure 17

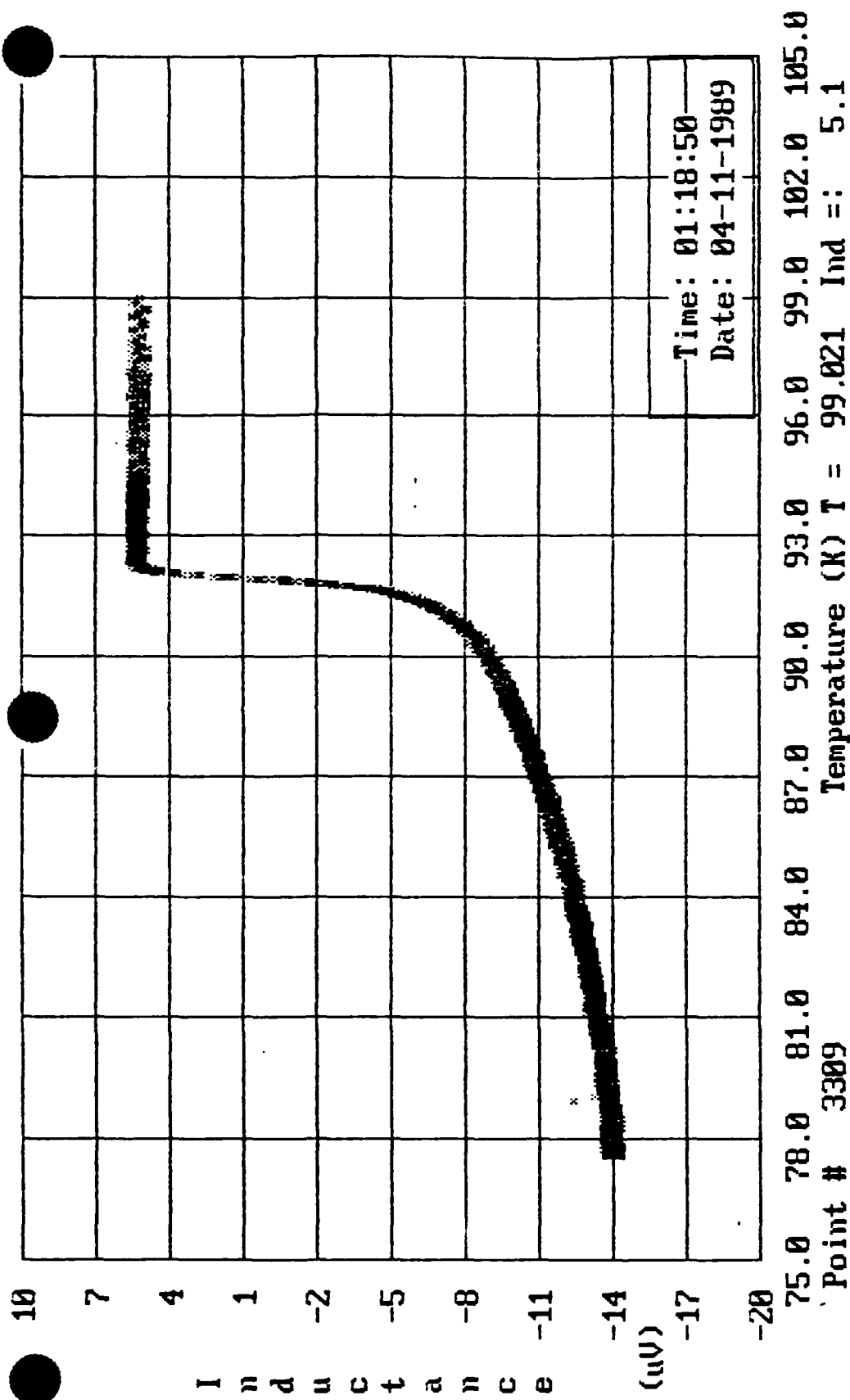


Figure 18

### Thin Films by Reactive Sputtering Using a Single, Multicomponent, Spherical Target

The thermionically enhanced sputtering technique, or triode process (Battelle patent #4,046,666) has been used to produce superconducting thin films of YBaCuO. Two aspects of this technology are unique. First, the spherical target design has resulted in excellent compositional uniformity of the deposited films on relatively large area substrates. Control of the stoichiometry of superconducting films is quite difficult using other deposition techniques because of differential angular sputtering yields and volatility of some of the components. Second, the triode process is well suited for the deposition of both thin and thick films. Extremely high rates of film deposition have been achieved, ranging up to several microns per hour.

The schematic for the sputtering system used in this work is given in Figure 19. At center is the sputtering target (cathode), which is the source of the sputtered material. The target is a 5 cm dia., water cooled copper sphere, coated with an 0.5-1.0mm thick plasma-sprayed YBaCuO layer. A xenon plasma is produced in the annulus between the target and the hemispherical cap. When a negative bias voltage is applied to the target,  $Xe^+$  ions attracted from the plasma sputter ions from the target surface. The sputtering system operates in a triode mode using a thermionically assisted plasma. A tungsten filament located below the target produces an electron current that generates the assisted plasma.

Excellent compositional uniformity as a function of spatial position on the substrate and time was achieved using the hollow, water-cooled, spherical target design. In Figure 20, mole fractions of Y, Ba, and Cu are given as a function of angles from the target equator, obtained by dissolution of the film in dilute nitric acid followed by ICP solution analysis. Compositional uniformity over substrate areas of more than 200 cm<sup>2</sup> were within 1 percent of the average value. The ability to produce uniform, large-area thin films is expected to be particularly important in electromagnetic window applications. The deposit composition was also highly stable with time, when the sputtering power density was maintained at 0.65 watts/cm<sup>2</sup> or less, corresponding to a deposition rate of approximately 0.4 microns/h. Sputtering power densities greater than 1.3 watts/cm<sup>2</sup> caused the target temperature to rise. This led to degradation of target surface through diffusion and other processes, and resulted in a loss of stoichiometry of the deposit, although the films remained spatially homogeneous.

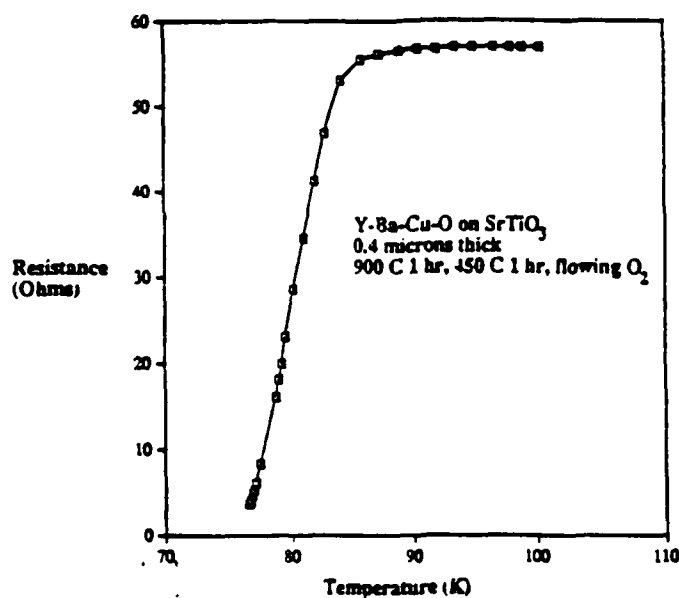


Figure 19. Four-point resistance versus temperature for a YBaCuO film on (100)- $\text{SrTiO}_3$  by spherical target sputtering. Deposition was performed at ambient temperatures.

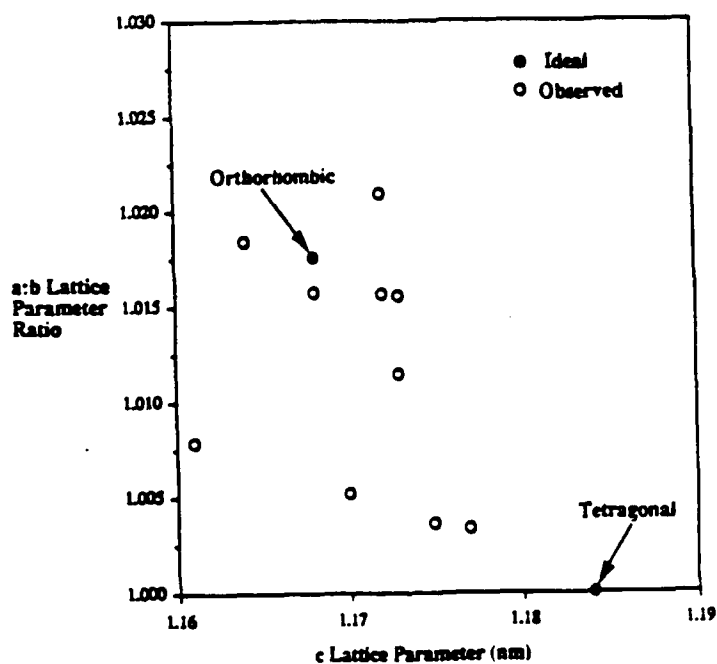


Figure 20. Ratio of a:b versus c for a series of sputtered YBaCuO thin films on (100)- $\text{SrTiO}_3$ , determined by XRD.

Table 1.

## BASIC MATERIAL PROPERTIES

	YBa <sub>2</sub> Cu <sub>3</sub> O <sub>7</sub> (1-2-3)	Sapphire (Al <sub>2</sub> O <sub>3</sub> )	Zirconia (ZrO <sub>2</sub> )	Magnesia (MgO)	Strontium Titanate (SrTiO <sub>3</sub> )
a,b (nm)	.382, .389	.476	.52	.421	.391
mismatch %		23	35	9	1.5
CTE (10 <sup>-6</sup> /K)	13	6	13.5	12	9.4
Δa (10 <sup>-6</sup> /K)		7	0.5	1	3.5
σ <sub>th</sub> (900 C) (MPa) E/(1-ν) = 120 GPa		750	50	110	380
t <sub>f</sub> <sup>*</sup> (microns)		0.2	40	8.3	0.7

Critical properties of thin films prepared by sputtering have not yet been optimized. While onset temperatures typically ranged from 88-92K, transition widths were 15-20K wide, as shown in the resistance versus temperature plot of Figure 21 for a YBaCuO film on (100)-SrTiO<sub>3</sub>. Current facilities were of insufficient sensitivity to measure magnetization in these thin films. XRD of the films indicated that the as-deposited films were amorphous. After heat treatment to 900°C and annealing at 450°C in flowing oxygen, the films were typically observed to have a structure intermediate between orthorhombic and tetragonal, apparent in the plot of a:b lattice parameter ratios versus the c lattice parameter of Figure 22. XRD of thin films is, by nature, somewhat difficult, with some of the peaks near the noise level. Peak height analysis gave evidence for epitaxial growth of the films, which was not as readily apparent in subsequent SEM analysis. Peaks observed at 2θ = 58 degrees indicate a splitting of the (213) and (123) peaks, consistent with the orthorhombic phase. The magnitude of the splitting and relative peak heights were not completely consistent with the orthorhombic phase, indicating instead that some oxygen deficiency existed. This was supported by the typical semiconducting behavior of the films in the four point resistance measurements.

It was observed that sputtered YBaCuO thin films on (100)-SrTiO<sub>3</sub> tended to develop microcracks following the 900°C heat treatment, when the film thickness exceeded 1.2 microns. This result may be understood using a simple fracture mechanics approach (Griffith energy balance). An observed failure criterion obtained at PNL from a large number of optical coatings, including oxides and nitrides, is

$$\sigma t = 200 \text{ J/m}^2 \quad (1)$$

where  $\sigma$  is stress within the film and  $t$  is the thickness. Applying the Griffith energy balance to thin film failure,

$$2g_s = (\sigma/E)\sigma t_f \quad (2)$$

where  $g_s$  is the surface energy of the YBaCuO film,  $E$  is Young's modulus, and  $t_f$  is the critical film thickness at which failure is expected. Estimating  $E=100$  GPA and  $g_s=0.5 \text{ Jm}^2$ . The critical film thickness for YBaCuO on (100)-SrTiO<sub>3</sub> can be estimated in this manner to be 0.7 microns and  $t_f$  to be 263 J/m<sup>2</sup>, which agrees quite well with observations. Results for other commonly used substrates are given in Table 1, which also includes lattice parameters, thermal expansion coefficients, differential thermal expansion between YBaCuO and each substrate. A critical film thickness of 40 microns is predicted for zirconia, because of the excellent thermal expansion match of the two materials; however, the lattice mismatch is sufficiently great that epitaxial growth is improbable. The lattice mismatch for MgO and YBaCuO is



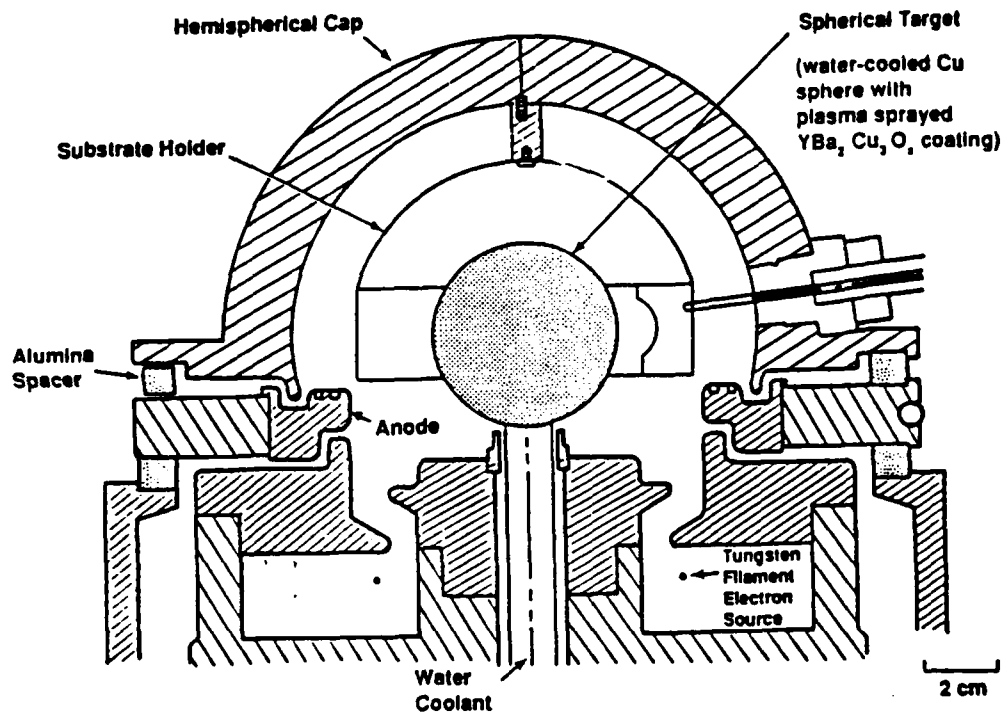


Figure 21. Schematic of spherical target triode sputtering system that utilizes a single, multicomponent target.

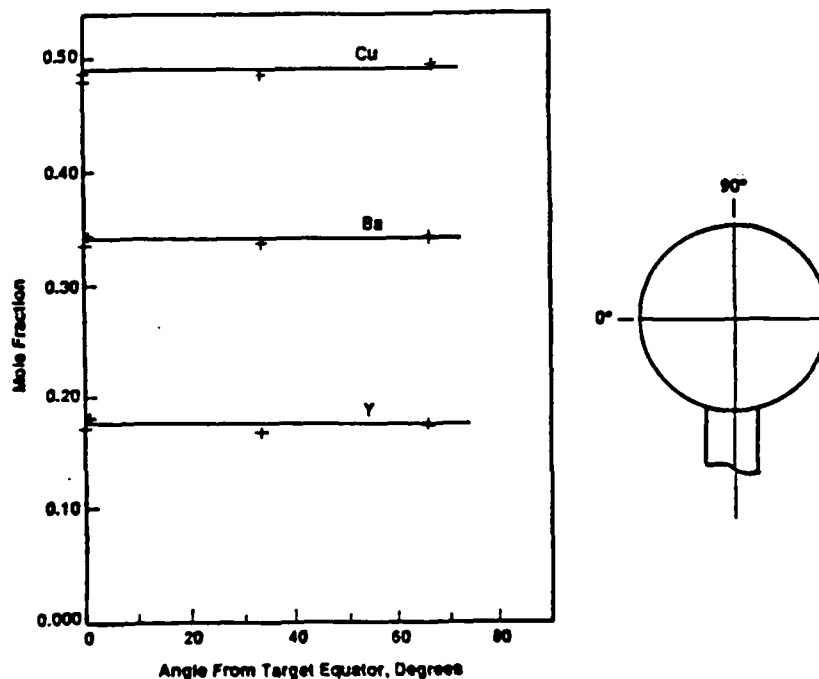


Figure 22. Mole fraction of Y, Ba, and Cu as a function of angle from the target equator. Using a spherical target triode sputtering system, compositionally homogeneous films can be made on substrates more than  $200 \text{ cm}^2$  in area.

smaller than the classical limit for epitaxial growth, with additionally a reasonable thermal expansion match, leading to a prediction of a critical film thickness of more than 8 microns. Of course, cracking problems could be avoided, at least in part, by processing the films in situ, thus avoiding the high temperature, post-deposition heat treatment. Compatibility with the commonly used electronic substrates of silicon and gallium arsenide would be improved substantially.

#### **Thin Films by Laser Ablation**

This technique uses a pulsed excimer (248 or 308 nm) or Nd:YAG (second harmonic, 532 nm) laser to uniformly ablate a target. As in the case of spherical target sputtering, the composition of the deposited film is identical to that of the target. Important operational parameters are laser spot size (typically 1 mm), energy density (1-3 mJ), wavelength of the laser (532 nm), pulse duration (30-40 ns), repetition rate (10 Hz), film deposition rate (0.1-3 nm/pulse), oxygen partial pressure (0-100 mtorr), target-substrate distance (4 cm), and target rotation (10 Hz planned). A schematic of a newly completed laser ablation chamber is given in Figure 23. This chamber allows thin films to be processed in-situ, avoiding a post-deposition heat treatment at high temperature that can lead to enhanced film-substrate reactions and loss of film stoichiometry.

Superconducting BiSrCaCuO thin films of good quality have been grown on (100)-MgO by laser ablation. A 4336 target composition was used to offset anticipated copper losses during post-deposition heat treatments. The films grew epitaxially and were free of microcracking, as revealed by SEM examinations. The principal phase present was the 4334 (onset temperature of 80 K and zero resistivity by 75K), appearing as approximately 10 micron diameter, flat grains. A smaller fraction of the 2223 phase (onset temperature 105 K) was also present. A four-point resistance versus temperature plot is given in Figure 24, showing a small deflection attributable to the high critical temperature phase. This phase has been shown elsewhere to be stabilized by substitutions of Pb for Bi in bulk materials. Critical currents using a  $5 \times 10^{-9}$  ohm-cm criterion exceeded  $10^3$  A/cm<sup>2</sup> at 70K. One possible application of such films is as an electromagnetic window, where electromagnetic signals may penetrate the thin film when in the normal state but be excluded in the superconducting state. This application requires the superconductor to be 1-2 microns thick, which is well within the range of thicknesses possible by this deposition method and well below the maximum film thickness for mechanical stability predicted by a Griffith energy balance.

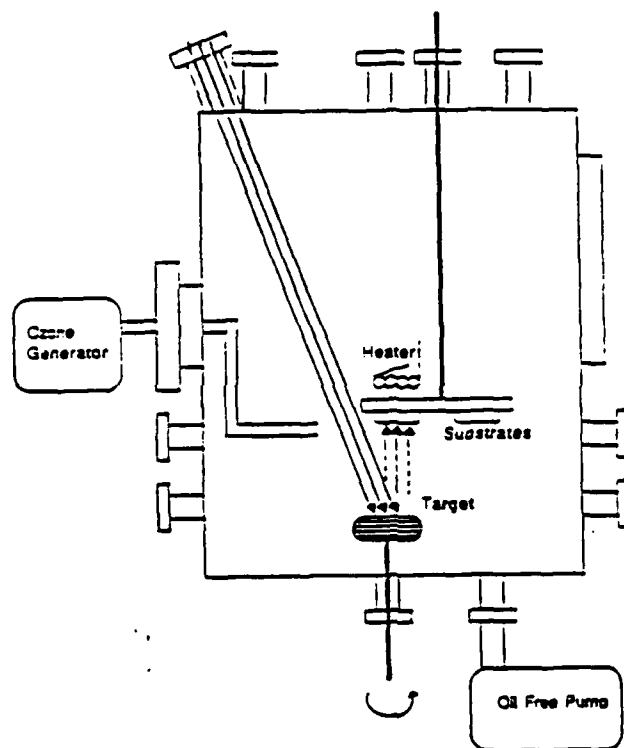


Figure 23. Schematic of a laser ablation system, capable of processing high quality superconducting thin films in-situ.

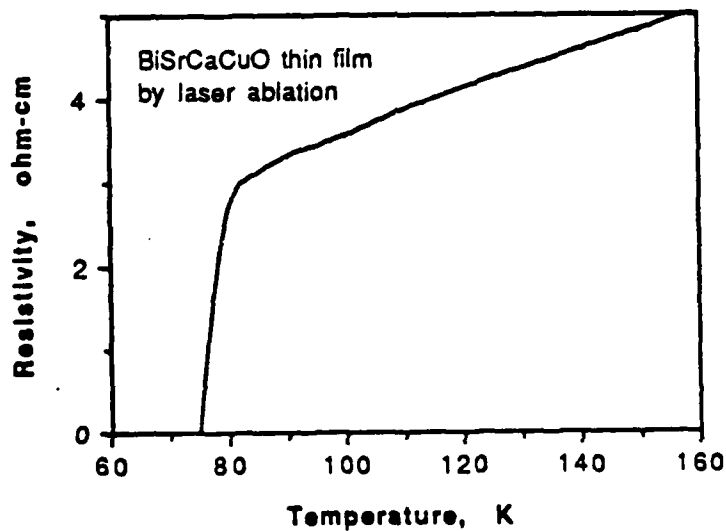


Figure 24. Four-point resistance versus temperature for a BiSrCaCuO thin film on (100)-MgO, prepared by laser ablation. The 4334 phase, with a critical temperature of 80K, was predominant.

### Thick Films by Plasma Spraying

Plasma-spraying is an attractive method to rapidly coat large, irregular areas with superconducting thick films. To maximize critical current densities in such films, requirements relating to stoichiometry, impurities, and orientation are similar to those of thin films. Problems specific to plasma-spraying include some loss of stoichiometry during deposition in the high temperature plasma, typical formation of a microstructure having a high density of voids, and a requirement of a post-deposition anneal to convert the largely amorphous as-deposited film to the orthorhombic phase.

Using a plasma spray apparatus, thick YBaCuO films were deposited onto MgO substrates for electronic switch applications and onto Cu metal spheres, which were then used as triode sputtering targets. A principal advantage of plasma spray methods is that very high deposition rates are possible, to greater than 100 microns per pass of the torch; substrates having complex shapes can be readily coated. In this method, YBaCuO powders were injected into a plasma where they were partially or completely melted and accelerated towards the substrate to be coated. Argon was used as both the plasma and powder feed gas at 30 and 5 L/min, respectively. The plasma current was approximately 300 A, at a power level of 40 kW. Powder feedstock particle sizes were typically 10-100 microns in diameter, while powder feed rates were of the order of 10 g/min. The torch to work piece distance was in the range of 75-100 mm. The plasma torch design allowed YBaCuO powder feedstock to be injected into the plasma at multiple points, allowing some control over the extent of powder heating.

Within the uncertainty associated with inductively coupled argon plasma spectroscopy (ICP), plasma-spraying operations did not measurably alter either the overall stoichiometry or add to the concentration of impurities in the YBaCuO deposit. Injection of YBaCuO powders into the plasma at the furthest downstream point was useful in limiting the extent of powder heating and volatilization of copper. Because spherical targets for sputter deposition of thin films are prepared by this process, verification that YBaCuO powder compositions are not severely altered is particularly important.

As-sprayed films both were largely amorphous, as determined by XRD, and porous. The thick films were readily converted to the orthorhombic phase by a high temperature anneal, to approximately 900°C. However, the porosity remained relatively high. Further refinement of the plasma-spray process to increase the density is of interest for sputtering targets, to enhance the thermal conductivity and thus the range of operating stability of such targets.

On MgO, onset temperatures (80% values) were varied from 88 to 91K, with zero resistance reached by 86K, as determined by the 4-point method. For plasma-sprayed films approximately 100 microns in

thickness, critical currents were fairly low, approximately 25 A/cm<sup>2</sup>, as determined by dc-transport using a 5x10<sup>-9</sup> ohm-cm criterion. Critical currents exceeded 3x10<sup>2</sup> A/cm<sup>2</sup> at 77K for YBaCuO-Ag cermet, with best results obtained for composites having 10% silver.

**(B) CHARACTERIZATION--  
MICROSTRUCTURE AND SUPERCONDUCTING PROPERTY**

**Microstructure--**During the year we have investigated the reaction sequencing for eight different precursors, fired in air and helium and cooled in air and oxygen. Maximum temperatures were restricted to 910°C in order to avoid undesirable reactions between the sample and the sample holder. Table 1 lists the specific precursors which were examined along with the reactions which were observed upon heating.

**Firing In Air**

The reaction sequencing in air was essentially the same with all eight precursors. Although there were some minor differences in terms of the temperatures at which the precursors began to react, the formation of 123-related phases appears to be kinetically controlled. For example, changing the heating rate from 0.5 to 10 deg/min in the case of Precursor A, resulted in a 75 C difference in the temperature at which an oxygen rich tetragonal 123 phase (LTT) first began to appear. In every precursor fired in air, the LTT phase was initially produced at about 775 C. From the X-ray spectra we have concluded that this phase is tetragonal but, since it does not have a split peak, it is probably an oxygen-rich 123 intermediate phase. More significant was the fact that this phase was not able to form a fully split tetragonal 123 phase at temperatures below 875 C. Moreover, this phase remains invariant during a wide variety of cooling schemes in both air and oxygen. That is, it does not form the orthorhombic 123 phase. An example of this is given in Figure 25a for Precursor B which shows the XRD spectra corresponding to the major (103,013) and secondary peaks (006,020,200) for the 123 species. The plot shows these peaks at a point just before cooling (i.e., after holding at 750 C for 1 hour) and after cooling to room temperature.

Using a platinum heating strip in the DXRD apparatus allows us to raise the maximum processing temperature to about 910 C. At these

TABLE 1

PRECURSORS

A	Co-precipitated Hydroxides (UW)
B	Citrate Gel (Boeing)
C	Ag-Doped Citrate Gel (Boeing)
D	Flashed Nitrates (UW)
E	"248" Citrate Gel (Boeing)
F	Freeze Dried Nitrates (Boeing)
G	Pre-Dried Citrate Gel (Boeing)
I	Freeze Dried (SRI)

REACTIONS

- (1) (Y-Ba-Cu) Precursor  $\rightarrow$  123 Tetragonal
- (2) (Y-Ba-Cu) Precursor  $\rightarrow$  123 Intermediate
- (3)  $2\text{YBa}_2\text{Cu}_3\text{O}_{7-x} \leftrightarrow \text{Y}_2\text{BaCuO}_5 + 2\text{BaCu}_2\text{O}_2 + \text{BaCuO}_2 + (3-x)/2\text{O}_2$
- (4)  $\text{Y}_2\text{BaCuO}_5 \leftrightarrow \text{Y}_2\text{BaO}_4 + \text{Cu} + 1/2\text{O}_2$
- (5) (Y-Ba-Cu) Precursor  $\rightarrow \text{Y}_2\text{BaCuO}_5 + 2\text{BaCu}_2\text{O}_2 + \text{BaCuO}_2 + (3x)/2 \text{O}_2$
- (6) (Y-Ba-Cu) Precursor  $\rightarrow \text{Y}_2\text{BaO}_4 + 3\text{BaCuO}_2 + 3\text{Cu} + (2-x)\text{O}_2$

TABLE 2

## RUNS IN HELIUM

		HEATING			COOL (in Air)		
SAMPLE		(T,t)max	T <sub>RXN</sub> <sup>o</sup>	RXN	Tswitch	(T,t)anneal	(123)RT
A	(A4)	715 - 75M	675	(1)+slight(3)	715	NONE	SINGLE PEAK
B	(B6)	745 - 15m	610	(1)+slight(3)	685	NONE	ORTHO
	(B8)	750 - 12h	610	(1)+slight(3)	680	NONE	ORTHO
	(B10) <sup>a</sup>	810 - 10m	700	(6)	810	NONE	SINGLE PEAK
	(B11) <sup>b</sup>	750 - 10m	625	(1)+lg(3)	750	500 - 6h	TETRAGONAL
C	(C2)	800 - 30m	635	(1)+slight(3)	730	NONE	SLIGHT ORTHO
D	(D2)	750 - 60m	650	(1)+slight(3)	750	NONE	SINGLE PEAK
	(D4)	840 - 2h	650	(1)+slight(3)	840	NONE	SINGLE PEAK
	(D6)	810 - 10m	675	(1)+slight(3)	810	NONE	SINGLE PEAK
E	(E1)	750 - 40m	680	(5) + (6)	685	NONE	SINGLE PEAK
F	(F4)	850 - 10m	640	(3)	850	500 - 2h	SINGLE PEAK
G	(G1)	730 - 20m	675	(5) + (6)	730	500 - 4h	SINGLE PEAK
	(G3) <sup>c</sup>	640 - 1M	640	slight(1) + (5) and (6)	640	500 - 1h	SINGLE PEAK

<sup>a</sup> switched to Helium too low (455°C), no burnout<sup>b</sup> after sitting in dessicator for 2 mos.<sup>c</sup> rapid heating (600 - 800° in 1 min)

temperatures, the LTT phase can be transformed into the well-split HTT phase although we have not been able to form a well-crystallized orthorhombic phase when the HTT phase is immediately cooled in various air-oxygen cooling/annealing cycles.

#### Formation of Tetragonal 123 in Helium

The motivation for firing in an oxygen-free environment was the desire to form single phase orthorhombic 123 at temperatures low enough ( $< 850$  C) so as to avoid grain growth. Table 2 is a list of individual runs for each of the first six precursors which were fired in helium along with some of the key observations;  $T_{rxn}$  is the temperature at which we first see significant reactions of the individual precursor phases, the RXN column lists the specific reactions which were observed at  $T_{rxn}$  and  $T_{switch}$  is the temperature at which the environment was switched back to air. Similar results were obtained for precursors H and I. First of all it is obvious that firing in an oxygen-free environment produces sharply split tetragonal 123 (Rxn (1) in Table 1) at much lower temperatures; 610 - 700 C. Figure 25 also shows a comparison of Precursor B fired in air (Fig 25a) and in helium (Fig 25b) where the differences in the two are readily apparent. Unfortunately, in an oxygen-free environment in every case, the tetragonal 123 immediately begins to decompose to the 211 phase according to reaction (3). The extent of the decomposition is dependent on the temperature-time history and also on the nature of the specific precursor. For example, in the case of Precursor B, the extent of reaction (3) is not significant up to temperatures as high as 750 C and for times as long as 8 hours. However, at 810 C (Run B10) the decomposition is very severe; proceeding all the way to elemental copper (Reaction (6)). In addition, the tetragonal 123 was not even observed in Precursors E, F and G. We believe that in these cases, the decomposition is almost instantaneous since we do observe small amounts of the tetragonal 123 in separate experiments where the heating is done very rapidly (10 seconds between 580 C and 700 C). Of particular significance here is the fact that the pretreatment of the precursors may be more important than originally thought. For example, the only difference between Precursor G and B is the fact that the latter was pre-dried at Boeing, using a slightly different drying procedure; yet no tetragonal 123 was observed in G whereas there was only slight decomposition in B (compare G1 with B6).

#### Reversibility of High Temperature Phases

Although the tetragonal 123 tends to decompose at high temperatures ( $>700$  C) when it is in an oxygen-free environment, we have found that the decomposition products can be reformed into the 123 phase if they are exposed to oxygen at sufficiently high temperatures. Figure 26 illustrates these phenomena for Precursor D. Starting at time = 7 min, the tetragonal 123 phase



FIGURE 25.

PRECURSOR B FIRED IN AIR AND IN HELIUM

(a) In Air



At Room Temp.



(b) In Helium

At 750 C



At Room Temp.

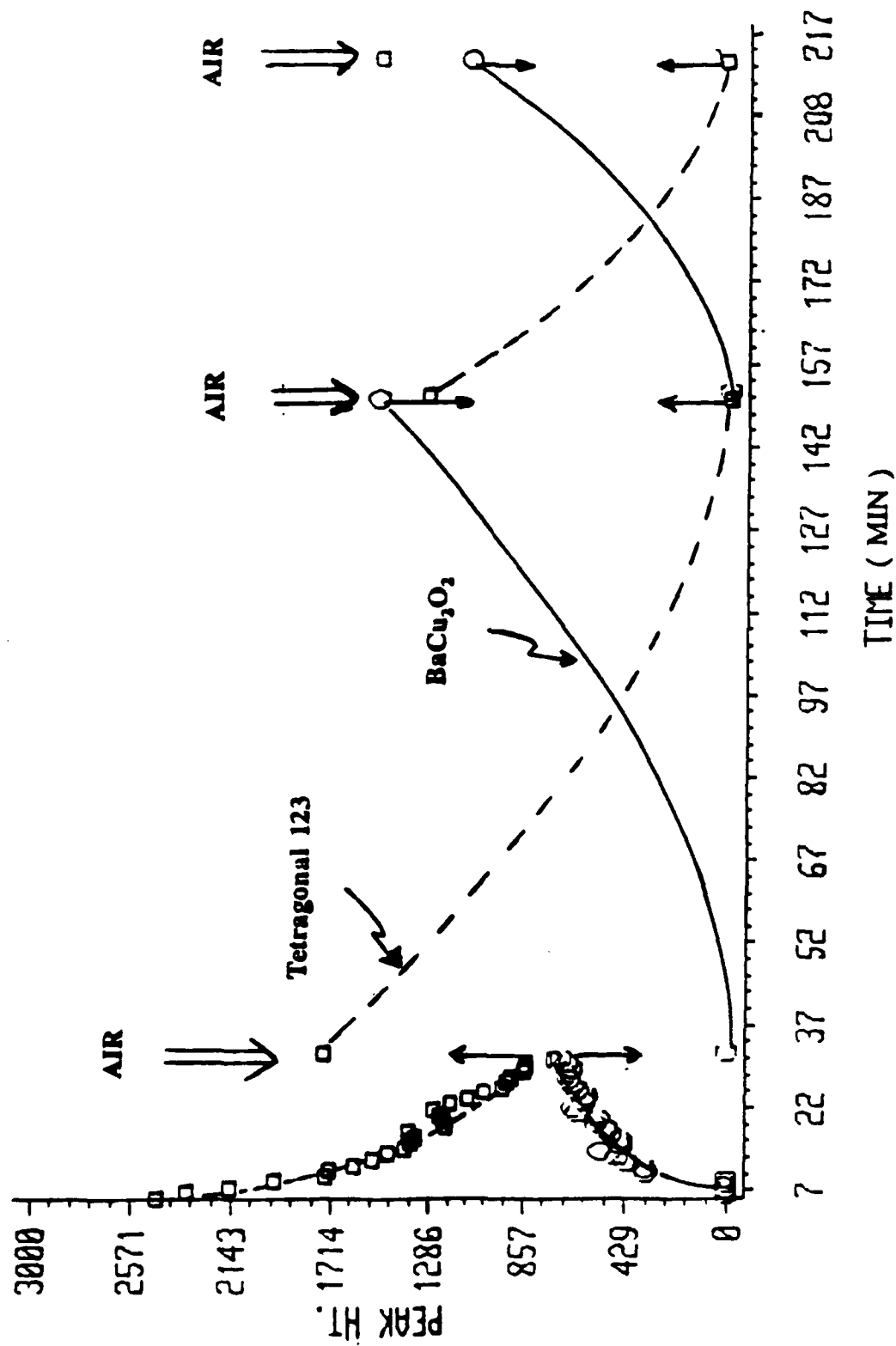


37.0 20.5 24.0 27.5 31.0 34.5

TWO - THETA

FIGURE 26.

# HIGH TEMPERATURE REVERSIBILITY (Flashed Nitrate, 840 °C)



is slowly decomposing in helium while one of the decomposition products ( $\text{BaCu}_2\text{O}_2$ ) increases. At time = 36 min, the environment is switched to air and there is a rapid reformation of the 123 species accompanied by a complete disappearance of  $\text{BaCu}_2\text{O}_2$ . During this reformation, it is an oxygen-rich 123 which initially forms but, after about 10 minutes, this phase transforms into sharply split tetragonal (HTT). As shown in Figure 26, the cycle can then be repeated by switching back to helium. However, the decomposition cannot be reversed if the switch to an oxygen environment is accomplished at too low a temperature. In another experiment in helium (with Precursor B), the tetragonal 123 began to form at about 610 C but completely decomposed according to reaction (3) by 800 C. In this experiment the temperature was then lowered to 550 C in helium and then switched to air. Rather than reformation of the 123 species, we observed further decomposition to elemental copper (reaction (4)). We believe this to be a thermodynamic limitation since 550 C is below the tetragonal-orthorhombic phase transition temperature (580-600 C). In other words, the decomposition products can be reversed to the tetragonal phase but not to the orthorhombic phase. Since the tetragonal phase is not favored (stable) below the transition temperature, switching to air results in further decomposition.

#### Formation of Orthorhombic 123

Although we have successfully formed the tetragonal 123 at low temperatures by firing in an oxygen-free environment, we have not been able to form single phase orthorhombic 123. When the precursors are fired in air, an oxygen-rich tetragonal 123 LTT is formed at about 800 C but it takes higher temperatures and longer soak times before it is able to form the HTT phase. It was not possible to form orthorhombic 123 from the oxygen-rich tetragonal 123 no matter what combinations of oxygen annealing were attempted. When firing in an oxygen-free environment, the HTT phase is readily formed at low temperatures but it is always accompanied by some decomposition products. The extent to which the decomposition products can be reformed into the 123 species when they are exposed to air, is not known. Whereas the decomposition products are undetected by XRD, the latter is only capable of detecting crystalline phases above the 3-5% level. Consequently, we do not always get the tetragonal-orthorhombic phase transition upon cooling. The best success to date was in a run with the citrate precursor where, after organic burnout (~ 550 C in air), the sample was heated at 5 deg/min in helium to 700 C. At this temperature the HTT phase was formed and, before significant decomposition could occur, the environment was switched to air. The sample was then heated in air to 800 C and held there for 15 hours, at which time it was cooled in air to room temperature at 5 deg/min. This sample exhibited the tetragonal-orthorhombic transition at about 575 C and, although it was not fully crystallized, it had a low but broad  $T_c$  (93 K by magnetic susceptibility measurements).

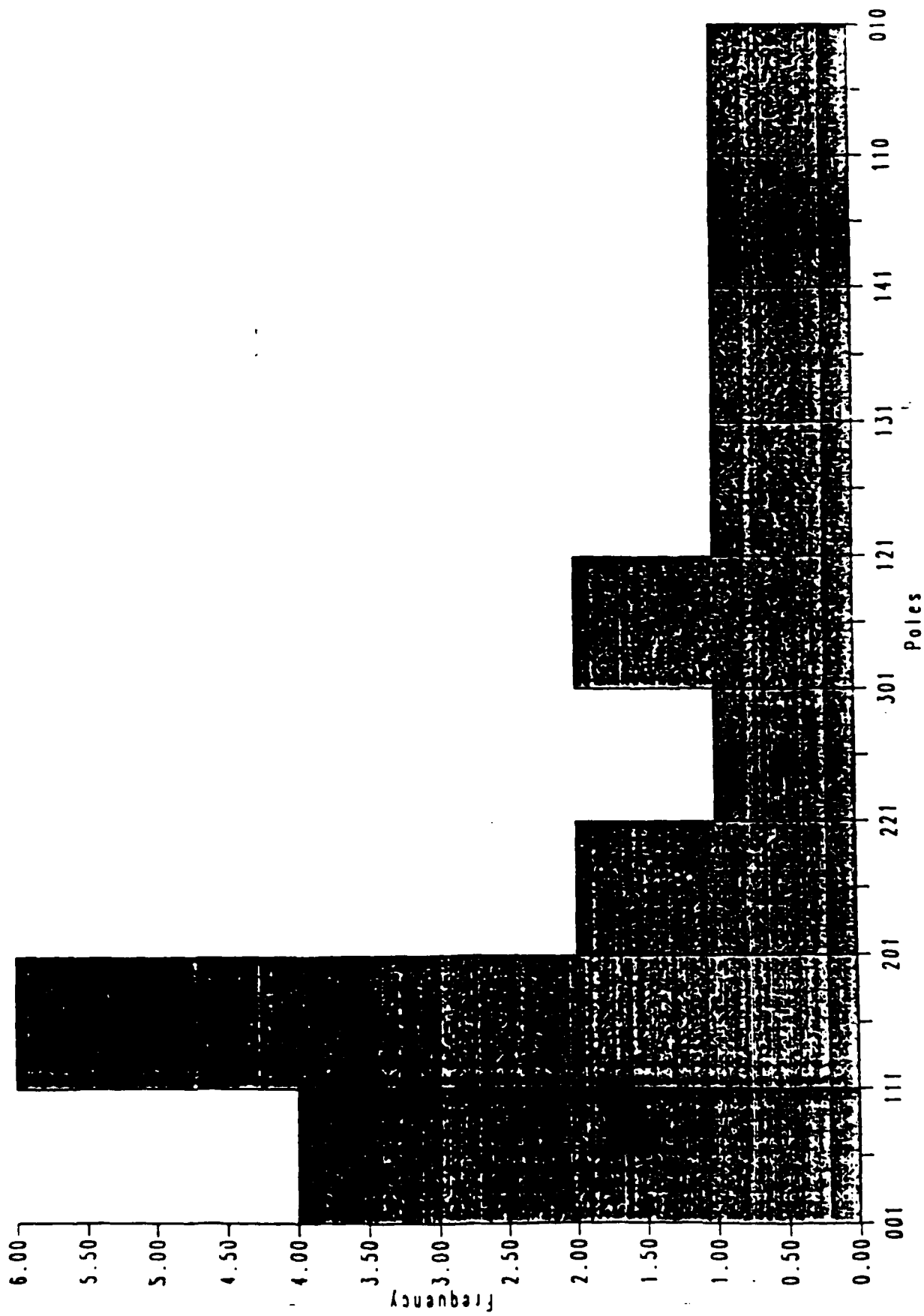


Figure 27.

### Tape Texture

Two tape-cast samples, one sintered at 950C for one hour, the other for six hours, were examined. X-ray diffraction was performed on the intact sintered tape and then again on the crushed powdered tape. The distribution of major zone axes closest to the tape plane is shown in Figure 27. When compared with computer simulated models, the observed increase in intensity of the (001) type peaks in the crushed powder sample indicated preferred grain growth along the a, b planes. When spectra from intact tape are compared, there is a further increase in these (001) type peaks as well as the (111) peak. This is characteristic of preferred orientation where the (001) and (111) type planes of the grains tend to lie close to the plane of the tape. Selected area diffraction patterns taken from a random sampling of grains bears this out.

It was hoped that examination of the six hour tape would point towards a trend in the extent of texturing. Unfortunately, difficulties in sample preparation resulted in a sample that showed unusually poor phase assemblage and was unsuitable for study. The experiments are continuing.

Studies on the correlation of processing conditions with microstructure and electrical properties revealed two empirical trends. Samples showing a broad  $T_c$  (14K) also exhibited a wider range of  $\Delta a/a$  values while those with narrow  $T_{c,s}$  (10K) showed a very narrow  $\Delta a/a$ . Samples having a broad  $\Delta a/a$  distribution naturally included some values significantly larger than the averages for that grain. These same samples showed a higher onset than the narrowly distributed samples, whose  $\Delta a/a$  averages were comparable to other samples. The results are summarized in the following table.

### Heat Treatment Effects On Grain Size

Microstructure/property relationships were extensively studied for freeze-dried, sol-gel, and solid state prepared monolithic  $YBa_2Cu_3O_{7-x}$ . These studies included pure, silver, and platinum doped  $YBa_2Cu_3O_{7-x}$ . Effects of dopants on the superconducting properties of the grains and grain boundaries were investigated. The studies were made possible by our recent interpretation of the ac susceptibility measurements of  $T_c$ .

The transition temperature widths for freeze-dried  $YBa_2Cu_3O_{7-x}$  sintered at different times are shown in Figure 28, where it can be observed that the sharpest transition temperatures were obtained for the samples sintered between 12-20 hours in oxygen. The samples sintered in air exhibited generally wider transitions which we attribute to oxygen deficiency. The wider transition

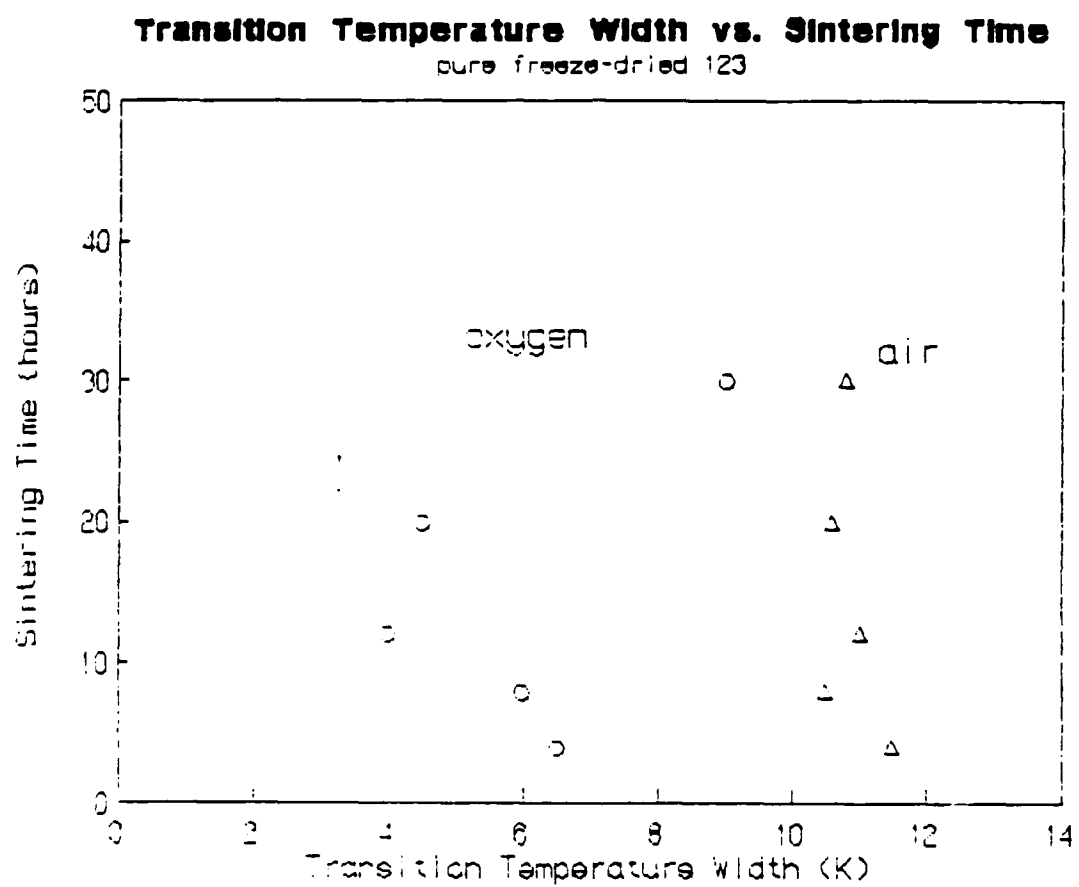


Figure 28

### Average Grain Size vs. Sintering Temperature

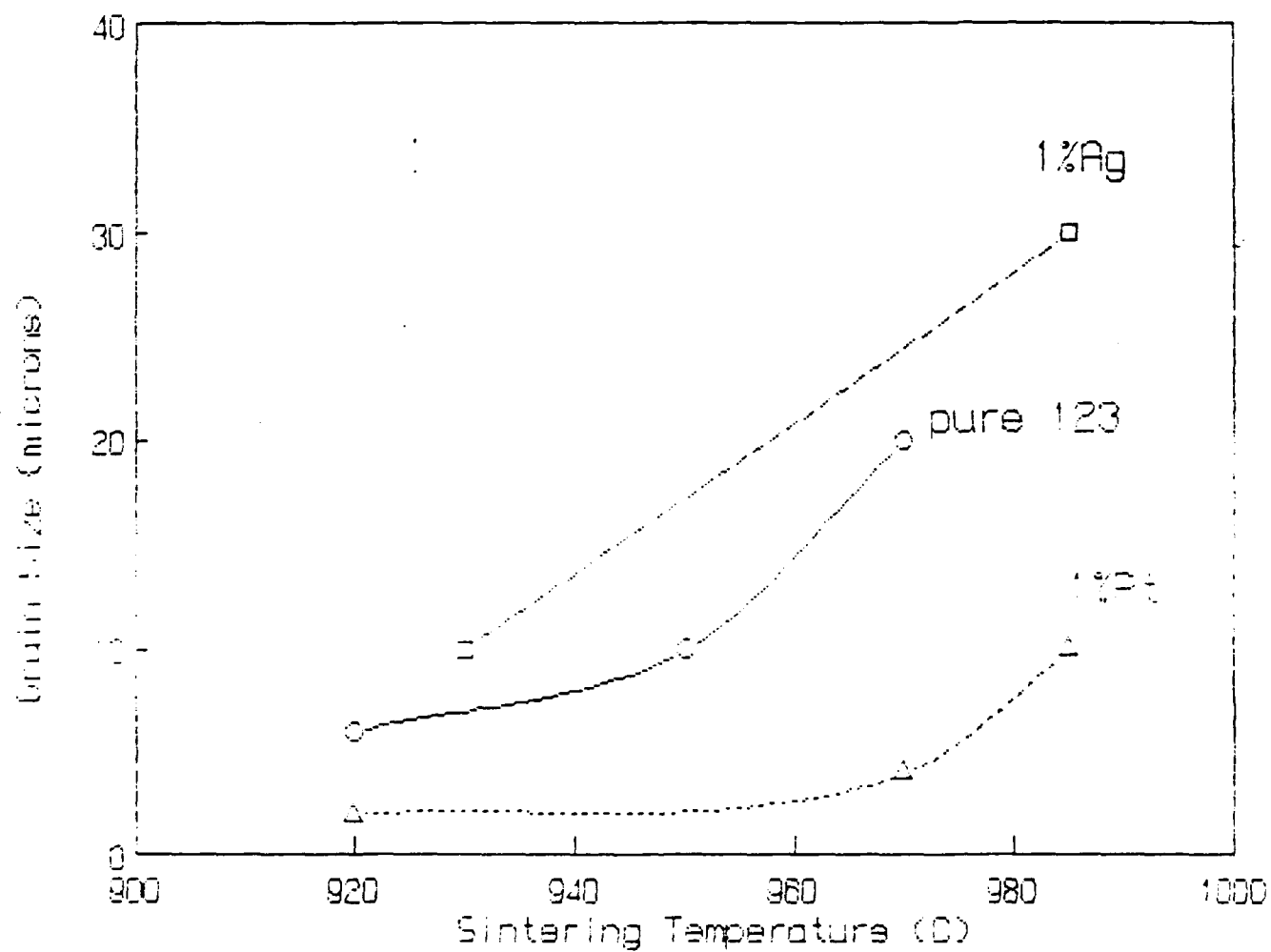


Figure 29

### Maximum Grain Size vs. Sintering Temperature

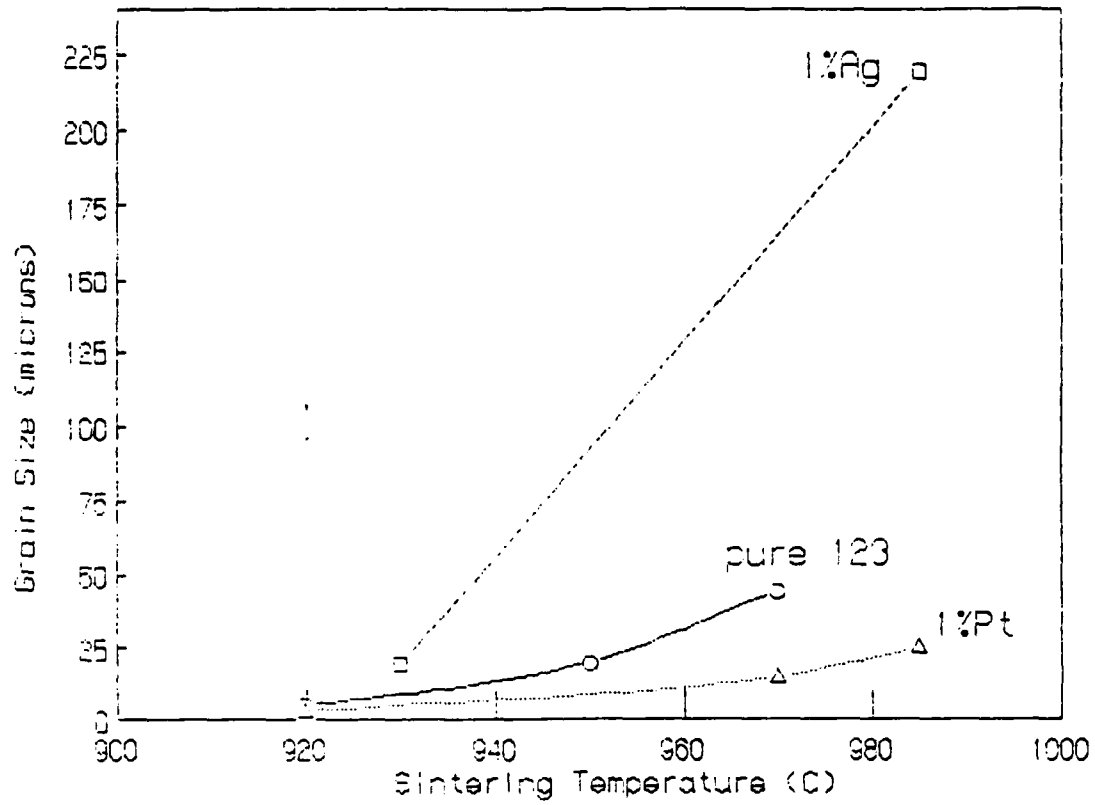


Figure 30



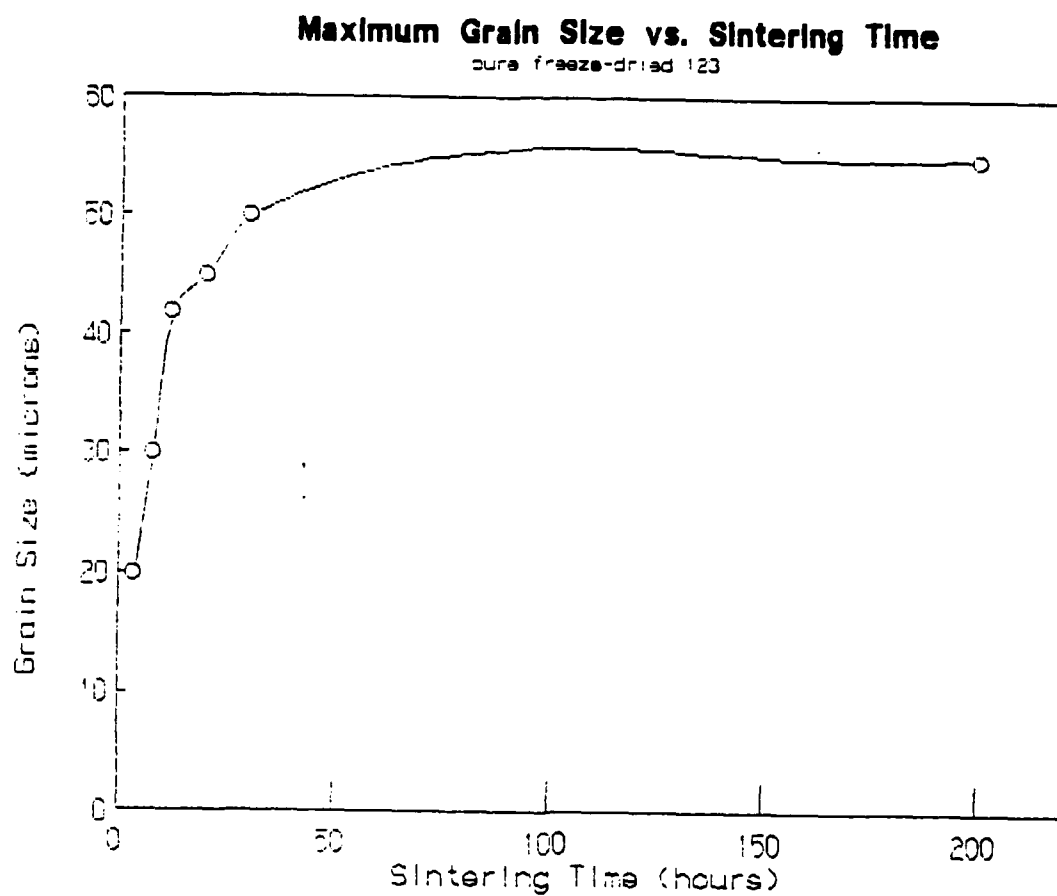


Figure 31

temperature widths can often be reduced by annealing the sample in oxygen. The transition temperature width and fine structure of the transition curve will be correlated to transport current density measurements next quarter. The maximum and average grain sizes versus sintering temperatures and times for pure, platinum, and silver doped  $\text{YBa}_2\text{Cu}_3\text{O}_{7-x}$  are plotted in Figures 29-31. The results show that the addition of platinum (1 at.%) to 123 reduces the grain size significantly, even at high temperatures, which might prove beneficial in the fiber processing to producedense fibers of small grain size morphology. On the other hand, the addition of silver increases the grain size by partial melting. The grain size effect is also seen in the transition temperature curves as well as in the current density measurements as discussed in the next section under Characterization.

**Superconducting Properties--**The mutual inductance apparatus (ac susceptibility) for measuring the superconducting transition temperature was calibrated with samples consisting of mixtures of orthorhombic and tetragonal phases. The results were in agreement with theory as shown in Figure 32 where flux exclusion is plotted as a function of increasing orthorhombic phase content. The dependency is nearly linear, allowing for experimental error. The transition temperature apparatus was also calibrated for electromagnetic unit exclusion thus giving us a direct quantitative magnitude for magnetic flux exclusion. We have measured detailed transition temperatures in over 100 superconducting samples. These results are now being interpreted and they will be directly correlated to measured transport current densities.

Figures 33-35 show flux exclusion results versus applied field for pure, platinum, and silver doped  $\text{YBa}_2\text{Cu}_3\text{O}_{7-x}$  samples. The flux exclusion amount for the pure 123 is much higher than for the silver and platinum doped 123 samples. Figure 34 shows the flux exclusion versus applied field for the 1% platinum doped 123 where it can be observed that the sample heated to 990C exhibited larger flux exclusion than the sample heated to only 950C. This result directly correlates with transport current density which is lower for the sample with smaller flux exclusion. There also seem to be different effects of applied fields on the transition temperature width and amount of flux exclusion for the pure, platinum, and silver doped 123. The transition temperature width for the 10% Ag doped sample doesn't seem to be dependent on the applied field but the pure and platinum samples are greatly effected by the field (Figure 36). This also correlates with the current density where the silver sample shows the highest current density of about  $4500 \text{ A/cm}^2$  when corrected for the self field effect. This result might be important in determining the role of weak links in the current transport mechanism through the bulk material. We are presently determining the nature of the weak links and the mechanism of the current transport so we can modify the material to improve the critical current density.

Current density results for varying silver content in the 123

compound are presented in Figure 37. This figure shows the optimum current density achieved in 10% Ag doped sample which has a dense, large grain size microstructure.

### Flux Exclusion vs. Orthorhombic Phase Content

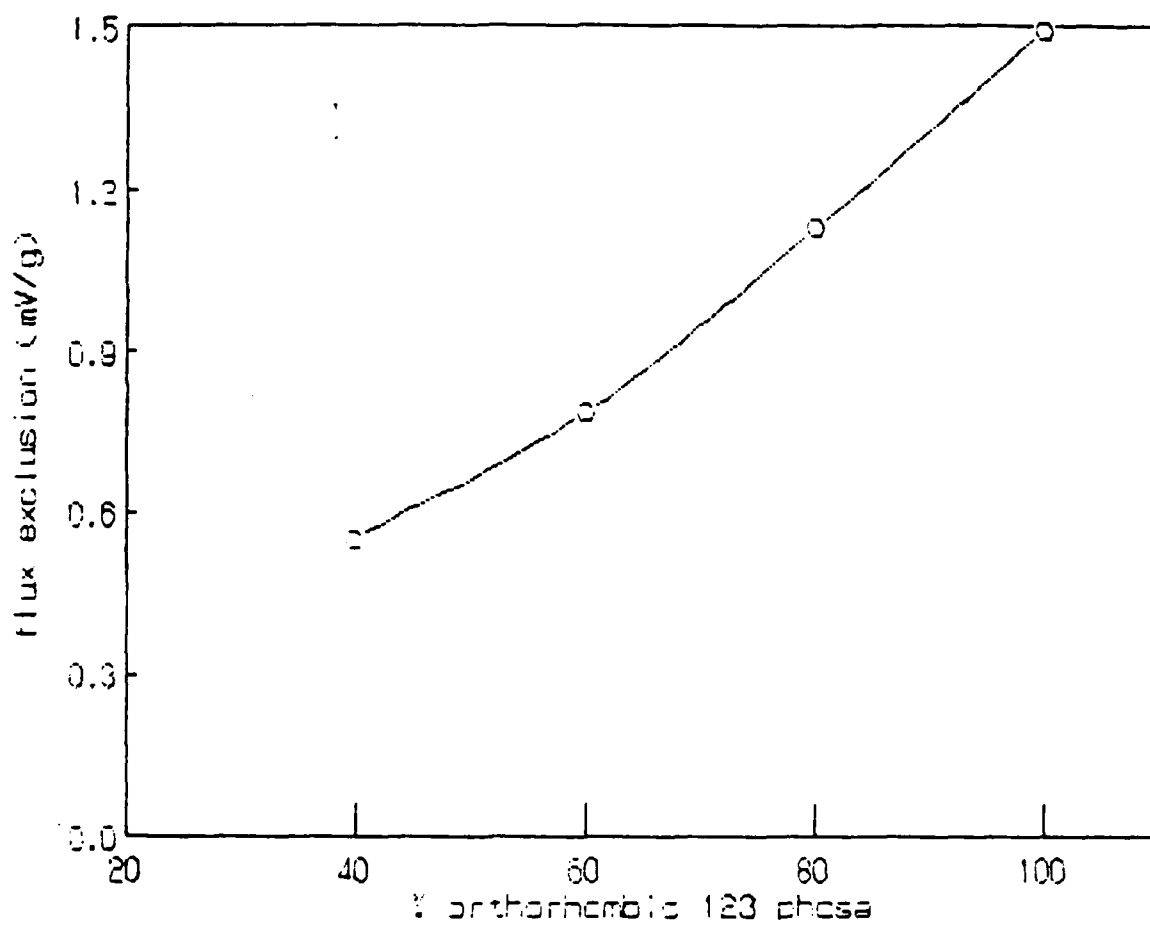


Figure 32

## Flux Exclusion vs. Applied Field

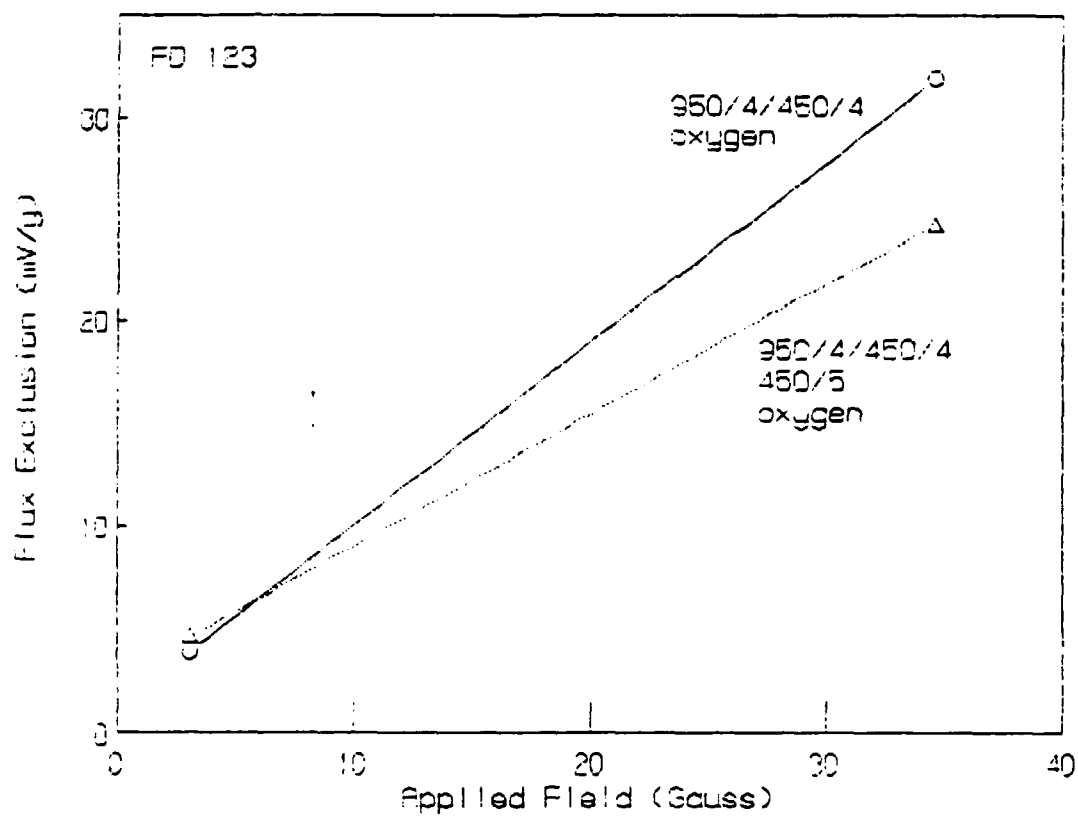


Figure 33

## Flux Exclusion vs. Applied Field

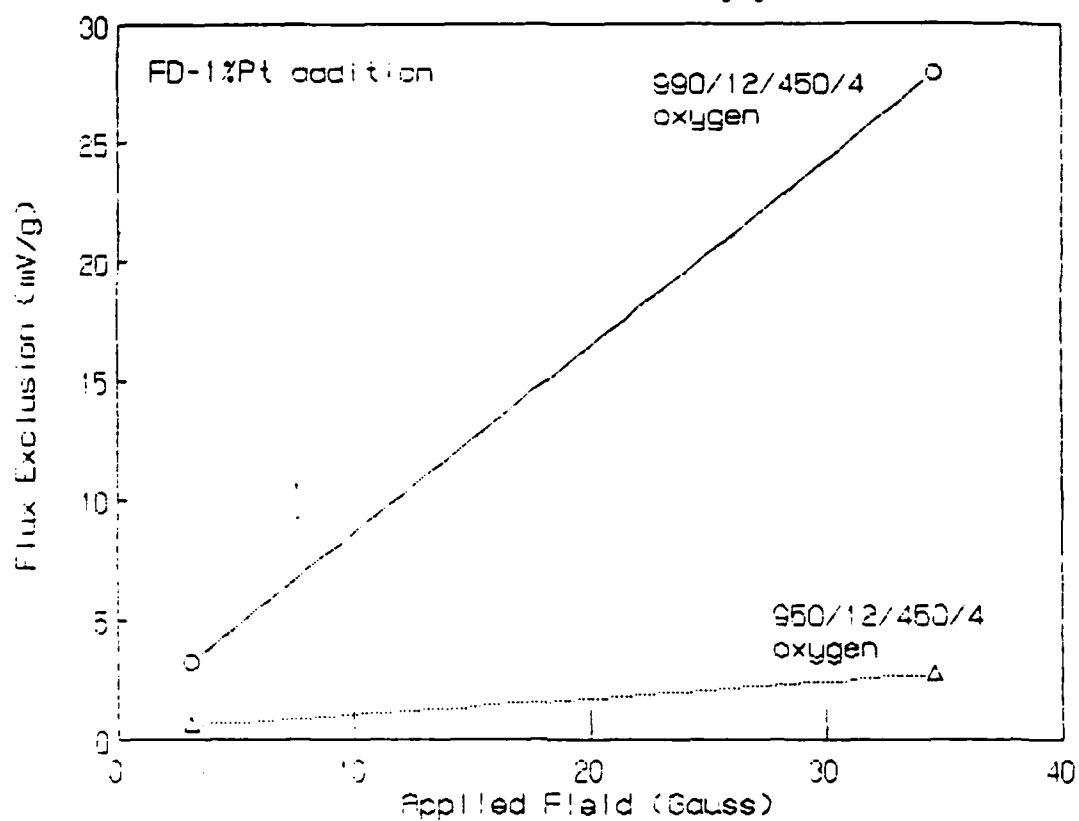


Figure 34

## Flux Exclusion vs. Applied Field

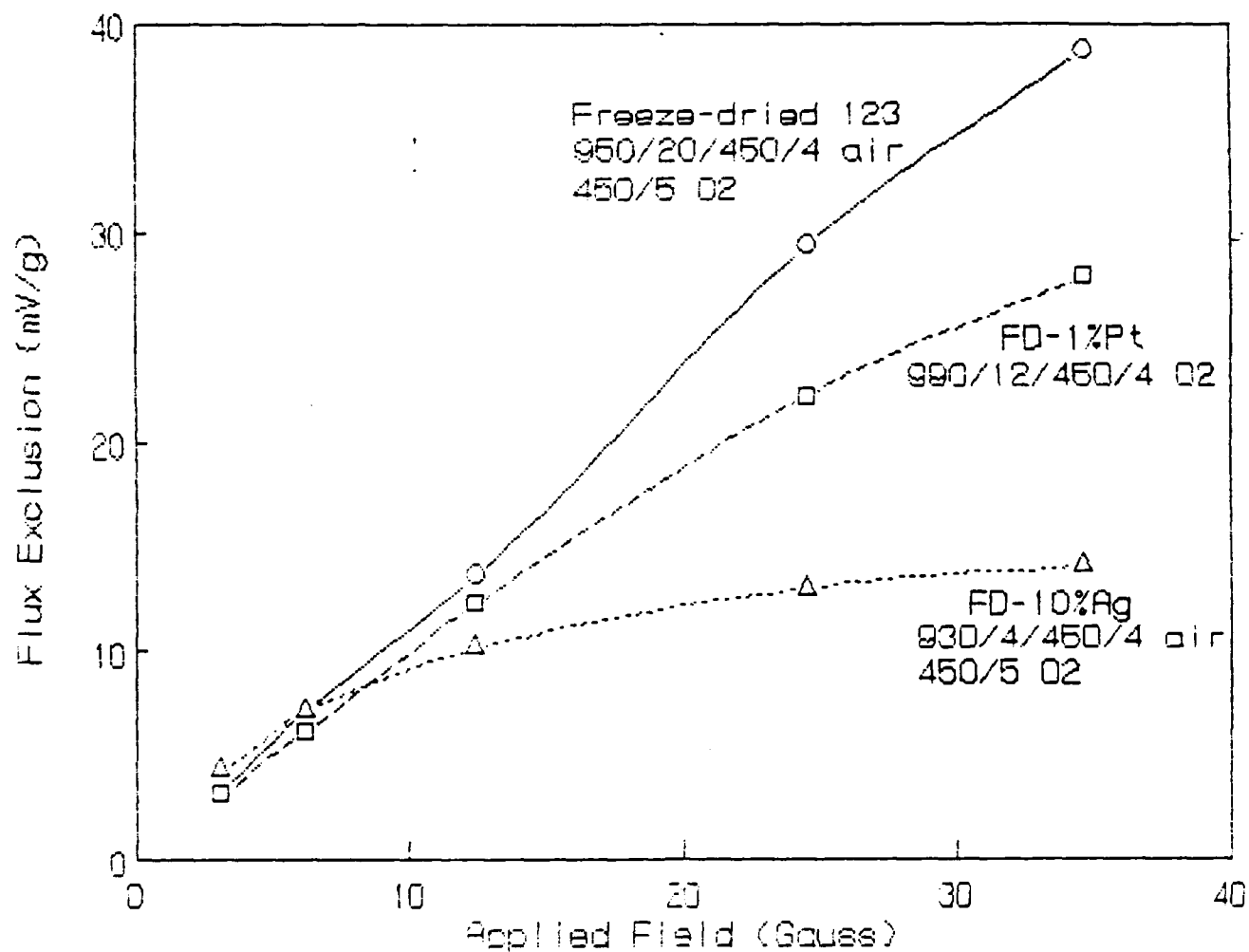


Figure 35

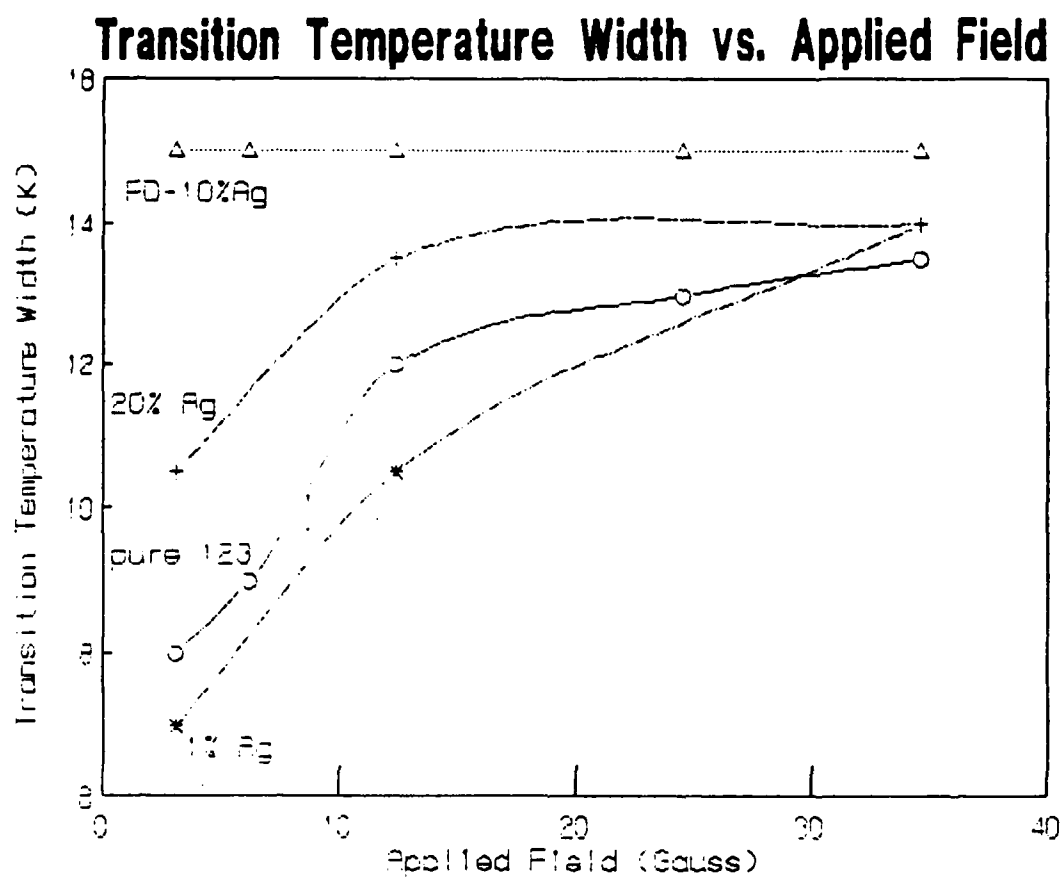


Figure 36



# SELF FIELD EFFECT ON CURRENT DENSITY

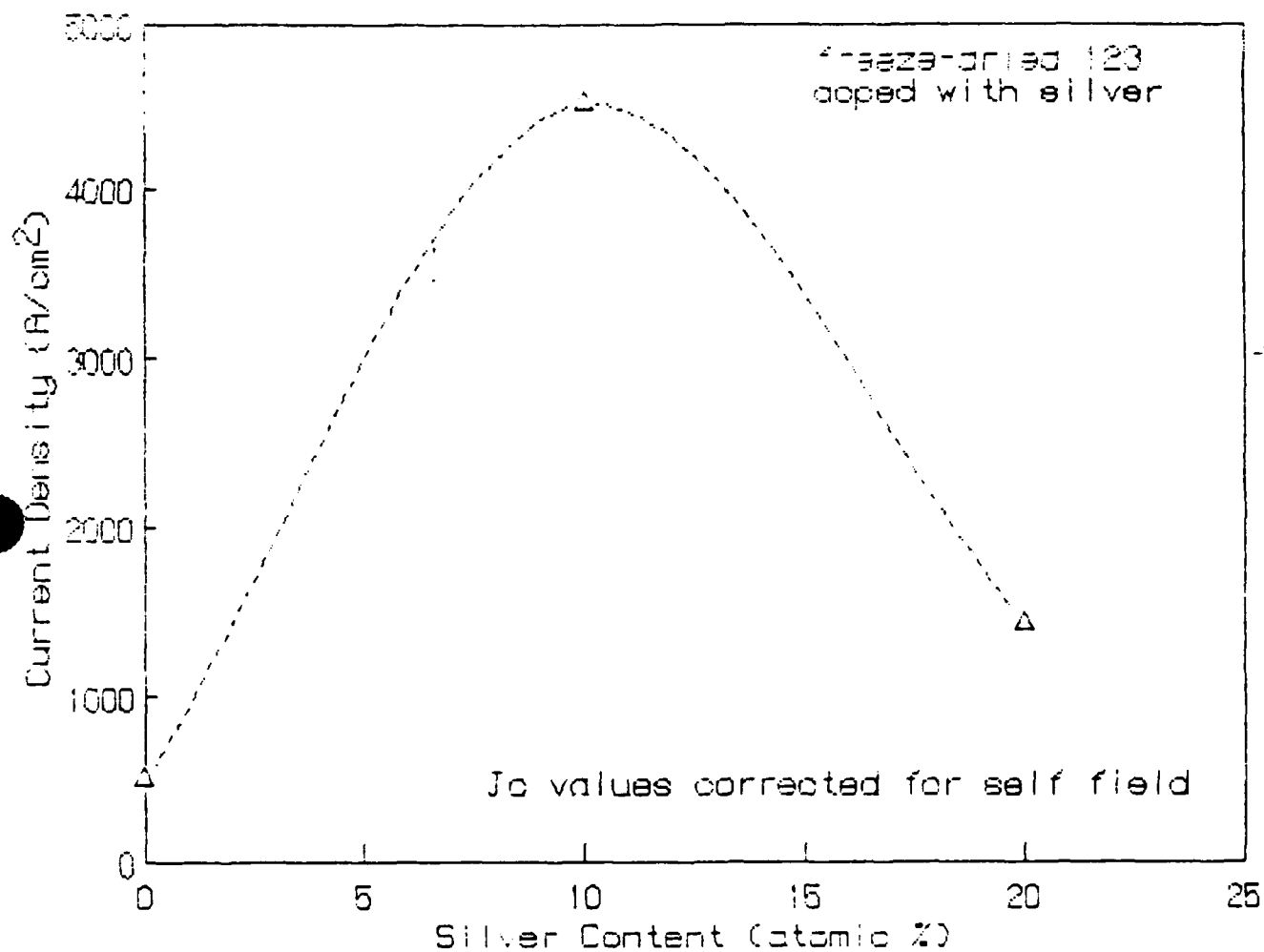


Figure 37

## (C) MODELING

### Phase Diagrams

A phase diagram calculation, using the same energy parameters as de Fontaine, was performed. The results, presented in **Figure 38**, show that the phase separation between the Orthorhombic and the DPO phase definitely exists in the lower temperature region. This implies that Dr. de Fontaine's phase diagram may need some correction. The theoretical modeling work will now move into the calculation of oxygen atomic diffusion in the Cu-O basal plane.

### XAFS Modeling

Using Yacoby's programs, initial studies were directed towards fitting the first shell only. Five oxygen sets of distances were used with EO and a k-independent phase shift as the variable parameters. The fitting range is 0.9-2.3 Å. A very good fit was obtained after eight attempts, even better than our original results. Second shell fitting with 33 sets of O, Y, Ba, Cu single, double and triple scattering paths were used. Three Debye-Waller factors (one for O, one for Y and Ba, one for Cu), three mean paths (same relationship as above) and four k-dependent phase shifts (each atom has one) were used as variable parameters in the beginning. Additional  $\lambda$  and k-dependent phase shifts were assigned to the second shell oxygens. After twenty attempts, a satisfactory fit was obtained.

### La<sub>2</sub>CuO<sub>4</sub>

A comparison between calculated and experimental spectra in La<sub>2</sub>CuO<sub>4</sub> is shown in **Figure 38**. Experiment and theory spectra were fourier filtered in real space with a window between 0 and 3.9 Å. The main points to note are that the overall magnitude and phase predicted by the theoretical calculation show general agreement with experiment. The differences arise in multiple scattering contributions not taken into account in the calculation. From the comparison between calculations using different muffin-tin radii, we conclude that the total amplitude of c is weakly sensitive to changes in the muffin-tin radii.

**Figures 39 and 40** illustrate the effect of charge redistribution in the Cu-O(1) bond of changes in the total charge of the bond, in the phase and amplitude of  $f_{\text{eff}}$ . We calculated the backscattering amplitude and phase for an oxygen atom located at 1.90 Å from the absorbing atom, using a neutral configuration (with  $r_s = 0.93$ , 1.35 Å) and including a 2p hole in the oxygen atom ( $r_s = 0.86$  Å). The following observations are made.

- Differences in the scattering amplitudes due to difference

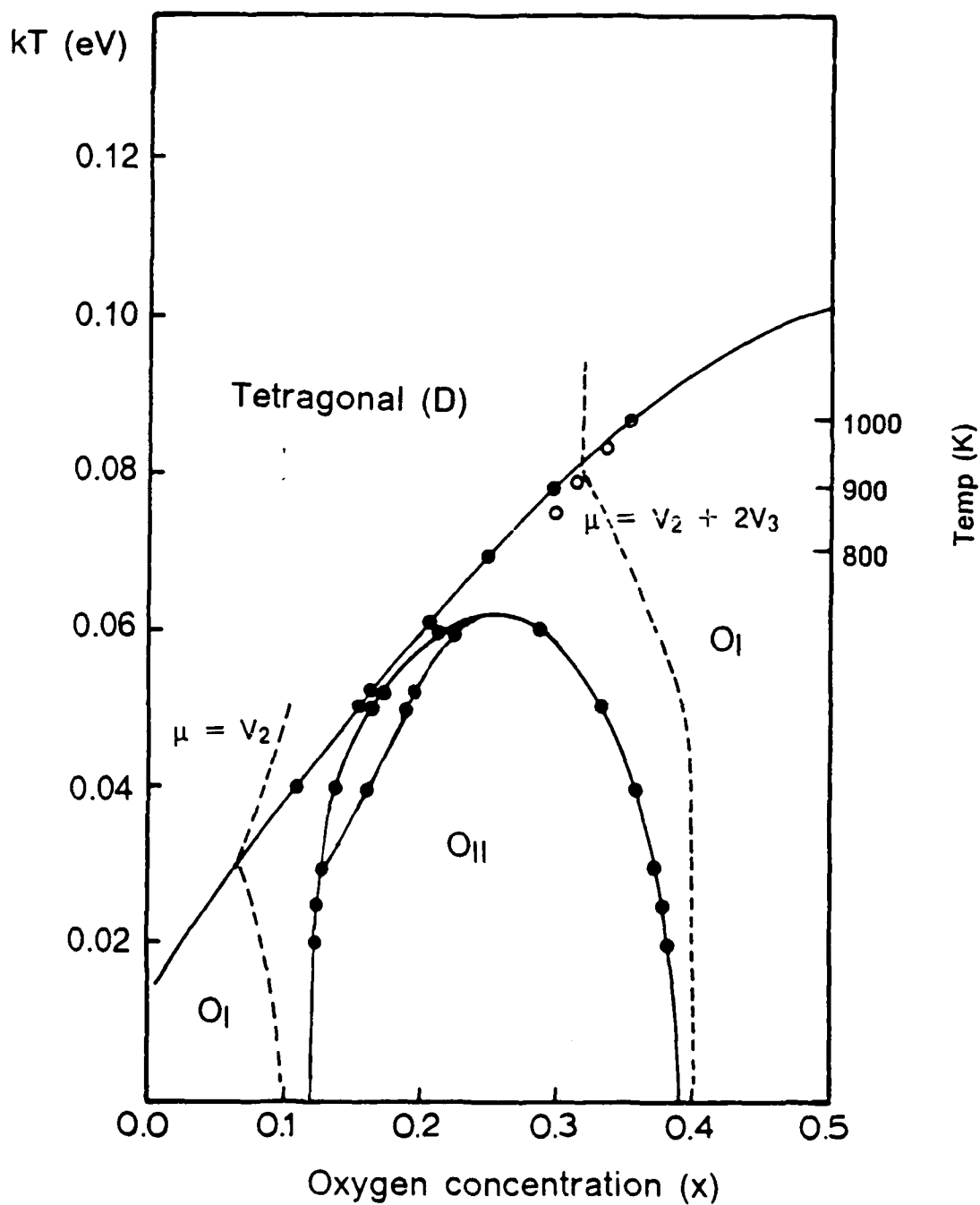


Fig. 38. Phase diagram with energy parameters  $\varepsilon = 0.09$  eV,  $v_2 = -0.2$  eV and  $v_3 = 0.05$  eV

in total charge can be as much as 20% at  $k = 5\bar{u}-1$ .

- At high energies, the backscattering phase is more sensitive to changes in charge distribution than the amplitude.

We have also compared the phase and amplitude of the contribution from the first shell O (1) in  $\text{La}_2\text{CuO}_4$  with the first shell oxygen contribution in 123 (see Figures 39 and 40). Experimental and calculated data were filtered in an identical manner and the 123 experimental data were corrected for structural disorder. The main conclusions we draw from this comparison are:

- The main difference in the amplitudes is due to the difference in local structure between  $\text{La}_2\text{CuO}_4$  and 123. The remaining difference provides weak evidence for a difference in charge distribution of one hole per four oxygen atoms, between the oxygen atoms in 123 and the O(1) atoms in  $\text{La}_2\text{CuO}_4$ .

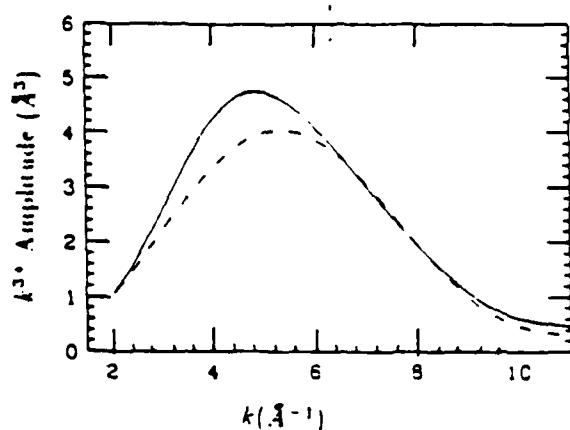
- Differences in the phase are consistent with uncertainties introduced by the potential construction.

#### Superconducting Properties

We have analyzed our susceptibility measurement of the superconducting transition in terms of ac losses associated with various microstructural features in  $\text{YBa}_2\text{Cu}_3\text{O}_{7-x}$ . These results provide a unique insight into inter- and intragranular superconducting and microstructural features. They also provide us with new insight into the nature of the weak-links and guidance toward improving critical current densities in an applied magnetic field. Publication is planned in the Fall MRS meeting.

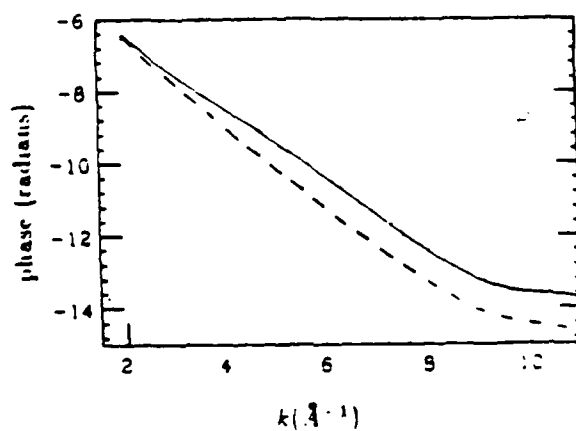
The net signal from the balanced pick-up coils contains in-phase and out-of-phase components, corresponding to the real and imaginary part of the ac susceptibility,  $X'$  and  $X''$ , respectively. Skin effect losses in the normal state and flux flow losses in the superconducting state do not effect our measurement at the 200 Hz we use. The real and imaginary components of two  $T_c$  measurements are shown in Figure 41 for 123 samples.

The ac susceptibility measurement is capable of discriminating between inter- and intragrain properties. Decreasing the temperature causes the grains to become superconducting at  $T_c$  onset but the weak-links are still resistive due to thermal fluctuations. Therefore the initial ac field induced screening currents only flow inside the grains. The intragrain current increases with decreasing temperature, leading to better screening, i.e. smaller  $X'$  and larger  $X''$ .



Total XAFS amplitude for Oxygen first shell contribution. Solid line corrected experiment. dot line theory for neutral atom dash line uncorrected experiment.

Figure 39.



Total XAFS phase for Oxygen first shell contribution. Solid line corrected experiment. dot line theory for neutral atom. dash line uncorrected experiment.

Figure 40.

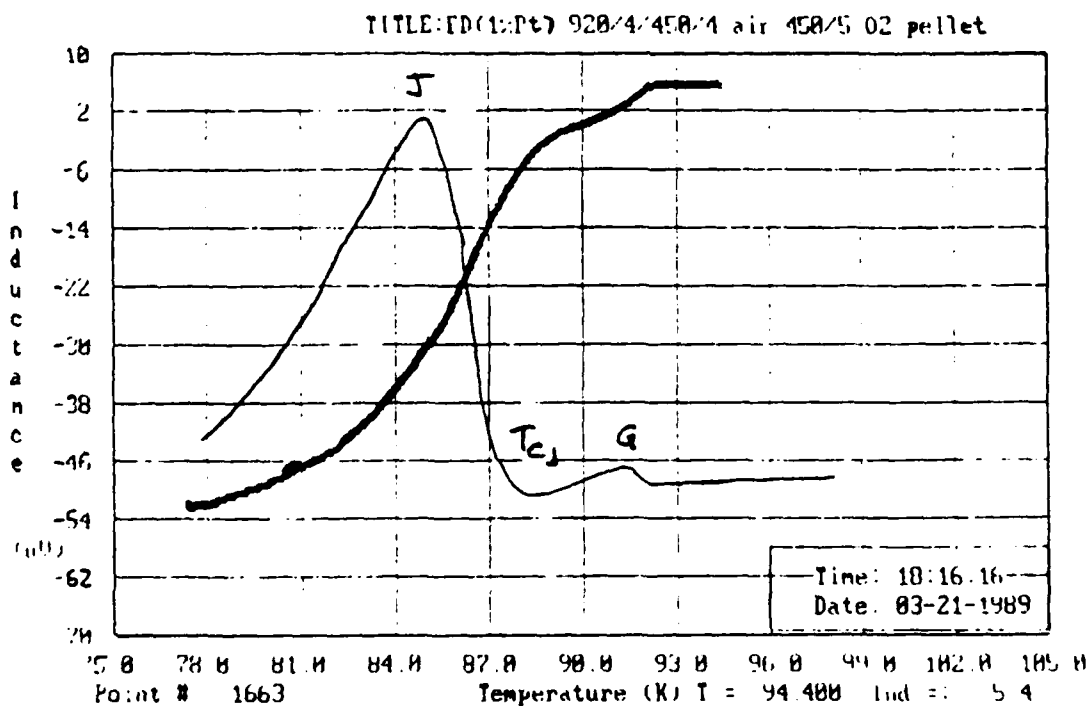
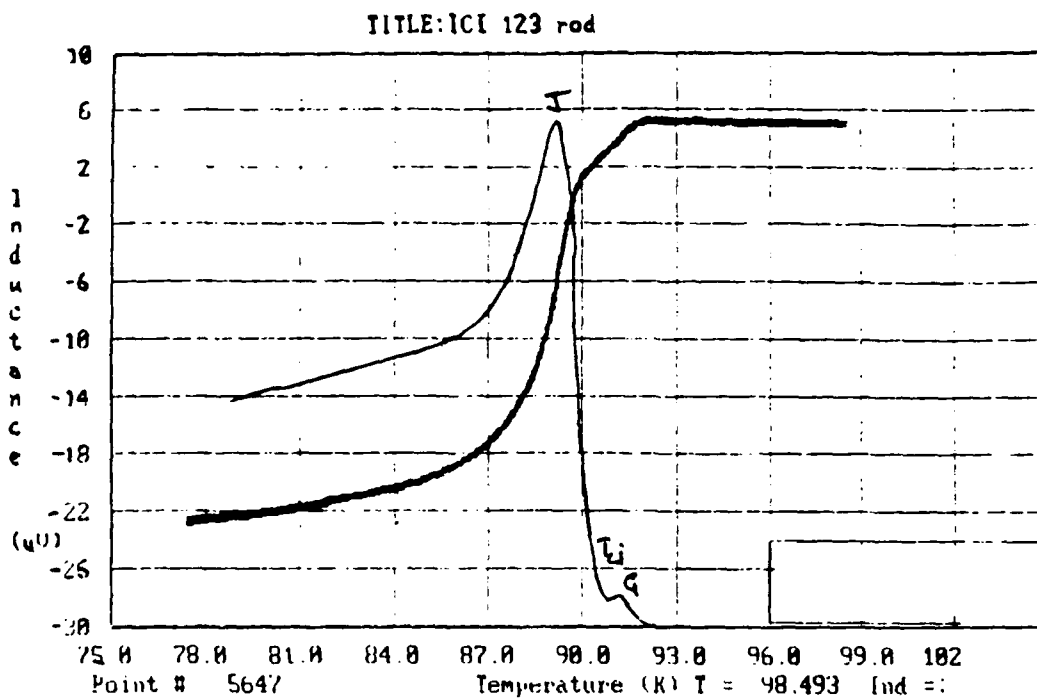


Figure 41.

The ac amplitude still reaches the center of the grains at this point. The imaginary part  $X''$ , which is proportional to the ac hysteresis losses has a maximum at the temperature where the penetration depth of the grain begins to be reduced below the grain's radius, denoted as "G" in the Figure 41. At this temperature the ac field no longer penetrates the whole grain and the volume in which hysteresis losses occurs shrinks, thus the first peak in  $X''$ .

The weak-links are able to carry a supercurrent if the temperature is below the phase locking temperature, noted as " $T_{cJ}$ ", at which the energy of the weak-link junction becomes equal to  $kT$ . This temperature corresponds to the shoulder of  $X'$  or the valley between both peaks in  $X''$ . Below this temperature macroscopic shielding currents through grains and weak-links are induced. The ac losses of the junctions increase below  $T_{cJ}$  and cause the intergrain maximum  $X''_J$ , at which the ac field just penetrates into the center of the specimen via the weak-link paths, "J" in Figure 41. In the temperature region below  $T_{cJ}$  the intergrain signal dominates compared to the intragrain one due to the much smaller intragrain penetration depth, i.e. the much larger  $j_{cG}$ . For this reason the ac susceptibility is representative of intergrain properties at  $T \leq T_{cJ}$ , and the loss curve is dominated by the intergrain peak.

The height, position, and width of the intergrain maximum reflects the intergrain volume, the intergrain critical current density and the distribution of the coupling energy or junction current. For instance, measurements of a low quality sample would show a broad maximum width with a low temperature center point. The ratio  $(X''_J/X''_G)_{\max}$  should decrease with decreasing intergrain volume and better homogeneity.

The current density data for our samples were analyzed for the self field effect that is associated with inducing a self field in a current density sample by passing a current through the sample during the experiment. These fields can be quite large for larger samples where 10's of amperes are being carried through the sample. The results obtained with transport current measurements were corrected for the self field generated by passing current. The self field effect on current density can be observed in Figure 42. Figure 43 shows a current density versus self field for a typical  $YBa_2Cu_3O_{7-x}$  sample of varying thickness. The sample shows higher critical current density as the thickness is decreased thus reducing the current being passed through it and hence self field is decreased. When the sample is corrected for the self field effect, the resulting zero-field current density is about the same for all the thicknesses. This shows the importance of reporting the current density values together with sample size and current used so results by different researchers can be directly compared.

## Self Field Effect on Current Density

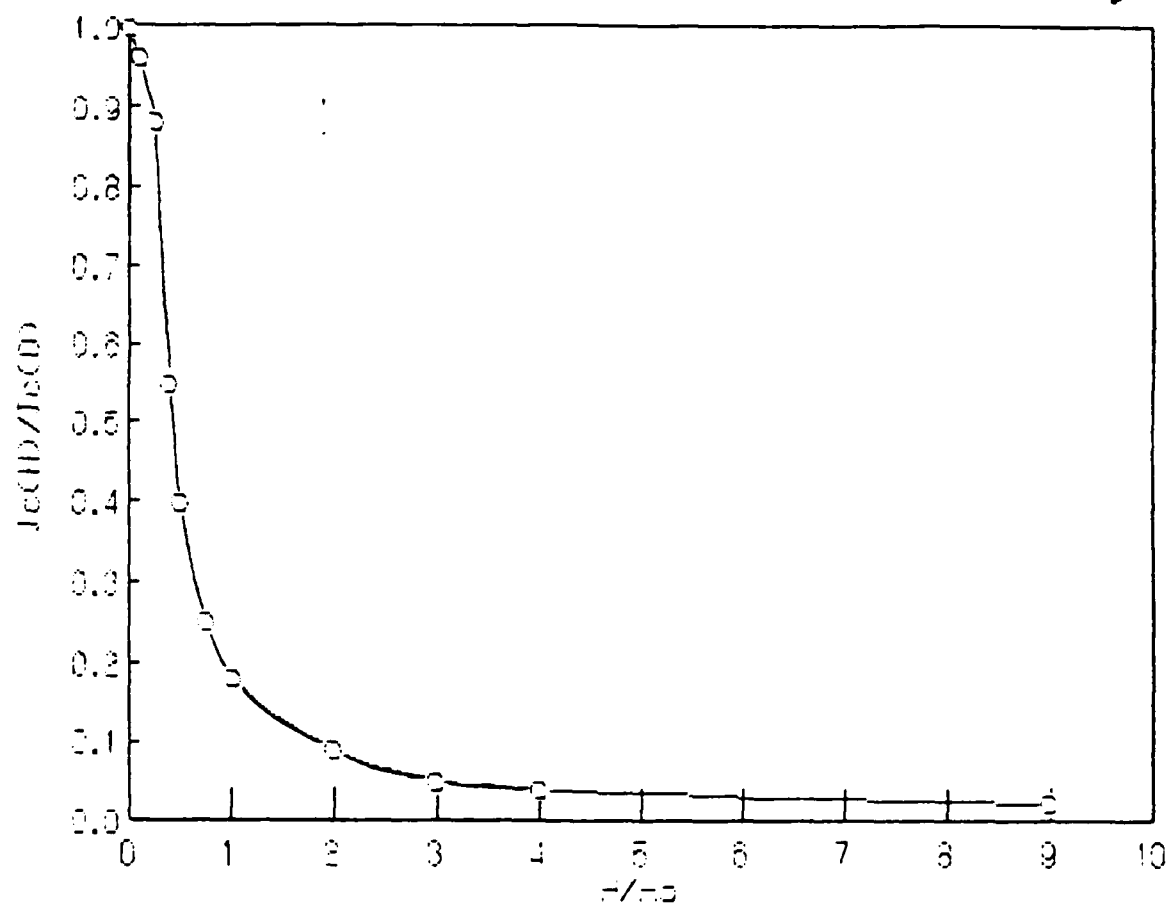


Figure 42.



## Current Density vs. Self Field

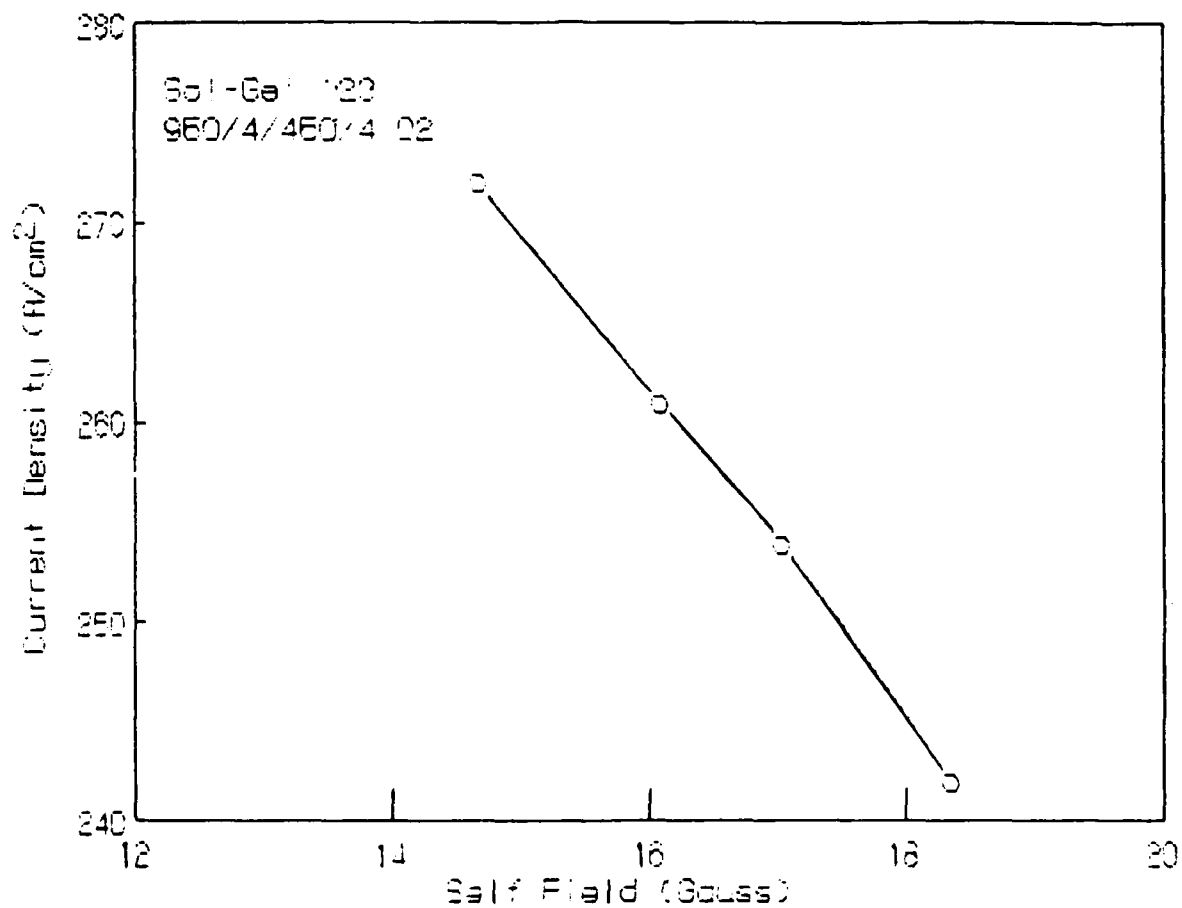


Figure 43.

#### (D) DEVICE REQUIREMENTS AND FABRICATION APPROACHES

##### Superconducting Rivet Gun

Among the potential devices we are exploring for application of superconductors is an electromagnetic rivet gun. In it, capacitors are replaced by magnetic energy stored in a flux-trapping magnet. **Figures 44 and 45** present superconducting design options that were considered. There are two basic components to the conventional electromagnetic rivet gun, the driver, and a capacitor bank which sits on the manufacturing floor. In the figures, Option #1 indicates that the capacitor is replaced by a superconducting coil which is quenched to provide the need current pulse to the driver. All other options have incorporated the quenching superconducting coil into the hand held driver. Option #4 includes a superconducting drive plate. This would eliminate the last remaining loss component, the magnetic diffusion of field lines into the driver plate when the superconducting coil quenches. In Options # 3 & 4 the charging battery source is replaced with a superconducting magnet which would provide a magnetic field source to energize the flux-trapping quench coil. In this way the high voltage high current leads between the source of power and the driver component can be eliminated. A schematic of the device representative of Option # 4 is presented in **Figure 46**.

There are many advantages to the superconducting rivet gun, these are summarized below.

---

## ADVANTAGES TO SUPERCONDUCTING RIVET GUN

Elimination of capacitor, leads, and switching circuits

safety  
operation in hazardous locations  
improved productivity  
weight

In conventional EM operation 97% of energy stored in capacitor is lost -- mostly due to electrical resistance

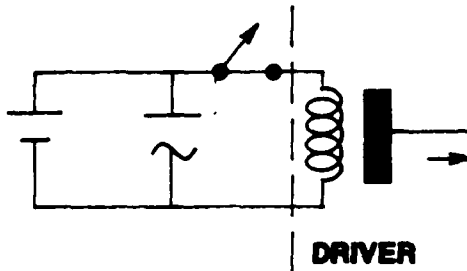
Only loss for superconductor is due to magnetic field diffusion into the drive plate

Feasible for low temperature superconductors and permanent flux-trapped magnets

---

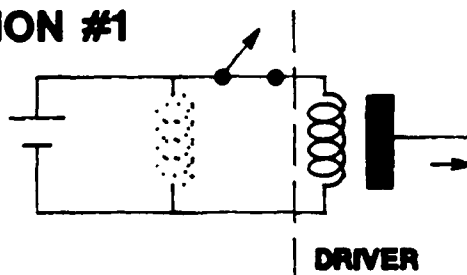
# SUPERCONDUCTING DESIGN OPTIONS

**SOA**



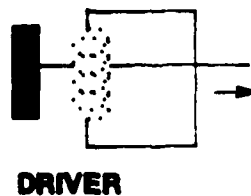
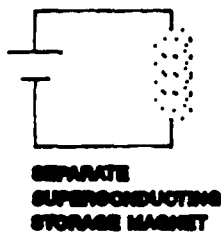
- DANGEROUS VOLTAGES
- CUMBERSOME LEADS

**OPTION #1**



- LOW VOLTAGE LEADS
- COULD BE DONE TODAY WITH LTS

**OPTION #2**

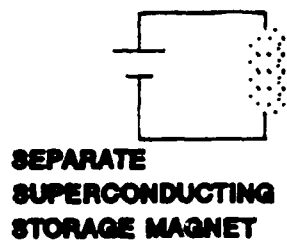


- NO LEADS
- NO DANGEROUS VOLTAGES

Figure 44.

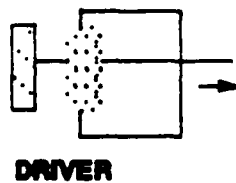
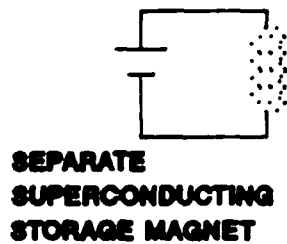
# SUPERCONDUCTING DESIGN OPTIONS

## OPTION #3



**TRANSFORMER REDUCES  
FIELD REQUIREMENT  
BUT ADDS WEIGHT**

## OPTION #4



**MOST EFFICIENT**

Figure 45.

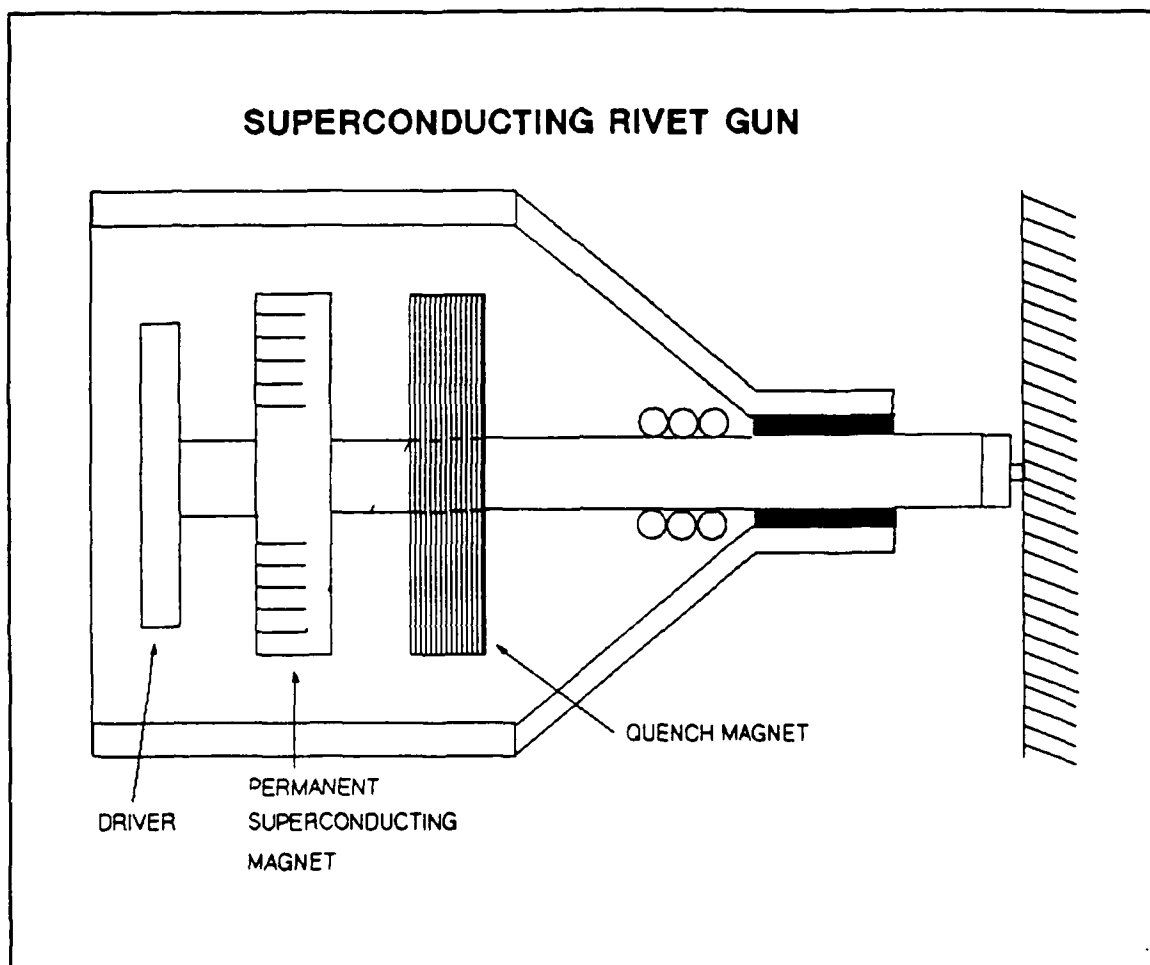


Figure 46.

In addition, our analyses show that this concept may in fact be feasible, and show payoff, even for conventional superconducting materials. If this proves to be an accurate assessment there would be substantial benefit to the general field of superconductivity, as summarized in the following table.

---

#### ADVANTAGES TO SUPERCONDUCTIVITY

Introduces superconductors on the manufacturing floor

high volume  
low cost  
superconducting devices

Builds experience with superconductors

cryogenics  
refrigeration  
new applications

---

During the first quarter of our program we showed the value of using permanent flux-trapped magnets made from the high temperature ceramic materials. These included the elimination of (1) electrical contacts to the superconductor and (2) the need to make long lengths of stable conductors from brittle materials. Our calculations, summarized in Figures 47-49 showed that operation at 77K provided the necessary heat capacity to enable devices to be built from bulk components which would be stable against flux-jumping.

A brief summary of our analyses of the superconducting rivet gun is presented in Figures 50-52. The feasibility of using a flux-trapped magnet was calculated, using the concept of the a threshold field for the first flux-jump,  $B_{fj}$ , in a bulk superconductor made of  $YBa_2Cu_3O_{7-x}$ . Employing the Bean model for flux penetration into the superconductor led to a value of the maximum trapped field,  $B_{trap}$ , equal to 3.1 Tesla, Figure 50.

Next the magnetic field required to drive rivets was calculated using actual data measured during the operation of an electromagnetic gun, Figure 51. A low aspect ratio coil shape was assumed, similar to the actual working device. The maximum applied field, from a separate superconducting storage magnet, is

## ADIABATIC OPERATION - ENTHALPY STABILIZATION 77K vs. 4.2K

MAXIMUM PERMISSIBLE ENERGY,  $E_{\max}$

$$E_{\max} = ex$$

e: MAXIMUM ENERGY DENSITY  
THE WINDING CAN RECEIVE  
AND STILL REMAIN  
SUPERCONDUCTING

x: MINIMUM PROPAGATING  
ZONE VOLUME

$$E_{\max} = C_m(T_c - T_{op}) \left( \frac{k_{ep}}{k_m} \right)^2 \left( \frac{k_m \Delta T_{op}}{\rho_m J_{mop}^2} \right)^{1.5}$$

$$\frac{E_{\max}^{77}}{E_{\max}^{4.2}} = 2 \times 10^4$$

Figure 47.



## **ADIABATIC OPERATION - ENTHALPY STABILIZATION 77K vs. 4.2K**

MAXIMUM PERMISSIBLE DISTURBANCE ENERGY IS

**$2 \times 10^4$  TIMES LARGER AT 77K!**

- MECHANICAL DISTURBANCES (CONDUCTOR MOTION, EPOXY CRACKING)  
MAY NO LONGER BE IMPORTANT
- FOR LOW  $E_{\max}$  DESIGNERS RELIED ON HIGH LATENT HEAT OF HELIUM  
(VIA PERCOLATION) FOR ADDED PROTECTION AGAINST DISTURBANCES  
-PERMEABLE WINDINGS

**CAN BUILD STRUCTURALLY STRONGER MAGNETS**

# CONDUCTOR DESIGN ISSUES - 77K

## ADIABATIC OPERATION DESIRED

KEEP DISTURBANCES < PERMISSIBLE ENERGY DENSITY

$$d_c < \sqrt{\frac{C_s \Delta T_{op}}{J_c}}$$

$d_c$ : CRITICAL CONDUCTOR DIAMETER

$$\frac{d_c^{77}}{d_c^{4.2}} \approx 100$$

$$d_c^{NB1} \sim 20 \mu m$$

## Feasibility Of Flux-Trapped Superconducting Magnets

$B_{fj}$ , threshold, is obtained by equating stored energy to that needed to raise the temperature to  $T_c$

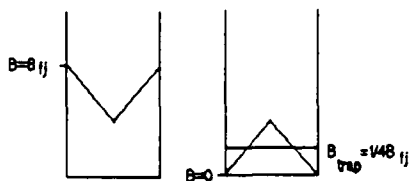
$$(B_{fj})/3\mu_0 = \int_{T_{bath}}^{T_c} \rho(\text{kg/m}^3) C(\text{J/kgK}) dT$$

$$C/\text{mass} = 157(\text{J/kgK})$$

$$T_c = 92\text{K}$$

$$T_{bath} = 77\text{K}$$

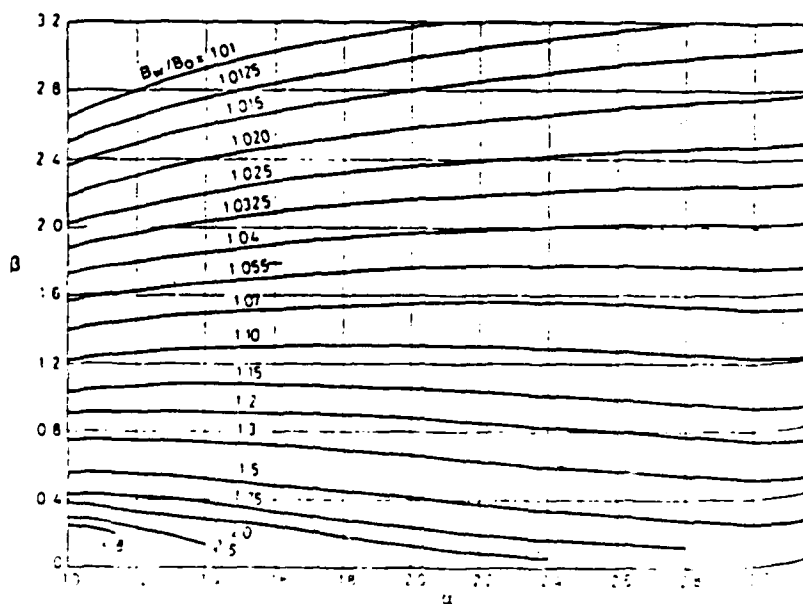
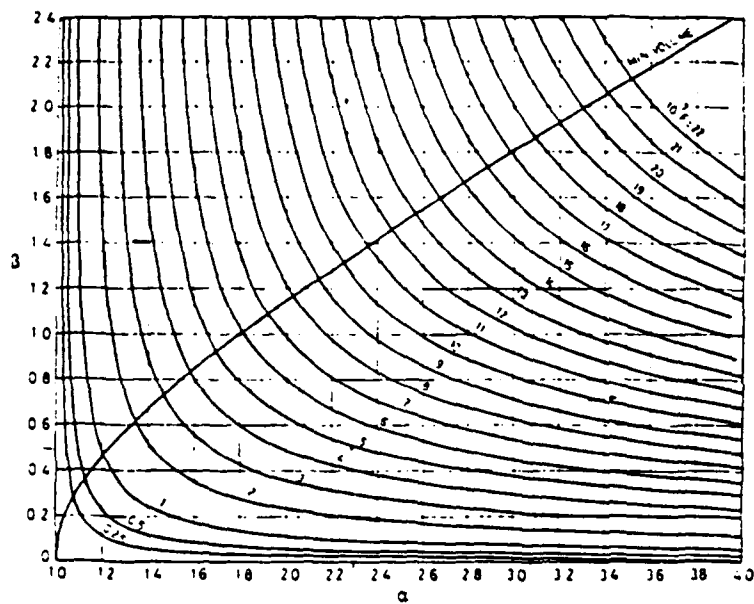
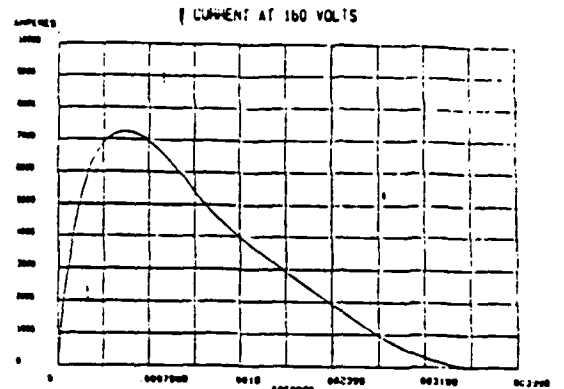
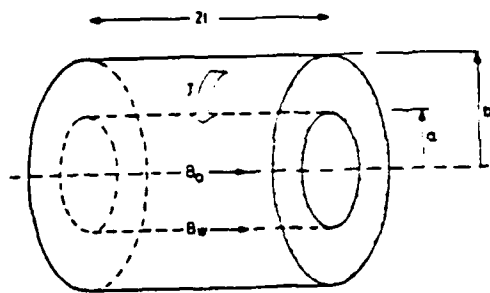
$$\rho = 6.4 \times 10^{-3}(\text{kg/m})$$



$B_{\text{trap}} = 3.1\text{tesla}$

Figure 50.

# MAGNETIC FIELD REQUIREMENTS



$$B_0 = JaF(\alpha\beta)$$

.

.

.

$$B_0 = 1900 \text{ gauss}$$

$$B_w = 2600 \text{ gauss}$$

THEREFORE MUST TRAP 2600 gauss

DRIVING FIELD IS:

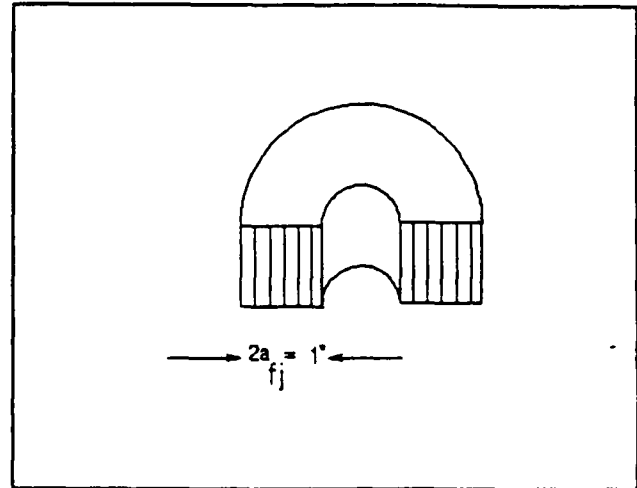
$$B_{\text{radial}} = 1/2 B_w = 1300 \text{ gauss}$$

Figure 51.

## CRITICAL CURRENT DENSITY REQUIREMENTS

$$B(T) = u_0 a_{fj} (m) J (A/cm^2)$$

$$J_c^{1 \text{ tesla}} = 6.2 \times 10^3 \text{ A/cm}^2$$



## SCALING FACTORS

### COIL WALL THICKNESS

	<u><math>J_c (A/cm^2)</math></u>
1"	$6.2 \times 10^3$
10"	$6.2 \times 10^2$
100"	$6.2 \times 10^1$

### FORCE ON DRIVER (LB/IN<sup>2</sup>)

	<u><math>J_c (A/cm^2)</math></u>
$2 \times 10^5$	$6.2 \times 10^3$
$2 \times 10^3$	$6.2 \times 10^2$
$2 \times 10^1$	$6.2 \times 10^1$

Figure 52.

2600 gauss. The actual trapped field, upon retraction of the gun from the storage magnet, is 1300 gauss.

To trapped the calculated field requires a certain critical current density for a given coil size. Figure 52 presents these scaling factors. The  $J_c$ 's available today using bulk sintered powders, and operating at a few thousand gauss, are only of the order of tens of amp/cm<sup>2</sup>, not nearly enough. If  $J_c$ 's of  $6.2 \times 10^3$  could be reached, reasonable sized devices could be made, i.e., a one inch wall thickness as seen in Figure 52.

It was informative to calculate the applied force at the head of the rivet driver, the temperature rise from the quench, and the material's structural requirements. This data is presented in the following tables.

---

#### APPLIED FORCES

Note: A loss factor of 1/2 is introduced due to magnetic field lines diffusing into the driver plate... there is a large payoff if the driver plate can be made superconducting.

$$H_{\text{radial}} = 1300 \text{ gauss}$$

$$F(\text{kNt}) = 1/2 u_0 H_r^2 [\text{area of driver plate}]$$

$$F = 6.6 \text{ kNt}$$

$$\text{Stress on } 3/16" \text{ 2024 rivet} = 2 \times 10^5 \text{ lbs/in}^2$$

---

---

#### TEMPERATURE RISE FROM QUENCH

$$E (\text{joules}) / V (\text{m}^3) = C \times m \, dT$$

$$H_w = 2600 \text{ gauss}$$

$$T = T_{\text{max}} - T_{\text{bath}}$$

$$T = 0.03\text{K}$$

---

#### Electromagnetic Window

A second application being considered is the use of thin films for

electromagnetic screening, see the Milestone Chart in the Executive Summary for details on how this work fits into the overall program. In the recent quarter we have modified a dielectrometer for measurement of permeability and reflectance at liquid nitrogen temperatures, see Figures 53-55.

We have begun to analyze various applications for their requirements. Figure 56 summarizes these initial efforts for an electromagnetic window. Skin depth calculations revealed that the superconductor needs to be about 1-2 microns thick. This dimension is primarily set by the requirement to have an electromagnetic signal penetrate the superconducting material when it is in the normal state, i.e., when the window is open.

#### Q Measurements On ICI's Superconducting Coil

We obtained a small coil courtesy of ICI. Its outer diameter was 7.4mm, wire diameter was 0.85mm, length 18.2mm, and it had 12 turns. The coils Q value was determined at room temperature, 300K, and as function of frequency at 77K. The results are presented in Figure 57. The coil did not perform as well a copper would have. A similar dimensioned copper coil would have been about 200 at 77K. The Q was limited by the sample's weak-links.

We also measured the transport critical current density. Although ICI claims  $J_{c1}$  as high as  $1000 \text{ A/cm}^2$  for their material, our measurements showed  $J_c$  equal to  $350 \text{ A/cm}^2$ . These numbers are based on an electrical resistivity criterion of  $5 \times 10^{-9} \text{ ohm cm}$ .

Self-field effects explain how ICI can, with some samples, achieve higher critical current densities. If we measure  $J_c$  on a very small diameter sample such that the total current at  $I_c$  is small, i.e., an ampere or two, then the self-field is small as well and the critical current density is not as greatly diminished as it would be with larger  $I_c$ 's. Interestingly, it even helps to have porous samples! You lose some area, assuming that you still just use the sample's cross-section to calculate  $J_c$ , but by further reducing the  $I_c$  value there is a bigger payoff accrued through the smaller self-field. Of course, for exactly these reasons,  $J_c$ 's determined without taking self-fields into account are erroneous.

A second alternative would be to measure  $J_c$  in an applied magnetic field. In either of these two cases,  $J_c$  could then be

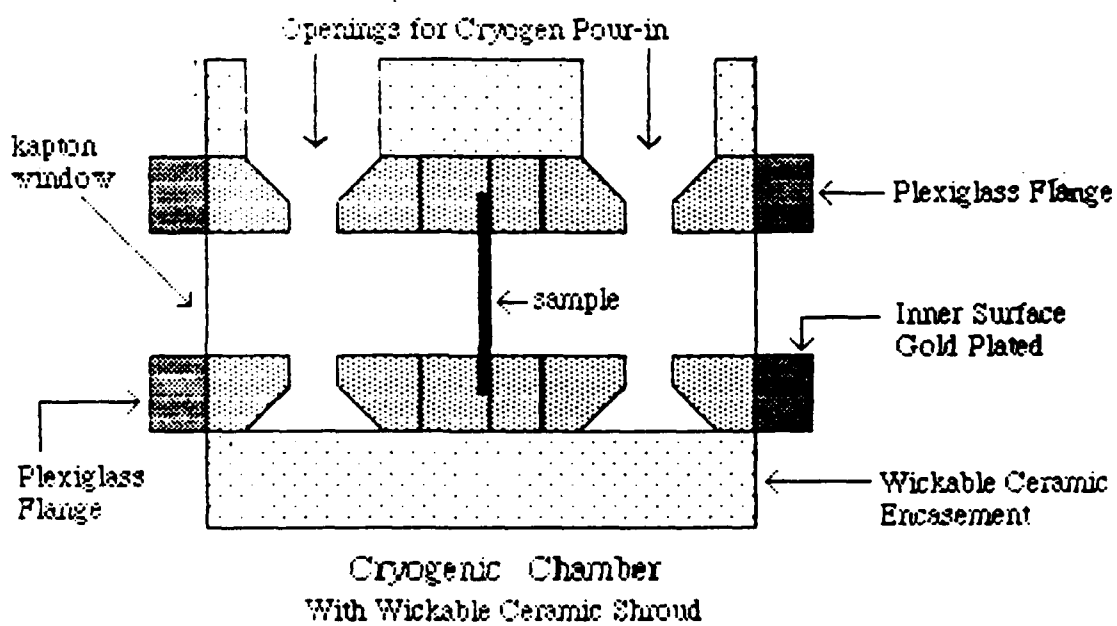
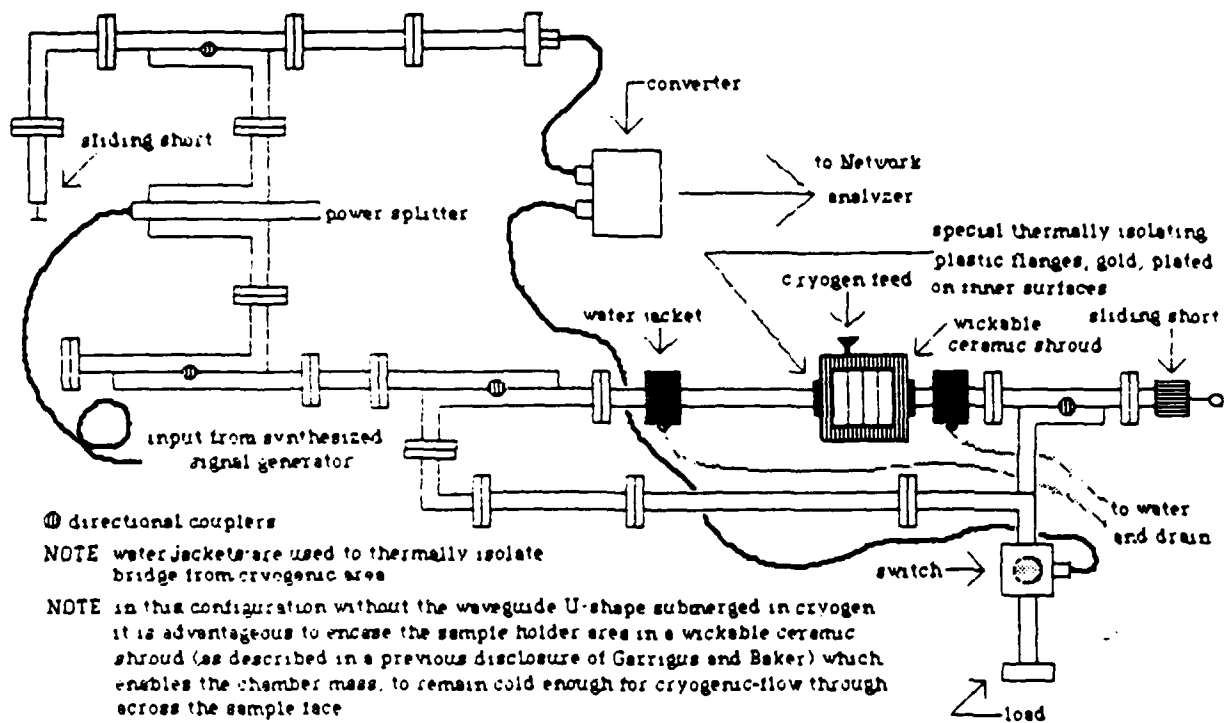


Figure 53.





Possible Bridge Configuration  
for Transmission and Reflection  
Cryogenic Microwave Measurements  
Without Changing Sample Position

Figure 54

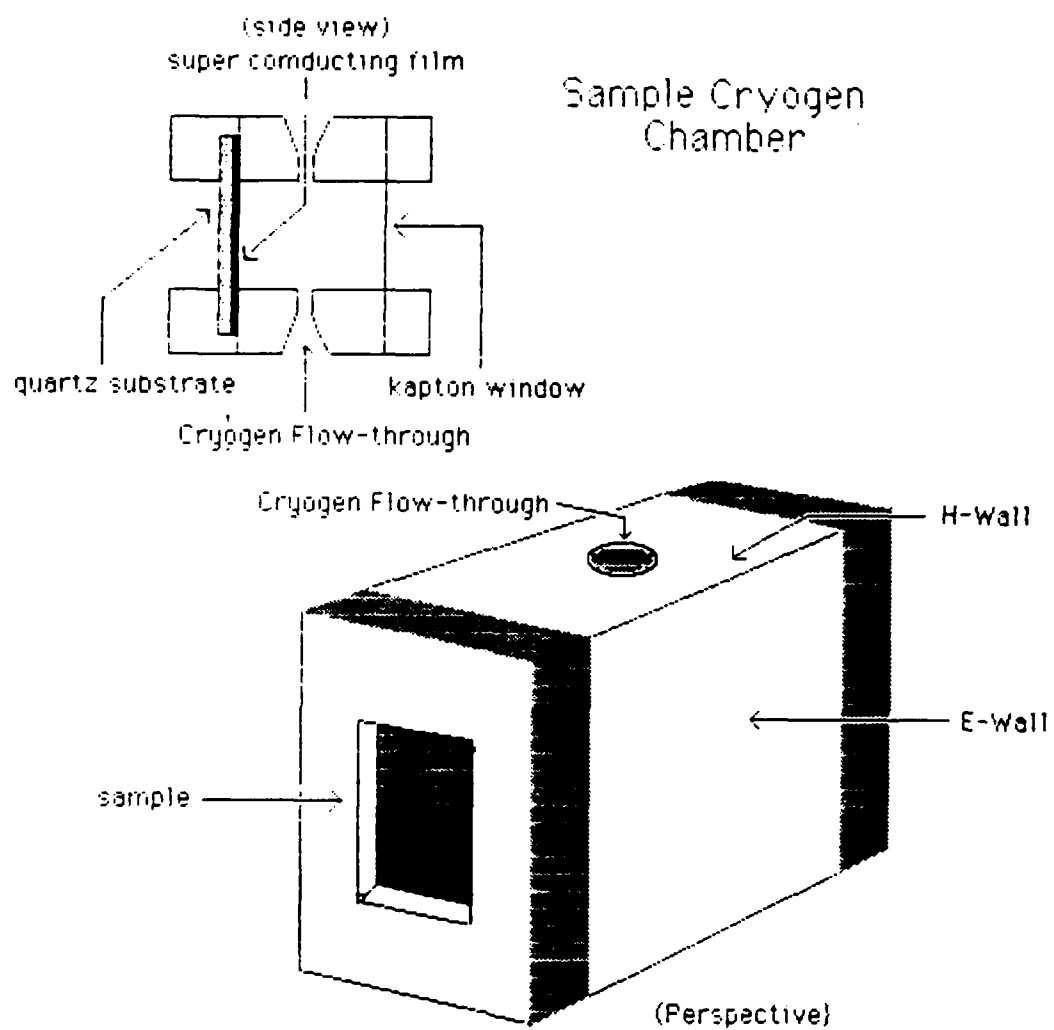
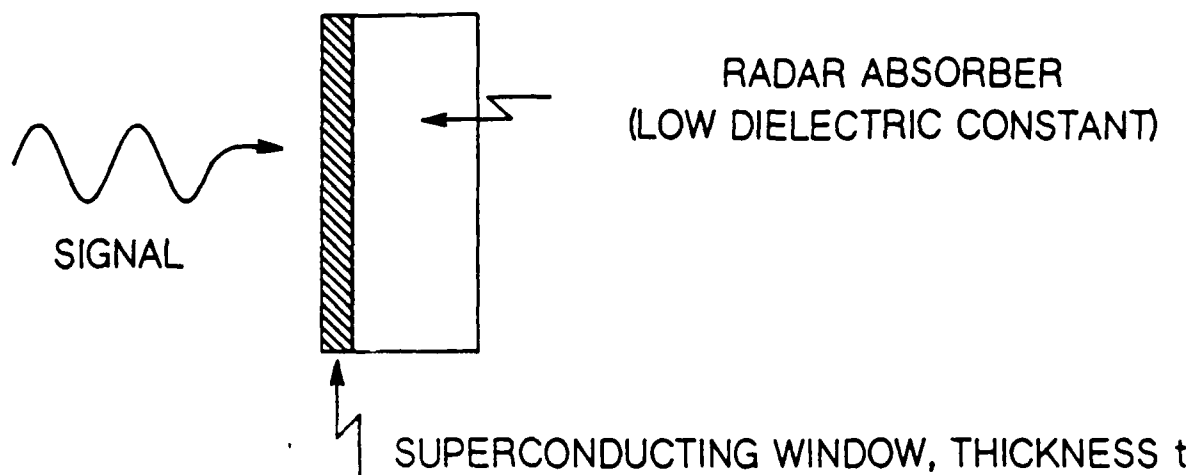


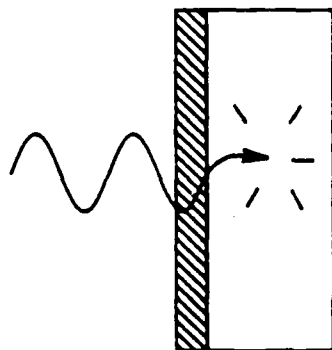
Figure 55

# RADAR WINDOW



WINDOW OPEN

$$T > T_c \text{ or } H_a > H_{c2}$$



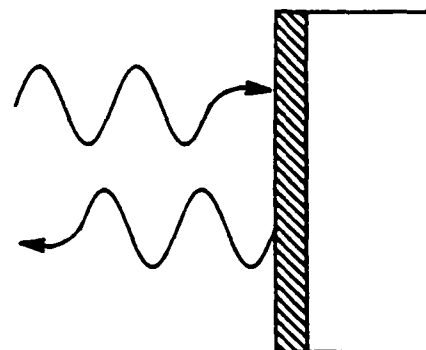
$$\text{SKIN DEPTH } \delta = \frac{1}{\sqrt{\pi f \mu \sigma}}$$

$$\delta = 9 \mu\text{m}$$

TO ABSORB  $\sim 2/3$

WINDOW CLOSED

$$T < T_c \text{ or } H_a < H_{c2}$$



$$f = 10 \text{ GHz X-BAND}$$

$$\mu = 1$$

$$\sigma = \frac{1}{300 \times 10^{-6} \Omega \cdot \text{cm}}$$

$\therefore t$  SHOULD BE  $\sim 1-2 \mu\text{m}$   
 $\lambda_{\text{SUPER}} = 0.2 \mu\text{m}$

Figure 56.

## Q of a Superconducting Coil

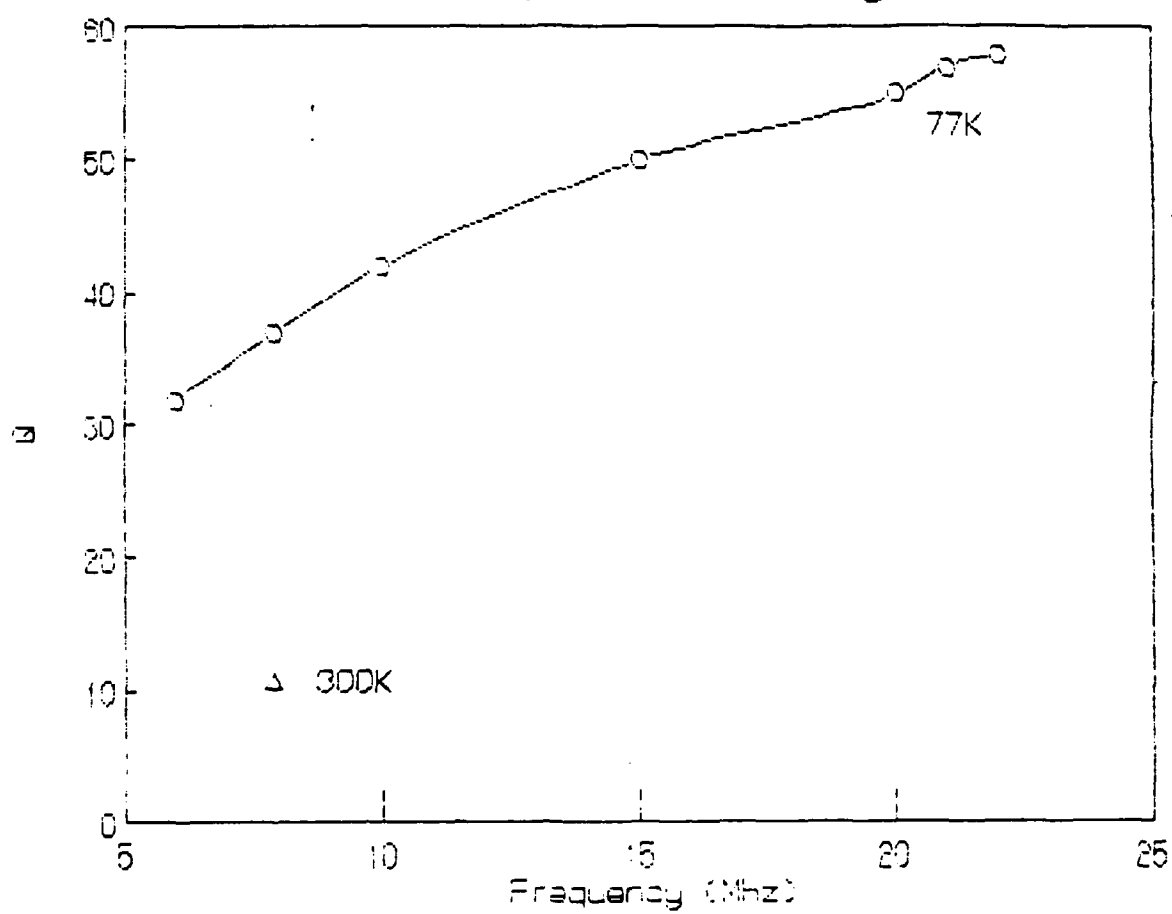


Figure 57.

meaningfully correlated with processing parameters, heat treatments, alloy contents etc.

#### GOALS FOR THE NEXT REPORTING PERIOD

Specific goals, objectives, and accomplishments for the next reporting period are presented in the accompanying Two Year Program Master Schedule.

**PROBLEM AREAS** Renewal money for the second and third years of contract work has apparently not yet been released by Congress to DARPA. To continue work in an efficient and timely manner this allocation should be received by Boeing for distribution to the subcontractors as soon as it is received.

**CORRECTIVE ACTION** DARPA and AFOSR were notified of the situation, and have taken preliminary steps to ensure readiness of paper work.

#### FOURTH QUARTER PUBLICATIONS

"Reaction Sequencing During Processing of the 123 Superconductor", W. J. Thompson et. al., J. Am. Ceramics Soc., 72 (10) 1977-79, Aug., 1989.

"Theory of Oxygen Diffusion in Tetragonal and Orthorhombic  $\text{YBa}_2\text{Cu}_3\text{O}_{7-x}$  Phases", R. Kikuchi et. al., Phys. Rev. B., Oct. 1989.

"Mechanism of Twin Formation and Nature of Tetragonal to Orthorhombic Transformation in  $\text{YBa}_2\text{Cu}_3\text{O}_{7-x}$ ", M. Sarikaya et. al., Phys. Rev. B., Oct. 1989.

"Structure of Interpenetrating Twins in  $\text{YBa}_2\text{Cu}_3\text{O}_{7-x}$ ", M. Sarikaya et. al., Phys. Rev. B., Oct. 1989.

"Equilibrium Atomic Distribution and Oxygen Kinetics Near the Twin Boundary in the  $\text{YBa}_2\text{Cu}_3\text{O}_{7-x}$  Superconducting Compound", R. Kikuchi et. al., J. Mater. Res., Oct. 1989.

W. J. Thompson et. al., "Reaction Sequencing During Processing of the 123 Superconductor", J. Am. Ceramic Soc., 72 [10], (1989).

M. Qian et. al., "Nickel Impurities in the  $\text{YBa}_2\text{Cu}_3\text{O}_{7-x}$  90K Superconductor", Phys. Rev. B 39, 9192 (May, 1989).

J. Whitmore et. al., "EXAFS of Oriented Single Crystal of  $\text{YBa}_2\text{Cu}_3\text{O}_{7-x}$ ", Physica B 158, 263 (1989).

R. Kikuchi et. al., "Low Temperature Cu-O Phase Diagram", submitted to Physica C (1989).

#### RECENT PRESENTATIONS

C.H. Henager, Jr., "Thin Film YBaCuO Superconductors Made by Sputter Deposition using a Spherical Target", Pacific Northwest Materials Conference, Seattle, WA, May 17-19, 1989.

M. Strasik et.al., "Microstructural and Superconducting Properties of Silver and Platinum Doped  $\text{YBa}_2\text{Cu}_3\text{O}_{7-x}$ ", Pacific Northwest Materials Conference, Seattle, WA, May 17-19, 1989.

K. A. Youngdahl et.al., "Synthesis and Characterization of Polymeric Precursors to High  $T_c$  Superconducting Ceramics for Fibers, Coatings, and Powders", Pacific Northwest Materials Conference, Seattle, WA, May 17-19, 1989.

M. Hoppe et. al., "Synthesis and High Temperature Chemistry of Organometallic Precursors to  $\text{YBa}_2\text{Cu}_3\text{O}_{7-x}$ ", Fourth International Conference on Ultrastructure, May 1989, Symp. Proc. in press.

#### FOURTH QUARTER PATENT DISCLOSURES

Title: Improved Electromagnetic Riveter Coil Geometry and Dynamics Using Superconductors.

Authors: Thomas Luhman, Paul Arntson, and Ronald Lawrence

Title: Electromagnetic Shutter With IR Transmission Capability.

Authors: Thomas Luhman and Darryl Garrigus

Title: A Superconducting Device For Electrical Circuit Protection.

Authors: Thomas Luhman and Mike Strasik

Title: A Superconducting Device for Sensing Electrical Current.

Authors: Thomas Luhman and Mike Strasik

Title: Method of Ceramic Fiber Fabrication Employing Non-Ceramic Gels.

Authors: Ilhan Aksay, Greg Stangle, and William Carty

Title: Method for Producing High-Temperature Superconducting Ceramic Products Employing Tractable Ceramic Precursors.

Authors: Richard Laine, Kay Youngdahl, Ilhan Aksay, Corrie Martin, and John Lanvtti "Superconductor Quenching Methods Useful With Electromagnetic Riveter", T. S. Luhman et. al.

# Effect of Silver Addition on Microstructural and Superconducting Properties of $\text{YBa}_2\text{Cu}_3\text{O}_{7-x}$ .

Michael Strasik, Thomas S. Luhman, Kay A. Youngdahl, and James E. Pillers

Boeing Aerospace and Electronics  
Advanced Materials Technology  
P.O. Box 3999, MS 73-09  
Seattle, Washington 98124

## 1. ABSTRACT

Silver doped samples of  $\text{YBa}_2\text{Cu}_3\text{Ag}_y\text{O}_{7-x}$  where  $y$  ranges from 0.01 to 0.2 were prepared by a freeze-drying or sol-gel technique. The pyrolyzed samples were found to exhibit a modified grain growth due to partial melting of the silver. Transition temperature curves and critical current densities were recorded as a function of the amount of silver added. The effect on transition temperature behavior increased dramatically from one to ten percent of added dopant. At 10 atomic % Ag, the transition temperature widths were broader and independent of applied magnetic field. There was a decrease in this behavior at levels from 10 to 20% Ag. Critical current densities for the 1% and 20% Ag additions were low with a maximum occurring at around 10% of added silver. The relationship of added silver to superconducting properties is discussed.

## 2. INTRODUCTION

In metallic superconductors, grain boundaries are the source of effective pinning centers of magnetic flux which in turn are responsible for the high critical current densities achievable in those materials. In the  $\text{YBa}_2\text{Cu}_3\text{O}_{7-x}$  oxide superconductors, grain boundaries have been identified as one of the sources contributing to the low critical current densities obtained in bulk sintered material. The extremely short superconducting coherence lengths of the oxides make their electrical and magnetic properties very sensitive to chemical and microstructural inhomogeneities within the grain boundaries. In

order to improve the current density of these compounds by eliminating the weak links associated with the grain boundaries, novel synthesis techniques must be developed to enable us to control the chemical and microstructural properties of the grain boundaries.

The addition of various metals into the  $\text{YBa}_2\text{Cu}_3\text{O}_{7-x}$  perovskite material has resulted in a wide range of properties dependent on the amount and type of dopant used. Doping using silver has achieved moderate success toward improving the electrical and mechanical properties of these materials.

There have been some reports of current densities of the Y-Ba-Cu-O materials being improved through the addition of silver alloys and dopants [1,2]. Several sources have attributed this increase in the  $J_c$  to texturing in the doped material resulting in crystal orientation along the (001) plane [3,4]. Silver, with a melting point of 961C, has also been postulated as increasing the oxygen content of the bulk material through the high solubility of oxygen in the silver [5]. This increased oxygen transport yields materials with higher current densities.

Silver has also been postulated in  $\text{YBa}_2\text{Cu}_3\text{O}_{7-x}$ -AgO composite materials as increasing flux trapping [6]. Results using a Hall probe on direct measurement of the trapped field as well as force measurements led to this conclusion. These materials were also found to suspend from the bottom of a permanent magnet, a phenomenon explained through magnetization measurements. Large hysteresis loops were recorded indicative of intense flux pinning [7].

Enhancement of the mechanical properties of shaped  $\text{YBa}_2\text{Cu}_3\text{O}_{7-x}$  materials has been observed in silver alloy materials. Tapes cast from silver doped  $\text{YBa}_2\text{Cu}_3\text{O}_{7-x}$  onto silver substrates exhibited increased flexibility while maintaining a high  $T_c$  and  $J_c$  [8]. The morphology of the silver doped ceramics was studied by



Simmins, et al., who found that the temperature of crystallization, formation of certain phases, and degree of twinning was all effected by the presence of the dopant material [9].

The consequences of adding silver as a dopant to these superconducting ceramics are numerous and probably inter-related. Studies in this area now need to address questions such as how the introduction of defects into the structure or grain boundary, such as silver atoms, effects the pinning of flux lines and how one can introduce pinning without decreasing other properties of the material. How can one systematically effect the grain growth in these materials using a modified form of melt texturing? And, exactly where is the silver located in the  $\text{YBa}_2\text{Cu}_3\text{O}_{7-x}$  and how does it effect the weak links? In these studies, we will attempt to address some of these concerns.

### 3. EXPERIMENTAL PROCEDURES

Silver doped samples of  $\text{YBa}_2\text{Cu}_3\text{Ag}_y\text{O}_{7-x}$  where  $y$  ranges from 0.01 to 0.2 were prepared by a freeze-drying or sol-gel technique. Stoichiometric amounts of  $\text{BaCO}_3$ ,  $\text{Y}_2(\text{CO}_3)_3 \cdot n\text{H}_2\text{O}$ ,  $\text{Cu}(\text{NO}_3)_2 \cdot 6\text{H}_2\text{O}$  and  $\text{AgNO}_3$  with purity ranging from 99 to 99.999% were used in the freeze-drying process. Powders were placed in deionized water and concentrated  $\text{HNO}_3$  was added, while stirring the mixture, until the solution was clear. Some solutions were heated slightly to help the dissolution process. Homogeneous mixing is assured in the freeze-drying process by spraying the solution into liquid nitrogen by which the solution is almost instantaneously frozen. This effectively achieves mixing on nearly a molecular scale that is unique to this process. Homogeneity of the sample must also be preserved during decomposition of the dry powder. This may be achieved by rapid decomposition of the mixture of anhydrous nitrates at  $750^\circ\text{C}$ . Anhydrous nitrates are very hygroscopic so care must be taken to keep the mixture as dry as possible before decomposition. Crystalline water present during decomposition may dissolve the

nitrates which may reduce the homogeneity of the sample, however, flash heating at 750C minimizes this incongruous melting. The powders were pressed into pellets at 40000 psi. Pellets were sintered in oxygen in the 930C to 990C range and then annealed at 450°C in oxygen.

The resulting material was examined by scanning and transmission electron microscopy with energy dispersive X-ray spectroscopy. X-ray diffraction studies established that the volume fraction of the  $\text{YBa}_2\text{Cu}_3\text{O}_{7-x}$  superconducting phase is >97%.

The transition temperatures of the pure and silver doped samples were studied using the ac susceptibility measurement that can discriminate between inter- and intragrain properties of the samples. The net signal from the balanced pick-up coils contains in-phase and out-of-phase components, corresponding to the real and imaginary part of the ac susceptibility,  $X'$  and  $X''$ , respectively. Skin effect losses in the normal state and flux flow losses in the superconducting state do not affect our measurement which is performed at 200 Hz.

The transport current densities were measured at 77K in zero applied field. The contacts were prepared by heat treating a silver paste on a sample in oxygen at 450C for four hours. Copper current and voltage leads were then soldered to the silver contact using pure indium. The resistivity criteria of  $10^{-9}$  ohm-cm was used for voltage onset. The resulting critical current densities were corrected for the self field effects on Josephson Junctions at the grain boundary, as will be discussed in the Results and Discussion section.

#### 4. RESULTS AND DISCUSSION

A freeze-drying technique proved to be superior to conventional solid state powder reaction method for producing very pure, homogeneous superconducting  $\text{YBa}_2\text{Cu}_3\text{O}_{7-x}$ . It also proved to be an excellent technique to produce homogeneous molecular silver

distribution in the silver doped  $\text{YBa}_2\text{Cu}_3\text{Ag}_y\text{O}_{7-x}$  as determined by scanning electron microscopy. The Energy Dispersive X-ray Analysis showed very uniform distribution of silver metal on surface as well as on the fracture surface of the samples with silver concentration,  $y$ , ranging from 1 to 10 atomic percent in  $\text{YBa}_2\text{Cu}_3\text{Ag}_y\text{O}_{7-x}$ . When the concentration exceeded 10 atomic percent, the solid solubility limit for silver, the silver segregated preferably in the grain boundaries. It also alloyed with the copper thus forming other phases hence depleting copper from the 123 phase. Silver substitution for copper resulted in the silver being segregated in the grain boundaries as well as additional undesirable phase formations.

In the grain growth studies for pure and silver doped  $\text{YBa}_2\text{Cu}_3\text{O}_{7-x}$  it was determined that the silver addition enhanced the grain growth through partial melting of the silver when the sintering temperature exceeded 960C, melting point of silver. Silver doped samples with silver concentrations above 10 at.% where the silver segregated in the grain boundaries, yielded grain growths very similar to the grain growth of the pure  $\text{YBa}_2\text{Cu}_3\text{O}_{7-x}$ . Figures 1-2 show experimental results of average and maximum grain size vs. sintering temperature, respectively. It can be observed that the maximum grain size in the 1% Ag doped sample was significantly higher than in the pure sample at the same sintering temperature. In fact, in the 1% Ag doped sample, we observed a sign of a local melt-texturing at 985C as can be demonstrated in Figure 3 (SEM micrograph of 1% Ag doped  $\text{YBa}_2\text{Cu}_3\text{O}_{7-x}$  sintered at 985C in oxygen).

#### T<sub>c</sub> Measurements

Transition temperature widths determined by ac susceptibility are partially dependent on the grain size, as well as chemical and oxygen homogeneity of grains and grain boundaries. A lot of information can be obtained by examining the shape of the transition temperature curves and their derivatives. An example of such a transition curve for 1% Ag doped 123 is shown in Figure 4.

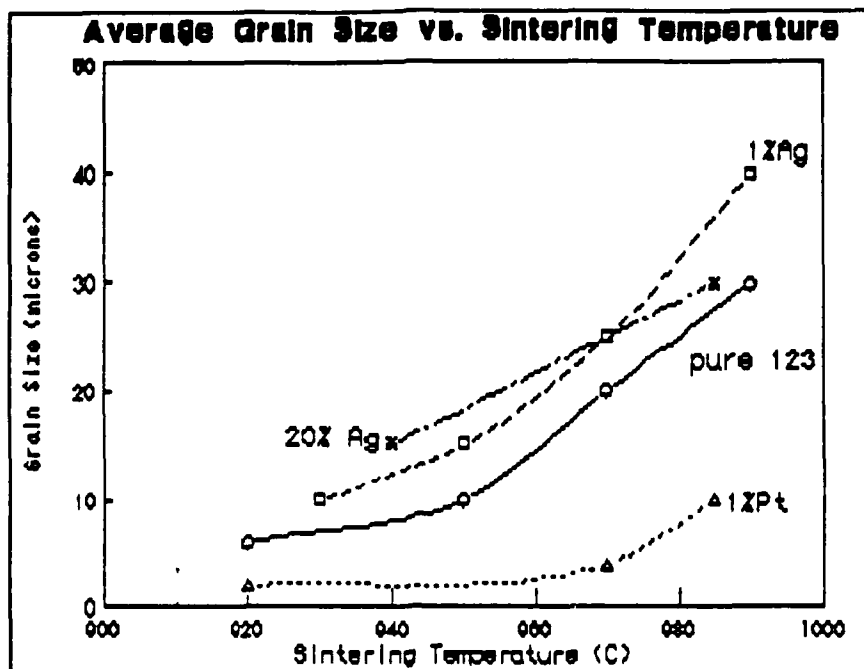


Figure 1. Average Grain Size vs. Sintering Temperature for Silver Doped 123

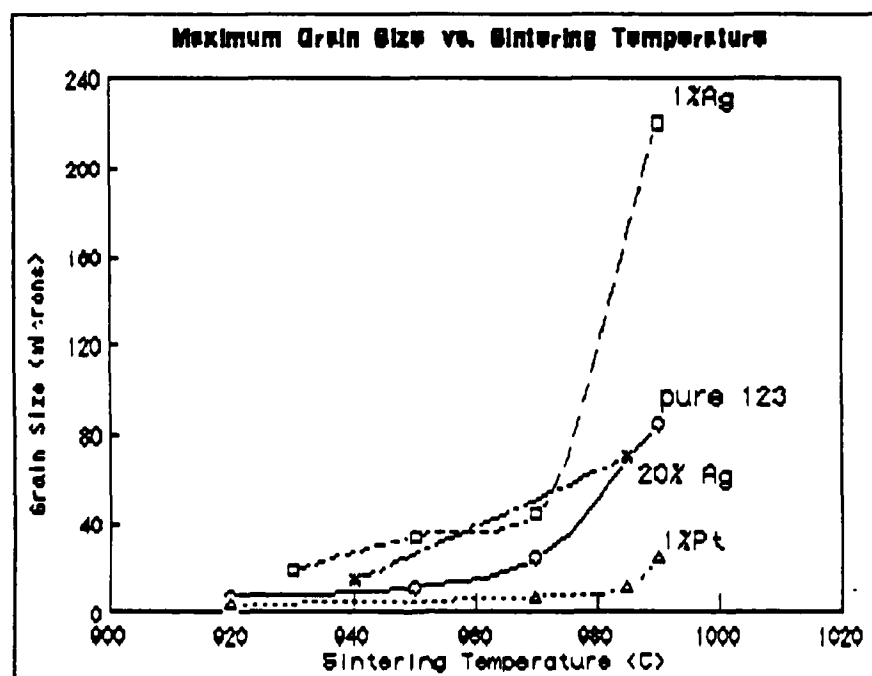


Figure 2. Maximum Grain Size vs. Sintering Temperature for Silver doped 123

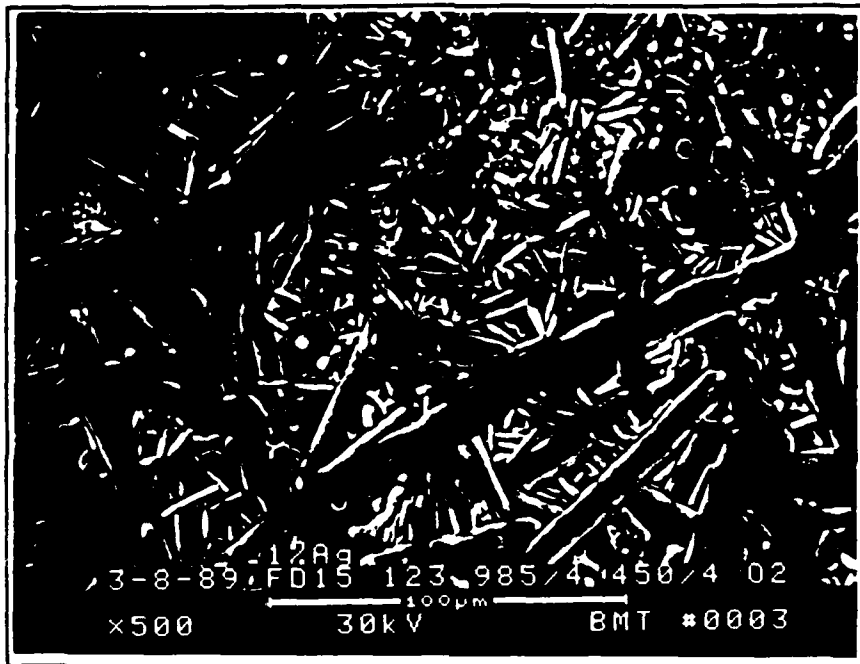


Figure 3. SEM micrograph of 1% Ag doped 123 sintered at 985C in oxygen.

As the sample is cooled, the grains become superconducting at  $T_c$  onset but the weak-links are still resistive due to thermal fluctuations. Therefore, the initial ac field induced screening currents only flow inside the grains. The intragrain current increases with decreasing temperature, leading to better screening, i.e. smaller  $X'$  and larger  $X''$ .

The ac amplitude still reaches the center of the grains at this point. The imaginary part  $X''$ , which is proportional to the ac hysteresis losses has a maximum at the temperature where the penetration depth of the grain begins to be reduced below the grain's radius. At this temperature the ac field no longer penetrates the whole grain and the volume in which the hysteresis losses occurs shrinks.

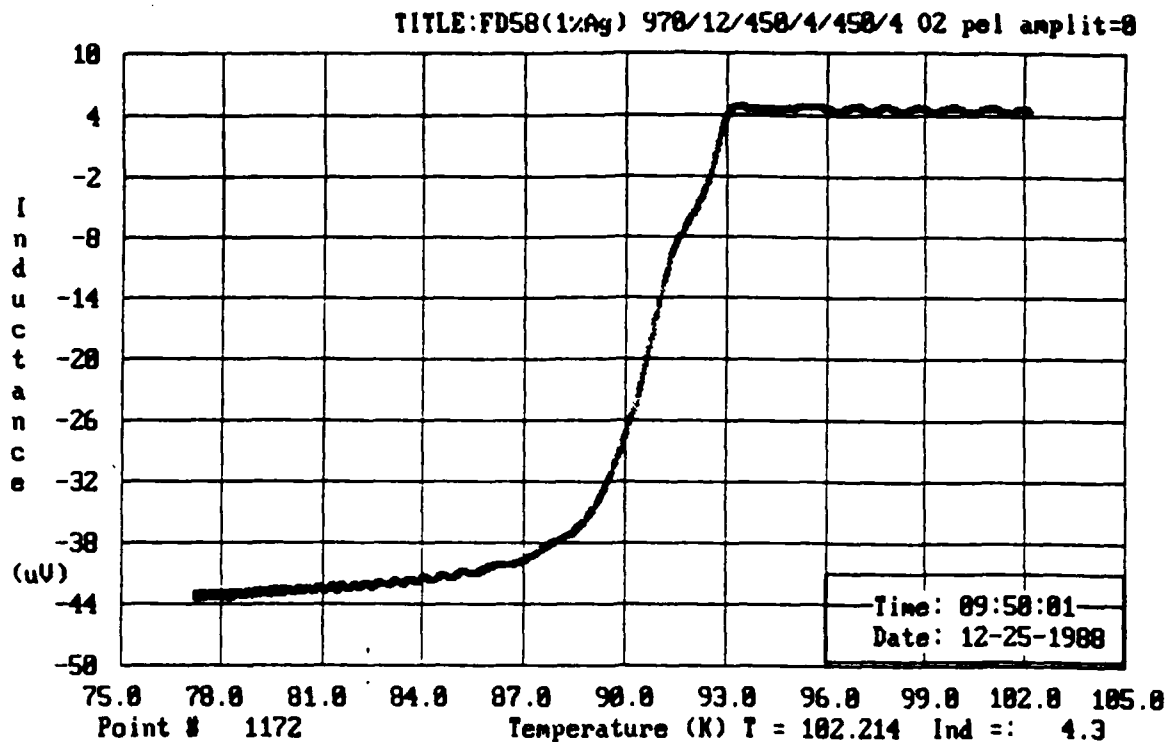


Figure 4. Transition Temperature Curve for  
1% Ag doped 123 sintered at 970C in  
oxygen measured at 3.15 Gauss

The weak-links are able to carry a supercurrent if the temperature is below the phase locking temperature at which the energy of the weak-link junction becomes equal to  $kT$ . This temperature corresponds to the shoulder of  $X'$  in transition temperature measurements. Below this temperature macroscopic shielding currents through grains and weak-links are induced. The ac losses of the junctions increase below  $T_c$  and cause the intergrain maximum  $X''$ , at which the ac field just penetrates into the center of the specimen via the weak-link paths. In the temperature region below  $T_c$  the intergrain signal dominates compared to the intragrain one due to the much smaller intragrain penetration depth. The height, position, and width of the intergrain maximum reflects the intergrain volume, the intergrain critical current density, and the distribution of the coupling energy or junction current.

The transition temperature widths for pure  $YBa_2Cu_3O_{7-x}$  sintered at different times and temperatures are shown in Figures 5-6, where it can be observed that the sharpest transition temperatures were

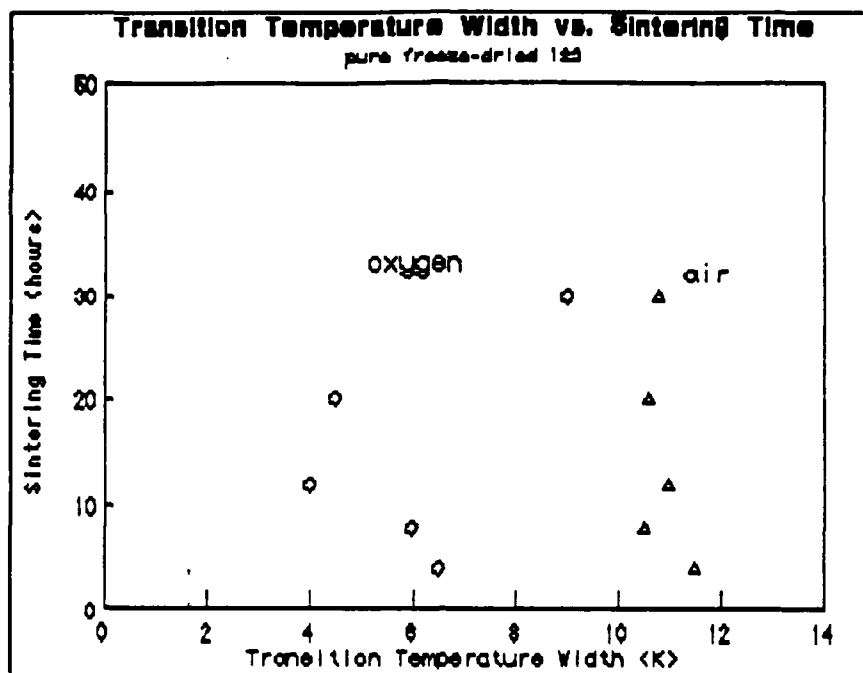


Figure 5. Transition Temperature Width vs. Sintering Time for pure freeze-dried 123

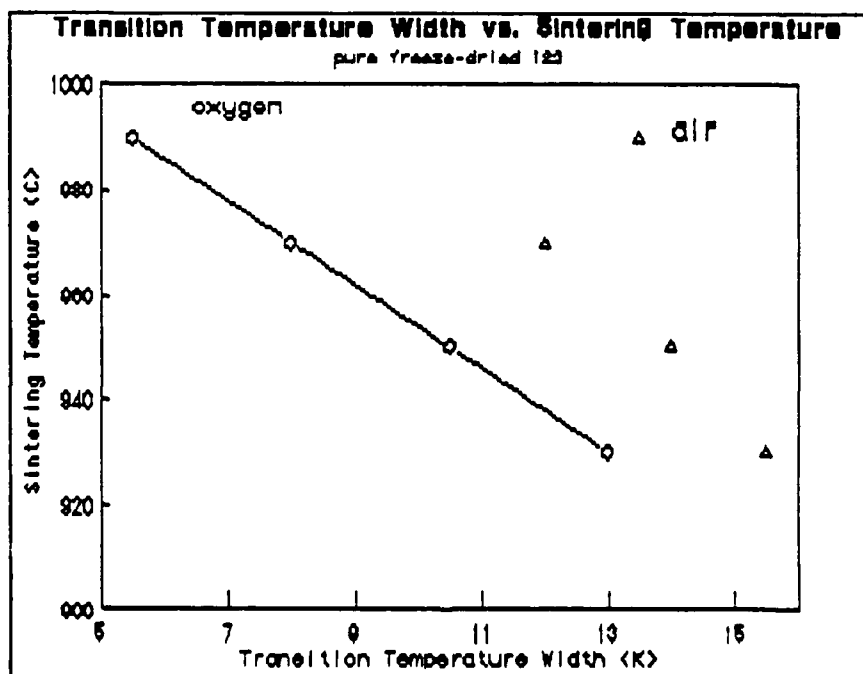


Figure 6. Transition Temperature Width vs. Sintering Temperature for pure freeze-dried 123.

obtained for the samples sintered between 12-20 hours in oxygen. The samples sintered in air exhibited generally wider transitions which were attributed mainly to oxygen deficiency. The wider transition widths could often be reduced by low temperature annealing of the samples in oxygen. Thus the shapes and widths of the transition temperature curves can be partially correlated to the oxygen stoichiometry for the same grain size samples. The shapes and widths of transition temperature curves will be directly correlated to the transport current densities of the pure and silver doped  $\text{YBa}_2\text{Cu}_3\text{O}_{7-x}$  samples.

#### $J_c$ Measurements

Self-fields, imposed by the transport current in a four probe current density measurement, have been shown to strongly influence the measured value of  $J_c$ .  $\text{YBa}_2\text{Cu}_3\text{O}_{7-x}$  samples were prepared in pellet forms approximately 2 mm thick, heat treated to produce orthorhombic phase, and sliced to a square cross-sectional shape. Critical current measurements, using a resistivity criterion of  $10^{-9}$  ohm-cm, were then made at 77K with no intentionally applied magnetic field other than the self-field employed. Consecutive measurements were made as a function of sample thickness. Sample thicknesses were varied by mechanical grinding.

The critical current, in amperes, decreased with decreasing sample size; however, the intrinsic  $J_c$ , in  $\text{Amp}/\text{cm}^2$ , increased. Self-fields were calculated for the various sample sizes and current values. The dependence of  $J_c$  on an applied magnetic field, the self-field, was found to agree with that predicted for a random array of Josephson Junctions [x]. Using this field dependence, true zero field values of  $J_c$  were calculated. Figures 7-8 show the results of these experiments and calculations. The self-field corrected current densities will be reported in all following results.



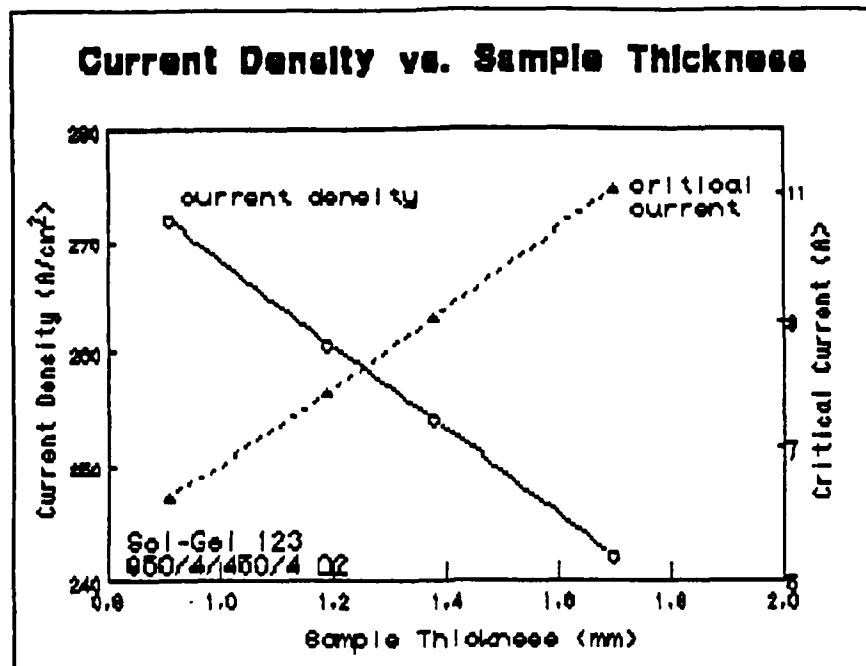


Figure 7. Current Density vs. Sample Thickness for pure 123

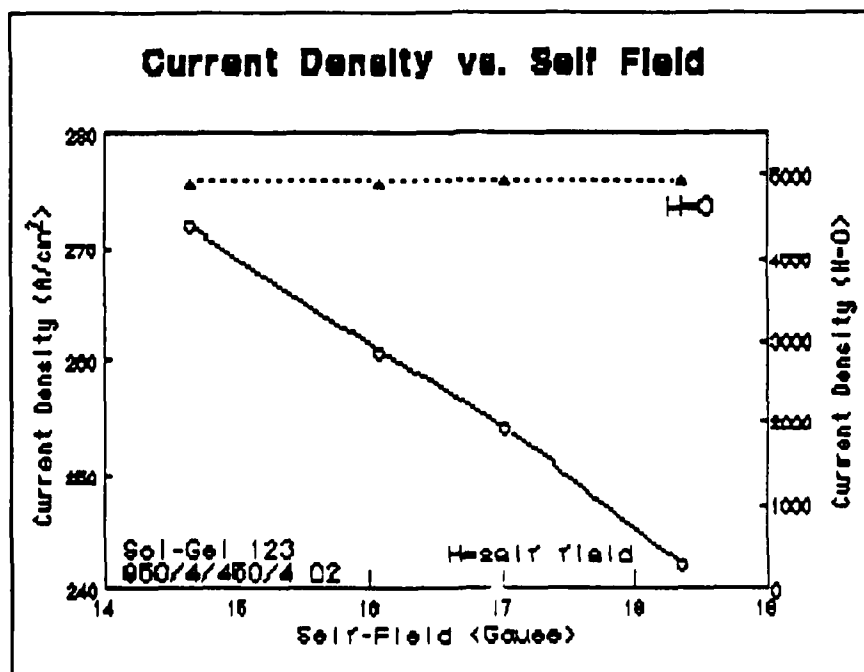


Figure 8. Current Density vs. Self Field Effect for pure 123

### Effects of Processing Conditions

Figure 9 shows results of transport current densities of pure 123 samples sintered in air and oxygen at different temperatures and annealed in air and oxygen at 450C. The annealing time of 8 hours at 450C was determined to be the optimum conditions for obtaining the highest critical current density as seen in Figure 10.

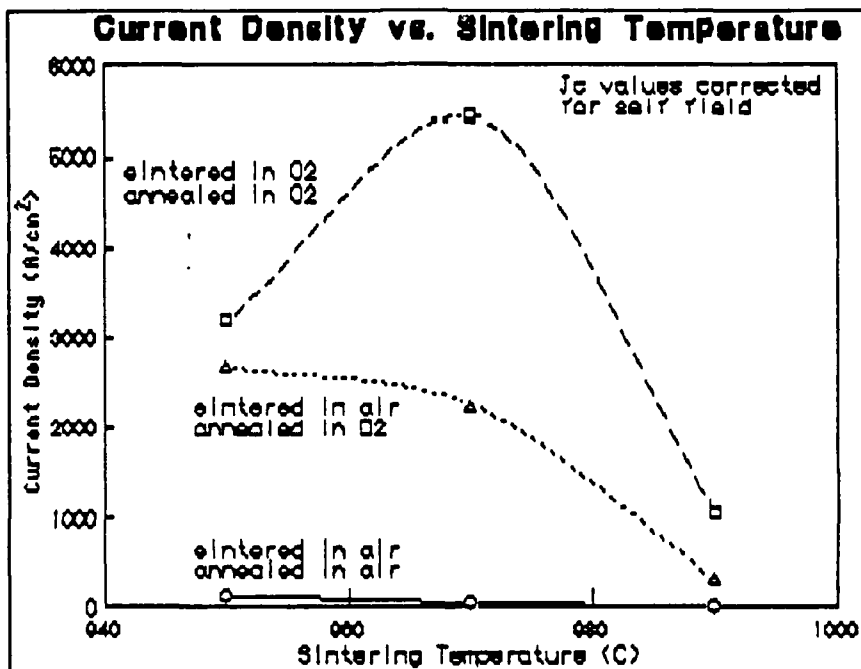


Figure 9. Current Density vs. Sintering Temperature for the pure 123

The results seen in Figure 9 show that the optimum processing temperature for sintering pure 123 is about 970C in oxygen atmosphere. When the samples were sintered in air atmosphere, the transition temperature widths were considerably wider than for the samples sintered in oxygen. The quantitative flux exclusion (indicating relative quantity of the orthorhombic phase) was also considerably lower for the samples processed in air indicating that air is not a suitable atmosphere for forming fully developed orthorhombic phase as seen in oxygen atmosphere. Samples processed in air and then annealed in oxygen still did not form fully developed orthorhombic phase. These results were also confirmed by X-ray diffraction studies which show clearly larger

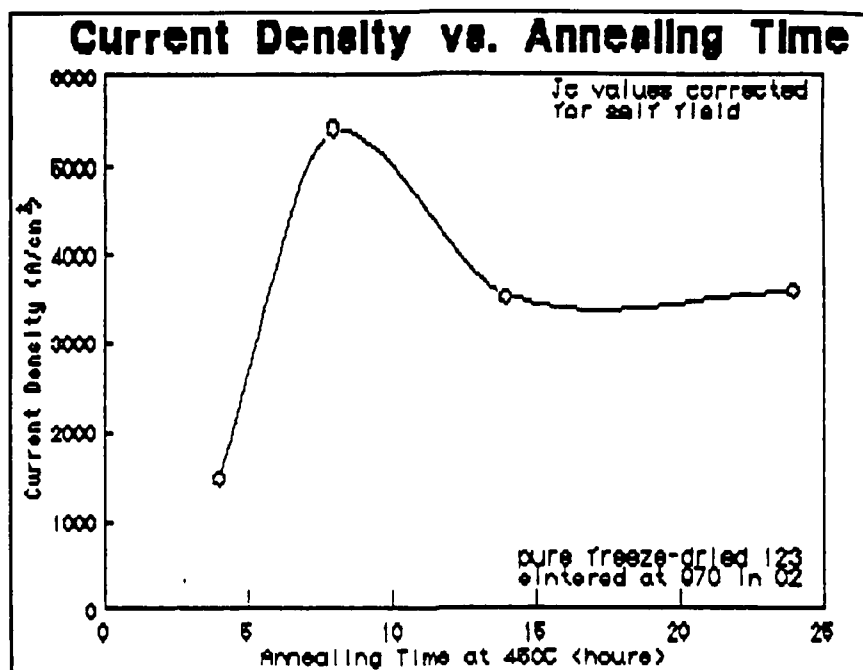


Figure 10. Current Density vs. Annealing Time for the pure 123.

splitting of the major peaks for the samples processed and annealed in oxygen. Hence, the critical current densities would be expected to be the highest for the samples processed and annealed in oxygen, with lower current densities obtained in the samples sintered in air and annealed in oxygen, and the lowest current density obtained in the samples sintered and annealed in air. These expected results were confirmed by experiments as shown in Figure 9. The critical current densities are also shown to be decreasing with increasing sintering temperatures for all samples (Figure 9). This experimental observation might be due to several factors. The grain growth increases with increasing sintering temperature, as discussed previously in this section, thus increasing the density of the 123. Due to the high anisotropy of the 123 compound, there is a large strain constriction on the randomly oriented growing grains of  $\text{YBa}_2\text{Cu}_3\text{O}_{7-x}$ . The strain increases with increasing density of the samples due to lack of strain relaxation mechanism thus increasing formation of microscopic and even macroscopic cracking. The resulting cracks severely limit the transport

critical current densities obtained in the 123 samples as demonstrated in Figure 11, where effect of maximum and average grain size on current density is shown. The flux exclusion was also decreasing with increasing density of the 123 samples which can be attributed to the slow oxygen diffusion rates through the dense sample hence inhibiting the formation of the orthorhombic phase.

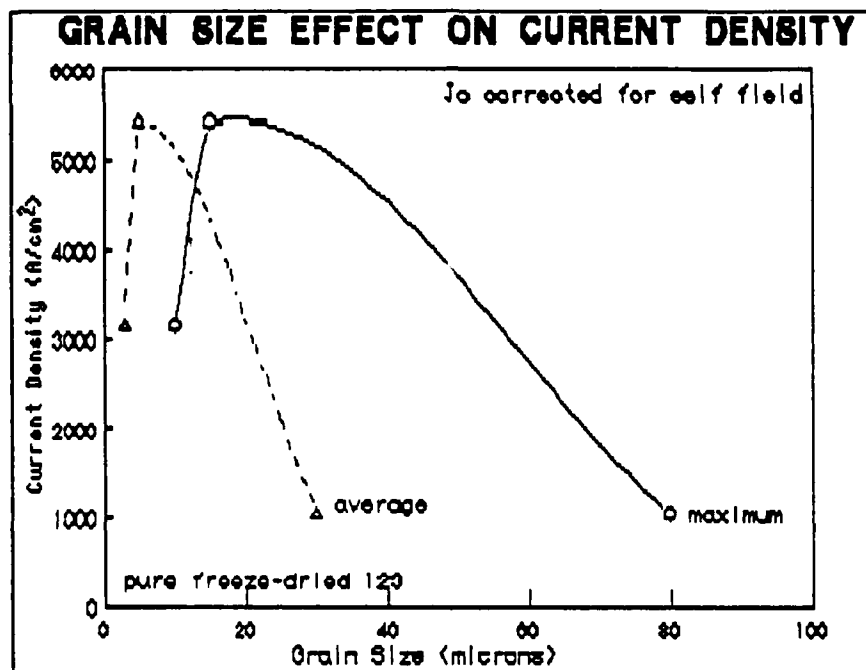


Figure 11. Grain Size Effect on Current Density for the pure 123

#### Effects of Silver Dopants.

The homogeneous distribution of silver up to 10 atomic % in the  $\text{YBa}_2\text{Cu}_3\text{O}_{7-x}$  compound did not seem to have a pronounced effect on the transition temperature behavior of the samples. However, when the silver content was 10% and higher the transition temperature behavior of the  $\text{YBa}_2\text{Cu}_3\text{O}_{7-x}$  was significantly altered, as can be summarized in Figures 12-13.

Silver doping lowered the total amount of flux exclusion, with the lowest exclusion obtained for the 10% Ag doped sample. The flux exclusion of the 20% Ag doped sample was between 1% Ag and

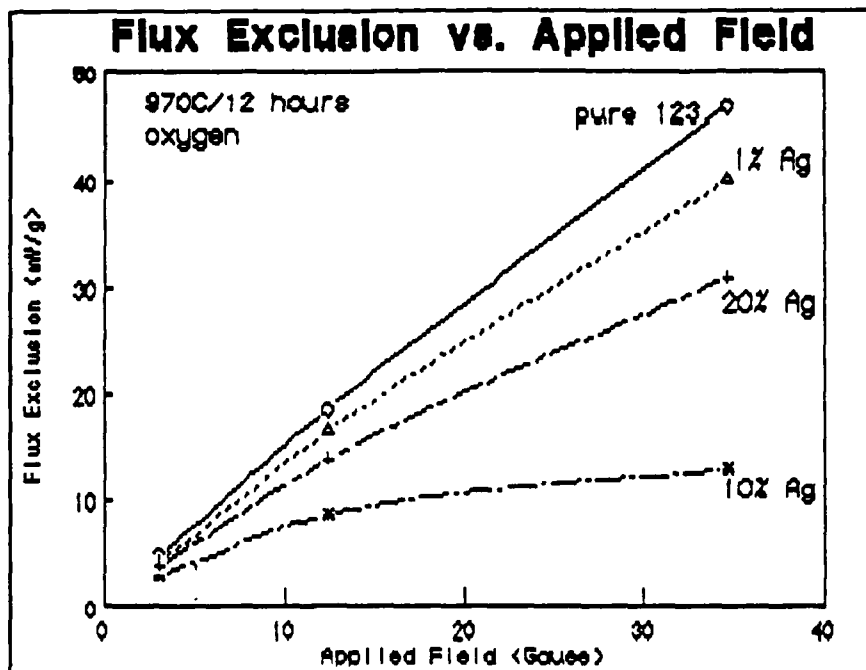


Figure 12. Flux Exclusion vs. Applied Field for pure and silver doped 123

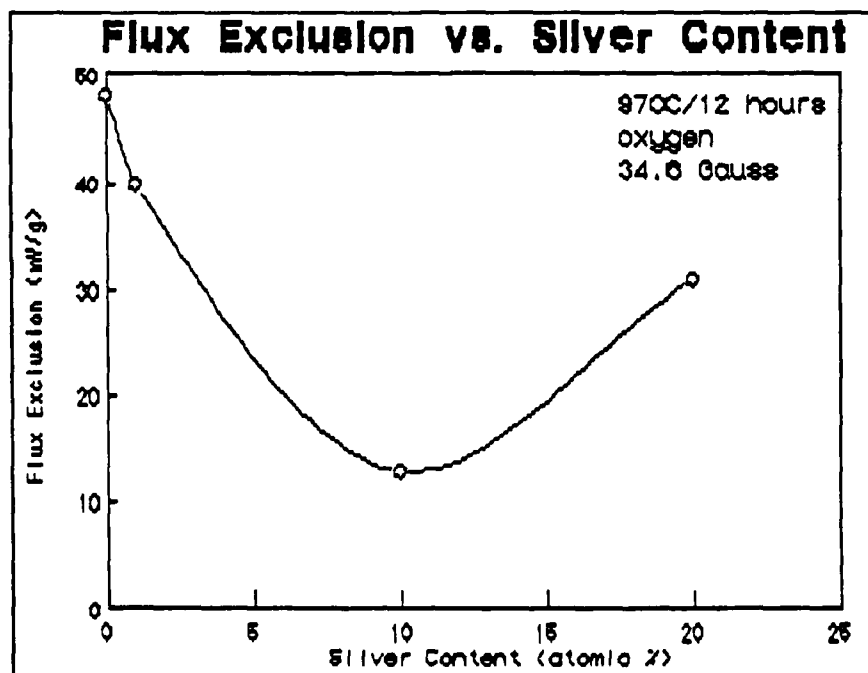


Figure 13. Flux Exclusion vs. Silver Content for the silver doped 123

10% Ag doped samples. This could be attributed to the fact that the 20% Ag actually crashed out of the solid solution yielding

material in the grain boundaries and most likely only a small percentage of Ag actually still remains alloyed within the 123 matrix. There were also inhomogeneities due to the formation of Cu-Ag alloy in the sample. The transition temperature width versus applied field is shown in Figure 14, where it can be seen that the behavior of the 10% Ag doped sample is clearly different from the other samples.

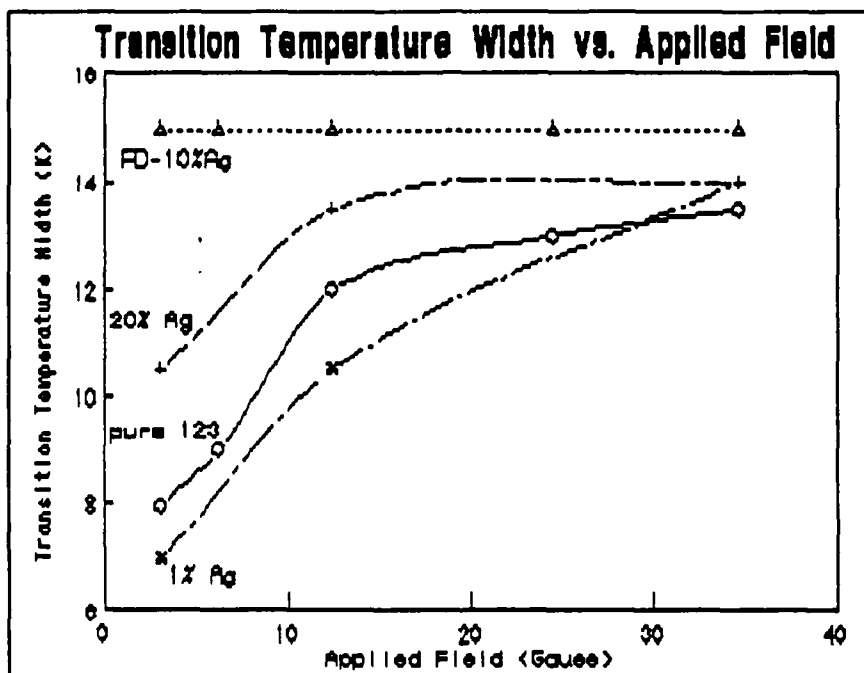


Figure 14. Transition Temperature Width vs Applied Field for pure and silver doped 123

The transition temperature width of that sample is totally independent of the applied field in the ac susceptibility measurements suggesting that there is possibly different mechanism of current transport occurring in the 10% Ag doped sample. The transition temperature width of the pure and 1% Ag doped sample increases with increasing applied field on the sample, suggesting that the field is destroying the weak links connecting individual grains thus increasing the transition temperature width. In the 10% Ag doped sample the transition temperature width is already very wide but is independent of the magnetic field thus suggesting, that there the nature of the weak links and grain boundaries is different. The transition

temperature behavior of the 20% Ag doped sample is only weakly dependent on the applied field as might be expected since the silver content is high enough for the sample to form some of the structure and morphology found in the 10% Ag doped sample, but in fact since the large amount of the silver precipitates in the grain boundaries, the transition temperature behavior should resemble the mixed state behavior of the pure and 10% Ag doped sample. This is indeed what is observed. The 20% Ag doped sample is very dense yet the flux exclusion is higher than the exclusion expected for an as dense pure 123 sample. This behavior might be explained by the silver metal enhancing oxygen diffusion into the bulk 123 compound during the low temperature annealing process.

The critical current density results as a function of silver doping for samples sintered at different temperatures in oxygen are shown in Figure 15.

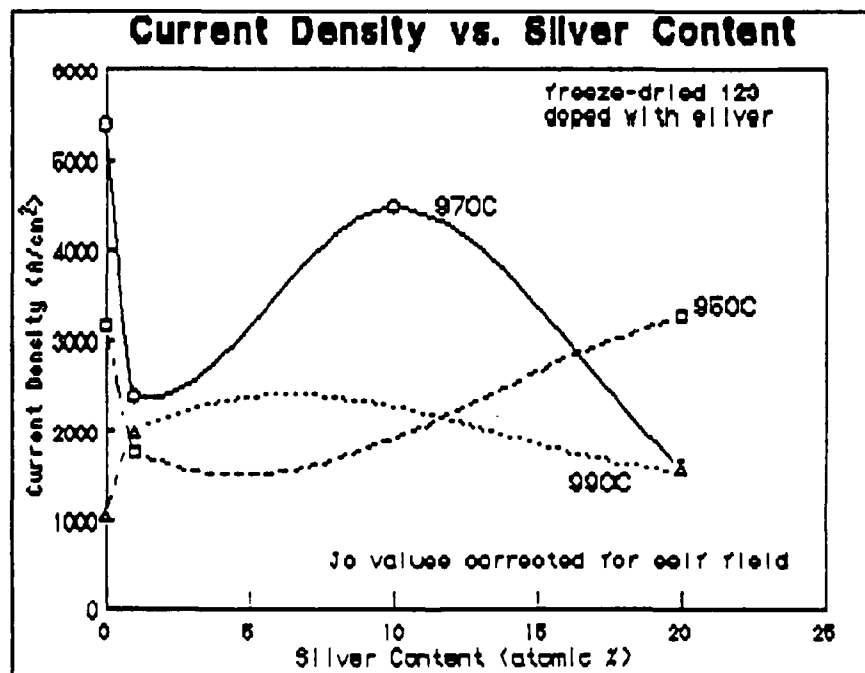


Figure 15. Current Density vs. Silver Content for the pure and silver doped 123

It can be seen that the current density decreased with the addition of 1% Ag, then increased and maximized at 10% Ag and

then gradually decreased with increasing silver content. The current density was always lower than that in the pure 123, although the current density of the 10% Ag doped sample was only slightly lower than in the pure 123 even though the flux exclusion of the former was 3 times lower than in latter. Depending on the exact position of the silver atoms in the  $\text{YBa}_2\text{Cu}_3\text{O}_{7-x}$  structure, this might suggest that the silver could be acting as flux pinning sites, thus possibly leading to the increased current density. The current density of the 1% Ag sample was much lower than that for the pure  $\text{YBa}_2\text{Cu}_3\text{O}_{7-x}$  due to a change in the morphology caused by the silver addition. The grains in the 1% Ag sample appear to be held very loosely together, thus increasing the resistance to the current flow through the sample. In the 20% Ag sample the actual amount of silver alloyed in the  $\text{YBa}_2\text{Cu}_3\text{O}_{7-x}$  matrix, while undetermined, is presumably similar to the 1% Ag case, with the remaining silver being present in the grain boundaries. In this case, the low current densities may be attributed to stress-induced microcracks which may be prevalent in the dense sample. There are also other phases present due to Ag-Cu alloying reactions thus further inhibiting the current flow across the grain boundaries. However, in the case of the 10% Ag addition, the problems of higher density and microcracks are partially overcome by the 'healing' effect of the silver metal causing the partial melting of the sample thus fusing the grains together. This fusion of the grains might help to minimize the grain boundary resistance, resulting in a higher  $J_c$ . The increased current densities may also be a result of an increased number of flux pinning sites caused by the silver defects. While the 20% Ag sample actually has more total silver present, there is actually less silver present in the solid solution than in the 10% case due to precipitation into the grain boundaries, thus accounting for the behavior observed.

As one would expect, grain size plays an important role in determining the current densities of these silver doped samples, Figure 16. Current densities increased with increasing grain



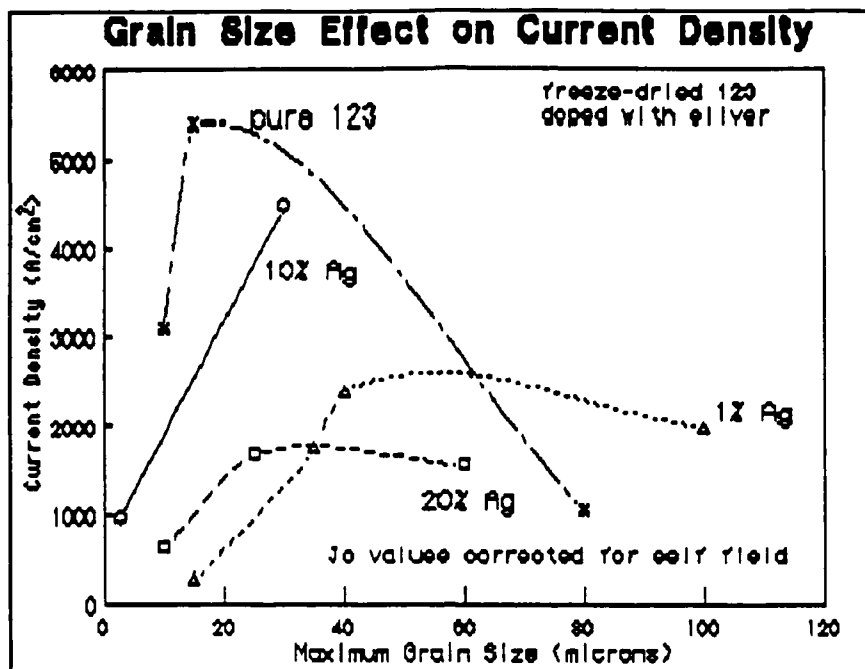


Figure 16. Grain Size Effect on Current Density of pure and silver doped 123.

size up to a certain level, after which the  $J_c$ 's tended to fall rapidly. As grain size increases the current progresses through fewer grain boundaries, thus experiencing fewer barriers. One would expect as the number of junctions is decreased, the current densities could be dramatically improved, and this is what is observed in single crystal and melt texturing studies. However, in bulk form, an increase in the grain size also corresponds to an increase in the density. As the sample becomes more dense, stress-induced microcracks develop, leading to the observed fall-off of current density values at higher grain sizes.

##### 5. SUMMARY AND CONCLUSIONS

A freeze drying technique was used to produce homogenous silver doped samples,  $\text{YBa}_2\text{Cu}_3\text{Ag}_y\text{O}_{7-x}$ , with the silver concentration ranging from one to twenty atomic percent. These samples exhibited changes in grain growth patterns due to the partial melting of silver when the sintering temperatures exceeded 960C/. At dopant levels less than 10%, there was no pronounced effect on the transition temperature behavior; however, 10% Ag samples

exhibited a marked change. Lower flux exclusion levels and wider transition widths independent of magnetic field suggested that the nature of the weak links and grain boundaries was much different. The 20% Ag sample exhibited behavior between that of the 1% and 10% due to the precipitation of a large amount of the silver out of the matrix into the grain boundaries.

The current density of the 1% Ag sample was much lower than that for the pure  $\text{YBa}_2\text{Cu}_3\text{O}_{7-x}$  due to a change in the morphology caused by the silver addition. In the 20% Ag sample the low current densities may be attributed to stress-induced microcracks which may be prevalent in the dense sample. There are also other phases present due to Ag-Cu alloying reactions thus further inhibiting the current flow across the grain boundaries. However, in the case of the 10% Ag addition, fusion of the grains might help to minimize the grain boundary resistance, resulting in a higher  $J_c$ . The increased current densities may also be a result of an increased number of flux pinning sites caused by the silver defects.

Many questions remain concerning these silver doped materials. The effect of the silver on the mechanism of current transmission through the bulk samples is still not clearly understood. Transmission electron microscopy and other studies are currently being carried out on these samples to determine the position of the silver and its role in determining the superconducting properties of these materials.

**EFFECTS OF METAL DOPING ON THE SHAPE OF AC  
SUSCEPTIBILITY CURVES OF  $\text{YBa}_2\text{Cu}_3\text{O}_{7-x}$**

M. Strasik; K. A. Youngdahl; J. E. Pillers; D. Santiago;  
and T. S. Luhman; Boeing Aerospace and Electronics,  
P.O. Box 3999, MS 73-09, Seattle, WA 98124-2499.

**ABSTRACT:**

Superconducting precursors were prepared through freeze drying or sol-gel techniques with the formula  $\text{YBa}_2\text{Cu}_3\text{M}_y\text{O}_{7-x}$  ( $y=0.01-0.2$ ). Dopants were chosen among the main group metals, first row transition metals, and noble metals. Additional dopant quantities, instead of substitutions, were employed to help induce the materials into the grain boundaries. The effects of these metal dopants on the shapes of  $T_c$  curves as determined by ac susceptibility curves and their relationship to measured transport current densities are examined.

**INTRODUCTION:**

Increases in the critical current densities ( $J_c$ 's) of bulk  $\text{YBa}_2\text{Cu}_3\text{O}_{7-x}$  have reached a plateau recently with measurements of  $\sim 10^3 \text{ A/cm}^2$  being the limit. In metallic superconductors, grain boundaries are the source of effective pinning centers of magnetic flux which in turn are responsible for the high critical current densities achievable in those materials. In the  $\text{YBa}_2\text{Cu}_3\text{O}_{7-x}$  oxide superconductors, grain boundaries have been identified as one of the sources contributing to the low critical current densities obtained in bulk sintered material. The extremely short superconducting coherence lengths of the oxides make their electrical and magnetic properties very sensitive to chemical and microstructural inhomogeneities within the grain boundaries. In order to improve the current density of these compounds by eliminating the weak links associated with the grain boundaries, novel synthesis techniques must be developed to enable us to control the chemical and microstructural properties of the grain boundaries.

The addition of various metals into the  $\text{YBa}_2\text{Cu}_3\text{O}_{7-x}$  perovskite material has resulted in a wide range of properties dependent on the amount and type of dopant used. Doping using silver has achieved moderate success toward improving the electrical and mechanical properties of these materials.

There have been some reports of current densities of the Y-Ba-Cu-O materials being improved through the addition of silver alloys and dopants. Several sources have attributed this increase in the  $J_c$  to texturing in the doped material resulting in crystal orientation along the (001) plane. Silver, with a melting point of 961C, has also been postulated as increasing the oxygen content of the bulk material through the high solubility of oxygen in the silver. This increased oxygen transport yields materials with higher current densities.

#### **EXPERIMENTAL:**

Dopants chosen for these experiments include Ag, Co, Pb, Ni, and Pt. Doped samples were prepared by one of two methods.

**Method A: Freeze-Drying.** An aqueous homogeneous solution of metal nitrates was prepared including the dopant material in ratios from one to twenty atomic percent. This solution was atomized directly into liquid nitrogen. The solution was kept frozen during which time a vacuum was pulled on the system. The water sublimed off of the mixture over a period of days resulting in an ultrafine, anhydrous, homogeneous powder. This powder was decomposed by flash heating to 700°C. Subsequent heat treatments, pelletization, and slicing resulted in (1 mm)<sup>2</sup> ceramic bars ready for analysis.

**Method B: Sol-Gel.** A citric acid/ethylene glycol mixture was condensed at 165°C, then diluted with water via the Pechini Method. To this solution, correct proportions of the metal acetates were added resulting in a homogeneous mixture. If the particular acetate of a dopant was not available, an organometallic substitution, not affecting the final composition, was made. The solution was reduced in volume and slowly heat

treated to 250°C. At this time the glassy gel was crushed, followed by further heat treatment to 900°C. Subsequent pelletization, cutting, and heat treatment provided (1mm)<sup>2</sup> ceramic bars ready for analysis.

**Instrumental Analysis:** The transition temperatures of the pure and doped samples were studied using the ac susceptibility measurement that can discriminate between inter- and intragrain properties of the samples. The net signal from the balanced pick-up coils contains in-phase and out-of-phase components, corresponding to the real and imaginary part of the ac susceptibility,  $X'$  and  $X''$ , respectively. Skin effect losses in the normal state and flux flow losses in the superconducting state do not affect our measurement which is performed at 200 Hz. Information concerning the  $T_c$  onset,  $T_c$  midpoints, and general, shape of the  $T_c$  and  $T_{c2}$  curves was obtained by this method.

Bulk critical current densities were obtained by placing four silver contacts at points along the (1mm)<sup>2</sup> bar. Lowest resistivities of these silver contacts were obtained by placing four small silver disks on the metal bar, heating shortly at 970°C, and annealing at 450°C in oxygen for four hours. Resistivities of  $10^{-6-7}$  ohm-cm<sup>2</sup> could be obtained by this method. Many of the earlier samples were recorded using silver paste contacts that had been annealed to 450°C for four hours in oxygen. Silver and/or copper leads were then soldered onto the silver contacts using indium metal and critical current densities were recorded at liquid nitrogen temperatures and no applied magnetic field. The resistivity criteria of  $10^{-9}$  ohm-cm was used for voltage onset. The resulting critical current densities were corrected for the self field effects on Josephson Junctions at the grain boundary, as will be discussed in the Results and Discussion section.

Metallography was performed on polished sections of the sintered bars. Additionally, the samples were mounted and scanning

electron microscopy with EDXS was performed to obtain additional information about the microstructure, chemical composition, and homogeneity of these materials.

Elemental analyses (ICP) were performed on representative samples of these materials through Amtest, Inc., of Redmond, WA. Samples were scanned for trace impurities (ppm) as well as their major components (%) during these analyses.

#### **RESULTS AND DISCUSSION:**

**Synthesis:** Preparation of these materials by the sol-gel or freeze-drying techniques allows for the formation of homogeneous, fine grained powders, a fact that has been confirmed by ICP and microscopic analysis. By adding the dopants into the precursor solution mixture, one is able to achieve an atomic distribution of the dopant metals throughout the 123 matrix. This allows for some unique consequences of the dopant materials to be observed, one's that would normally be missed in normal solid state chemical preparation. This is most readily observed in the case of the dopant silver. To introduce silver into the  $\text{YBa}_2\text{Cu}_3\text{O}_{7-x}$  matrix, one may add it in a number of different ways. It may be added to a precursor mixture as either silver powder or silver oxide, or it may be added as a soluble complex in the precursor solution. Marked differences in the properties of the resultant materials are noted by utilizing the former method including the predominance of silver/copper eutectics. This arises because the distribution of silver formed in the transformation to ceramic product is not very uniform. The silver material has a tendency to ball up in areas along the grain boundary. Conversely, if the silver is distributed atomically throughout the structure, it has a tendency to be soluble in the 123 matrix up to certain concentrations. Different morphology and superconducting properties are observed when this occurs.

For the basis of comparison, all of the doped materials were heated according to identical heat treatment schedules. The

values chosen were those that had previously been successful in the formation of undoped  $\text{YBa}_2\text{Cu}_3\text{O}_{7-x}$ . Thus, all samples were heated to  $970^\circ\text{C}$  for twelve hours followed by an anneal at  $450^\circ\text{C}$  all in an oxygen atmosphere.

**$T_c$  Measurements:** Transition temperature widths determined by ac susceptibility are partially dependent on the grain size, as well as chemical and oxygen homogeneity of grains and grain boundaries. A lot of information can be obtained by examining the shape of the transition temperature curves and their derivatives. The shapes of  $T_c$  curves can be directly correlated to measured critical current densities.

As the sample is cooled, the grains become superconducting at  $T_c$  onset but the weak-links are still resistive due to thermal fluctuations. Therefore, the initial ac field induced screening currents only flow inside the grains. The intragrain current increases with decreasing temperature, leading to better screening, i.e. smaller  $X'$  and larger  $X''$ . The ac amplitude still reaches the center of the grains at this point. The imaginary part  $X''$ , which is proportional to the ac hysteresis losses has a maximum at the temperature where the penetration depth of the grain begins to be reduced below the grain's radius. At this temperature ( $T_{c1}$ ) the ac field no longer penetrates the whole grain and the volume in which the hysteresis losses occurs shrinks. The weak-links are able to carry a supercurrent if the temperature is below the phase locking temperature at which the energy of the weak-link junction becomes equal to  $kT$ . This temperature corresponds to the shoulder of  $X'$  in transition temperature measurements. Below this temperature macroscopic shielding currents through grains and weak-links are induced. The ac losses of the junctions increase below  $T_c$  and cause the intergrain maximum  $X''$ , at which the ac field just penetrates into the center of the specimen via the weak-link paths. In the temperature region below  $T_c$  the intergrain signal dominates compared to the intragrain one due to the much smaller intragrain

penetration depth ( $T_{c2}$ ). The height, position, and width of the intergrain maximum reflects the intergrain volume, the intergrain critical current density, and the distribution of the coupling energy or junction current.

As discussed in previous papers, the pure and doped material displaying a  $T_{c2}$  is indicative of weak links in the grain boundary phases. Figures 1-3 show an ac magnetic susceptibility curves for the 1% Co doped  $\text{YBa}_2\text{Cu}_3\text{Co}_{0.01}\text{O}_{7-x}$ . The amplitude and position of the midpoint of these  $T_c$  values can be more easily derived by calculating and plotting the derivatives of the  $T_c$  curves. Differences in the shape and position of  $T_{c1}$  and  $T_{c2}$  were readily seen by this method as represented in Figures 4-5 for the 1% Co doped  $\text{YBa}_2\text{Cu}_3\text{Co}_{0.01}\text{O}_{7-x}$ . When a magnetic field (3-35 Gauss) is applied to the 1% doped Co system, the values of  $T_{c2}$  midpoints shift to lower and lower temperatures. A clue as to the amount of material that is present in the grain boundaries vs. that alloyed into the 123 matrix may be given by examining the shape of the  $T_c$  curves. While  $T_{c2}$  is indicative of the weak link material,  $T_{c1}$  give a good measure of the bulk matrix material. Changes in the shape of  $T_{c1}$  would therefore reflect changes in 123 matrix. This would include effects like alloying of the dopant metals into the matrix and substitution into one of the matrix sites. From the derivatized curves, one can obtain values for the width at half height for both  $T_{c1}$  and  $T_{c2}$ . This may be used as a measure for the amount of alloying occurring in the material. For a sample such as 1% Co,  $\Delta T_{c1}$  is fairly small ( $\sim 2\text{K}$ ), and the cobalt would lie outside of the metal oxide matrix. The transition temperature width increases with increasing applied field. This behavior shows the weak link dependence on the applied field for the dopant modified grain boundaries. When one examines the  $T_{c1}$  behavior of the 1% Co doped sample, it can be observed that the intrinsic superconducting properties of the grains are not dependent on the applied field at all as can be seen in Figures 4-5. This observation is supported by results shown in Figure 5 where  $T_c$



TITLE:SG24(1%Co) 970/12/450/4/450/4 02 pel amp=0

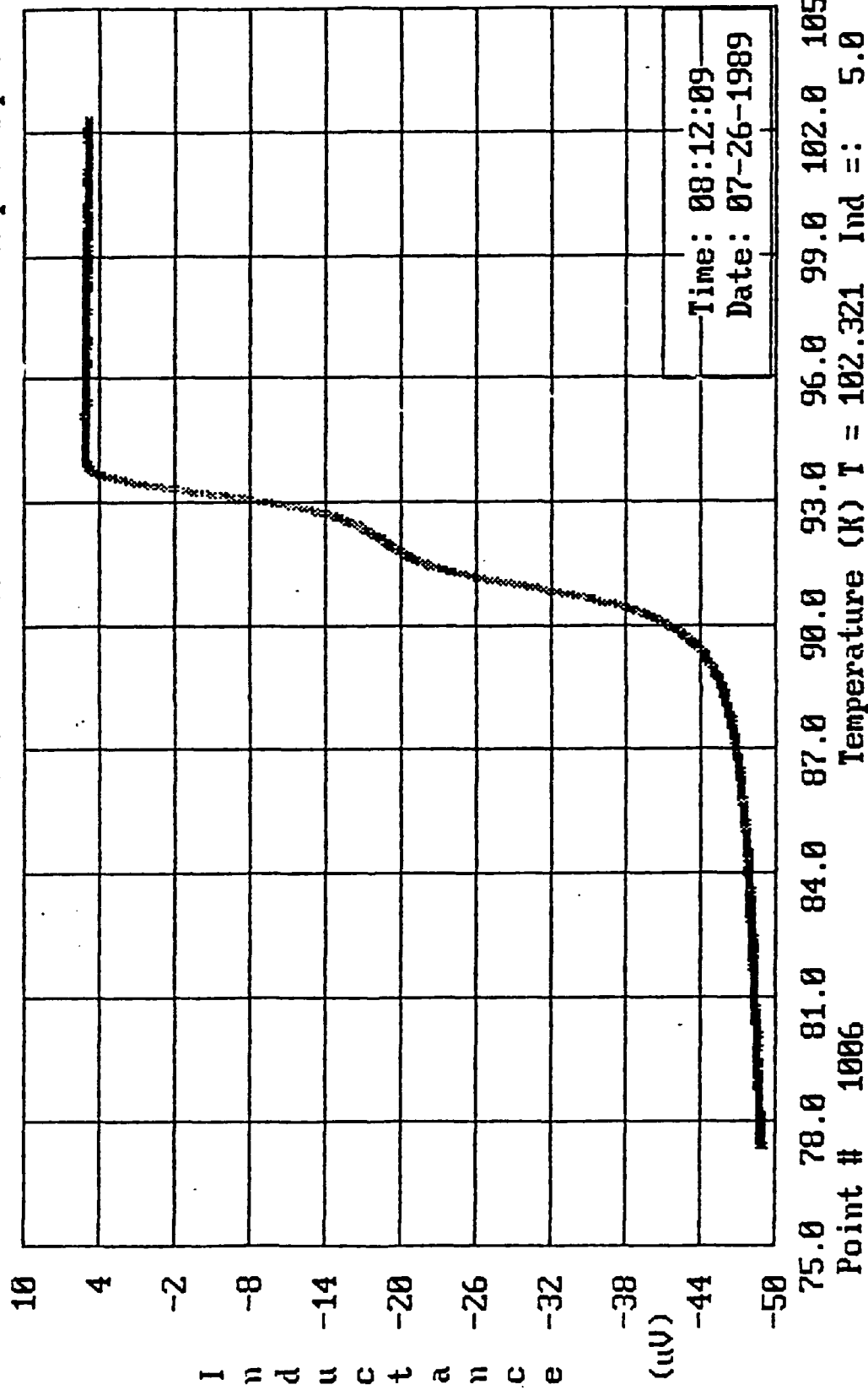


Figure 1. AC Magnetic Susceptibility Curve for the  $\text{YBa}_2\text{Cu}_3\text{Co}_{0.01}\text{O}_{7-x}$ .  $H=3$  Gauss

TITLE:SG24(1%Co) 970/12/450/4/450/4 02 pel amp=2

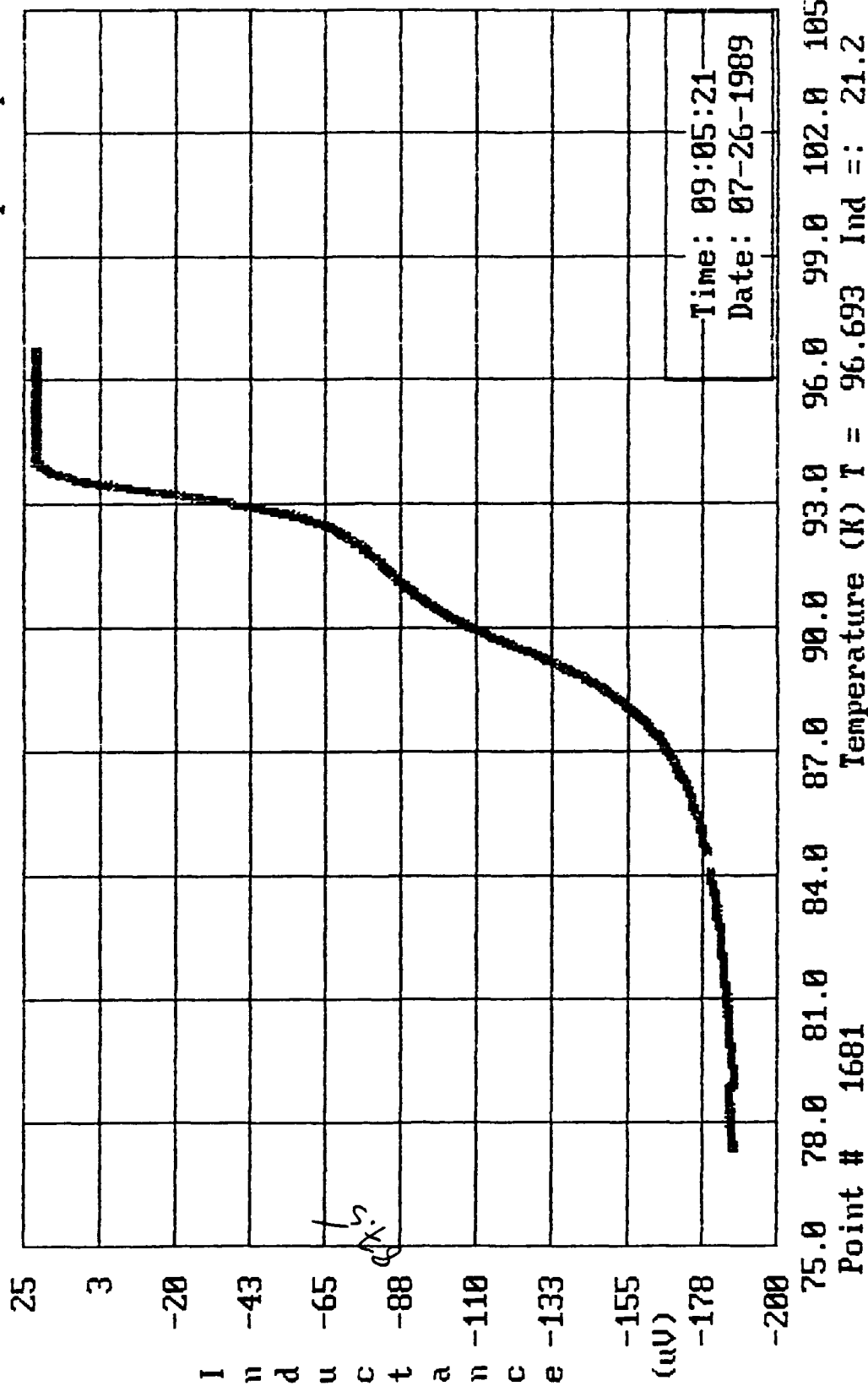
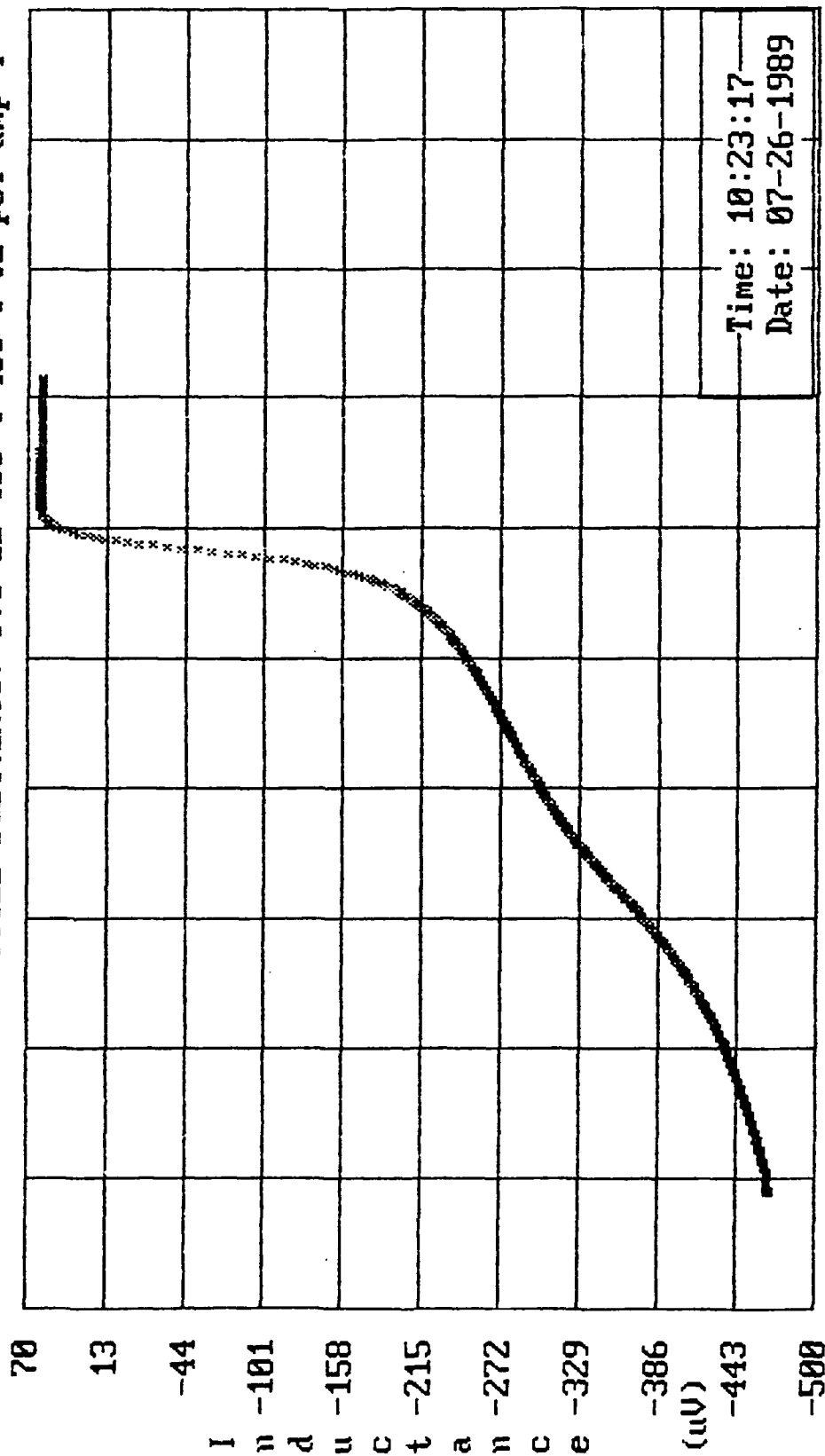


Figure 2. AC Magnetic Susceptibility Curve for the  $\text{YBa}_2\text{Cu}_3\text{Co}_{0.01}\text{O}_{7-x}$ .  $H=12$  Gauss

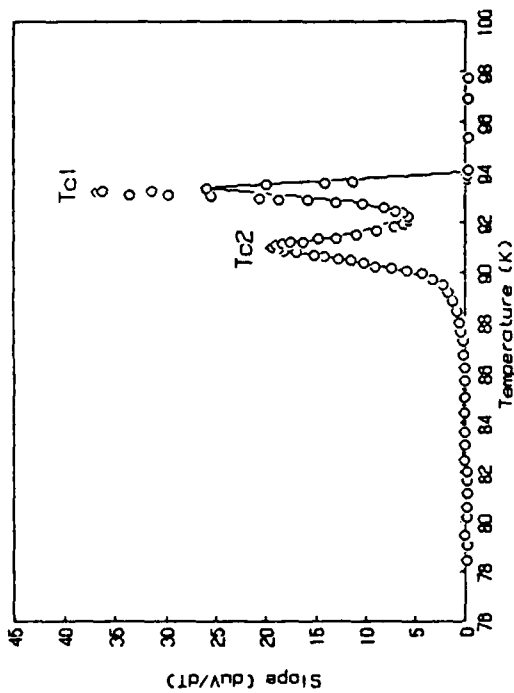
TITLE:SG24(1%Co) 970/12/450/4/450/4 02 pel amp=4



Point # 563  
 Temperature (K) T = 96.429 Ind =: 60.2

Figure 3. AC Magnetic Susceptibility Curve for the  $\text{YBa}_2\text{Cu}_3\text{Co}_{0.01}\text{O}_{7-x}$ .  $H=35$  Gauss

SG24 (1%Co) 970/12/450/4 02 H=3G



SG24 (1%Co) 970/12/450/4 02 H=12G

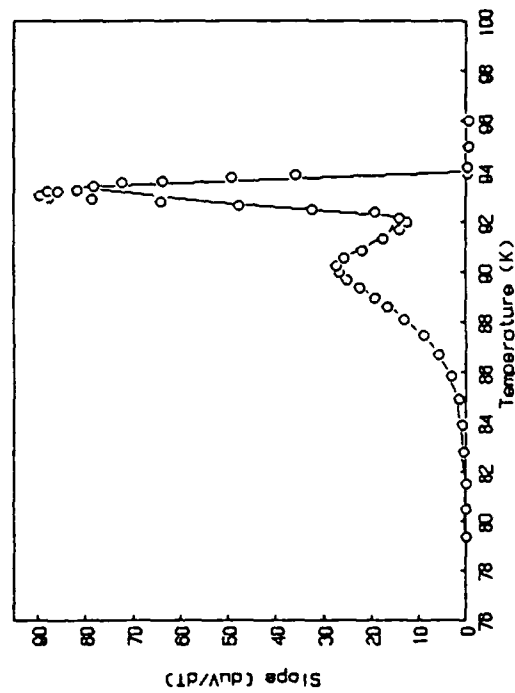
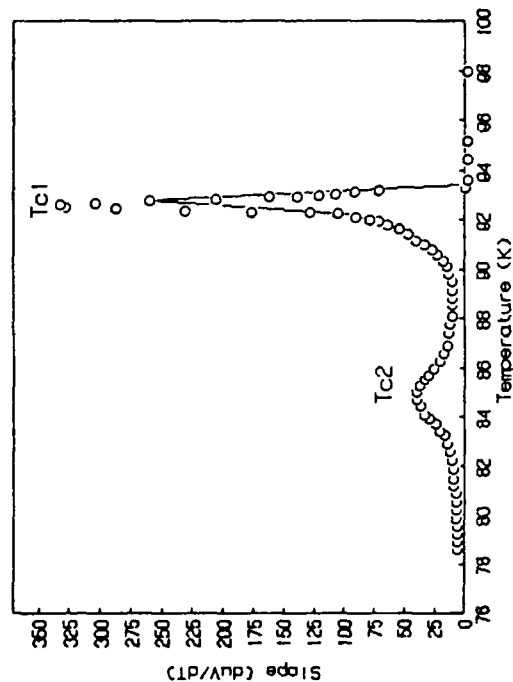


Figure 4. Derivative of AC Magnetic Susceptibility Curve for the  $\text{YBa}_2\text{Cu}_3\text{Co}_{0.01}\text{O}_{7-x}$

SG24 (1%Co) 970/12/450/4 02 H=35G



SG24 (1%Co) 970/12/450/4 02 H=35G

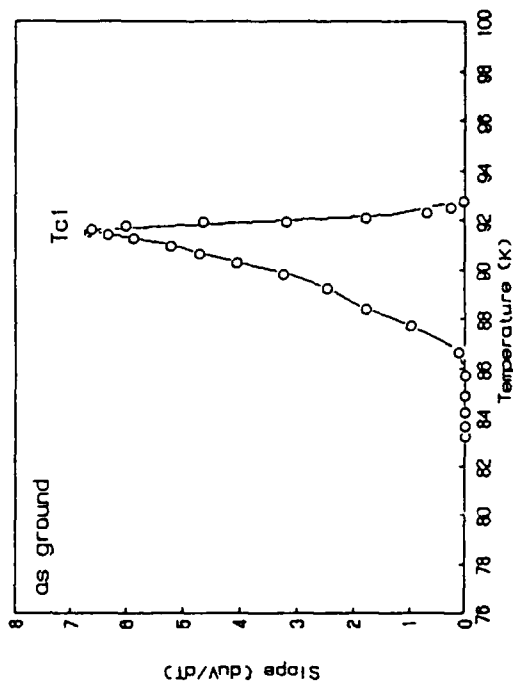
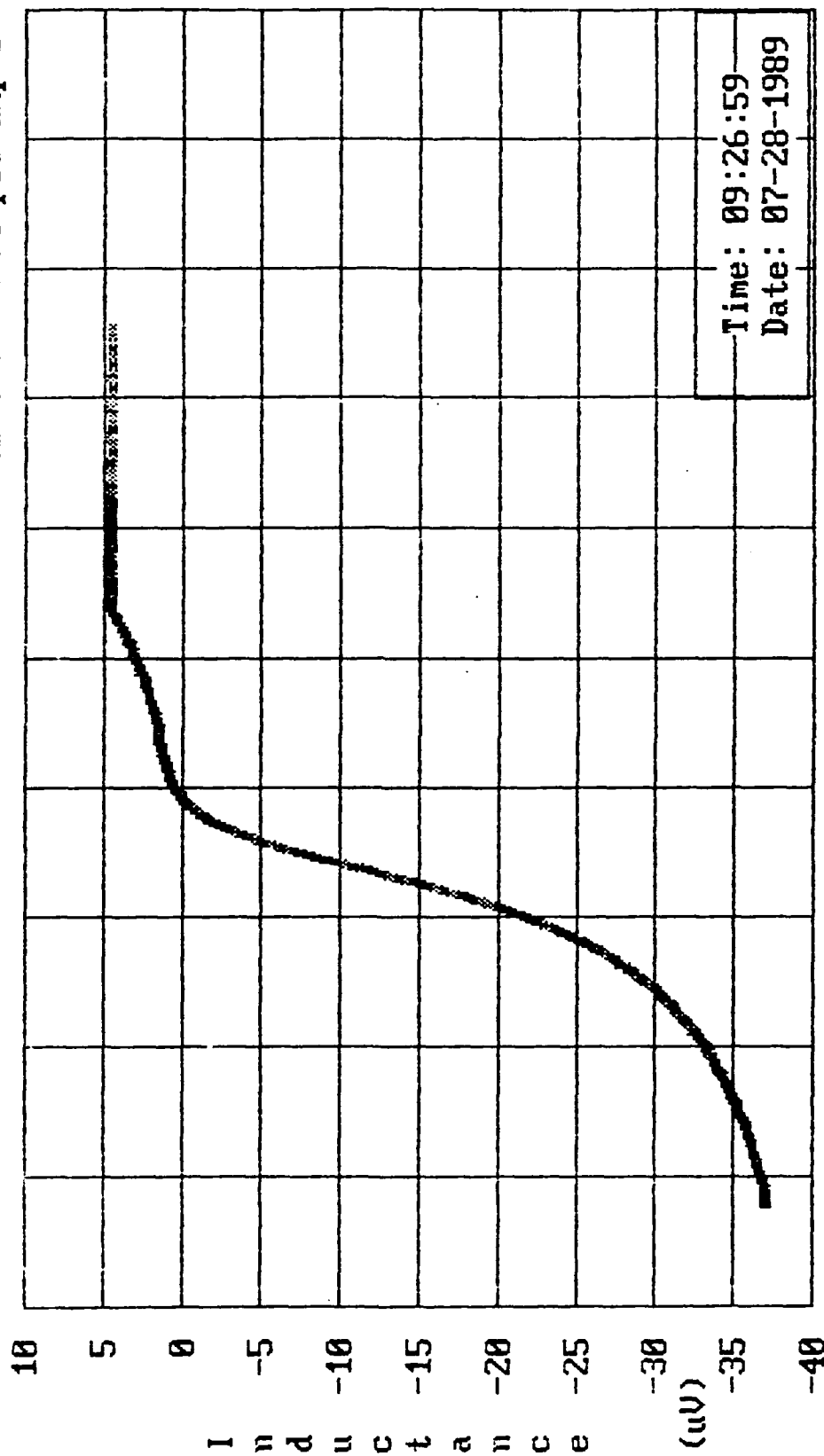


Figure 5. Derivative of AC Magnetic Susceptibility Curve for the  $\text{YBa}_2\text{Cu}_3\text{Co}_{0.01}\text{O}_{7-x}$

behavior is seen for the 1% Co doped sample that was crushed below the grain size. The weak links present in the grain boundaries were destroyed by grinding the sample to the grain size thus completely eliminating the  $T_{c2}$  peak and showing only transition temperature  $T_{c1}$  corresponding to pure  $YBa_2Cu_3O_{7-x}$  grains. In contrast to the Co doped sample, Figures 6-10 show the  $T_c$  curves for 1% Ni doped  $YBa_2Cu_3Ni_{0.01}O_{7-x}$  sample. In these results, it is fairly obvious that the Ni influenced the structure and superconducting properties of the  $YBa_2Cu_3O_{7-x}$  grains as well as grain boundaries. It can be seen in these figures that the Ni doped sample contains only very small amount of good superconducting phase (although some Ni is alloyed with the  $YBa_2Cu_3O_{7-x}$  as will be evident from the following analysis) as manifested by a small  $T_{c1}$  peak. The amplitude of the  $T_{c2}$  peak is much larger than in the Co doped sample with  $T_{c2}$  midpoint position being significantly lower than in the Co doped sample representing Ni doped grain boundary phases. This shows that the grain boundary phase is the majority superconducting phase present in this sample. The bottom portion of Figure 10 shows the transition temperature behavior of the Ni doped sample displaying 2 peaks rather than just one as in the Co doped sample. The two peaks support the theory that some nickel alloys with the  $YBa_2Cu_3O_{7-x}$  itself thus influencing the superconducting properties even of the individual grains as evidenced by the presence of  $T_{c1}$  and  $T_{c2}$  peaks which are decreasing with increasing applied field even in the crushed material. Crushing the Ni doped sample to the grain size eliminates the grain boundaries but does not eliminate the two peaks in the transition temperature measurement which proves the above hypothesis about nickel alloying with  $YBa_2Cu_3O_{7-x}$ .

**Current Density Measurements:** These ac magnetic susceptibility results can be directly correlated to the measured critical current densities. As the magnetic field is increased at liquid nitrogen temperatures, the critical current density decreases, corresponding to the amount of weak links that are transformed

TITLE:SG25a(1/2Ni) 970/12/450/4/450/4 02 pel amp=0



Point # 1012  
 Temperature (K) T = 97.643 Ind =: 4.5

Figure 6. AC Magnetic Susceptibility Curve for the  $\text{YBa}_2\text{Cu}_3\text{Ni}_{0.01}\text{O}_{7-x}$ .  $H=3$  Gauss

TITLE:SG25(1/Ni) 970/12/450/4/450/4 02 per amp=2

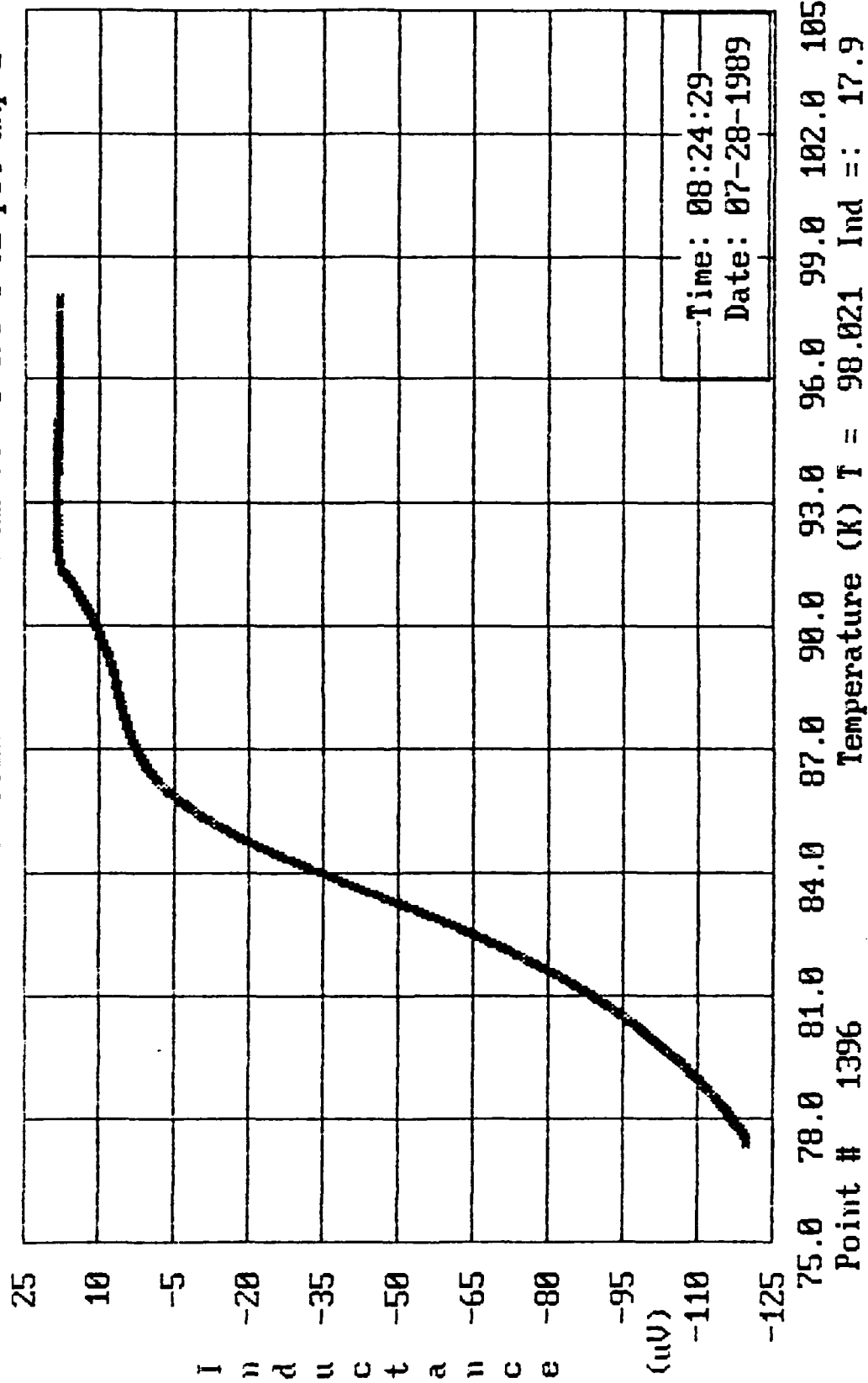


Figure 7. AC Magnetic Susceptibility Curve for the  $\text{YBa}_2\text{Cu}_3\text{Ni}_{0.01}\text{O}_{7-x}$ .  $H=12$  Gauss



TITLE:SG25(1%Ni) 970/12/450/4/450/4 02 pel amp=4

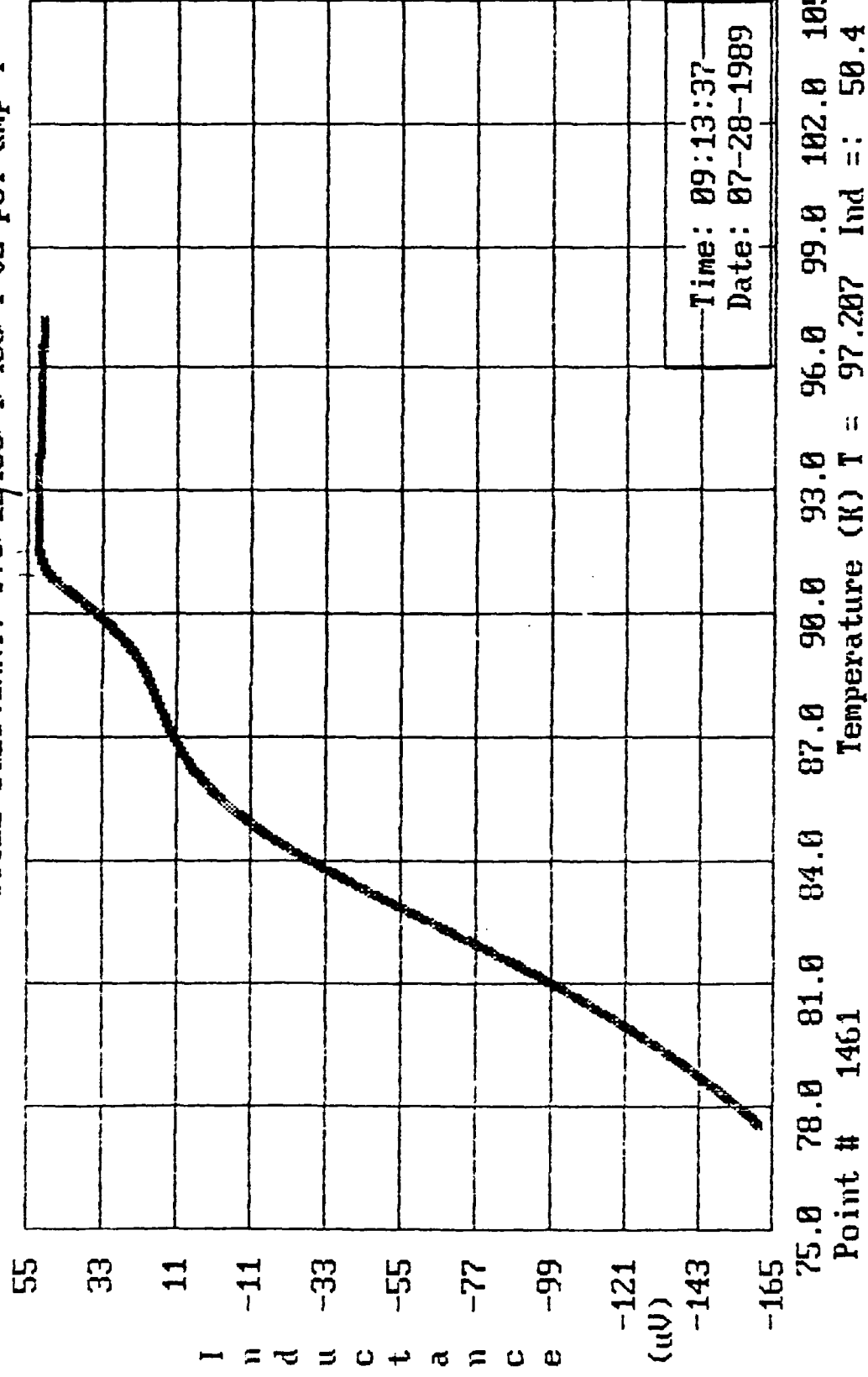
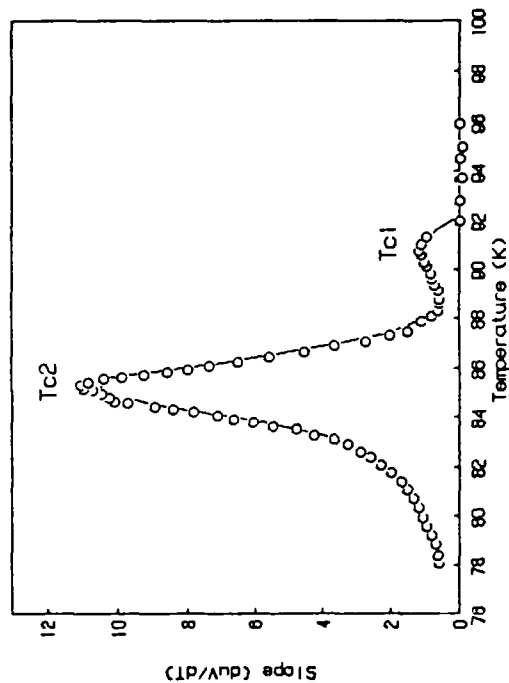


Figure 8. AC Magnetic Susceptibility curve for the  $\text{YBa}_2\text{Cu}_3\text{Ni}_{0.01}\text{O}_{7-x}$ .  $H=35$  Gauss

SG25 (1%Ni) 970/12/450/4 02 H=3G



SG25 (1%Ni) 970/12/450/4 02 H=12G

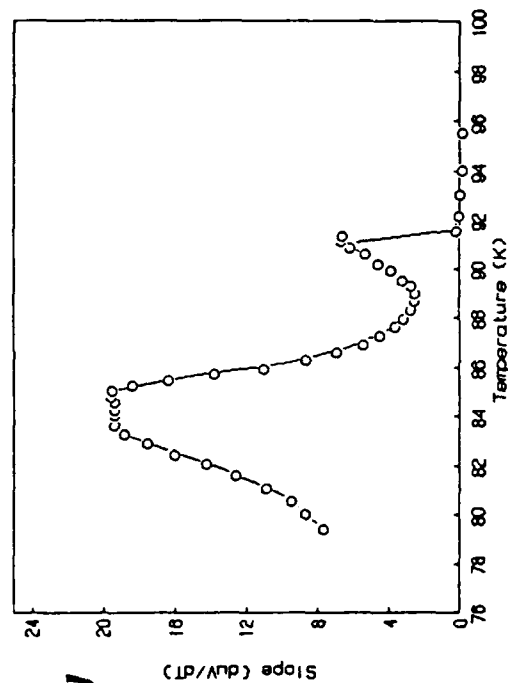
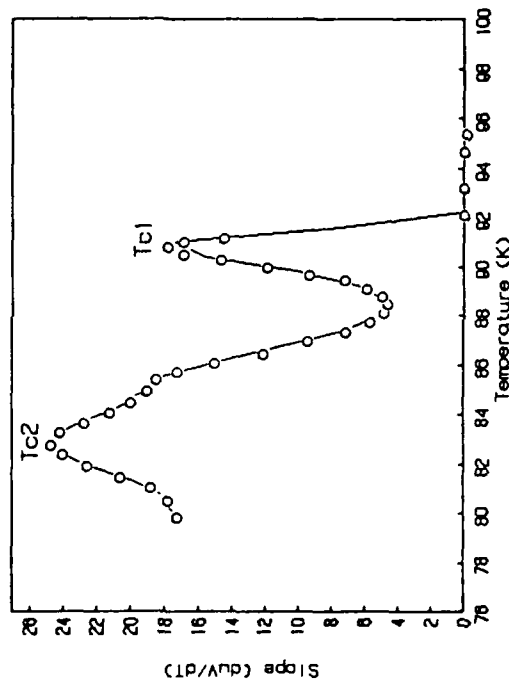


Figure 9. Derivative of AC Magnetic Susceptibility Curve for the  $\text{YBa}_2\text{Cu}_3\text{Ni}_{0.01}\text{O}_{7-x}$

SG25 (1%Ni) 970/12/450/4 02 H=35G



SG25 (1%Ni) 970/12/450/4 02 H=35G

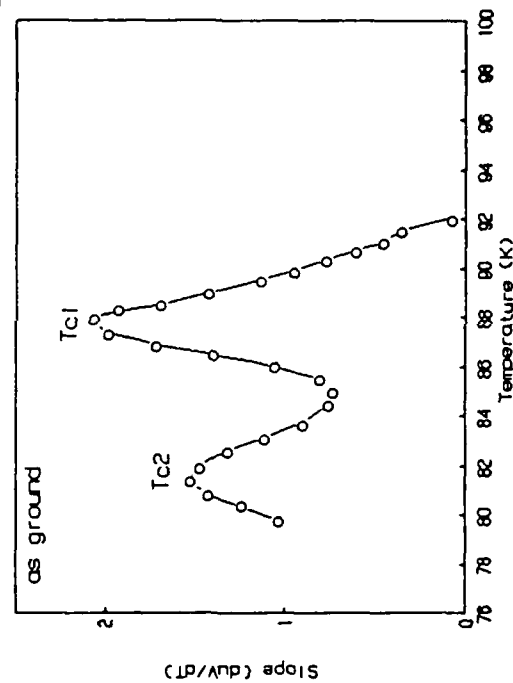


Figure 10. Derivative of AC Magnetic Susceptibility Curve for the  $\text{YBa}_2\text{Cu}_3\text{Ni}_{0.01}\text{O}_{7-x}$

into normal resistive state by the decrease in  $T_{c2}$ . This occurs until all of the weak links are destroyed. And this is what is experimentally observed in these dopant materials. For the materials that display a higher  $T_{c2}$ , there is a general tendency to possess higher current carrying capacity. For example, the 1% Co sample had a  $T_{c2}$  that varied from 91K to 84.7K over the applied magnetic field range from 3.15G to 34.64G. A 1% Ni sample had a  $T_{c2}$  that varied from 85K to 82K over the same applied field range. If one examines the  $J_c$  values (uncorrected for self field) for these two materials at liquid nitrogen temperatures, for 1% Co  $J_c=190$  A/cm<sup>2</sup> and for 1% Ni  $J_c=70$  A/cm<sup>2</sup>. (Note: These values were measured using silver paste contacts annealed for four hours in oxygen at 450°C. Considerably higher values have been realized for across the board measurements using silver metal contacts melted directly onto the substrate.)

One also notices a change in the amplitudes of  $T_{c1}$  vs.  $T_{c2}$  as one spans the range of metal dopants. However, these numbers are not absolute numbers and may only be compared on a qualitative basis. A dopant (1%) such as cobalt, which displayed good superconducting properties, showed a higher ratio of  $T_{c1}/T_{c2}$  than dopants which displayed poorer properties, such as 1% Ni. Thus, the latter material conducts through its weak links more than higher  $J_c$  materials, and these weak links are easily destroyed by the application of small magnetic fields leading to large losses of superconductivity. By this method, one can see how materials with fewer weak links, and smaller  $T_{c2}$  amplitudes, are better superconductors. More detailed current density studies under applied magnetic field are presently being performed and will be included in the final version of this paper.

**Microscopy.** Representative samples of these dopant materials were examined by scanning electron microscopy (SEM) and metallography. Both fractured portions and the surface were examined. Even at these minimal dopant levels, i.e. one percent, significant changes in the microstructure of the ceramics were

realized. For instance, variations in the amount of twinning were observed in samples that displayed low current densities. The 1%Ni sample had few areas of twinning and had a relatively low current carrying capacity.

**Future Directions:** Because of the necessity of obtaining higher critical current densities for practical applications, drastic measures must be taken to alter the materials. Chemical alterations may provide the opportunity for this to occur. In order to improve the current carrying abilities of this material, the connectivity between the grains must be improved. One way to accomplish this is through liquid phase sintering, however; conventional liquid phase sintering occurs through eutectic melting which causes off-stoichiometric areas and extraneous non-superconducting phases to be present at the grain boundaries. Through the addition of doped metals, one may be able to depress the melting point of the alloyed material, thus allowing liquid phase sintering to take place through different means. To obtain a measure of the melting point depression in these materials, one must do differential thermal analyses (DTA). If a material can be found that exhibits a lower melting temperature, one may be able to induce intergrain epitaxial growth. As 123 material grows between the grains, in an idealistic fashion, gluing the grains together, the dopant material will still remain. In most cases, the dopant will be a hindrance to overall transport mechanisms. Therefore a method for removing the dopant material after it has served its use would need to be devised. This may be accomplished in the case of lead. Lead has a melting point of 328°C and a boiling point of 1740°C. Thus, at the sintering temperatures that are used in preparing these samples (900-1000°C) the lead is volatilizing out of the sample at a certain rate. Since lead melts at such a low temperature, it also has the advantage of increasing the density of the samples through liquid phase (namely lead) sintering. For a case where two pellets of the same size, one undoped and one with 10% Pb, were sintered side by side at 910°C, the lead sample experienced a

shrinkage to  $2/3$  the size of the undoped material.

These doped materials will also be looked at in the context of melt texturing. The altered grain growth patterns associated with the doped materials may be used to our advantage in producing aligned grains with good connectivity. Selected specimens from this preliminary work will be used in such a future study.

#### **ACKNOWLEDGEMENTS**

The authors gratefully acknowledge the support by DARPA/AFOSR under Contract No. F49620-88-C-0143.

**EFFECTS OF METAL DOPING ON THE SUPERCONDUCTING  
PROPERTIES OF  $\text{YBa}_2\text{Cu}_3\text{O}_{7-x}$**

K. A. Youngdahl; M. Strasik; J. E. Pillers; D. Santiago;  
and T. S. Luhman, Boeing Aerospace and Electronics,  
P.O. Box 3999, MS 73-09, Seattle, WA 98124-2499.

**ABSTRACT:**

Superconducting precursors were prepared through freeze drying or sol-gel techniques with the formula  $\text{YBa}_2\text{Cu}_3\text{M}_y\text{O}_{7-x}$  ( $y=0.01-0.2$ ). Dopants were chosen among the main group metals, first row transition metals, and noble metals. Additional dopant quantities, instead of substitutions, were employed to help induce the materials into the grain boundaries. The effects of these metal dopants on the transport current densities, critical temperatures, ac susceptibility curves and microstructures is examined.

**INTRODUCTION:**

Increases in the critical current densities ( $J_c$ 's) of bulk  $\text{YBa}_2\text{Cu}_3\text{O}_{7-x}$  have reached a plateau recently with measurements of  $\sim 10^3 \text{ A/cm}^2$  being the limit. Much higher  $J_c$  values have been achieved in thin films as well as single crystal substrates which have led many to believe that the limiting factor in the current carrying capacity of these materials is a grain boundary or weak link effect. Low  $J_c$ 's have been attributed to a combination of critical current anisotropy and poor coupling across grain boundaries, factors which are eliminated in thin films and single crystals. Thus, one needs to look for ways to modify the grain boundaries themselves to result in increased intergrain coupling. One method has been through a physical changing of the grain boundaries via melt-texturing. Increases over two orders of magnitude have been achieved through these ends. However, melt texturing does not eliminate the grain boundaries, it just reduces the number of them, thus one must look for a means of improving the borders themselves. By modifying the grain boundaries chemically, one might be able to effect changes in the

current carrying capacity of the bulk material. The addition of metal dopants into the  $\text{YBa}_2\text{Cu}_3\text{O}_{7-x}$  matrix is a method that has been examined by many research groups. Most commonly, conducting metals such as silver are added, or substitutions for an element, such as copper, are carried out. In these studies, we will look at the influence of added dopants to the 123 materials, that is  $\text{YBa}_2\text{Cu}_3\text{M}_y\text{O}_{7-x}$  ( $y=0.01-0.2$ ). By adding the metal dopants as additions instead of substitutions, one decreases the possibility of the dopants being soluble in the matrix material, for substitutions cause vacancies which are readily filled by substitute metals. Therefore, the dopants are more likely to move into the grain boundary area, thus localizing their effects. A variety of metal dopants were chosen including representatives of the main group elements, first row transition metals, and noble metals.

#### **EXPERIMENTAL:**

Dopants chosen for these experiments include Ag, Ca, Cr, Co, Fe, La, Pb, Li, Mg, Mn, Ni, Pt, Sr, Ti, V, Zn, and Zr. Doped samples were prepared by one of two methods.

**Method A: Freeze-Drying.** An aqueous homogeneous solution of metal nitrates was prepared including the dopant material in ratios from one to twenty atomic percent. This solution was atomized directly into liquid nitrogen. The solution was kept frozen during which time a vacuum was pulled on the system. The water sublimed off of the mixture over a period of days resulting in an ultrafine, anhydrous, homogeneous powder. This powder was decomposed by flash heating to  $700^\circ\text{C}$ . Subsequent heat treatments, pelletization, and slicing resulted in  $(1\text{ mm})^2$  ceramic bars ready for analysis.

**Method B: Sol-Gel.** A citric acid/ethylene glycol mixture was condensed at  $165^\circ\text{C}$ , then diluted with water via the Pechini Method. To this solution, correct proportions of the metal acetates were added resulting in a homogeneous mixture. If the particular acetate of a dopant was not available, an organometallic substitution, not affecting the final composition,



was made. The solution was reduced in volume and slowly heat treated to 250°C. At this time the glassy gel was crushed followed by further heat treatment to 900°C. Subsequent pelletization, cutting, and heat treatment provided (1mm)<sup>2</sup> ceramic bars ready for analysis.

**Instrumental Analyses:** The (1mm)<sup>2</sup> bars were examined by a number of analytical techniques. Small portions of the pellets (~5mg) were used in ac magnetic susceptibility tests. Information concerning the  $T_c$  onset,  $T_c$  midpoints, and general, shape of the  $T_{c1}$  and  $T_{c2}$  curves was obtained by this method.

Bulk critical current densities were obtained by placing four silver contacts at points along the (1mm)<sup>2</sup> bar. Lowest resistivities of these silver contacts were obtained by placing four small metal disks on the metal bar, heating briefly at 970°C, and annealing at 450°C in oxygen for four hours. Resistivities of  $10^{-6-7}$  ohm-cm<sup>2</sup> could be obtained by this method. Many of the earlier samples were recorded using silver paste contacts that had been annealed to 450°C for four hours in oxygen. Silver and/or copper leads were then soldered onto the silver contacts using indium metal and critical current densities were recorded at liquid nitrogen temperatures and no applied field.

Metallography was performed on polished sections of the sintered bars. Additionally, the samples were mounted and scanning electron microscopy was performed to obtain additional information about the microstructure and morphology of these materials.

Elemental analyses (ICP) were performed on representative samples of these materials through Amtest, Inc., of Redmond, WA. Samples were scanned for trace impurities (ppm) as well as their major components (%) during these analyses.

## **RESULTS AND DISCUSSION:**

**Synthesis:** Preparation of these materials by the sol-gel or freeze-drying techniques allows for the formation of homogeneous, fine grained powders, a fact that has been confirmed by ICP and

microscopic analysis. By adding the dopants into the precursor solution mixture, one is able to achieve an atomic distribution of the dopant metals throughout the 123 matrix. This allows for some unique consequences of the dopant materials to be observed, one's that would normally be missed in normal solid state chemical preparation. This is most readily observed in the case of the dopant silver. To introduce silver into the  $\text{YBa}_2\text{Cu}_3\text{O}_{7-x}$  matrix, one may add it in a number of different ways. It may be added to a precursor mixture as either silver powder or silver oxide, or it may be added as a soluble complex in the precursor solution. Marked differences in the properties of the resultant materials are noted by utilizing the former method including the predominance of silver/copper eutectics. This arises because the distribution of silver formed in the transformation to ceramic product is not very uniform. The silver material has a tendency to ball up in areas along the grain boundary. Conversely, if the silver is distributed atomically throughout the structure, it has a tendency to be soluble in the 123 matrix up to certain concentrations. Different morphology and superconducting properties are observed when this occurs.

For the basis of comparison, all of the doped materials were heated according to identical heat treatment schedules. The values chosen were those that had previously been successful in the formation of undoped  $\text{YBa}_2\text{Cu}_3\text{O}_{7-x}$ . Thus, all samples were heated to  $970^\circ\text{C}$  for twelve hours followed by an anneal at  $450^\circ\text{C}$  all in an oxygen atmosphere. Other heat treatment schedules were attempted, but for the majority of dopant materials, this one resulted in the highest quality materials.

**Flux Exclusion Measurements:** Flux exclusion curves were recorded for all of the dopant materials. Large differences in the shape of the curve were noted throughout the spectrum of dopant metals used. These differences manifest themselves as two separate  $T_c$  values,  $T_{c1}$  and  $T_{c2}$ , as shown in a representative curve, depicted in Figure 1. The amplitude and position of the midpoint of these  $T_c$  values was more easily derived by calculating and plotting the derivatives of these curves. Differences in the shape and

TITLE:SG24(1%Co) 978/12/450/4/450/4 02 pel amp=0

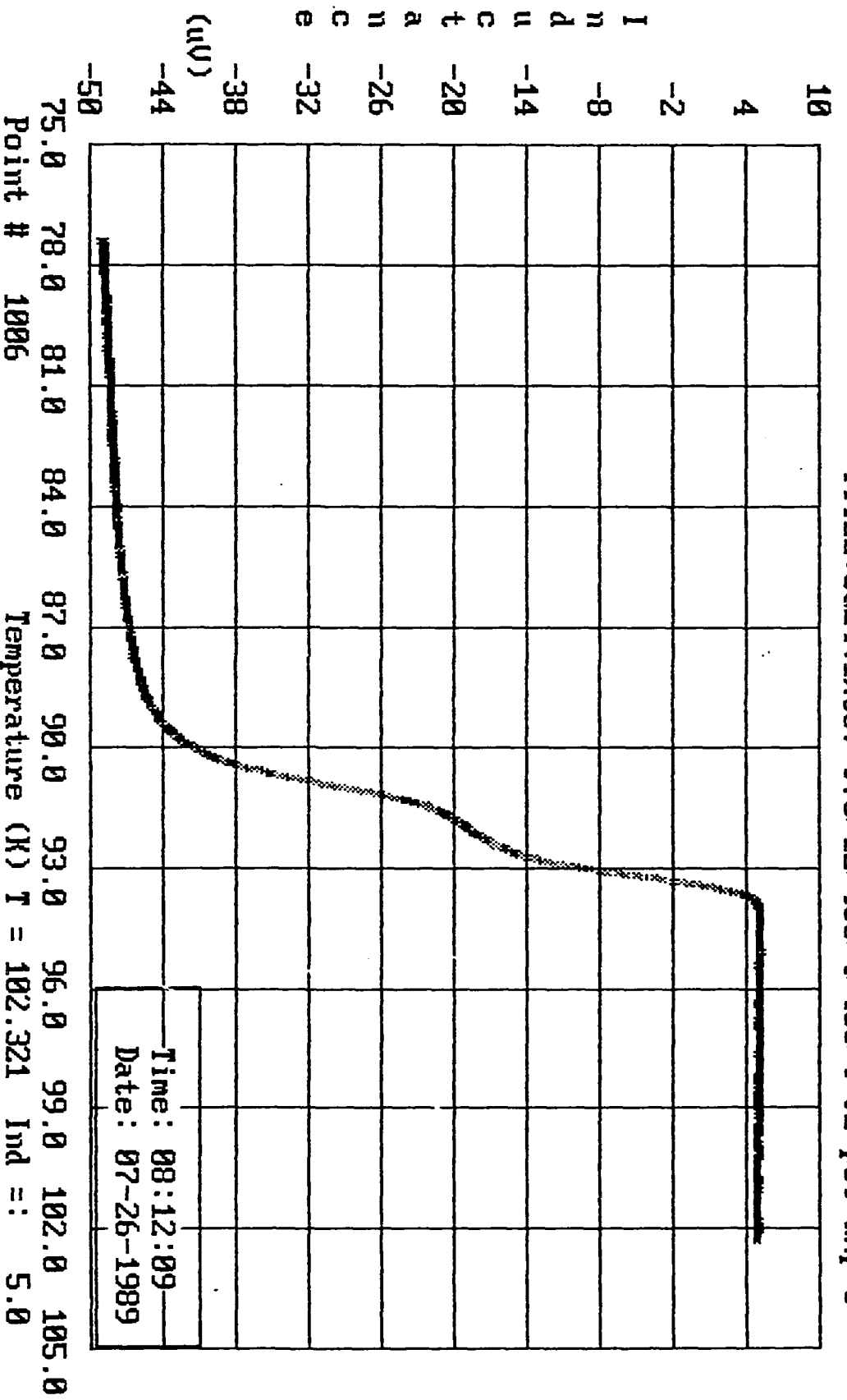


Figure 1. AC Magnetic Susceptibility Curve for the Doped Sample  $\text{YBa}_2\text{Cu}_3\text{Co}_{0.01}\text{O}_{7-x}$ .

position of  $T_{c1}$  and  $T_{c2}$  were readily seen by this method as represented in Figure 2. Values for  $T_{c1}$  and  $T_{c2}$  for all of the dopant materials, at least those observed down to liquid nitrogen temperatures, are recorded in Table 1.

As discussed in previous papers, the material displaying a  $T_{c2}$  appears to be indicative of weak links in the structure. These weak links are associated with a low current transport across the grain boundaries in the material. This is evidenced by the fact that the  $T_{c2}$  disappears when the pelletized sample is crushed to the grain size and the flux exclusion remeasured. When a magnetic field is applied to the system (3.15-34.64G), the values of  $T_{c2}$  move to lower and lower temperatures. Figure 3 displays the values of  $T_{c2}$  plotted against the number of valence electrons for the first row transition metal series. This corresponds to what is observed in measuring critical current densities. As the magnetic field is increased at liquid nitrogen temperatures, the critical current density goes down, corresponding to the amount of weak links that are driven normal by the decrease in  $T_{c2}$ . This occurs until all of the weak links are gone. And this is what is experimentally observed in these dopant materials. For the materials that display a higher  $T_{c2}$ , there is a general tendency to possess higher current carrying capacity. For example, the 1% Co sample had a  $T_{c2}$  that varied from 91.01K to 84.76K over the applied magnetic field range from 3.15G to 34.64G. A 1% Mg sample had a  $T_{c2}$  that varied from 80.17K to 79.00K over the same applied field range. If one examines the  $J_c$  values (uncorrected for self field) for these two materials at liquid nitrogen temperatures, for 1% Co  $J_c=190$  A/cm<sup>2</sup> and for 1% Mg  $J_c=16$  A/cm<sup>2</sup>. (Note: These values were measured using silver paste contacts annealed for four hours in oxygen at 450°C. Considerably higher values have been realized for across the board measurements using silver metal contacts melted directly onto the substrate.)

One also notices a change in the amplitudes of  $T_{c1}$  vs.  $T_{c2}$  as one spans the range of metal dopants. However, these numbers are not absolute numbers and may only be compared on a qualitative

SG24 (1%Co) 970/12/450/4 02 H=3G

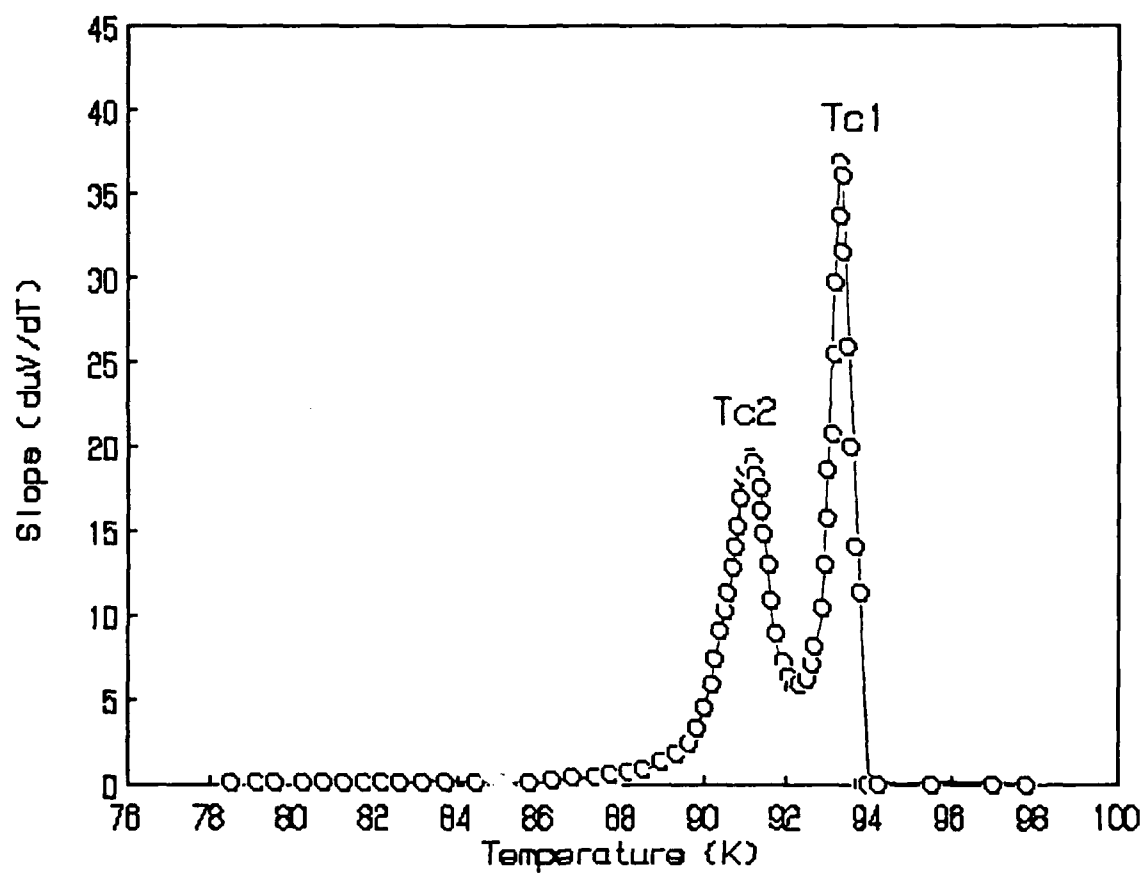
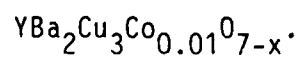


Figure 2. Derivatized AC Magnetic Susceptibility Curve Showing Values of Tc1 and Tc2 for the Doped Sample



**Table 1. Tc Midpoint Values for Doped Superconductor Materials.**

<u>Sample</u>	<u>Dopant</u>	<u>Tc(1)</u>	<u>Tc(2)</u>
SG15-0	Ti	91.50	88.20
SG15-2		93.27	86.04
SG15-4		93.07	81.29
SG16-0	V	93.55	88.28
SG16-2		93.25	84.62
SG16-4		93.10	78.46
SG17-0	Pb	91.78	88.70
SG17-2		91.20	87.14
SG17-4		91.17	87.86
SG23-0	Mn	92.19	89.53
SG23-2		92.25	87.71
SG23-4		91.82	83.75
SG24-0	Co	93.26	91.01
SG24-2		93.17	90.33
SG24-4		92.64	84.76
SG25-0	Ni	90.19	85.26
SG25-2		91.21	84.07
SG25-4		90.60	85.46
SG26-0	Sr	90.35	87.76
SG26-2		89.22	86.29
SG26-4		89.68	82.06
SG27-0	Mg	86.21	80.17
SG27-2		85.83	79.34
SG27-4		85.89	79.00
FD30-0	--	---	89.82
FD30-2		91.30	87.60
FD30-4		91.73	84.68
FD58-0	Ag	92.84	90.72
FD58-2		92.75	88.99
FD58-4		92.19	85.06
SG35	La	91.29	83.83
SG36	Cr	91.81	88.06
SG33	Zn		
SG44	Fe		

## Tc(2) Midpoint vs. # of d Electrons

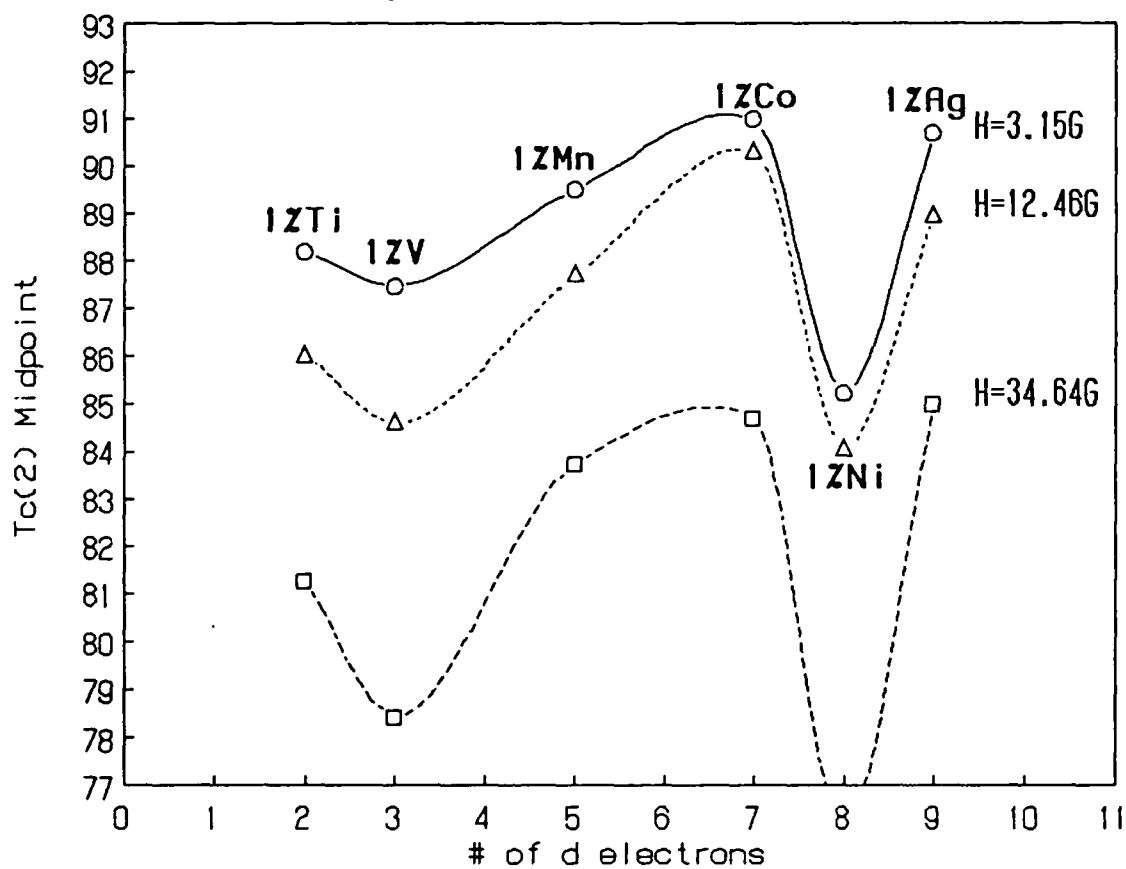


Figure 3. Tc2 Midpoint Values for the First Row Transition Metal Series vs. the Number of Valence Electrons.

basis. A dopant (1%) such as cobalt, which displayed good superconducting properties, showed a higher ratio of  $T_{c1}/T_{c2}$  than dopants which displayed poorer properties, such as 1% Ni. Thus, the latter material conducts through its weak links more than higher  $J_c$  materials, and these weak links are easily destroyed by the application of small magnetic fields leading to large losses of superconductivity. By this method, one can see how materials with fewer weak links, and smaller  $T_{c2}$ 's, are better superconductors.

**Current Density Measurements:** Bulk current density measurements were recorded for all of these materials at liquid nitrogen temperatures and are recorded in Table 2. Most of these measurements were performed using silver paste contacts and are thus do not represent the optimum values for these samples. However, for the purpose of comparison, these values may be used. Figure 4 is a plot of the current density (corrected for self field) vs. the number of valence electrons for the transition metal series. This plot demonstrates the effect that the transition metal series has on the current carrying capacity of the superconductors. With the exception of the noble metal silver, the current density seems to follow a smooth distribution with a maximum at the center of the transition metal series, around manganese and cobalt. Near the ends of the series, namely titanium and zinc, much lower current densities were observed. As mentioned earlier, the current density appears somewhat related to the values of  $T_{c2}$ , with greater current densities being obtained for materials with higher values of  $T_{c2}$ .

**Microscopy.** Representative samples of these dopant materials were examined by scanning electron microscopy (SEM) and metallography. Both fractured portions and the surface were examined. Even at these minimal dopant levels, i.e. one percent, significant changes in the microstructure of the ceramics were realized. For instance, variations in the amount of twinning were observed in samples that displayed low current densities. The 1%Ni sample had few areas of twinning and had a relatively low current carrying capacity. The 1%Pb sample had much more



**TABLE 2. Current Density Measurements for  $\text{YBa}_2\text{Cu}_3\text{M}_y\text{O}_{7-x}$  at Liquid Nitrogen Temperatures.<sup>1</sup>**

<u>Filename</u>	<u>Dopant</u>	<u>Contacts</u>	<u><math>J_c(\text{A/cm}^2)</math></u>	<u><math>J_c(0)(\text{A/cm}^2)</math></u> <sup>2</sup>
SG-10	---	Paste	272	5042
SG-15	1%Ti	Paste	86	226
SG-16	1%V	Paste	197	1313
SG-17	1%Pb	Paste	261	2490
SG-19	5%Pb	Paste	199	1475
SG-22	1%Zr	Paste	0	0
SG-23	1%Mn	Paste	196	1870
SG-24	1%Co	Paste	190	1660
SG-25	1%Ni	Paste	72	180
SG-26	1%Sr	Paste	202	1685
SG-27	1%Mg	Paste	16	17
FD-58	1%Ag	Paste	216	2400
FD-45	1%Pt	Paste	110	524
SG-35	1%La	Paste	43	
SG-36	1%Cr		173	
SG-44	1%Fe	Metal	95	

<sup>1</sup>All samples were heat treated to 970C for twelve hours in oxygen followed by an oxygen anneal for 12 hours at 450C. Silver paste contacts annealed at 450C for four hours were used unless denoted as metal contacts which were described in the text.

<sup>2</sup> $J_c(0)$  denotes current density corrected for self field effects.

## Current Density vs. # of d-Electrons

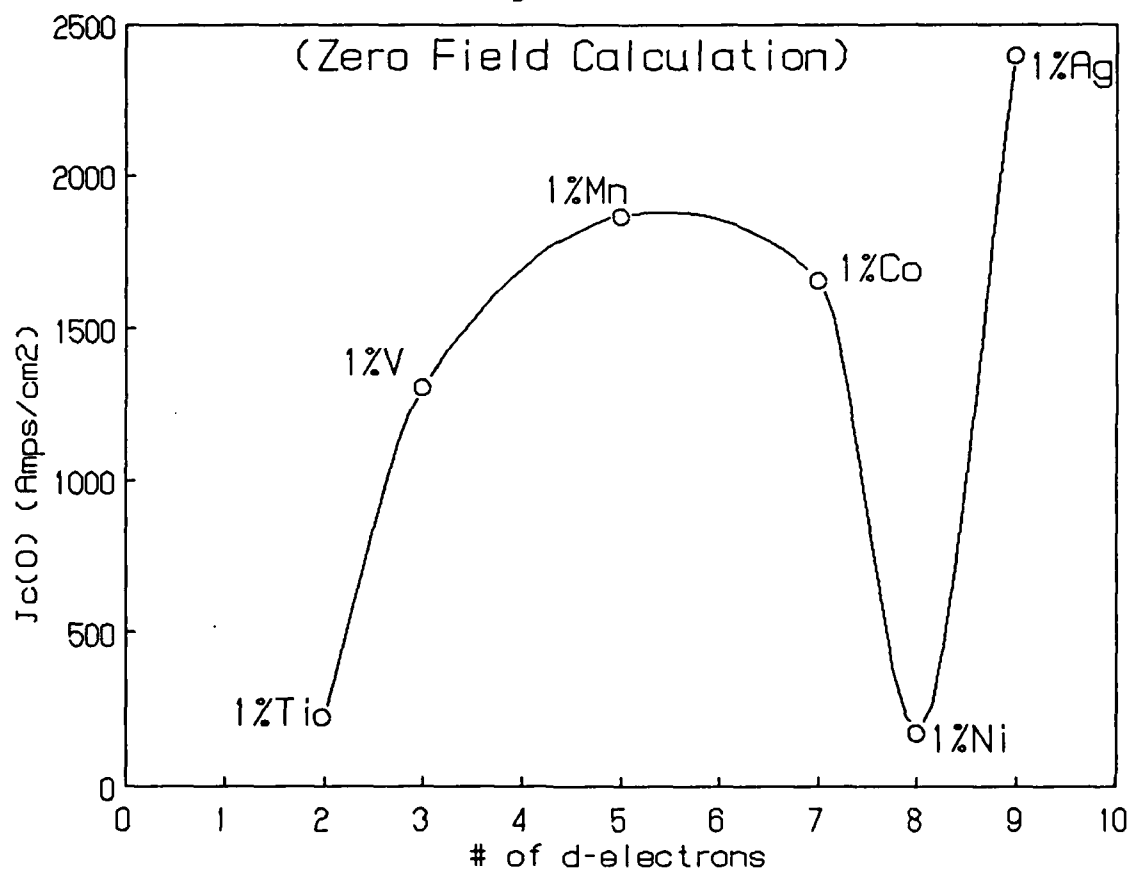


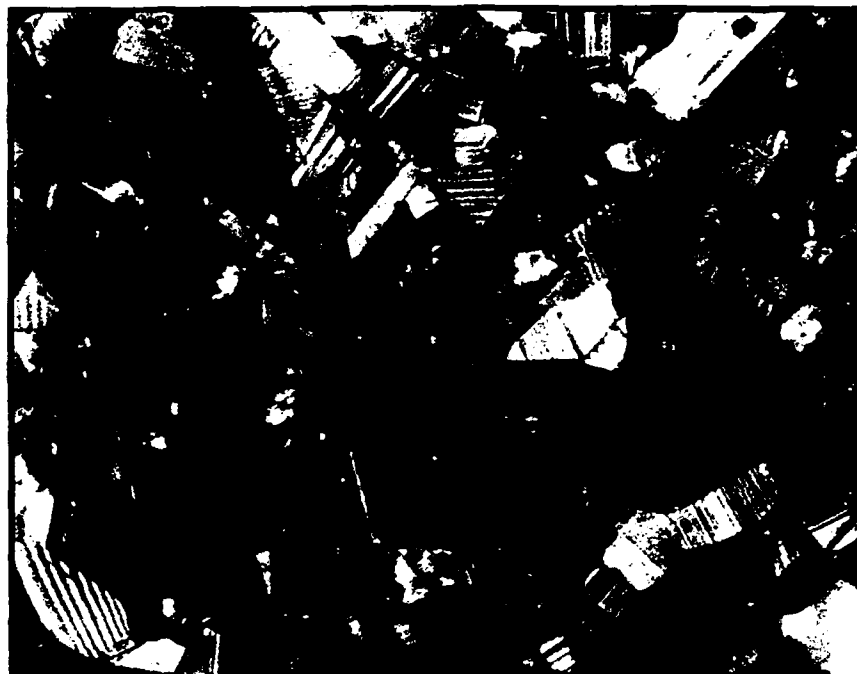
Figure 4. Current Density (as Corrected for Self Field) vs. the Number of Valence Electrons for the First Row Transition Metal Series.

extensive areas of twinning and likewise carried much greater current, Figure 5.

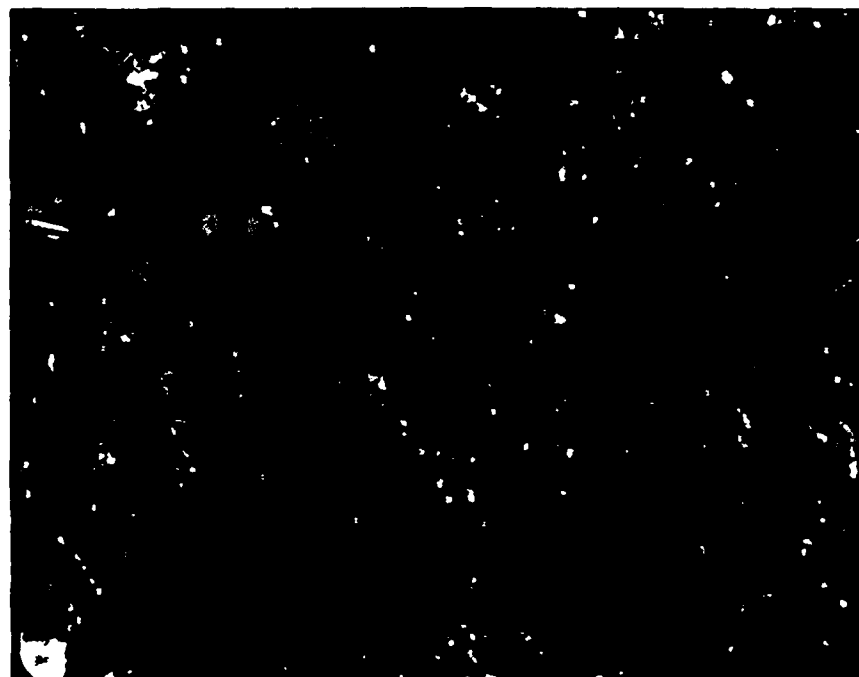
All of these samples possessed a great amount of porosity at these temperatures. In fact, in many cases it was difficult to see how it was possible to find a continuous percolation pathway throughout the entire sample. Different dopants had the ability to limit grain growth patterns in the overall structure. Additionally, in many cases it appeared that sintering was prevented between the grains by the formation of extraneous phases. Some grains seemed to be surrounded by a layer of material whose conductivity was questionable.

This was true in the cases of the 1%Ag and the 1%Ti, Figure 6. However, these two samples behaved very differently with the silver being a good superconductor and the titanium a poor superconductor. This could be explainable if the material present in the grain boundaries was simply the dopant material. If the silver was the material in the boundary layer, one can imagine how current could be carried through. However, if titanium was present in the grain boundaries, it would most likely exist as the oxide, which is an insulating material. Thus, the current carrying capacity would be severely diminished. The situation is certainly not as simplistic as this, as some of the dopant material will be alloyed into the  $\text{YBa}_2\text{Cu}_3\text{O}_{7-x}$  matrix, but an analogous situation might be occurring.

**Alloys.** A clue as to the amount of material that is present in the grain boundaries vs. that alloyed into the 123 matrix may be given by examining the shape of the  $T_c$  curves. While  $T_{c2}$  is indicative of the weak link material,  $T_{c1}$  give a good measure of the bulk matrix material. Changes in the shape of  $T_{c1}$  would therefore reflect changes in 123 matrix. This would include things like alloying of the dopant metals into the matrix and substitution into one of the matrix sites. From the derivatized curves, one can obtain values for the width at half height for both  $T_{c1}$  and  $T_{c2}$ . This may be used as a measure for the amount of alloying occurring in the material. For a sample such as 1%Co,  $\Delta T_{c1}$  is fairly small ( $\sim 2\text{K}$ ), and the cobalt would lie

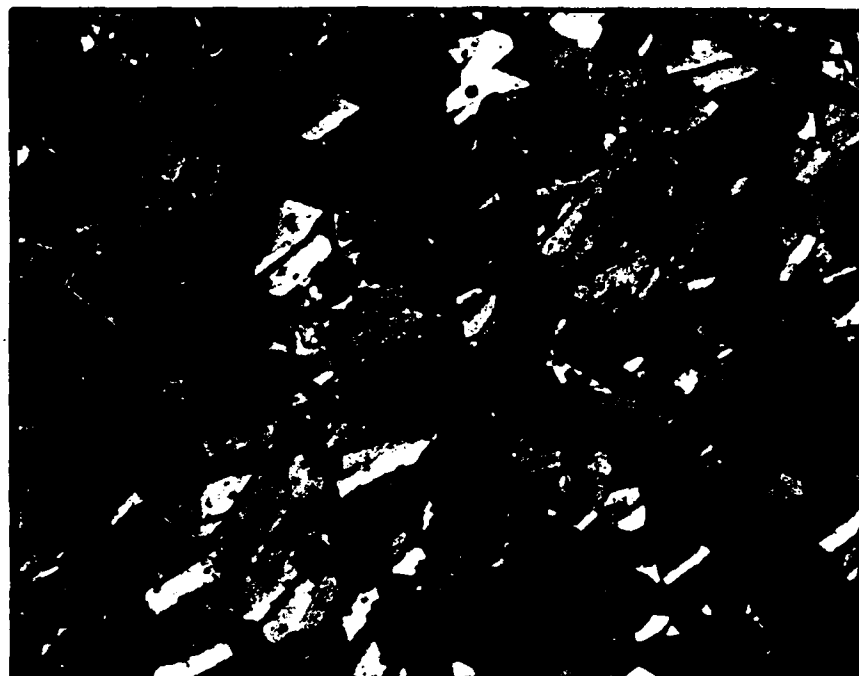


5617b-970 (1% Pb) 1000X

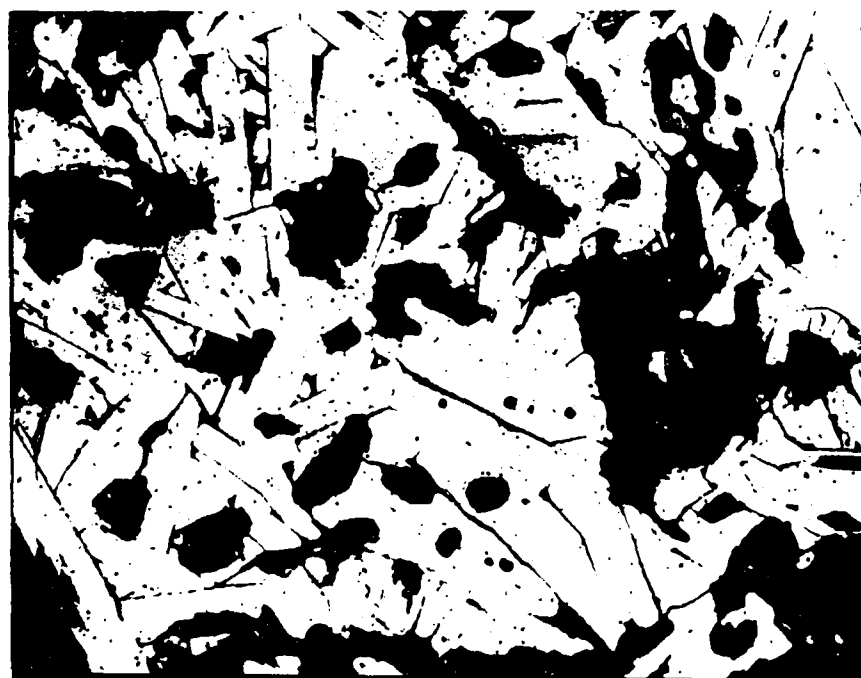


565 970 (1% Ni) 1000X

Figure 5. Optical micrographs of doped materials (1%Pb-upper; 1%Ni-lower) at 1000X showing degree of twinning.



FD58-970 1% Ag 500X



5615-970 (1% Ti) 500X

Figure 6. Optical micrographs of doped materials (1%Ag-upper; 1%Ti-lower) showing the presence of intergranular material.

outside of the metal oxide matrix. For a sample such as 1%Cr,  $\Delta T_{c1}$  is somewhat larger ( $\sim 4K$ ), the curve shape is altered significantly and would be representative of some of the material being substituted into the  $YBa_2Cu_3O_{7-x}$  matrix, Figure 7. The nature of this effect on the superconducting properties of the material is not readily discernible.

**Future Directions:** Because of the necessity of obtaining higher critical current densities for practical applications, drastic measures must be taken to alter the materials. Chemical alterations may provide the opportunity for this to occur. In order to improve the current carrying abilities of this material, the connectivity between the grains must be improved. One way to accomplish this is through liquid phase sintering, however; conventional liquid phase sintering occurs through eutectic melting which causes off-stoichiometric areas and extraneous non-superconducting phases to be present at the grain boundaries. Through the addition of doped metals, one may be able to depress the melting point of the alloyed material, thus allowing liquid phase sintering to take place through different means. To obtain a measure of the melting point depression in these materials, one must do differential thermal analyses (DTA). If a material can be found that exhibits a lower melting temperature, one may be able to induce intergrain epitaxial growth. As 123 material grows between the grains, in an idealistic fashion, gluing the grains together, the dopant material will still remain. In most cases, the dopant will be a hindrance to overall transport mechanisms. Therefore a method for removing the dopant material after it has served its use would need to be devised. This may be accomplished in the case of lead. Lead has a melting point of  $328^\circ C$  and a boiling point of  $1740^\circ C$ . Thus, at the sintering temperatures that are used in preparing these samples ( $900-1000^\circ C$ ) the lead is volatilizing out of the sample at a certain rate. Since lead melts at such a low temperature, it also has the advantage of increasing the density of the samples through liquid phase (namely lead) sintering. For a case where two pellets of the same size, one undoped and one with 10% Pb, were

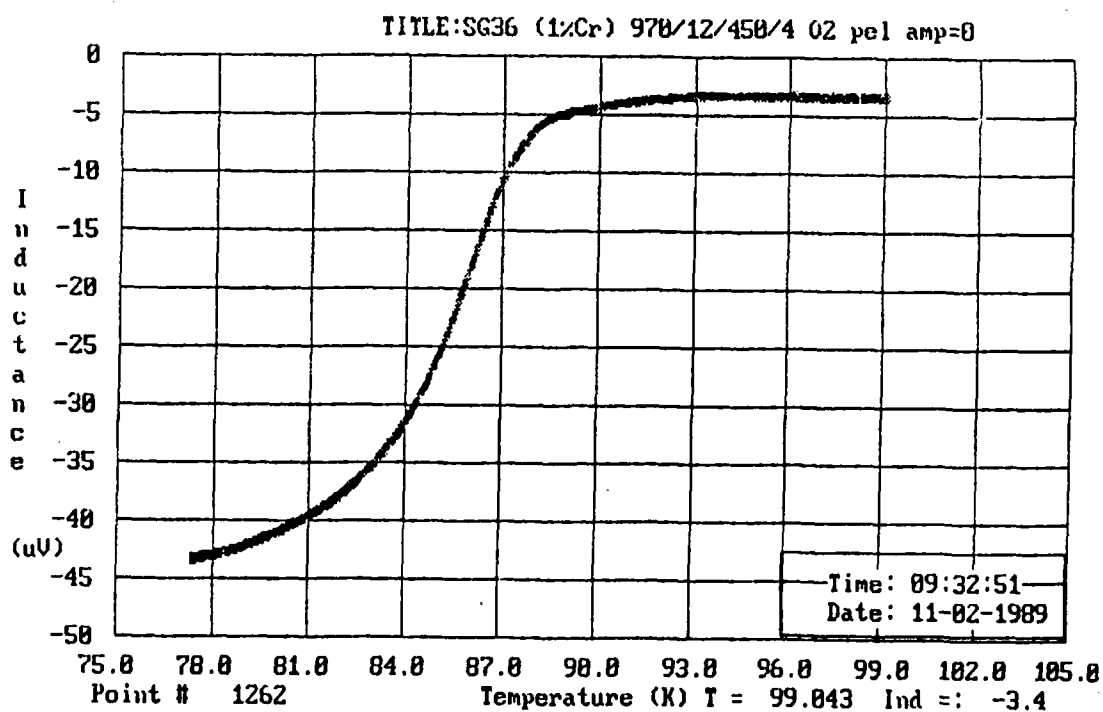
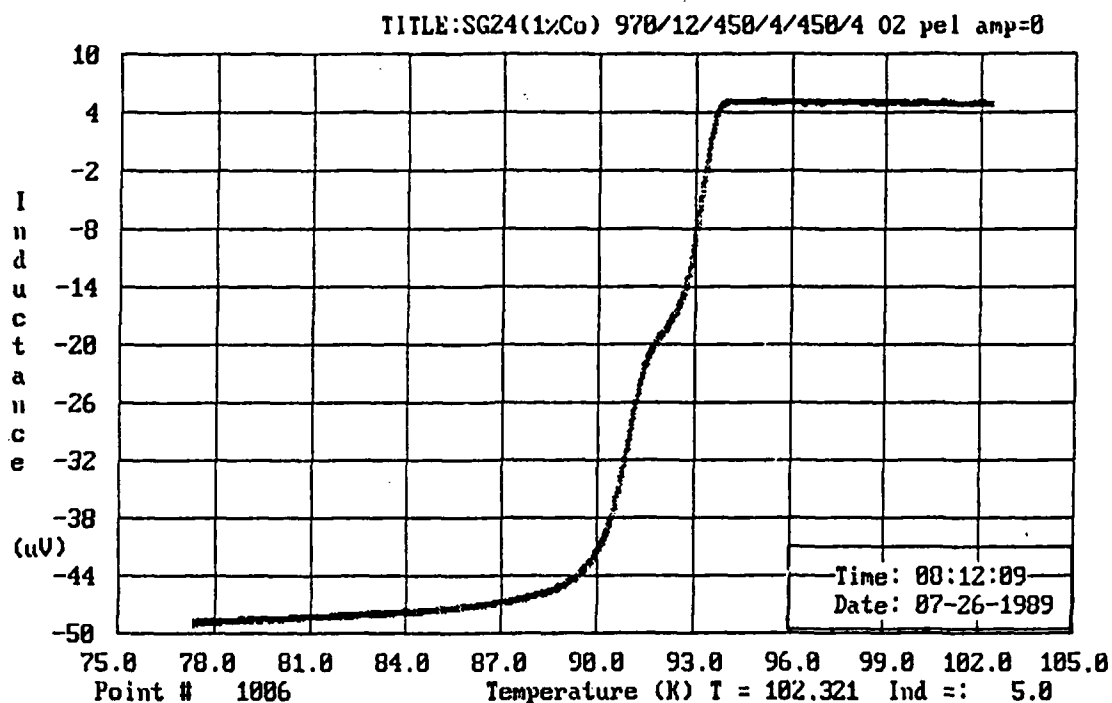


Figure 7. AC magnetic susceptibility curves for two comparable doped samples (1%Co-upper; 1%Cr-lower) illustrating the variable effect that these metal dopants have on the shape of the  $T_c$  curve.

sintered side by side at 910°C, the lead sample experienced a shrinkage to 2/3 the size of the undoped material.

These doped materials will also be looked at in the context of melt texturing. The altered grain growth patterns associated with the doped materials may be used to our advantage in producing aligned grains with good connectivity. Selected specimens from this preliminary work will be used in such a future study.

#### **ACKNOWLEDGEMENTS**

The authors gratefully acknowledge the support by DARPA/AFOSR under Contract No F49620-88-C-0143.



# Summary of Lattice Parameter Variation Analysis in $\text{YBa}_2\text{Cu}_3\text{O}_{7-x}$ by a Novel Technique

*Brad Thiel*

*2 November, 1989*

## 1.0 Introduction

Local lattice parameter variations in  $\text{YBa}_2\text{Cu}_3\text{O}_{7-x}$  have been observed and reported in the literature by many workers<sup>1</sup>. Work done by Cava et. al.<sup>2</sup> and Tarascon et. al.<sup>3</sup> suggest that these variations may be caused by changes in the oxygen concentration in the lattice. It has also been demonstrated by a number of researchers, including Cava and Tarascon, that the bulk lattice parameters appear to be related to the onset of superconductivity,  $T_c$ . Theoretical work done by Khachaturyan<sup>4</sup> indicates that oxygen concentration variations are to be expected, but occur in an ordered manner. Each of these works will be reviewed followed by a discussion of our own work substantiating their results.

## 2.0 Literature Review

### *2.1 Cava and Batlogg, et. al.<sup>2</sup>*

Samples prepared from simple metal oxides were annealed in flowing oxygen to produce what they claimed to be an oxygen stoichiometry of 7.0. The samples were subsequently annealed in an oxygen gettering environment to produce samples with varying oxygen contents

as determined by weight loss. Bulk lattice parameters were determined using conventional x-ray diffraction and were plotted versus oxygen content. They speculated that oxygen was being removed from the "b" direction lattice sites in the Cu-O basal plane. The formation of these oxygen vacancies shortened the average value of the b lattice parameter but also resulted in a corresponding increase in the average a value. The lattice parameters converge, that is the structure becomes tetragonal, around oxygen 6.5. The resulting lattice parameter is  $3.86\text{\AA}$ , exactly the average value of the  $a_0$  and  $b_0$  parameters for oxygen 7.0.

Additionally, the superconducting onset temperature ( $T_c$ ) was measured and plotted with respect to oxygen content. It was found that removal of up to 0.2 oxygens had little effect on the transition onset, after which, the  $T_c$  fell to around 60K. This plateau was also maintained until oxygen dropped below 6.5. They claimed this behavior is consistent with the ordering of oxygen in the lattice, occurring at a stoichiometry of 6.67. However, the lattice parameters which are recorded show a fair degree of scatter along with some minor deviations which are difficult to rationalize. The problems come from two sources. First, the lattice parameters are determined from x-ray diffraction and only represent a bulk average, and second, their experiment assumes that a constant variation of oxygen content is allowed. This assumption breaks down in the presence of oxygen ordered domains, and necessarily breaks down on an atomic scale. A much more reasonable explanation involves the existence of ordered oxygen domains with specific stoichiometries and lattice parameters as proposed by Khachaturyan and evidenced by Chen and ourselves. In this case, when oxygen is first lowered from 7.0, domains of another specific oxygen content are formed. As overall oxygen content is lowered, the ratio of these domains adjusts accordingly, until the creation of a third variant is favored. Because, initially, most of the sample remains at oxygen 7.0, it is reasonable to expect the  $T_c$  to be relatively invariant.

Similar experiments were also performed by Tarascon and Bagley<sup>3</sup>, using TGA methods to determine bulk oxygen content. They were able to produce lattice parameter and  $T_c$  versus oxygen content virtually identical to those of Cava. Their experiments also suffered from the same over-sights. In addition to  $T_c$  curves, they also showed flux exclusion curves for various samples. Almost all of these showed a double stepped form, with drops at 91K and at 60K. This behavior is in accordance with the  $T_c$  versus oxygen content shown by both teams when viewed from our proposed perspective of specific oxygen ordering values.

## 2.2 Chen, et. al.<sup>5</sup>

Chen performed TEM analysis on the samples studied by Cava, et. al., looking for further evidence of the oxygen ordering. By looking at single crystals he was able to reduce, but not eliminate, the problems associated with examining a bulk sample. Because subdomains still exist within single grains, "poly-domain" effects are still present much as the way polycrystalline effects are notable in bulk samples. Evidence for vacancy ordering came from the appearance of superlattice reflections occurring between the (000) and (010) lattice reflections. Because the material is twinned, these reflections appear to occur in both the a and b directions. The strongest evidence came from samples with bulk oxygen content of 6.67. These showed superlattice reflections at the  $(1/3, 0, 0)$  and  $(2/3, 0, 0)$  positions, indicating a vacancy ordering of  $1/3$ , consistent with the oxygen stoichiometry. This would also suggest that the sample did indeed possess a uniform oxygen concentration as  $1/3$  is one of the values allowed in Khachaturyan's work. Similar reflections occurred at the position  $(1/2, 0, 0)$  for oxygen 6.5. For other oxygen contents, the extra spots would appear to be elongated or smeared. This is actually the result of multiple periodicities being present as would be the case when the bulk oxygen content is not in accordance with the integer ratios specified by Khachaturyan. Other reflections were also seen in the  $2/5$  and  $3/5$  positions for some oxygen stoichiometries.

These results prompted Chen to postulate that superlattice reflections should be observed at position  $(x, 0, 0)$  for local oxygen stoichiometry  $7-x$ . No other extra reflections corresponding to other values of  $x$  were reported. Although it is generally true that a reflection at a specific position is indicative of some oxygen content, this explanation places no restriction on the values of  $x$  permitted, allowing for a continuous variation. This, although sensible enough, is not a thermodynamically acceptable situation. An explanation for the lack of other values of superlattice reflections being absent comes from Khachaturyan's work. Only certain periodicities are permitted, and of the allowed ordered states, only  $n/3$ ,  $n/5$ , and  $1/2$  are spaced wide enough to be distinct. Higher orders of periodicity contribute to an overall background between (000) and (100). This is especially true if multiple high order periodicities are present and overlapping. Additionally, for a given diffraction condition, an increased number of reflections in a superlattice family, requires a decreased intensity for each individual reflection. In other words, on average, the  $2/5$  and  $3/5$  reflections will be dimmer than a  $1/2$  reflection.

### 2.3 Khachaturyan and Morris<sup>3</sup>

Khachaturyan has proposed that when the oxygen stoichiometry of  $\text{YBa}_2\text{Cu}_3\text{O}_{7-x}$  drops below 7.0, that the material undergoes a series of spinodal decompositions into various phases of specific oxygen contents and ordering. The resulting "ultra-fine domains" would have oxygen stoichiometries corresponding to  $\text{YBa}_2\text{Cu}_3\text{O}_{7 - n/(2n+1)}$ . In other words, oxygen vacancies in the lattice at positions corresponding to  $\frac{n}{2n+1}$ , e.g.;  $1/3$  ( $n=1$ ),  $2/5$  ( $n=2$ ), and  $3/7$  ( $n=3$ ). The limiting case as  $n \rightarrow \infty$  is  $1/2$ . Each of these phases has an easily calculated oxygen content ranging from 7.0 for  $n=0$  to 6.5 in the limiting case. These predictions, based on theoretical thermodynamic calculations provide "quantized" values for  $X$ . Consideration of the reciprocal space consequences of this ordering predicts exactly the superlattice reflections seen by Chen but forbids the continuous variation of  $X$  which they proposed. Khachaturyan noted that such homologous oxide series are known to exist in materials with mixed valence cations as is the case with copper in the 1:2:3 case.

The direct implication of this in our work is the prediction of the existence of only certain, discrete values for  $\Delta a/a$ . Following the experiments done by both Cava and Tarascon, it also follows that these phases or domains will also have characteristic values for  $T_c$ . Thus a bulk material's superconducting transition behavior is not necessarily complex, but merely a composite of contributions from the various domains which exist. The profile of the flux exclusion curve could be predicted by the relative amounts of each domain type and their respective transition temperatures. The picture is further complicated by the affects of grain size and penetration depth.

### 3.0 Microstructure - Properties Relationship Studies

Our primary interest is to establish the relationship that exists between the various processing parameters at our control, the resultant microstructures developed under those conditions, and their impact on the subsequent superconducting properties. Among the processing variables at our disposal are heating and cooling rates, sintering time and temperatures, sintering atmosphere, deliberate doping of impurities (i.e. silver), and the overall chemical and physical homogeneity of the precursor materials. Superconducting properties that must be considered are onset temperature(s) for the superconducting transition ( $T_c$ ), the transition width for the particular sample ( $\Delta T_c$ ), total amount of flux exclusion, and critical current density. Given the inherently complex nature of the relationships between these variables, it is not

difficult to imagine that seemingly conflicting results in the literature may only be differing manifestations of the same cause. Further, it is quite conceivable that some identical properties may be achieved in samples produced by two entirely different paths. For example, the multiple periodicity domains discussed in the previous sections could easily be present in varying amounts which would give nominally identical bulk lattice parameters and oxygen contents but may have notably different  $T_c$  values. Such is the case with the four samples we have chosen to study.

### 3.1 Experimental Design

Superlattice reflections are not necessarily the only manifestations of multiple periodicity domains in the electron diffraction pattern. As previously discussed, the existence of several periodicities, particularly higher frequencies, contributing to the diffraction pattern will result in a low contrast smear between the (000) and (100) reflections with a poor signal to noise ratio. Only when samples have been processed in such a way that promotes the predominant growth of one type of periodicity can these reflections be accurately identified. For example in the case of Chen, one of the samples was subjected to conditions designed to ensure that the sample was uniformly as close to  $O_{6.67}$  as possible, thus encouraging the formation of 2/3 ordered domains.

While the superlattice reflections are secondary effects due to oxygen vacancy periodicity, another effect of the vacancies are to produce local variations in the average lattice parameters. This has the effect of changing the positions of the primary diffracted spots. Again, if a distribution of lattice parameters (periodicity domains) is present, the primary diffracted spots will be smeared out with an intensity distribution representative of the relative amounts of the periodicity domains. Taking microdensitometer traces of selected primary diffraction spots, it is possible to deconvolute the intensity distributions to return the distribution of lattice parameters. For our purposes, it is preferred not to measure the exact magnitude of the lattice parameters, but to obtain the distribution of orthorhombicity;  $\Delta a/a$ , according to the method of Sarikaya and Stern<sup>1</sup> where

$$\frac{\Delta a}{a} = \frac{2(b - a)}{b_0 + a_0}$$

In their method, the separation between the (110) type twin-split reflections in milliradians is equivalent to the local value of  $\Delta a/a$  when the sample is in a 001 orientation. Sarikaya and Stern have demonstrated that this variation exists by performing microdiffraction studies in

and around the bodies and tips of twins. By taking selected area diffraction patterns of entire single grains, the (110) type reflection will contain all of the lattice parameter distribution present in that grain. The resulting intensity distribution is created by the convolution of a  $\Delta a/a$  distribution function with some gaussian-type function related to the diffraction conditions such as structure factor and shape effects. We may obtain this gaussian diffraction function from a tracing of the ( $\bar{1}$ 10) diffracted spot which will have the same structure and shape factors but will not undergo twin-splitting. A unique feature to this system is the root-mean-square of the  $a$  and  $b$  lattice parameters is a constant for all values of oxygen content in the region of interest, that is between  $O_{7.0}$  and  $O_{6.5}$ . This implies that all of the intensity distribution will lie on an arc normal to the  $g$  vector of the diffracted spot. Hence, by tracing the (110) spots normal to their  $g$  vector, and the ( $\bar{1}$ 10) spot parallel to its  $g$  vector, we are provided with the correct gaussian shape function. Because the two-dimensional twin boundaries may cause some streaking parallel to the (110)  $g$  vector, this technique also eliminates these contributions to the intensity distribution.

Additionally, the analysis also must make the following assumptions and stipulations; the sample must be free from bends and strains which would cause smearing of the diffracted spots. This problem is eliminated for us by the use of as-processed powders so that single grains may be studied in isolation. Visual inspection of the bright-field image in the TEM also will allow the operator to evaluate the detrimental impact of any other strain fields present. Secondly, the deconvolution assumes that the kinematical approximation of diffraction applies. If the sample is too thick relative to the mean free path of the incident electrons, Bloch wave interferences will create additional effects in the diffraction volume which may be difficult to correct. Choosing very thin crystals and using higher accelerating voltages will reduce this problem. If a grain is questionable, a quick examination of the low loss region of the electron energy loss spectrum (EELS) gives a good qualitative indicator of a samples thickness to mean-free-path ratio.

### *3.2 Test Samples*

For this experiment, we chose for samples, each with unique processing histories and superconducting properties but with nominally identical x-ray diffraction patterns and oxygen contents. The goal of the project is to determine what changes at the nano-structural level might be giving rise to the variations in the properties. Information on the four samples is given in the table below.

No.	Heating Rate	Soak Temp	Soak Time	Cooling Rate	Other	$T_c$
#1	1°C·min <sup>-1</sup>	950° C	1 hr	1°C·min <sup>-1</sup>	air	93K
#2	1	950	6	1	air	93K
#3	1	950	6	1	oxygen	91K
#4	1	950	6	1	air + O <sub>2</sub> anneal	90K

In addition to the lattice parameter variation, these samples are also being studied considering such microstructural features such as grain size effects, twin size distributions, impurity phase distribution, and carbon content. However, the most realistic scenario involves a complicated interplay between many factor, some intrinsic to the material, such as penetration depth, and others specific the the sample being studied, such as grain size. Evaluation of total flux exclusion, for instance, is related to both of these which are not necessarily separable.

### 3.3 Magnetic Flux Exclusion

In order to characterize each samples response to external applied magnetic fields, magnetic flux exclusion tests are performed. The samples are placed in a 0.3T field and cooled from 95K down to 77K and the expelled flux is measured. This type of measurement indicates the onset temperature of superconductivity, the total amount of flux excluded on a per gram basis, and the width of the transition region. The transition width appears to be related to the sequential onset temperatures of the various ordered domains with the highest  $T_c$  value appearing as the bulk onset. The total amount of flux excluded is largely dependent on the particle sizes below 40 $\mu\text{m}^5$ . Average particle sizes of the grains will also be recorded in the study to confirm this correlation.

## 4.0 Results

The resulting  $\Delta a/a$  distributions were remarkable in that they did indeed show markedly different distributions but the weighted mean value coincided exactly with the bulk lattice

parameters determined by x-ray diffraction. At this time, a direct correlation with the magnetic flux exclusion properties has not been made as those measurements have not been performed yet. However, the results obtained from the distributions, when interpreted according to the previously cited literature, suggest a connection between distribution of periodicity domains indicated by the  $\Delta a/a$  distributions and the behavior of the flux exclusion curves over the transition temperature range,  $\Delta T_c$ .

Most significantly, the  $\Delta a/a$  distributions indicated that only certain values seemed to be allowed, those values being 2.05%, 1.9, 1.77, 1.71, 1.50, 1.30, and 1.0%. By combining the work done by the discussed literature on lattice parameters versus oxygen content, with the theory of ordered periodicity domains, and our own work, we were able to derive an approximate equation which accurately describes the change of lattice parameters with total oxygen content. A plot of the  $a$  and  $b$  parameters versus oxygen content is shown in figure 1, with an inset showing the experimental results typical of the previously discussed authors and several others. A plot of  $\Delta a/a$  versus oxygen content is straightforward from this information. (Figure 2) The equations are as follows;

$$a = 3.818 - 0.0068 * \ln(2x - 1)$$

$$b = 3.898 + 0.0061 * \ln(2x - 1)$$

where  $x$  is the ordering parameter. It is straightforward to show that  $x$  is also the value of  $\delta$  in the oxygen stoichiometry  $6 + \delta$  goes from 0.5 to 1.0 giving an oxygen stoichiometry range of 6.5 to 7.0. This allows the argument of the log function to range from 0 to 1.0 making this the fraction of orthorhombic unit cells present at that local oxygen concentration. It is important to note that while the average  $b$  lattice parameter naturally decreases when oxygen is removed from that direction, the average  $a$  parameter actually increases with removal of oxygen from  $b$ . When the low order values of Khachaturyan's ordering parameter are put in for  $x$ , namely, 1.0, 4/5, 5/7, 2/3, 3/5, 5/9, and 1/2, the resulting  $\Delta a/a$  values are identical to those found by our deconvolution analysis.

## 5.0 Future Work

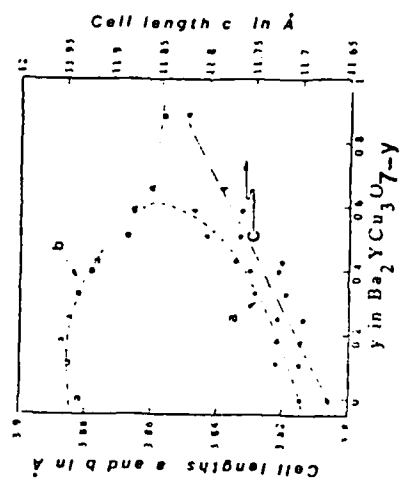
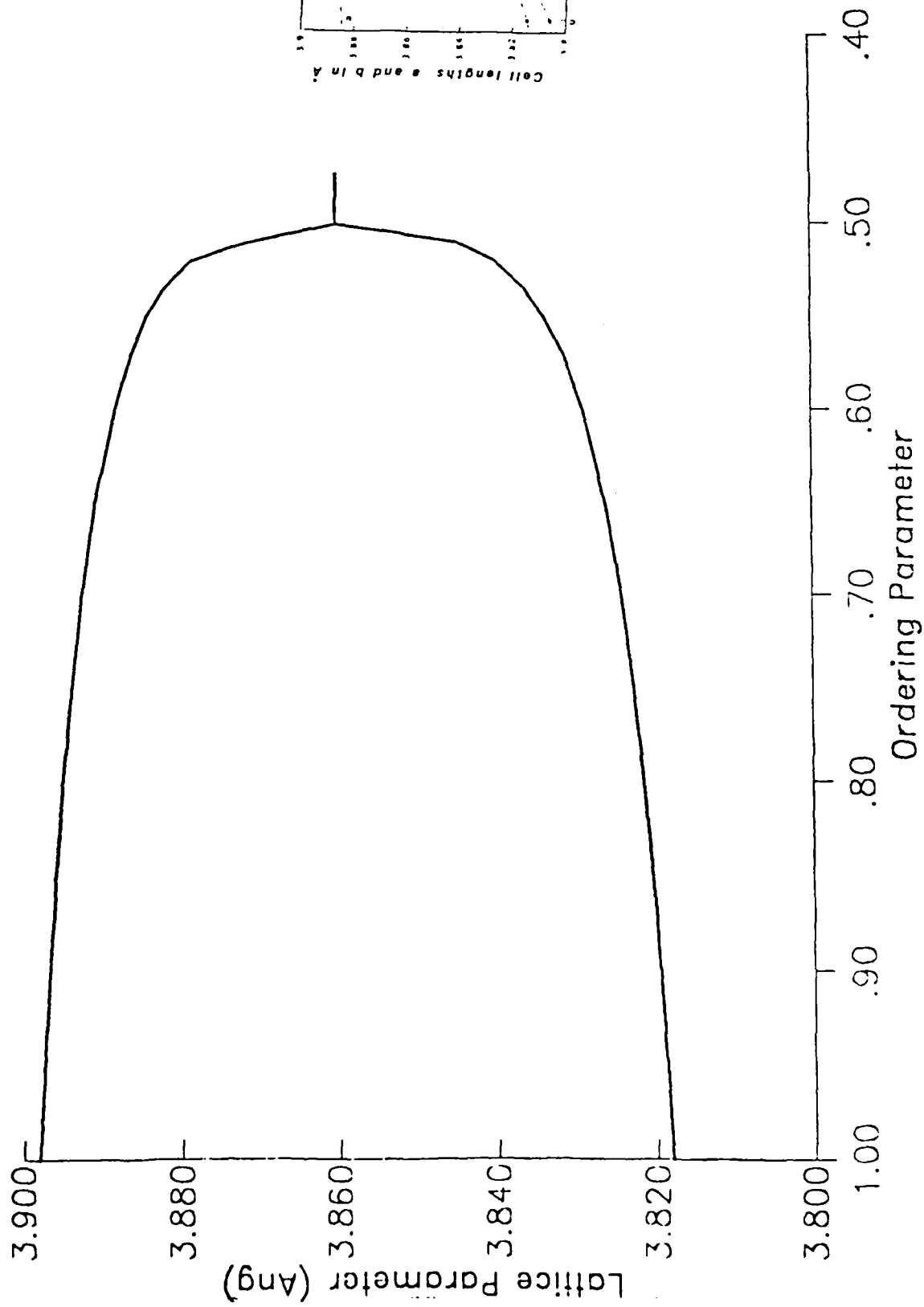
Various other studies still need to be completed to fully characterize the relation between properties and microstructure. Primarily, the magnetic flux exclusion measurements are necessary to confirm our results presented here. Additionally, twin size distribution studies are

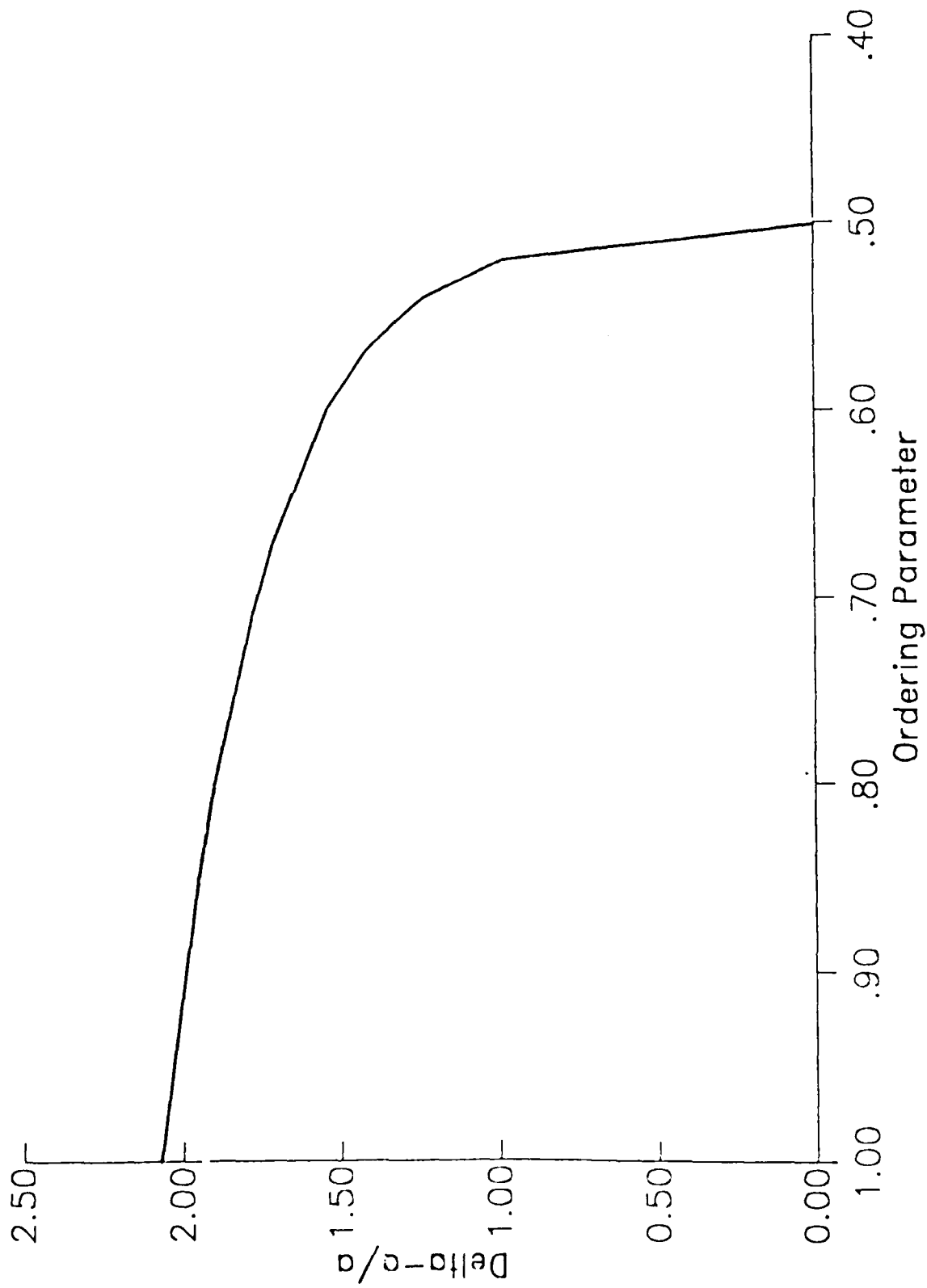


currently being performed to determine if any correlation exists there. Finally, carbon contents of the four samples are being carried out to detect and quantify the presence of carbon and possibly the form. This information may provide clues as to the location of carbon in the microstructure.

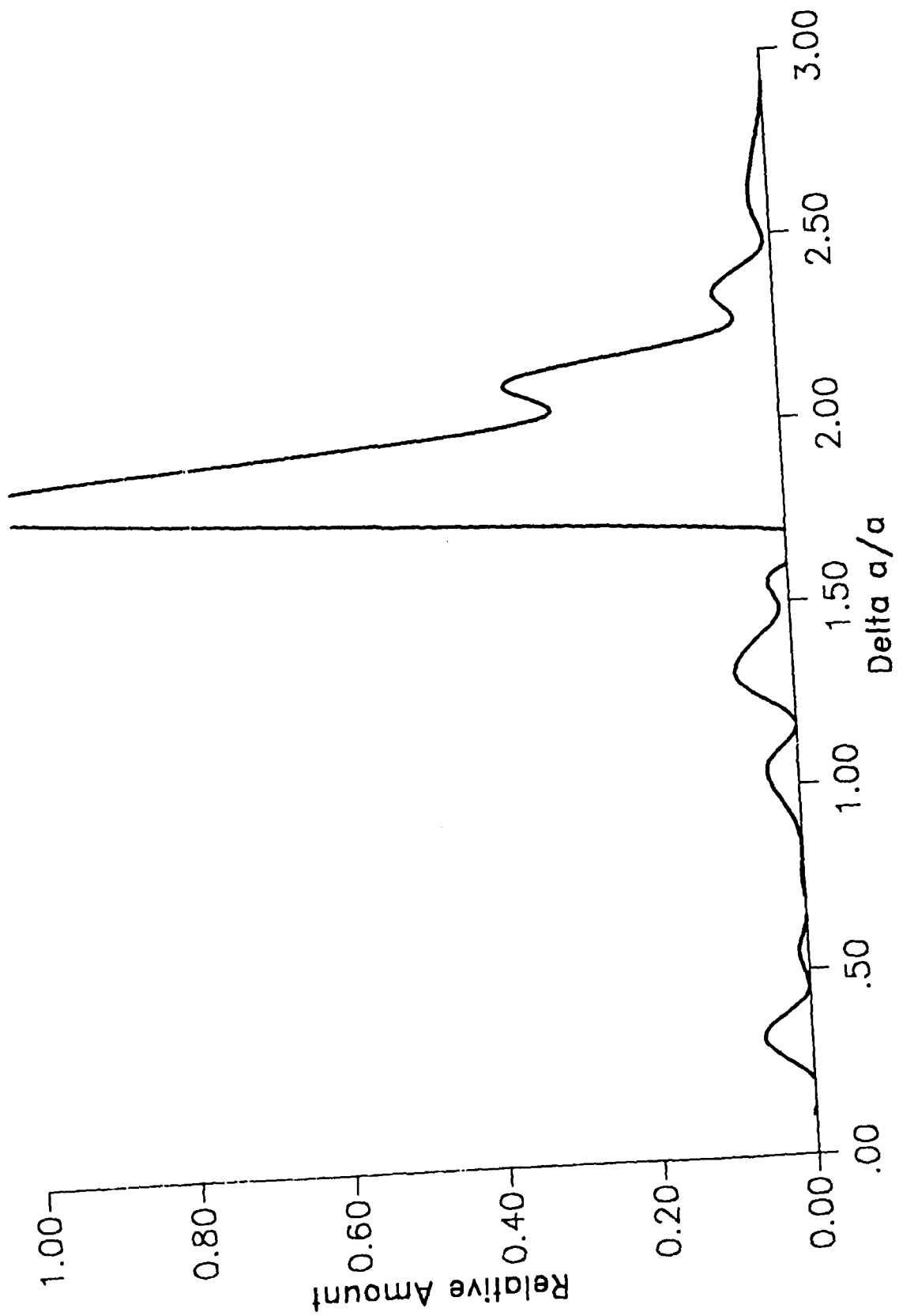
## 6.0 References

1. M. Sarikaya and E.A. Stern, "Local Structural Variations in  $\text{YBa}_2\text{Cu}_3\text{O}_{7-x}$ ", Phys. Rev. B., Vol. 37, No. 16, pp. 9373-9381, 1988.
2. R.J. Cava, B. Batlogg, C.H. Chen, E.A. Reitman, S.M. Zahurak, and D. Werder, "Single Phase Bulk Superconductor in Annealed  $\text{Ba}_2\text{YCu}_3\text{O}_{7-x}$  ( $0.3 < x < 0.4$ ) with Correlated Oxygen Vacancies in the Cu-O Chains", Phys. Rev. B., Vol. 36, p 5719-5721, 1987
3. J.M. Tarascon and B.G. Bagley, "Oxygen Stoichiometry and the High  $T_c$  Superconducting Oxides", MRS Bulletin, p 53-57, January 1989
4. A.G. Khachaturyan and J.W. Morris, Jr., "Homologous Series Transient Oxides in Nonstoichiometry High  $T_c$   $\text{YBa}_2\text{Cu}_3\text{O}_{7-x}$ ", Phys. Rev. Lett.
5. A.D. Hibbs, F.J. Eberhardt, A.M. Campbell and S. Male, "Effect of Particle Size on the Magnetization of High  $T_c$  Powders", Cryogenics, Vol. 28, pp. 678-680, 1988.

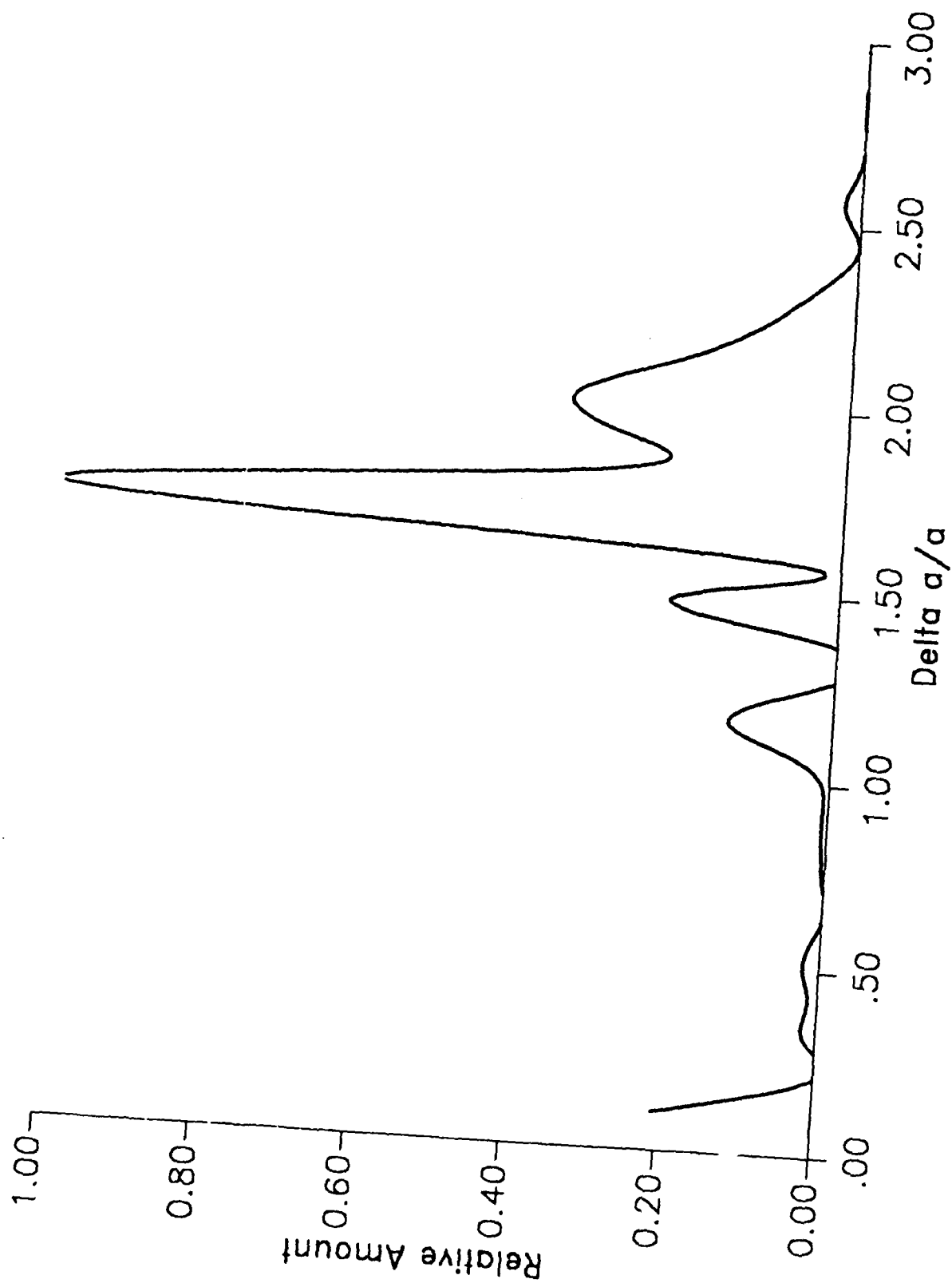




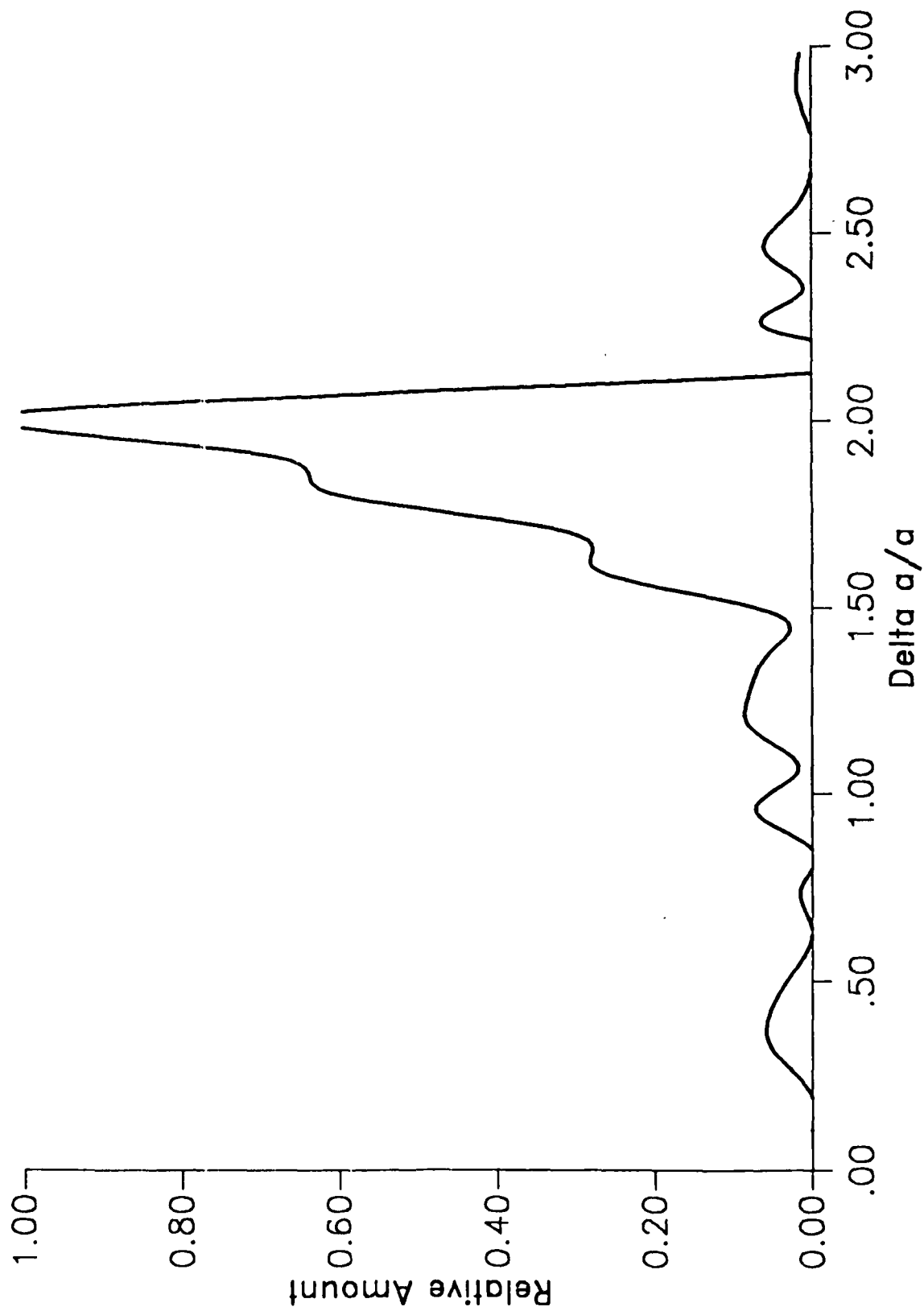
1/950/1/1 AIR



1/950/6/1 AIR



1/950/6/1 02



1/950/6/1 AIR +  
5/450/12/1 02

